

1 SEARCH FOR PRODUCTION OF A HIGGS BOSON AND A SINGLE TOP
2 QUARK IN MULTILEPTON FINAL STATES IN pp COLLISIONS AT $\sqrt{s} = 13$
3 TeV.

4 by

5 Jose Andres Monroy Montañez

A DISSERTATION

7 Presented to the Faculty of

8 The Graduate College at the University of Nebraska

In Partial Fulfilment of Requirements

10 For the Degree of Doctor of Philosophy

11 Major: Physics and Astronomy

12 Under the Supervision of Kenneth Bloom and Aaron Dominguez

13 Lincoln, Nebraska

14 July, 2018

15 SEARCH FOR PRODUCTION OF A HIGGS BOSON AND A SINGLE TOP
16 QUARK IN MULTILEPTON FINAL STATES IN pp COLLISIONS AT $\sqrt{s} = 13$
17 TeV.

18 Jose Andres Monroy Montañez, Ph.D.

19 University of Nebraska, 2018

20 Adviser: Kenneth Bloom and Aaron Dominguez

²¹ Table of Contents

²²	Table of Contents	iii
²³	List of Figures	viii
²⁴	List of Tables	xiii
²⁵	1 Theoretical approach	1
²⁶	1.1 Introduction	1
²⁷	1.2 Standard model of particle physics	2
²⁸	1.2.1 Fermions	4
²⁹	1.2.1.1 Leptons	5
³⁰	1.2.1.2 Quarks	7
³¹	1.2.2 Fundamental interactions	11
³²	1.2.3 Gauge invariance.	15
³³	1.2.4 Gauge bosons	17
³⁴	1.3 Electroweak unification and the Higgs mechanism	18
³⁵	1.3.1 Spontaneous symmetry breaking (SSB)	26
³⁶	1.3.2 Higgs mechanism	30
³⁷	1.3.3 Masses of the gauge bosons	33
³⁸	1.3.4 Masses of the fermions	34

39	1.3.5	The Higgs field	35
40	1.3.6	Production of Higgs bosons at LHC	36
41	1.3.7	Higgs boson decay channels	40
42	1.4	Experimental status of the anomalous Higgs-fermion coupling	42
43	1.5	Associated production of a Higgs boson and a single top quark	44
44	1.6	CP-mixing in tH processes	49
45	2	The CMS experiment at the LHC	54
46	2.1	Introduction	54
47	2.2	The LHC	55
48	2.3	The CMS experiment	65
49	2.3.1	CMS coordinate system	68
50	2.3.2	Tracking system	70
51	2.3.3	Silicon strip tracker	73
52	2.3.4	Electromagnetic calorimeter	74
53	2.3.5	Hadronic calorimeter	76
54	2.3.6	Superconducting solenoid magnet	77
55	2.3.7	Muon system	79
56	2.3.8	CMS trigger system	80
57	2.3.9	CMS computing	81
58	3	Event generation, simulation and reconstruction	86
59	3.1	Event generation	87
60	3.2	Monte Carlo Event Generators.	90
61	3.3	CMS detector simulation.	92
62	3.4	Event reconstruction.	94
63	3.4.1	Particle-Flow Algorithm.	94

64	3.4.1.1	Missing transverse energy.	108
65	3.4.2	Event reconstruction examples	109
66	5	Statistical methods	112
67	5.1	Multivariate analysis	112
68	5.1.1	Decision trees	116
69	5.1.2	Boosted decision trees (BDT)	119
70	5.1.3	Overtraining	121
71	5.1.4	Variable ranking	122
72	5.1.5	BDT output example	122
73	5.2	Statistical inference	123
74	5.2.1	Nuisance parameters	124
75	5.2.2	Maximum likelihood estimation method	125
76	5.3	Upper limits	126
77	5.4	Asymptotic limits	130
78	6	Search for production of a Higgs boson and a single top quark in multilepton final states in pp collisions at $\sqrt{s} = 13$ TeV	132
80	6.1	Introduction	132
81	6.2	<i>tHq</i> signature	136
82	6.3	Background processes	137
83	6.4	Data and MC Samples	139
84	6.4.1	Full 2016 data set	139
85	6.4.2	Triggers	140
86	6.4.3	MC samples	143
87	6.5	Object Identification	145
88	6.5.1	Lepton reconstruction and identification	146

89	6.5.2	Lepton selection efficiency	152
90	6.5.3	Jets and b -jet tagging	156
91	6.5.4	Missing Energy MET	157
92	6.6	Event selection	158
93	6.7	Background modeling and predictions	159
94	6.7.1	$t\bar{t}V$ and diboson backgrounds	160
95	6.7.2	Non-prompt and charge mis-ID backgrounds	162
96	6.8	Pre-selection yields	166
97	6.9	Signal discrimination	167
98	6.9.1	MVA classifiers evaluation	169
99	6.9.2	Discriminating variables	171
100	6.9.3	BDTG classifiers response	175
101	6.9.4	Additional discriminating variables	177
102	6.9.5	Signal extraction procedure	179
103	6.9.6	Binning and selection optimization	181
104	6.10	Signal model	183
105	A Datasets and triggers		188
106	B Additional plots		192
107	B.1	Pre-selection kinematic variables	192
108	B.2	BDTG input variables for $2lss$ channel	196
109	B.3	Input variables distributions from BDTG classifiers	197
110	C Other binning strategies		201
111	D BDTG output variation with κ_V/κ_t		204

112	E $tHq-t\bar{t}H$ overlap	205
113	F Cross sections and Branching ratios scalings	207
114	Bibliography	207
115	References	214

¹¹⁶ List of Figures

117	1.1	Standard Model of particle physics.	3
118	1.2	Transformations between quarks	11
119	1.3	Fundamental interactions in nature.	12
120	1.4	SM interactions diagrams	13
121	1.5	Neutral current processes	19
122	1.6	Spontaneous symmetry breaking mechanism	27
123	1.7	SSB Potential form	28
124	1.8	Potential for complex scalar field	29
125	1.9	SSB mechanism for complex scalar field	30
126	1.10	Proton-Proton collision	36
127	1.11	Proton PDFs	37
128	1.12	Higgs boson production mechanism Feynman diagrams	38
129	1.13	Higgs boson production cross section and decay branching ratios	39
130	1.14	κ_t - κ_V plot of the coupling modifiers. ATLAS and CMS combination.	42
131	1.15	Higgs boson production in association with a top quark	45
132	1.16	Cross section for tHq process as a function of κ_t	48
133	1.17	Cross section for tHW process as a function of κ_{Htt}	48
134	1.18	NLO cross section for tX_0 and $t\bar{t}X_0$.	52

135	1.19 NLO cross section for $tWX_0, t\bar{t}X_0$.	53
136	2.1 CERN accelerator complex	55
137	2.2 LHC protons source. First acceleration stage.	56
138	2.3 The LINAC2 accelerating system at CERN.	57
139	2.4 LHC layout and RF cavities module.	58
140	2.5 LHC dipole magnet.	60
141	2.6 Integrated luminosity delivered by LHC and recorded by CMS during 2016	62
142	2.7 LHC interaction points	63
143	2.8 Multiple pp collision bunch crossing at CMS.	65
144	2.9 Layout of the CMS detector	66
145	2.10 CMS detector transverse slice	67
146	2.11 CMS detector coordinate system	69
147	2.12 CMS tracking system schematic view.	70
148	2.13 CMS pixel detector	71
149	2.14 SST Schematic view.	73
150	2.15 CMS ECAL schematic view	75
151	2.16 CMS HCAL schematic view	77
152	2.17 CMS solenoid magnet	78
153	2.18 CMS Muon system schematic view	79
154	2.19 CMS Level-1 trigger architecture	81
155	2.20 WLCG structure	82
156	2.21 Data flow from CMS detector through hardware Tiers	84
157	3.1 Event generation process.	87
158	3.2 Particle flow algorithm.	95
159	3.3 Stable cones identification	102

160	3.4	Jet reconstruction.	104
161	3.5	Jet energy corrections.	106
162	3.6	Secondary vertex in a b-hadron decay.	107
163	3.7	HIG-13-004 Event 1 reconstruction.	109
164	3.8	$e\mu$ event reconstruction.	110
165	3.9	Recorded event reconstruction.	111
166	5.1	Scatter plots-MVA event classification.	114
167	5.2	Scalar test statistical.	115
168	5.3	Decision tree.	116
169	5.4	Decision tree output example.	119
170	5.5	BDT output example.	122
171	5.6	t_r p.d.f. assuming each H_0 and H_1	128
172	5.7	Illustration of the CL_s limit.	129
173	5.8	Example of Brazilian flag plot	130
174	6.1	Analysis strategy workflow	135
175	6.2	tHq event signature	136
176	6.3	$t\bar{t}$ and $t\bar{t}W$ events signature	139
177	6.4	Trigger efficiency for the same-sign $\mu\mu$ category	141
178	6.5	Trigger efficiency for the $e\mu$ category	142
179	6.6	Trigger efficiency for the $3l$ category	143
180	6.7	tHq and tHW cross section in the κ_t - κ_V phase space	144
181	6.8	Tight vs loose lepton selection efficiencies in the $2lss$ channel.	154
182	6.9	Tight vs loose lepton selection efficiencies in the $3l$ channel.	155
183	6.10	Kinematic distributions in the diboson control region.	161
184	6.11	Fake rates	164

185	6.12 Electron mis-ID probabilities.	166
186	6.13 Distributions of discriminating variables for the event pre-selection for the same-sign $\mu^\pm\mu^\pm$ channel (top row), the same-sign $e^\pm\mu^\pm$ channel (middle row) and three lepton channel (bottom row), normalized to 35.9fb^{-1} , before fitting the signal discriminant to the observed data. Uncertainties are statistical and unconstrained (pre-fit) normalization systematics. The shape of the two tH signals for $\kappa_t = -1.0$ is shown, normalized to their respective cross sections for $\kappa_t = -1.0, \kappa_V = 1.0$	168
193	6.14 MVA classifiers performance.	170
194	6.15 BDTG classifier Input variables distributions.	172
195	6.16 BDT input variables. Discrimination against $t\bar{t}$ and $t\bar{t}V$ in $3l$ channel. . .	173
196	6.17 Correlation matrices for the BDT input variables.	174
197	6.18 BDTG classifier response. Default parameters.	175
198	6.19 BDTG classifier output.	176
199	6.20 Additional discriminating variables distributions.	178
200	6.21 2D BDT classifier output planes	179
201	6.22 Binning overlaid on the S/B ratio map on the plane of classifier outputs.	180
202	6.23 Binning combination scheme.	182
203	6.24 Scaling of the tHq , tHW , and $t\bar{t}H$ production cross section with κ_t/κ_V . . .	184
204	B.1 Distributions of input variables to the BDT for signal discrimination, three lepton channel, normalized to their cross section and to 35.9fb^{-1}	193
206	B.2 Distributions of input variables to the BDT for signal discrimination, in $\mu^\pm\mu^\pm$ channel, normalized to their cross section and to 35.9fb^{-1}	194
208	B.3 Distributions of input variables to the BDT for signal discrimination, in $e^\pm\mu^\pm$ channel, normalized to their cross section and to 35.9fb^{-1}	195

210	B.4 Distributions of input variables to the BDT for signal discrimination, two 211 lepton same sign channel.	196
212	B.5 BDT input variables. Discrimination against $t\bar{t}$ in $2lss$ channel.	197
213	B.6 BDT input variables. Discrimination against $t\bar{t}V$ in $2lss$ channel.	198
214	B.7 BDT input variables. Discrimination against $t\bar{t}$ in $3l$ channel.	199
215	B.8 BDT input variables. Discrimination against $t\bar{t}V$ in $3l$ channel.	200
216	C.1 Binning by S/B regions for $2lss$ (left) and $3l$ (right).	201
217	C.2 Final bins (corresponding to S/B regions in the 2D plane)	202
218	C.3 Binning into geometric regions using a k -means algorithm.	203
219	C.4 Final bins using a k -means algorithm.	203
220	D.1 BDTG output variation with κ_V/κ_t	204
221	F.1 Scaling of the tHq , tHW , and $t\bar{t}H$ production cross sections (left) and 222 of the $H \rightarrow WW^*$, $H \rightarrow \tau\tau$, and $H \rightarrow ZZ^*$ branching ratios (right), as a 223 function of κ_t/κ_V , for three different values of κ_V	207

²²⁴ List of Tables

225	1.1	Fermions of the SM.	4
226	1.2	Fermion masses.	5
227	1.3	Lepton properties.	7
228	1.4	Quark properties.	8
229	1.5	Fermion weak isospin and weak hypercharge multiplets.	9
230	1.6	Fundamental interactions features.	14
231	1.7	SM gauge bosons.	18
232	1.8	Higgs boson properties.	36
233	1.9	Predicted branching ratios for a SM Higgs boson with $m_H = 125 \text{ GeV}/c^2$	41
234	1.10	Predicted SM cross sections for tH production at $\sqrt{s} = 13 \text{ TeV}$	46
235	1.11	Predicted enhancement of the tHq and tHW cross sections at LHC	49
236	6.1	Trigger efficiency scale factors and associated uncertainties.	142
237	6.2	MC signal samples.	144
238	6.3	Effective areas, for electrons and muons.	150
239	6.4	Requirements on each of the three muon selections.	152
240	6.5	Criteria for each of the three electron selections.	153
241	6.6	Summary of event pre-selection.	158
242	6.7	Electron charge mis-ID probabilities.	165

243	6.8	Expected and observed yields for 35.9fb^{-1} after the pre-selection in all final states. Uncertainties are statistical only.	167
244	6.9	Signal yields split by decay channels of the Higgs boson.	169
245	6.10	BDTG input variables.	171
246	6.11	Configuration used in the final BDTG training.	176
247	6.12	Input variables ranking for BDTG classifiers	177
248	6.13	ROC-integral for all the testing cases.	179
249	6.14	Selection cuts optimization.	181
250	6.15	Limit variation as a function of bin size.	182
251	6.16	Limit variation as a function of bin size in the same-sign dimuon channel. (In bold: the final bin borders used in the $2lss$ channel.)	183
252	6.17	κ_t/κ_V ratios.	186
253	A.1	Full 2016 dataset.	188
254	A.2	HLT	189
255	A.3	κ_V and κ_t combinations.	190
256	A.4	List of background samples used in this analysis (CMSSW 80X).	191
257	E.1	Differences in event selection between this analysis and the $t\bar{t}H$ multilepton analysis.	205
258	E.2	Individual and shared event yields between this analysis (tHq) and $t\bar{t}H$ multilepton selections.	206
259	F.1	Scalings of Higgs decay branching ratios vs. κ_t and $\kappa_V = 0.5$ for the resolved model.	208
260	F.2	Scalings of Higgs decay branching ratios vs. κ_t and $\kappa_V = 1.0$ for the resolved model.	209

267	F.3	Scalings of Higgs decay branching ratios vs. κ_t and $\kappa_V = 1.5$ for the resolved	
268		model.	210
269	F.4	Scalings of cross section times BR for the resolved model, for the different	
270		$t\bar{t}H$, tHq , tHW signal components and $\kappa_V = 0.5$	211
271	F.5	Scalings of cross section times BR for the resolved model, for the different	
272		$t\bar{t}H$, tHq , tHW signal components and $\kappa_V = 1.0$	212
273	F.6	Scalings of cross section times BR for the resolved model, for the different	
274		$t\bar{t}H$, tHq , tHW signal components and $\kappa_V = 1.5$	213

²⁷⁵ **Chapter 1**

²⁷⁶ **Theoretical approach**

²⁷⁷ **1.1 Introduction**

²⁷⁸ The physical description of the universe is a challenge that physicists have faced by
²⁷⁹ making theories that refine existing principles and proposing new ones in an attempt
²⁸⁰ to embrace emerging facts and phenomena.

²⁸¹ At the end of 1940s Julian Schwinger [1] and Richard P. Feynman [2], based on
²⁸² the work of Sin-Itiro Tomonaga [3], developed an electromagnetic theory consistent
²⁸³ with special relativity and quantum mechanics that describes how matter and light
²⁸⁴ interact; the so-called *quantum electrodynamics* (QED) was born.

²⁸⁵ QED has become the blueprint for developing theories that describe the universe.
²⁸⁶ It was the first example of a quantum field theory (QFT), which is the theoretical
²⁸⁷ framework for building quantum mechanical models that describes particles and their
²⁸⁸ interactions. QFT is composed of a set of mathematical tools that combines classical
²⁸⁹ fields, special relativity and quantum mechanics, while keeping the quantum point
²⁹⁰ particles and locality ideas.

²⁹¹ This chapter gives an overview of the standard model of particle physics, starting

292 with a description of the particles and their interactions, followed by a description of
 293 the electroweak interaction, the Higgs boson and the associated production of Higgs
 294 boson and a single top quark (tH). The description contained in this chapter is based
 295 on References [4–6].

296 1.2 Standard model of particle physics

297 The *standard model of particle physics (SM)* describes particle physics at the funda-
 298 mental level in terms of a collection of interacting particles and fields. The full picture
 299 of the SM is composed of three fields¹ whose excitations are interpreted as particles
 300 called mediators or force-carriers, a set of fields whose excitations are interpreted as
 301 elementary particles interacting through the exchange of those mediators, and a field
 302 that gives the mass to elementary particles. Figure 1.1 shows a scheme of the SM
 303 particles’ organization. In addition, for each of the particles in the scheme there exists
 304 an antiparticle with the same mass and opposite quantum numbers. The existence of
 305 antiparticles is a prediction of the relativistic quantum mechanics from the solution
 306 of the Dirac equation for which a negative energy solution is also possible. In some
 307 cases a particle is its own anti-particle, like photon or Higgs boson.

308 The mathematical formulation of the SM is based on group theory and the use of
 309 Noether’s theorem [8] which states that for a physical system modeled by a Lagrangian
 310 that is invariant under a group of transformations a conservation law is expected. For
 311 instance, a system described by a time-independent Lagrangian is invariant (symmet-
 312 ric) under time changes (transformations) with the total energy conservation law as
 313 the expected conservation law. In QED, the charge operator (Q) is the generator of

¹ The formal and complete treatment of the SM is out of the scope of this document, however a plenty of textbooks describing it at several levels are available in the literature. The treatment in References [5, 6] is quite comprehensive and detailed. Note that gravitational field is not included in the standard model formulation

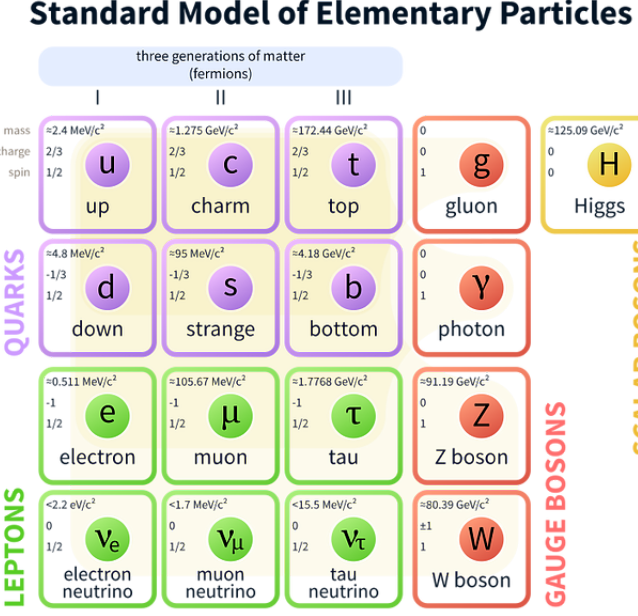


Figure 1.1: Schematic representation of the Standard Model of particle physics. The SM is a theoretical model intended to describe three of the four fundamental forces of the universe in terms of a set of particles and their interactions. [7].

314 the U(1) symmetry which according to the Noether's theorem means that there is a
 315 conserved quantity; this conserved quantity is the electric charge and thus the law
 316 conservation of electric charge is established.

317 In the SM, the symmetry group $SU(3)_C \otimes SU(2)_L \otimes U(1)_Y$ describes three of the
 318 four fundamental interactions in nature (see Section 1.2.2): strong interaction (SI),
 319 weak interaction (WI) and electromagnetic interactions (EI) in terms of symmetries
 320 associated to physical quantities:

- 321 • Strong: $SU(3)_C$ associated to color charge
- 322 • Weak: $SU(2)_L$ associated to weak isospin and chirality
- 323 • Electromagnetic: $U(1)_Y$ associated to weak hypercharge and electric charge
- 324 It will be shown that the electromagnetic and weak interactions are combined in

325 the so-called electroweak interaction where chirality, hypercharge, weak isospin and
 326 electric charge are the central concepts.

327 **1.2.1 Fermions**

328 The basic constituents of the ordinary matter at the lowest level, which form the set
 329 of elementary particles in the SM formulation, are quarks and leptons. All of them
 330 have spin 1/2, therefore they are classified as fermions since they obey Fermi-Dirac
 331 statistics. There are six *flavors* of quarks and three of leptons organized in three
 332 generations, or families, as shown in Table 1.1.

		Generation		
Type		1st	2nd	3rd
Leptons	Charged	Electron (e)	Moun(μ)	Tau (τ)
	Neutral	Electron neutrino (ν_e)	Muon neutrino (ν_μ)	Tau neutrino (ν_τ)
Quarks	Up-type	Up (u)	Charm (c)	Top (t)
	Down-type	Down (d)	Strange (s)	Bottom (b)

Table 1.1: Fermions of the SM. There are six flavors of quarks and three of leptons, organized in three generations, or families, composed of two pairs of closely related particles. The close relationship is motivated by the fact that each pair of particles is a member of an $SU(2)_L$ doublet that has an associated invariance under isospin transformations. WI between leptons is limited to the members of the same generation; WI between quarks is not limited but greatly favored, to same generation members.

333

334 There is a mass hierarchy between generations (see Table 1.2), where the higher
 335 generation particles decays to the lower one, which can explain why the ordinary
 336 matter is made of particles from the first generation. In the SM, neutrinos are modeled
 337 as massless particles so they are not subject to this mass hierarchy; however, today it
 338 is known that neutrinos are massive so the hierarchy could be restated. The reason
 339 behind this mass hierarchy is one of the most important open questions in particle
 340 physics, and it becomes more puzzling when noticing that the mass difference between

341 first and second generation fermions is small compared to the mass difference with
 342 respect to the third generation.

Lepton	Mass (MeV/c ²)	Quark	Mass (MeV/c ²)
e	0.51	u	2.2
μ	105.65	c	1.28×10^3
τ	1776.86	t	173.1×10^3
ν_e	Unknown	d	4.7
ν_μ	Unknown	s	96
τ_μ	Unknown	b	4.18×10^3

Table 1.2: Fermion masses [9]. Generations differ by mass in a way that has been interpreted as a mass hierarchy. Approximate values with no uncertainties are used, for comparison purpose.

343

344 Usually, the second and third generation fermions are produced in high energy
 345 processes, like the ones recreated in particle accelerators.

346 **1.2.1.1 Leptons**

347 A lepton is an elementary particle that is not subject to the SI. As seen in Table 1.1,
 348 there are two types of leptons, the charged ones (electron, muon and tau) and the
 349 neutral ones (the three neutrinos). The electric charge (Q) is the property that gives
 350 leptons the ability to participate in the EI. From the classical point of view, Q plays
 351 a central role determining, among others, the strength of the electric field through
 352 which the electromagnetic force is exerted. It is clear that neutrinos are not affected
 353 by EI because they don't carry electric charge.

354 Another feature of the leptons that is fundamental in the mathematical description
 355 of the SM is the chirality, which is closely related to spin and helicity. Helicity
 356 defines the handedness of a particle by relating its spin and momentum such that
 357 if they are parallel then the particle is right-handed; if spin and momentum are

358 antiparallel the particle is said to be left-handed. The study of parity conservation
 359 (or violation) in β -decay has shown that only left-handed electrons/neutrinos or right-
 360 handed positrons/anti-neutrinos are created [10]; the inclusion of that feature in the
 361 theory was achieved by using projection operators for helicity, however, helicity is
 362 frame dependent for massive particles which makes it not Lorentz invariant and then
 363 another related attribute has to be used: *chirality*.

364 Chirality is a purely quantum attribute which makes it not so easy to describe in
 365 graphical terms but it defines how the wave function of a particle transforms under
 366 certain rotations. As with helicity, there are two chiral states, left-handed chiral (L)
 367 and right-handed chiral (R). In the highly relativistic limit where $E \approx p \gg m$ helicity
 368 and chirality converge, becoming exactly the same for massless particles.

369 In the following, when referring to left-handed (right-handed) it will mean left-
 370 handed chiral (right-handed chiral). The fundamental fact about chirality is that
 371 while EI and SI are not sensitive to chirality, in WI left-handed and right-handed
 372 fermions are treated asymmetrically, such that only left-handed fermions and right-
 373 handed anti-fermions are allowed to couple to WI mediators, which is a violation of
 374 parity. The way to translate this statement in a formal mathematical formulation is
 375 based on the isospin symmetry group $SU(2)_L$.

376 Each generation of leptons is seen as a weak isospin doublet.² The left-handed
 377 charged lepton and its associated left-handed neutrino are arranged in doublets of
 378 weak isospin $T=1/2$ while their right-handed partners are singlets:

$$\begin{pmatrix} \nu_l \\ l \end{pmatrix}_L, l_R := \begin{pmatrix} \nu_e \\ e \end{pmatrix}_L, \begin{pmatrix} \nu_\mu \\ \mu \end{pmatrix}_L, \begin{pmatrix} \nu_\tau \\ \tau \end{pmatrix}_L, e_R, \mu_R, \tau_R, \nu_{eR}, \nu_{\mu R}, \nu_{\tau R} \quad (1.1)$$

379 The isospin third component refers to the eigenvalues of the weak isospin operator

² The weak isospin is an analogy of the isospin symmetry in strong interaction where neutron and proton are affected equally by strong force but differ in their charge.

380 which for doublets is $T_3 = \pm 1/2$, while for singlets it is $T_3 = 0$. The physical meaning
 381 of this doublet-singlet arrangement falls in that the WI couples the two particles in
 382 the doublet by exchanging the interaction mediator while the singlet member is not
 383 involved in WI. The main properties of the leptons are summarized in Table 1.3.

384 Although all three flavor neutrinos have been observed, their masses remain un-
 385 known and only some estimations have been made [11]. The main reason is that
 386 the flavor eigenstates are not the same as the mass eigenstates which implies that
 387 when a neutrino is created its mass state is a linear combination of the three mass
 388 eigenstates and experiments can only probe the squared difference of the masses. The
 389 Pontecorvo-Maki-Nakagawa-Sakata (PMNS) mixing matrix encodes the relationship
 390 between flavor and mass eigenstates.

Lepton	$Q(e)$	T_3	L_e	L_μ	L_τ	Lifetime (s)
Electron (e)	-1	-1/2	1	0	0	Stable
Electron neutrino(ν_e)	0	1/2	1	0	0	Unknown
Muon (μ)	-1	-1/2	0	1	0	2.19×10^{-6}
Muon neutrino (ν_μ)	0	1/2	0	1	0	Unknown
Tau (τ)	-1	-1/2	0	0	1	290.3×10^{-15}
Tau neutrino (ν_τ)	0	1/2	0	0	1	Unknown

Table 1.3: Lepton properties [9]. Q: electric charge, T_3 : weak isospin. Only left-handed leptons and right-handed anti-leptons participate in the WI. Anti-particles with inverted T_3 , Q and lepton number complete the leptons set but are not listed. Right-handed leptons and left-handed anti-leptons, neither listed, form weak isospin singlets with $T_3 = 0$ and do not take part in the weak interaction.

391

392 1.2.1.2 Quarks

393 Quarks are the basic constituents of protons and neutrons. The way quarks join to
 394 form bound states, called *hadrons*, is through the SI. Quarks are affected by all the
 395 fundamental interactions which means that they carry all the four types of charges:
 396 color, electric charge, weak isospin and mass.

Flavor	$Q(e)$	I_3	T_3	B	C	S	T	B'	Y	Color
Up (u)	2/3	1/2	1/2	1/3	0	0	0	0	1/3	r,b,g
Charm (c)	2/3	0	1/2	1/3	1	0	0	0	4/3	r,b,g
Top(t)	2/3	0	1/2	1/3	0	0	1	0	4/3	r,b,g
Down(d)	-1/3	-1/2	-1/2	1/3	0	0	0	0	1/3	r,b,g
Strange(s)	-1/3	0	-1/2	1/3	0	-1	0	0	-2/3	r,b,g
Bottom(b)	-1/3	0	-1/2	1/3	0	0	0	-1	-2/3	r,b,g

Table 1.4: Quark properties [9]. Q: electric charge, I_3 : isospin, T_3 : weak isospin, B: baryon number, C: charmness, S: strangeness, T: topness, B' : bottomness, Y: hypercharge. Anti-quarks posses the same mass and spin as quarks but all charges (color, flavor numbers) have opposite sign.

397

398 Table 1.4 summarizes the features of quarks, among which the most remarkable
 399 is their fractional electric charge. Note that fractional charge is not a problem, given
 400 that quarks are not found isolated, but serves to explain how composed particles are
 401 formed out of two or more valence quarks³.

402 Color charge is responsible for the SI between quarks and is the symmetry ($SU(3)_C$)
 403 that defines the formalism to describe SI. There are three colors: red (r), blue (b)
 404 and green (g) and their corresponding three anti-colors; thus each quark carries one
 405 color unit while anti-quarks carries one anti-color unit. As explained in Section 1.2.2,
 406 quarks are not allowed to be isolated due to the color confinement effect, hence, their
 407 features have been studied indirectly by observing their bound states created when

- 408 • one quark with a color charge is attracted by an anti-quark with the correspond-
 409 ing anti-color charge forming a colorless particle called a *meson*.

 410 • three quarks (anti-quarks) with different color (anti-color) charges are attracted
 411 among them forming a colorless particle called a *baryon (anti-baryon)*.

³ Hadrons can contain an indefinite number of virtual quarks and gluons, known as the quark and gluon sea, but only the valence quarks determine hadrons' quantum numbers.

412 In practice, when a quark is left alone isolated a process called *hadronization* occurs
 413 where the quark emits gluons (see Section 1.2.4) which eventually will generate new
 414 quark-antiquark pairs and so on; those quarks will recombine to form hadrons that
 415 will decay into leptons. This proliferation of particles looks like a *jet* coming from
 416 the isolated quark. More details about the hadronization process and jet structure
 417 will be given in chapter3.

418 In the first version of the quark model (1964), M. Gell-Mann [12] and G. Zweig
 419 [13, 14] developed a consistent way to classify hadrons according to their properties.
 420 Only three quarks (u, d, s) were involved in a scheme in which all baryons have baryon
 421 number $B=1$ and therefore quarks have $B=1/3$; non-baryons have $B=0$. Baryon
 422 number is conserved in SI and EI which means that single quarks cannot be created
 423 but in pairs $q - \bar{q}$.

424 The scheme organizes baryons in a two-dimensional space (I_3 - Y); Y (hyper-
 425 charge) and I_3 (isospin) are quantum numbers related by the Gell-Mann-Nishijima
 426 formula [15, 16]:

$$Q = I_3 + \frac{Y}{2} \quad (1.2)$$

427 where $Y = B + S + C + T + B'$ are the quantum numbers listed in Table 1.4.

428 There are six quark flavors organized in three generations (see Table 1.1) fol-
 429 lowing a mass hierarchy which, again, implies that higher generations decay to first
 430 generation quarks.

	Quarks			T_3	Y_W	Leptons			T_3	Y_W
Doublets	$(\frac{u}{d'})_L$	$(\frac{c}{s'})_L$	$(\frac{t}{b'})_L$	$(\frac{1/2}{-1/2})$	$1/3$	$(\nu_e)_L$	$(\nu_\mu)_L$	$(\nu_\tau)_L$	$(\frac{1/2}{-1/2})$	-1
Singlets	u_R	c_R	t_R	0	$4/3$	ν_{eR}	$\nu_{\mu R}$	$\nu_{\tau R}$	0	-2

Table 1.5: Fermion weak isospin and weak hypercharge multiplets. Weak hypercharge is calculated through the Gell-Mann-Nishijima formula 1.2 but using the weak isospin and charge for quarks.

431

432 Isospin doublets of quarks are also defined (see Table 1.5), and same as for neutrinos,
 433 the WI eigenstates are not the same as the mass eigenstates which means that
 434 members of different quark generations are connected by the WI mediator; thus, up-
 435 type quarks are coupled not to down-type quarks (the mass eigenstates) directly but
 436 to a superposition of down-type quarks (q'_d ; *the weak eigenstates*) via WI according
 437 to:

438

$$\begin{aligned} q'_d &= V_{CKM} q_d \\ \begin{pmatrix} d' \\ s' \\ b' \end{pmatrix} &= \begin{pmatrix} V_{ud} & V_{us} & V_{ub} \\ V_{cd} & V_{cs} & V_{cb} \\ V_{td} & V_{ts} & V_{tb} \end{pmatrix} \begin{pmatrix} d \\ s \\ b \end{pmatrix} \end{aligned} \quad (1.3)$$

439 where V_{CKM} is known as Cabibbo-Kobayashi-Maskawa (CKM) mixing matrix [17,18]
 440 given by

$$\begin{pmatrix} |V_{ud}| & |V_{us}| & |V_{ub}| \\ |V_{cd}| & |V_{cs}| & |V_{cb}| \\ |V_{td}| & |V_{ts}| & |V_{tb}| \end{pmatrix} = \begin{pmatrix} 0.97427 \pm 0.00015 & 0.22534 \pm 0.00065 & 0.00351^{+0.00015}_{-0.00014} \\ 0.22520 \pm 0.00065 & 0.97344 \pm 0.00016 & 0.0412^{+0.0011}_{-0.0005} \\ 0.00867^{+0.00029}_{-0.00031} & 0.0404^{+0.0011}_{-0.0005} & 0.999146^{+0.000021}_{-0.000046} \end{pmatrix}. \quad (1.4)$$

441 The weak decays of quarks are represented in the diagram of Figure 1.2; again
 442 the CKM matrix plays a central role since it contains the probabilities for the differ-
 443 ent quark decay channels, in particular, note that quark decays are greatly favored
 444 between generation members.

445 CKM matrix is a 3×3 unitary matrix parametrized by three mixing angles and
 446 the *CP-mixing phase*; the latter is the parameter responsible for the Charge-Parity

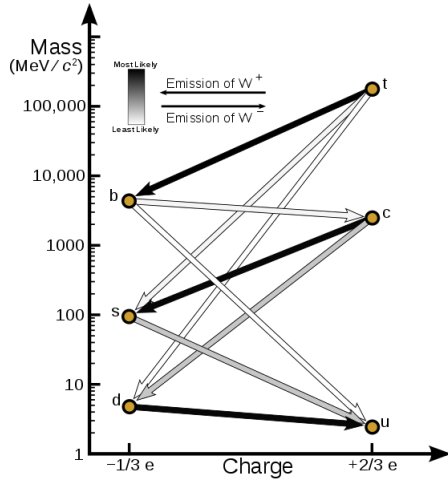


Figure 1.2: Transformations between quarks through the exchange of a WI. Higher generations quarks decay to first generation quarks by emitting a W boson. The arrow color indicates the likelihood of the transition according to the grey scale in the top left side which represent the CKM matrix parameters [19].

447 symmetry violation (CP-violation) in the SM. The fact that the top quark decays
 448 almost all the time to a bottom quark is exploited in this thesis when making the
 449 selection of the signal events by requiring the presence of a jet tagged as a jet coming
 450 from a b quark in the final state.

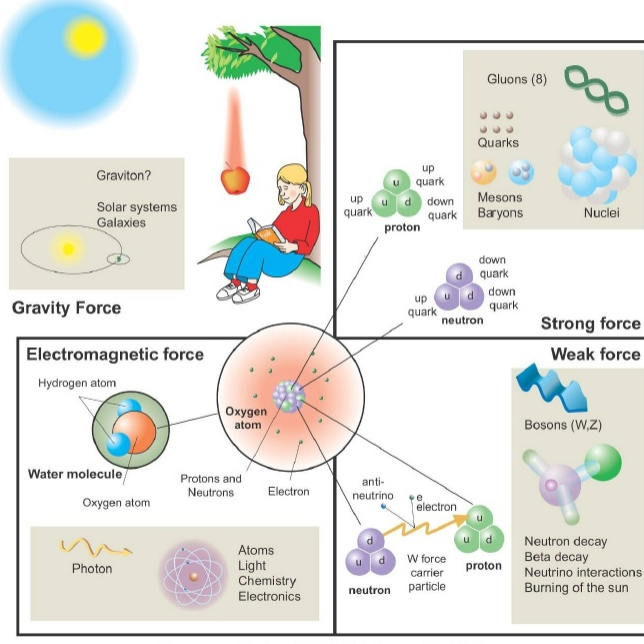
451 1.2.2 Fundamental interactions

452 Even though there are many manifestations of force in nature, like the ones repre-
 453 sented in Figure 1.3, we can classify all of them in four fundamental interactions:

- 454 • *Electromagnetic interaction (EI)* affects particles that are *electrically charged*,
 455 like electrons and protons. Figure 1.4a. shows a graphical representation, known
 456 as *Feynman diagram*, of electron-electron scattering.
- 457 • *Strong interaction (SI)* described by Quantum Chromodynamics (QCD). Hadrons
 458 like the proton and the neutron have internal structure given that they are com-

Fundamental interactions.

Illustration: Typoform



Summer School KPI 15 August 2009

Figure 1.3: Fundamental interactions in nature. Despite the many manifestations of forces in nature, we can track all of them back to one of the fundamental interactions. The most common forces are gravity and electromagnetic given that all of us are subject and experience them in everyday life.

459 posed of two or more valence quarks⁴. Quarks have fractional electric charge
 460 which means that they are subject to electromagnetic interaction and in the case
 461 of the proton they should break apart due to electrostatic repulsion; however,
 462 quarks are held together inside the hadrons against their electrostatic repulsion
 463 by the *Strong Force* through the exchange of *gluons*. The analog to the electric
 464 charge is the *color charge*. Electrons and photons are elementary particles as
 465 quarks but they don't carry color charge, therefore they are not subject to SI. A
 466 Feynman diagram for gluon exchange between quarks is shown in Figure 1.4b.

- 467 • *Weak interaction (WI)* described by the weak theory (WT), is responsible, for
 468 instance, for the radioactive decay in atoms and the deuterium production

⁴ Particles made of four and five quarks are exotic states not so common.

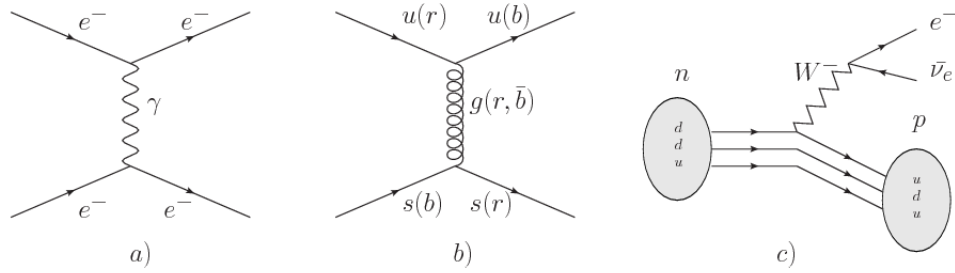


Figure 1.4: Feynman diagrams representing the interactions in SM; a) EI: e - e scattering; b) SI: gluon exchange between quarks ; c) WI: β -decay

within the sun. Quarks and leptons are the particles affected by the weak interaction; they possess a property called *flavor charge* (see 1.2.1) which can be changed by emitting or absorbing one weak force mediator. There are three mediators of the *weak force* known as Z boson in the case of electrically neutral flavor changes and W^\pm bosons in the case of electrically charged flavor changes. The *weak isospin* is the WI analog to electric charge in EI, and color charge in SI, and defines how quarks and leptons are affected by the weak force. Figure 1.4c. shows the Feynman diagram of β -decay where a neutron (n) is transformed in a proton (p) by emitting a W^- particle.

- *Gravitational interaction (GI)* described by General Theory of Relativity (GR). It is responsible for the structure of galaxies and black holes as well as the expansion of the universe. As a classical theory, in the sense that it can be formulated without even appeal to the concept of quantization, it implies that the space-time is a continuum and predictions can be made without limitation to the precision of the measurement tools. The latter represents a direct contradiction of the quantum mechanics principles. Gravity is deterministic while quantum mechanics is probabilistic; despite that, efforts to develop a quantum theory of gravity have predicted the *graviton* as mediator of the gravitational

487 force⁵.

Interaction	Acts on	Relative strength	Range (m)	Mediators
Electromagnetic (QED)	Electrically charged particles	10^{-2}	Infinite	Photon
Strong (QCD)	Quarks and gluons	1	10^{-15}	Gluon
Weak (WI)	Leptons and quarks	10^{-6}	10^{-18}	W^\pm, Z
Gravitational (GI)	Massive particles	10^{-39}	Infinite	Graviton

Table 1.6: Fundamental interactions features [20].

488

489 Table 1.6 summarizes the main features of the fundamental interactions. The
 490 strength of the interactions is represented by the coupling constants which depend
 491 on the energy scale at which the interaction is evaluated, therefore, it is the relative
 492 strength of the fundamental forces that reveals the meaning of strong and weak; in
 493 a context where the relative strength of the SI is 1, the EI is about hundred times
 494 weaker and WI is about million times weaker than the SI. A good description on how
 495 the relative strength and range of the fundamental interactions are calculated can
 496 be found in References [20, 21]. In the everyday life, only EI and GI are explicitly
 497 experienced due to the range of these interactions; i.e., at the human scale distances
 498 only EI and GI have appreciable effects, in contrast to SI which at distances greater
 499 than 10^{-15} m become negligible. Is it important to clarify that the weakness of the
 500 WI is attributed to the fact that its mediators are highly massive which affects the
 501 propagators of the interaction, as a result, the effect of the coupling constant is
 502 reduced.

⁵ Actually a wide variety of theories have been developed in an attempt to describe gravity; some famous examples are string theory and supergravity.

503 **1.2.3 Gauge invariance.**

504 QED was built successfully on the basis of the classical electrodynamics theory (CED)
 505 of Maxwell and Lorentz, following theoretical and experimental requirements imposed
 506 by

- 507 • Lorentz invariance: independence on the reference frame.
- 508 • Locality: interacting fields are evaluated at the same space-time point to avoid
 509 action at a distance.
- 510 • Renormalizability: physical predictions are finite and well defined.
- 511 • Particle spectrum, symmetries and conservation laws already known must emerge
 512 from the theory.
- 513 • Local gauge invariance.

514 The gauge invariance requirement reflects the fact that the fundamental fields
 515 cannot be directly measured but associated fields which are the observables. Electric
 516 (**E**) and magnetic (**B**) fields in CED are associated with the electric scalar potential
 517 V and the vector potential **A**. In particular, **E** can be obtained by measuring the
 518 change in the space of the scalar potential (ΔV); however, two scalar potentials
 519 differing by a constant f correspond to the same electric field. The same happens
 520 in the case of the vector potential **A**; thus, different configurations of the associated
 521 fields result in the same set of values of the observables. The freedom in choosing one
 522 particular configuration is known as *gauge freedom*; the transformation law connecting
 523 two configurations is known as *gauge transformation* and the fact that the observables
 524 are not affected by a gauge transformation is called *gauge invariance*.

525 When the gauge transformation:

$$\begin{aligned} \mathbf{A} &\rightarrow \mathbf{A} - \Delta f \\ V &\rightarrow V - \frac{\partial f}{\partial t} \end{aligned} \tag{1.5}$$

526 is applied to Maxwell equations, they are still satisfied and the fields remain invariant.
 527 Thus, CED is invariant under gauge transformations and is called a *gauge theory*.
 528 The set of all gauge transformations form the *symmetry group* of the theory, which
 529 according to the group theory, has a set of *group generators*. The number of group
 530 generators determine the number of *gauge fields* of the theory.

531 As mentioned in the first lines of Section 1.2, QED has one symmetry group ($U(1)$)
 532 with one group generator (the Q operator) and one gauge field (the electromagnetic
 533 field A^μ). In CED there is not a clear definition, beyond the historical convention,
 534 of which fields are the fundamental and which are the associated, but in QED the
 535 fundamental field is A^μ . When a gauge theory is quantized, the gauge fields are
 536 quantized and their quanta are called *gauge bosons*. The word boson characterizes
 537 particles with integer spin which obey Bose-Einstein statistics.

538 As will be detailed in Section 1.3, interactions between particles in a system can
 539 be obtained by considering first the Lagrangian density of free particles in the sys-
 540 tem, which of course is incomplete because the interaction terms have been left out,
 541 and demanding global phase transformation invariance. Global phase transforma-
 542 tion invariance means that a gauge transformation is performed identically to every point
 543 in the space⁶ and the Lagrangian remains invariant. Then, the global transforma-
 544 tion is promoted to a local phase transformation (this time the gauge transformation
 545 depends on the position in space) and again invariance is required.

⁶ Here space corresponds to the 4-dimensional space i.e. space-time.

546 Due to the space dependence of the local transformation, the Lagrangian density is
 547 not invariant anymore. In order to reinstate the gauge invariance, the gauge covariant
 548 derivative is introduced in the Lagrangian and with it the gauge field responsible for
 549 the interaction between particles in the system. The new Lagrangian density is gauge
 550 invariant, includes the interaction terms needed to account for the interactions and
 551 provides a way to explain the interaction between particles through the exchange of
 552 the gauge boson.

553 This recipe was used to build QED and the theories that aim to explain the
 554 fundamental interactions.

555 1.2.4 Gauge bosons

556 The importance of the gauge bosons comes from the fact that they are the force
 557 mediators or force carriers. The features of the gauge bosons reflect those of the fields
 558 they represent and they are extracted from the Lagrangian density used to describe
 559 the interactions. In Section 1.3, it will be shown how the gauge bosons of the EI and
 560 WI emerge from the electroweak Lagrangian. The SI gauge bosons features are also
 561 extracted from the SI Lagrangian but it is not detailed in this document. The main
 562 features of the SM gauge bosons will be briefly presented below and summarized in
 563 Table 1.7.

- 564 • **Photon.** EI occurs when the photon couples to (is exchanged between) parti-
 565 cles carrying electric charge; however, The photon itself does not carry electric
 566 charge, therefore, there is no coupling between photons. Given that the photon
 567 is massless the EI is of infinite range, i.e., electrically charged particles interact
 568 even if they are located far away one from each other; this also implies that
 569 photons always move with the speed of light.

- 570 • **Gluon.** SI is mediated by gluons which just as photons are massless. They
 571 carry one unit of color charge and one unit of anticolor charge, hence, gluons
 572 can couple to other gluons. As a result, the range of the SI is not infinite
 573 but very short due to the attraction between gluons, giving rise to the *color*
 574 *confinement* which explains why color charged particles cannot be isolated but
 575 live within composite particles, like quarks inside protons.
- 576 • **W, Z.** W^\pm and Z, are massive which explains their short-range. Given that
 577 the WI is the only interaction that can change the flavor of the interacting
 578 particles, the W boson is the responsible for the nuclear transmutation where
 579 a neutron is converted into a proton or vice versa with the involvement of an
 580 electron and a neutrino (see Figure 1.4c). The Z boson is the responsible for the
 581 neutral weak processes like neutrino elastic scattering where no electric charge
 582 but momentum transference is involved. WI gauge bosons carry isospin charge
 583 which makes interaction between them possible.

Interaction	Mediator	Electric charge (e)	Color charge	Weak Isospin	mass (GeV/c ²)
Electromagnetic	Photon (γ)	0	No	0	0
Strong	Gluon (g)	0	Yes -octet	No	0
Weak	W^\pm	± 1	No	± 1	80.385 ± 0.015
	Z	0	No	0	91.188 ± 0.002

Table 1.7: SM gauge bosons main features [9].

584

585 1.3 Electroweak unification and the Higgs 586 mechanism

587 Physicists dream of building a theory that contains all the interactions in one single
 588 interaction, i.e., showing that at some scale in energy all the four fundamental inter-

actions are unified and only one interaction emerges in a *Theory of everything*. The first sign of the feasibility of such unification came from success in the construction of the CED. Einstein spent years trying to reach that full unification, which by 1920 only involved electromagnetism and gravity, with no success; however, a new partial unification was achieved in the 1960's, when S.Glashow [22], A.Salam [23] and S.Weinberg [24] independently proposed that electromagnetic and weak interactions are two manifestations of a more general interaction called *electroweak interaction* (EWI). EWI was developed by following the useful prescription provided by QED and the gauge invariance principles.

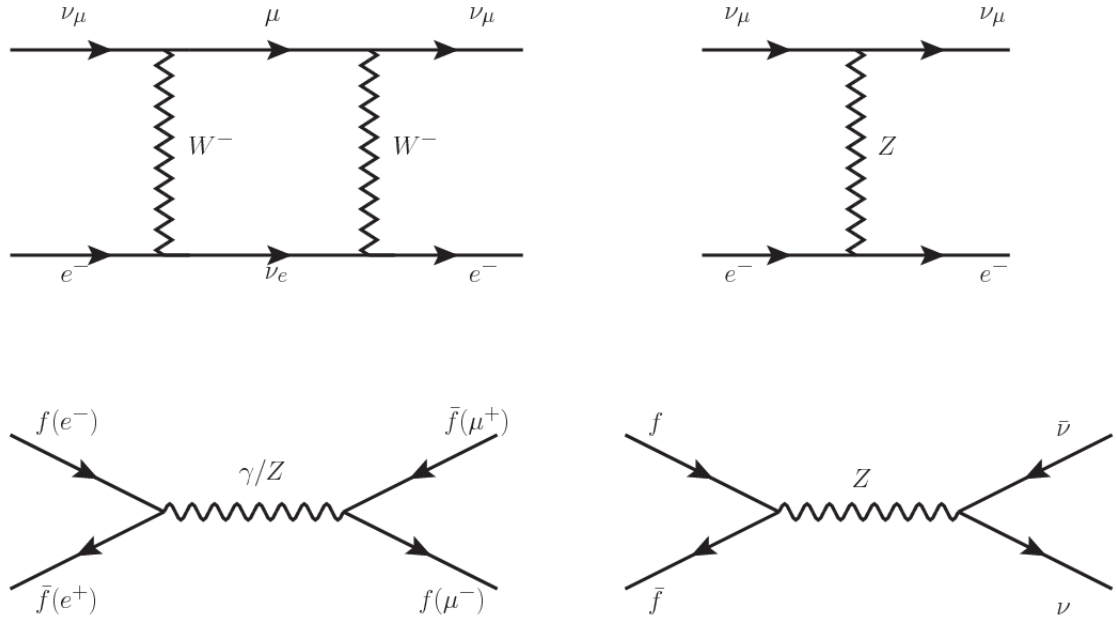


Figure 1.5: Top: $\nu_\mu - e^-$ scattering going through charged currents (left) and neutral currents (right). Bottom: neutral current processes for charged fermions (left) and involving neutrinos (right). While neutral current processes involving only charged fermions can proceed through EI or WI, those involving neutrinos can only proceed via WI.

The *classic* weak theory developed by Fermi, did not have the concept of the W boson but instead it was treated as a point interaction with the dimensionful constant G_F associated with it. It works really well at low energies very far off the W mass

601 shell. When going up in energy, the theory of weak interactions involving the W
 602 boson is capable of explaining the β -decay and in general the processes mediated by
 603 W^\pm bosons. However, there were some processes like the $\nu_\mu - e$ scattering which
 604 would require the exchange of two W bosons (see Figure 1.5 top diagrams) giving
 605 rise to divergent loop integrals and then non-finite predictions. The EWI theory, by
 606 including neutral currents involving fermions via the exchange of a neutral bosons Z,
 607 overcomes those divergences and the predictions become realistic.

608 Neutral weak interaction vertices conserve flavor in the same way as the electro-
 609 magnetic vertices do, but additionally, the Z boson can couple to neutrinos which
 610 implies that processes involving charged fermions can proceed through EI or WI but
 611 processes involving neutrinos can proceed only through WI.

612 The prescription to build a gauge theory of the WI consists of proposing a free
 613 field Lagrangian density that includes the particles involved; next, by requesting
 614 invariance under global phase transformations first and generalizing to local phase
 615 transformations invariance later, the conserved currents are identified and interactions
 616 are generated by introducing gauge fields. Given that the goal is to include the EI
 617 and WI in a single theory, the group symmetry considered should be a combination of
 618 $SU(2)_L$ and $U(1)_{em}$, however the latter cannot be used directly because the EI treats
 619 left and right-handed particles indistinctly in contrast to the former. Fortunately, the
 620 weak hypercharge, which is a combination of the weak isospin and the electric charge
 621 (Eqn. 1.2) is suitable to be used since it is conserved by the EI and WI. Thus, the
 622 symmetry group to be considered is

$$G \equiv SU(2)_L \otimes U(1)_Y \quad (1.6)$$

623 The following treatment applies to any of the fermion generations, but for sim-

624 plicity the first generation of leptons will be considered [5, 6, 25, 26].

625 Given the first generation of leptons

$$\psi_1 = \begin{pmatrix} \nu_e \\ e^- \end{pmatrix}_L, \quad \psi_2 = \nu_{eR}, \quad \psi_3 = e_R^- \quad (1.7)$$

626 the charged fermionic currents are given by

$$J_\mu \equiv J_\mu^+ = \bar{\nu}_{eL} \gamma_\mu e_L, \quad J_\mu^\dagger \equiv J_\mu^- = \bar{e}_L \gamma_\mu \nu_{eL} \quad (1.8)$$

627 and the free Lagrangian is given by

$$\mathcal{L}_0 = \sum_{j=1}^3 i\bar{\psi}_j(x) \gamma^\mu \partial_\mu \psi_j(x). \quad (1.9)$$

628 Mass terms are included directly in the QED free Lagrangians since they preserve
 629 the invariance under the symmetry transformations involved which treat left and right
 630 handed particles similarly, however mass terms of the form

$$m_W^2 W_\mu^\dagger(x) W^\mu(x) + \frac{1}{2} m_Z^2 Z_\mu(x) Z^\mu(x) - m_e \bar{\psi}_e(x) \psi_e(x) \quad (1.10)$$

631 which represent the mass of W^\pm , Z and electrons, are not invariant under G trans-
 632 formations, therefore the gauge fields described by the EWI are in principle massless.

633 Experiments have shown that the EWI gauge fields are not massless [27–30];
 634 however, they have to acquire mass through a mechanism compatible with the gauge
 635 invariance; that mechanism is known as the *Higgs mechanism* and will be considered
 636 later in this Section. The global transformations in the combined symmetry group G
 637 can be written as

$$\begin{aligned}
\psi_1(x) &\xrightarrow{G} \psi'_1(x) \equiv U_Y U_L \psi_1(x), \\
\psi_2(x) &\xrightarrow{G} \psi'_2(x) \equiv U_Y \psi_2(x), \\
\psi_3(x) &\xrightarrow{G} \psi'_3(x) \equiv U_Y \psi_3(x)
\end{aligned} \tag{1.11}$$

638 where U_L represent the $SU(2)_L$ transformation acting only on the weak isospin dou-
 639 blet and U_Y represent the $U(1)_Y$ transformation acting on all the weak isospin mul-
 640 tiplets. Explicitly

$$U_L \equiv \exp\left(i \frac{\sigma_i}{2} \alpha^i\right), \quad U_Y \equiv \exp(i y_i \beta) \quad (i = 1, 2, 3) \tag{1.12}$$

641 with σ_i the Pauli matrices and y_i the weak hypercharges. In order to promote the
 642 transformations from global to local while keeping the invariance, it is required that
 643 $\alpha^i = \alpha^i(x)$, $\beta = \beta(x)$ and the replacement of the ordinary derivatives by the covariant
 644 derivatives

$$\begin{aligned}
D_\mu \psi_1(x) &\equiv \left[\partial_\mu + ig\sigma_i W_\mu^i(x)/2 + ig'y_1 B_\mu(x) \right] \psi_1(x) \\
D_\mu \psi_2(x) &\equiv \left[\partial_\mu + ig'y_2 B_\mu(x) \right] \psi_2(x) \\
D_\mu \psi_3(x) &\equiv \left[\partial_\mu + ig'y_3 B_\mu(x) \right] \psi_3(x)
\end{aligned} \tag{1.13}$$

645 introducing in this way four gauge fields, $W_\mu^i(x)$ and $B_\mu(x)$, in the process. The
 646 covariant derivatives (Eqn. 1.13) are required to transform in the same way as fermion
 647 fields $\psi_i(x)$ themselves, therefore, the gauge fields transform as:

$$\begin{aligned} B_\mu(x) &\xrightarrow{G} B'_\mu(x) \equiv B_\mu(x) - \frac{1}{g'} \partial_\mu \beta(x) \\ W_\mu^i(x) &\xrightarrow{G} W_\mu^{i\prime}(x) \equiv W_\mu^i(x) - \frac{i}{g} \partial_\mu \alpha_i(x) - \varepsilon_{ijk} \alpha_i(x) W_\mu^j(x). \end{aligned} \quad (1.14)$$

648 The G invariant version of the Lagrangian density 1.9 can be written as

$$\mathcal{L}_0 = \sum_{j=1}^3 i \bar{\psi}_j(x) \gamma^\mu D_\mu \psi_j(x) \quad (1.15)$$

649 where free massless fermion and gauge fields and fermion-gauge boson interactions
 650 are included. The EWI Lagrangian density must additionally include kinetic terms
 651 for the gauge fields (\mathcal{L}_G) which are built from the field strengths, according to

$$B_{\mu\nu}(x) \equiv \partial_\mu B_\nu - \partial_\nu B_\mu \quad (1.16)$$

$$W_{\mu\nu}^i(x) \equiv \partial_\mu W_\nu^i(x) - \partial_\nu W_\mu^i(x) - g \varepsilon^{ijk} W_\mu^j W_\nu^k \quad (1.17)$$

652 the last term in Eqn. 1.17 is added in order to hold the gauge invariance; therefore,

$$\mathcal{L}_G = -\frac{1}{4} B_{\mu\nu}(x) B^{\mu\nu}(x) - \frac{1}{4} W_{\mu\nu}^i(x) W_i^{\mu\nu}(x) \quad (1.18)$$

653 which contains not only the free gauge fields contributions, but also the gauge fields
 654 self-interactions and interactions among them.

655 The three weak isospin conserved currents resulting from the $SU(2)_L$ symmetry
 656 are given by

$$J_\mu^i(x) = \frac{1}{2} \bar{\psi}_1(x) \gamma_\mu \sigma^i \psi_1(x) \quad (1.19)$$

657 while the weak hypercharge conserved current resulting from the $U(1)_Y$ symmetry is
 658 given by

$$J_\mu^Y = \sum_{j=1}^3 \bar{\psi}_j(x) \gamma_\mu y_j \psi_j(x) \quad (1.20)$$

659 In order to evaluate the electroweak interactions modeled by an isos triplet field
 660 W_μ^i that couples to isospin currents J_μ^i with strength g and additionally the singlet
 661 field B_μ which couples to the weak hypercharge current J_μ^Y with strength $g'/2$. The
 662 interaction Lagrangian density to be considered is

$$\mathcal{L}_I = -g J^{i\mu}(x) W_\mu^i(x) - \frac{g'}{2} J^{Y\mu}(x) B_\mu(x) \quad (1.21)$$

663 Note that the weak isospin currents are not the same as the charged fermionic cur-
 664 rents that were used to describe the WI (Eqn. 1.8), since the weak isospin eigenstates
 665 are not the same as the mass eigenstates, but they are closely related

$$J_\mu = \frac{1}{2}(J_\mu^1 + iJ_\mu^2), \quad J_\mu^\dagger = \frac{1}{2}(J_\mu^1 - iJ_\mu^2). \quad (1.22)$$

666 The same happens with the gauge fields W_μ^i which are related to the mass eigen-
 667 states W^\pm by

$$W_\mu^+ = \frac{1}{\sqrt{2}}(W_\mu^1 - iW_\mu^2), \quad W_\mu^- = \frac{1}{\sqrt{2}}(W_\mu^1 + iW_\mu^2). \quad (1.23)$$

668 The fact that there are three weak isospin conserved currents is an indication that
 669 in addition to the charged fermionic currents, which couple charged to neutral leptons,
 670 there should be a neutral fermionic current that does not involve electric charge
 671 exchange; therefore, it couples neutral fermions or fermions of the same electric charge.
 672 The third weak isospin current contains a term that is similar to the electromagnetic

673 current (j_μ^{em}), indicating that there is a relation between them and resembling the
 674 Gell-Mann-Nishijima formula 1.2 adapted to electroweak interactions

$$Q = T_3 + \frac{Y_W}{2}. \quad (1.24)$$

675 Just as Q generates the $U(1)_{em}$ symmetry, the weak hypercharge generates the
 676 $U(1)_Y$ symmetry as said before. It is possible to write the relationship in terms of
 677 the currents as

$$j_\mu^{em} = J_\mu^3 + \frac{1}{2} J_\mu^Y. \quad (1.25)$$

678 The neutral gauge fields W_μ^3 and B_μ cannot be directly identified with the Z
 679 and the photon fields since the photon interacts similarly with left and right-handed
 680 fermions; however, they are related through a linear combination given by

$$A_\mu = B_\mu \cos \theta_W + W_\mu^3 \sin \theta_W \quad (1.26)$$

$$Z_\mu = -B_\mu \sin \theta_W + W_\mu^3 \cos \theta_W$$

where θ_W is known as the *Weinberg angle*. The interaction Lagrangian is now given by

$$\begin{aligned} \mathcal{L}_I = -\frac{g}{\sqrt{2}}(J^\mu W_\mu^+ + J^{\mu\dagger} W_\mu^-) - & \left(g \sin \theta_W J_\mu^3 + g' \cos \theta_W \frac{J_\mu^Y}{2} \right) A^\mu \\ & - \left(g \cos \theta_W J_\mu^3 - g' \sin \theta_W \frac{J_\mu^Y}{2} \right) Z^\mu \end{aligned} \quad (1.27)$$

681 the first term is the weak charged current interaction, while the second term is the

682 electromagnetic interaction under the condition

$$g \sin \theta_W = g' \cos \theta_W = e, \quad \frac{g'}{g} = \tan \theta_W \quad (1.28)$$

683 contained in the Eqn.1.25; the third term is the neutral weak current.

684

685 Note that the neutral fields transformation given by the Eqn. 1.26 can be written
 686 in terms of the coupling constants g and g' as:

$$A_\mu = \frac{g' W_\mu^3 + g B_\mu}{\sqrt{g^2 + g'^2}}, \quad Z_\mu = \frac{g W_\mu^3 - g' B_\mu}{\sqrt{g^2 + g'^2}}. \quad (1.29)$$

687 So far, the Lagrangian density describing the non-massive EWI is:

$$\mathcal{L}_{nmEWI} = \mathcal{L}_0 + \mathcal{L}_G \quad (1.30)$$

688 where fermion and gauge fields have been considered massless because their regular
 689 mass terms are manifestly non invariant under G transformations; therefore, masses
 690 have to be generated in a gauge invariant way. The mechanism by which this goal is
 691 achieved is known as the *Higgs mechanism* and is closely connected to the concept of
 692 *spontaneous symmetry breaking*.

693 1.3.1 Spontaneous symmetry breaking (SSB)

694 Figure 1.6 left shows a steel nail (top) which is subject to an external force; the form
 695 of the potential energy is also shown (bottom).

696 Before reaching the critical force value, the system has rotational symmetry with
 697 respect to the nail axis; however, after the critical force value is reached the nail buck-

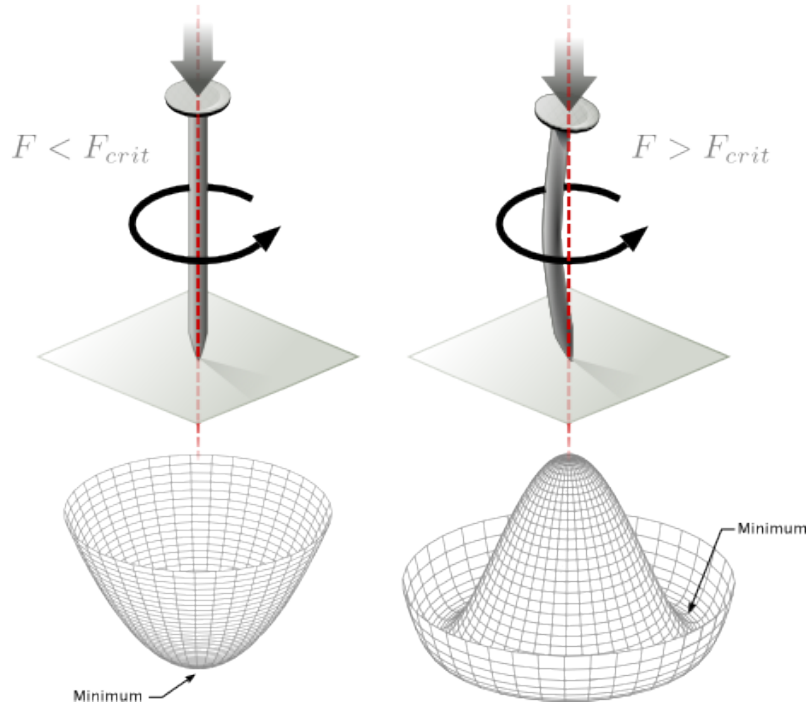


Figure 1.6: Spontaneous symmetry breaking mechanism. The steel nail, subject to an external force (top left), has rotational symmetry with respect to its axis. When the external force overcomes a critical value the nail buckles (top right) choosing a minimal energy state (ground state) and thus *breaking spontaneously the rotational symmetry*. The potential energy (bottom) changes but holds the rotational symmetry; however, an infinite number of asymmetric ground states are generated and circularly distributed in the bottom of the potential [31].

698 les (top right). The form of the potential energy (bottom right) changes appearing a
 699 set of infinity minima but preserving its rotational symmetry. Right before the nail
 700 buckles there is no indication of the direction the nail will bend because any of the
 701 directions are equivalent, but once the nail bends, choosing a direction, an arbitrary
 702 minimal energy state (ground state) is selected and it does not share the system's
 703 rotational symmetry. This mechanism for reaching an asymmetric ground state is
 704 known as *spontaneous symmetry breaking*.

705 The lesson from this analysis is that the way to introduce the SSB mechanism
 706 into a system is by adding the appropriate potential to it.

707 Figure 1.7 shows a plot of the potential $V(\phi)$ in the case of a scalar field ϕ

$$V(\phi) = \mu^2 \phi^\dagger \phi + \lambda (\phi^\dagger \phi)^2 \quad (1.31)$$

If $\mu^2 > 0$ the potential has only one minimum at $\phi = 0$ and describes a scalar field with mass μ . If $\mu^2 < 0$ the potential has a local maximum at $\phi = 0$ and two minima at $\phi = \pm\sqrt{-\mu^2/\lambda}$ which enables the SSB mechanism to work.

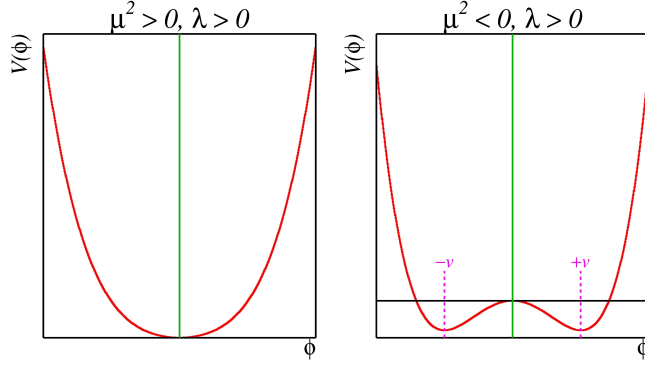


Figure 1.7: Shape of the potential $V(\phi)$ for $\lambda > 0$ and: $\mu^2 > 0$ (left) and $\mu^2 < 0$ (right). The case $\mu^2 < 0$ corresponds to the potential suitable for introducing the SSB mechanism by choosing one of the two ground states which are connected via reflection symmetry. [31].

In the case of a complex scalar field $\phi(x)$

$$\phi(x) = \frac{1}{\sqrt{2}}(\phi_1 + i\phi_2) \quad (1.32)$$

the Lagrangian (invariant under global $U(1)$ transformations) is given by

$$\mathcal{L} = (\partial_\mu \phi)^\dagger (\partial^\mu \phi) - V(\phi), \quad V(\phi) = \mu^2 \phi^\dagger \phi + \lambda (\phi^\dagger \phi)^2 \quad (1.33)$$

where an appropriate potential has been added in order to introduce the SSB.

As seen in Figure 1.8, the potential has now an infinite number of minima circularly distributed along the ξ -direction which makes possible the occurrence of the SSB by choosing an arbitrary ground state; for instance, $\xi = 0$, i.e. $\phi_1 = v, \phi_2 = 0$

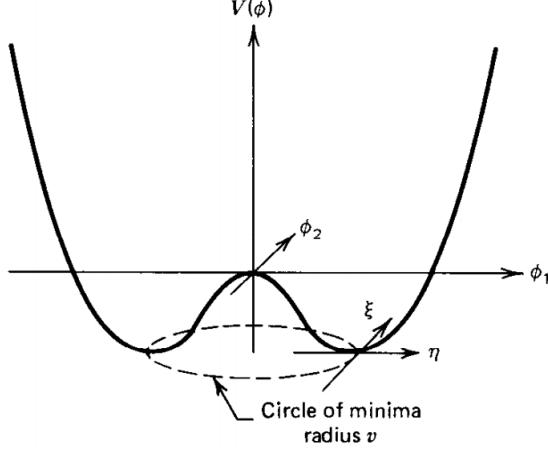


Figure 1.8: Potential for complex scalar field. There is a circle of minima of radius v along the ξ -direction [6].

$$\phi_0 = \frac{v}{\sqrt{2}} \exp(i\xi) \xrightarrow{\text{SSB}} \phi_0 = \frac{v}{\sqrt{2}} \quad (1.34)$$

717 As usual, excitations over the ground state are studied by making an expansion
 718 about it; thus, the excitations can be parametrized as:

$$\phi(x) = \frac{1}{\sqrt{2}}(v + \eta(x) + i\xi(x)) \quad (1.35)$$

719 which when substituted into Eqn. 1.33 produces a Lagrangian in terms of the new
 720 fields η and ξ

$$\mathcal{L}' = \frac{1}{2}(\partial_\mu \xi)^2 + \frac{1}{2}(\partial_\mu \eta)^2 + \mu^2 \eta^2 - V(\phi_0) - \lambda v \eta (\eta^2 + \xi^2) - \frac{\lambda}{4}(\eta^2 + \xi^2)^2 \quad (1.36)$$

721 where the last two terms represent the interactions and self-interaction between the
 722 two fields η and ξ . The particular feature of the SSB mechanism is revealed when
 723 looking to the first three terms of \mathcal{L}' . Before the SSB, only the massless ϕ field is

724 present in the system; after the SSB there are two fields of which the η -field has
 725 acquired mass $m_\eta = \sqrt{-2\mu^2}$ while the ξ -field is still massless (see Figure 1.9).

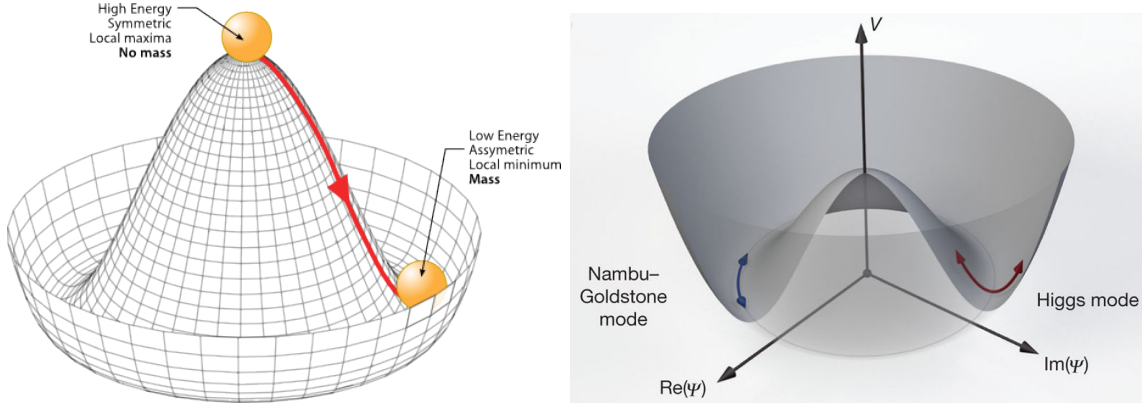


Figure 1.9: SSB mechanism for a complex scalar field [31, 32].

726 Thus, the SSB mechanism serves as a method to generate mass but as a side ef-
 727 fect a massless field is introduced in the system. This fact is known as the Goldstone
 728 theorem and states that a massless scalar field appears in the system for each con-
 729 tinuous symmetry spontaneously broken. Another version of the Goldstone theorem
 730 states that “if a Lagrangian is invariant under a continuous symmetry group G , but
 731 the vacuum is only invariant under a subgroup $H \subset G$, then there must exist as many
 732 massless spin-0 particles (Nambu-Goldstone bosons) as broken generators.” [26] The
 733 Nambu-Goldstone boson can be understood considering that the potential in the ξ -
 734 direction is flat so excitations in that direction are not energy consuming and thus
 735 represent a massless state.

736 1.3.2 Higgs mechanism

737 When the SSB mechanism is introduced in the formulation of the EWI in an attempt
 738 to generate the mass of the so far massless gauge bosons and fermions, an interesting
 739 effect is revealed. In order to keep the G symmetry group invariance and generate

740 the mass of the EW gauge bosons, a G invariant Lagrangian density (\mathcal{L}_S) has to be
 741 added to the non massive EWI Lagrangian (Eqn. 1.30)

$$\mathcal{L}_S = (D_\mu \phi)^\dagger (D^\mu \phi) - \mu^2 \phi^\dagger \phi - \lambda (\phi^\dagger \phi)^2, \quad \lambda > 0, \mu^2 < 0 \quad (1.37)$$

$$D_\mu \phi = \left(i\partial_\mu - g \frac{\sigma_i}{2} W_\mu^i - g' \frac{Y}{2} B_\mu \right) \phi \quad (1.38)$$

742 ϕ has to be an isospin doublet of complex scalar fields so it preserves the G invariance;
 743 thus ϕ can be defined as:

$$\phi = \begin{pmatrix} \phi^+ \\ \phi^0 \end{pmatrix} \equiv \frac{1}{\sqrt{2}} \begin{pmatrix} \phi_1 + i\phi_2 \\ \phi_3 + i\phi_4 \end{pmatrix}. \quad (1.39)$$

744 The minima of the potential are defined by

$$\phi^\dagger \phi = \frac{1}{2} (\phi_1^2 + \phi_2^2 + \phi_3^2 + \phi_4^2) = -\frac{\mu^2}{2\lambda}. \quad (1.40)$$

745 The choice of the ground state is critical. By choosing a ground state, invariant
 746 under $U(1)_{em}$ gauge symmetry, the photon will remain massless and the W^\pm and Z
 747 bosons masses will be generated which is exactly what is needed. In that sense, the
 748 best choice corresponds to a weak isospin doublet with $T_3 = -1/2$, $Y_W = 1$ and $Q = 0$
 749 which defines a ground state with $\phi_1 = \phi_2 = \phi_4$ and $\phi_3 = v$:

$$\phi_0 \equiv \frac{1}{\sqrt{2}} \begin{pmatrix} 0 \\ v \end{pmatrix}, \quad v^2 \equiv -\frac{\mu^2}{\lambda}. \quad (1.41)$$

750 where the vacuum expectation value v is fixed by the Fermi coupling G_F according
 751 to $v = (\sqrt{2}G_F)^{1/2} \approx 246$ GeV.

752 The G symmetry has been broken and three Nambu-Goldstone bosons will appear.

753 The next step is to expand ϕ about the chosen ground state as:

$$\phi(x) = \frac{1}{\sqrt{2}} \exp\left(\frac{i}{v} \sigma_i \theta^i(x)\right) \begin{pmatrix} 0 \\ v + H(x) \end{pmatrix} \approx \frac{1}{\sqrt{2}} \begin{pmatrix} \theta_1(x) + i\theta_2(x) \\ v + H(x) - i\theta_3(x) \end{pmatrix} \quad (1.42)$$

754 to describe fluctuations from the ground state ϕ_0 . The fields $\theta_i(x)$ represent the
 755 Nambu-Goldstone bosons while $H(x)$ is known as *Higgs field*. The fundamental fea-
 756 ture of the parametrization used is that the dependence on the $\theta_i(x)$ fields is factored
 757 out in a global phase that can be eliminated by taking the physical *unitary gauge*
 758 $\theta_i(x) = 0$. Therefore the expansion about the ground state is given by:

$$\phi(x) \frac{1}{\sqrt{2}} \begin{pmatrix} 0 \\ v + H(x) \end{pmatrix} \quad (1.43)$$

759 which when substituted into \mathcal{L}_S (Eqn. 1.37) results in a Lagrangian containing the
 760 now massive three gauge bosons W^\pm, Z , one massless gauge boson (photon) and
 761 the new Higgs field (H). The three degrees of freedom corresponding to the Nambu-
 762 Goldstone bosons are now integrated into the massive gauge bosons as their lon-
 763 gitudinal polarizations which were not available when they were massless particles.
 764 The effect by which vector boson fields acquire mass after an spontaneous symmetry
 765 breaking, but without an explicit gauge invariance breaking is known as the *Higgs*
 766 *mechanism*.

767 The mechanism was proposed by three independent groups: F.Englert and R.Brout
 768 in August 1964 [33], P.Higgs in October 1964 [34] and G.Guralnik, C.Hagen and
 769 T.Kibble in November 1964 [35]; however, its importance was not realized until
 770 S.Glashow [22], A.Salam [23] and S.Weinberg [24], independently, proposed that elec-
 771 tromagnetic and weak interactions are two manifestations of a more general interac-
 772 tion called *electroweak interaction* in 1967.

773 **1.3.3 Masses of the gauge bosons**

774 The masses of the gauge bosons are extracted by evaluating the kinetic part of La-
 775 grangian \mathcal{L}_S in the ground state (known also as the vacuum expectation value), i.e.,

$$\left| \left(\partial_\mu - ig \frac{\sigma_i}{2} W_\mu^i - i \frac{g'}{2} B_\mu \right) \phi_0 \right|^2 = \left(\frac{1}{2} v g \right)^2 W_\mu^+ W^{-\mu} + \frac{1}{8} v^2 (W_\mu^3, B_\mu) \begin{pmatrix} g^2 & -gg' \\ -gg' & g'^2 \end{pmatrix} \begin{pmatrix} W^{3\mu} \\ B^\mu \end{pmatrix} \quad (1.44)$$

776 comparing with the typical mass term for a charged boson $M_W^2 W^+ W^-$

$$M_W = \frac{1}{2} v g. \quad (1.45)$$

The second term in the right side of the Eqn.1.44 comprises the masses of the neutral bosons, but it needs to be written in terms of the gauge fields Z_μ and A_μ in order to be compared to the typical mass terms for neutral bosons, therefore using Eqn. 1.29

$$\begin{aligned} \frac{1}{8} v^2 [g^2 (W_\mu^3)^2 - 2gg' W_\mu^3 B^\mu + g'^2 B_\mu^2] &= \frac{1}{8} v^2 [g W_\mu^3 - g' B_\mu]^2 + 0[g' W_\mu^3 + g B_\mu]^2 \quad (1.46) \\ &= \frac{1}{8} v^2 [\sqrt{g^2 + g'^2} Z_\mu]^2 + 0[\sqrt{g^2 + g'^2} A_\mu]^2 \end{aligned}$$

777 and then

$$M_Z = \frac{1}{2} v \sqrt{g^2 + g'^2}, \quad M_A = 0 \quad (1.47)$$

778 **1.3.4 Masses of the fermions**

779 The lepton mass terms can be generated by introducing a gauge invariant Lagrangian
 780 term describing the Yukawa coupling between the lepton field and the Higgs field

$$\mathcal{L}_{Yl} = -G_l \left[(\bar{\nu}_l, \bar{l})_L \begin{pmatrix} \phi^+ \\ \phi^0 \end{pmatrix} l_R + \bar{l}_R (\phi^-, \bar{\phi}^0) \begin{pmatrix} \nu_l \\ l \end{pmatrix} \right], \quad l = e, \mu, \tau. \quad (1.48)$$

781 After the SSB and replacing the usual field expansion about the ground state
 782 (Eqn.1.41) into \mathcal{L}_{Yl} , the mass term arises

$$\mathcal{L}_{Yl} = -m_l (\bar{l}_L l_R + \bar{l}_R l_L) - \frac{m_l}{v} (\bar{l}_L l_R + \bar{l}_R l_L) H = -m_l \bar{l} \left(1 + \frac{H}{v} \right) \quad (1.49)$$

783

$$m_l = \frac{G_l}{\sqrt{2}} v \quad (1.50)$$

784 where the additional term represents the lepton-Higgs interaction. The quark masses
 785 are generated in a similar way as lepton masses but for the upper member of the
 786 quark doublet a different Higgs doublet is needed:

$$\phi_c = -i\sigma_2 \phi^* = \begin{pmatrix} -\bar{\phi}^0 \\ \phi^- \end{pmatrix}. \quad (1.51)$$

787 Additionally, given that the quark isospin doublets are not constructed in terms
 788 of the mass eigenstates but in terms of the flavor eigenstates, as shown in Table 1.5,
 789 the coupling parameters will be related to the CKM matrix elements; thus, the quark
 790 Lagrangian is given by:

$$\mathcal{L}_{Yq} = -G_d^{i,j} (\bar{u}_i, \bar{d}'_i)_L \begin{pmatrix} \phi^+ \\ \phi^0 \end{pmatrix} d_{jR} - G_u^{i,j} (\bar{u}_i, \bar{d}'_i)_L \begin{pmatrix} -\bar{\phi}^0 \\ \phi^- \end{pmatrix} u_{jR} + h.c. \quad (1.52)$$

791 with $i, j = 1, 2, 3$. After SSB and expansion about the ground state, the diagonal form

792 of \mathcal{L}_{Yq} is:

$$\mathcal{L}_{Yq} = -m_d^i \bar{d}_i d_i \left(1 + \frac{H}{v}\right) - m_u^i \bar{u}_i u_i \left(1 + \frac{H}{v}\right) \quad (1.53)$$

793 Fermion masses depend on arbitrary couplings G_l and $G_{u,d}$ and are not predicted
794 by the theory.

795 1.3.5 The Higgs field

796 After the characterization of the fermions and gauge bosons as well as their interac-
797 tions, it is necessary to characterize the Higgs field itself. The Lagrangian \mathcal{L}_S in Eqn.
798 1.37 written in terms of the gauge bosons is given by

$$\mathcal{L}_S = \frac{1}{4} \lambda v^4 + \mathcal{L}_H + \mathcal{L}_{HV} \quad (1.54)$$

799

$$\mathcal{L}_H = \frac{1}{2} \partial_\mu H \partial^\mu H - \frac{1}{2} m_H^2 H^2 - \frac{1}{2v} m_H^2 H^3 - \frac{1}{8v^2} m_H^2 H^4 \quad (1.55)$$

800

$$\mathcal{L}_{HV} = m_H^2 W_\mu^+ W^{\mu-} \left(1 + \frac{2}{v} H + \frac{2}{v^2} H^2\right) + \frac{1}{2} m_Z^2 Z_\mu Z^\mu \left(1 + \frac{2}{v} H + \frac{2}{v^2} H^2\right) \quad (1.56)$$

801 The mass of the Higgs boson is deduced as usual from the mass term in the Lagrangian
802 resulting in:

$$m_H = \sqrt{-2\mu^2} = \sqrt{2\lambda}v \quad (1.57)$$

803 however, it is not predicted by the theory either. The experimental measurement of
804 the Higgs boson mass have been performed by the *Compact Muon Solenoid (CMS)*
805 experiment and the *A Toroidal LHC Appartus (ATLAS)* experiments at the *Large
806 Hadron Collider (LHC)*, [36–38], and is presented in Table 1.8.

Property	Value
Electric charge	0
Color charge	0
Spin	0
Weak isospin	-1/2
Weak hypercharge	1
Parity	1
Mass (GeV/c^2)	$125.09 \pm 0.21 \text{ (stat.)} \pm 0.11 \text{ (syst.)}$

Table 1.8: Higgs boson properties. Higgs mass is not predicted by the theory and the value here corresponds to the experimental measurement.

1.3.6 Production of Higgs bosons at LHC

At the LHC, Higgs bosons are produced as a result of the collision of two counter-rotating protons beams. A detailed description of the LHC machine will be presented in chapter 2.

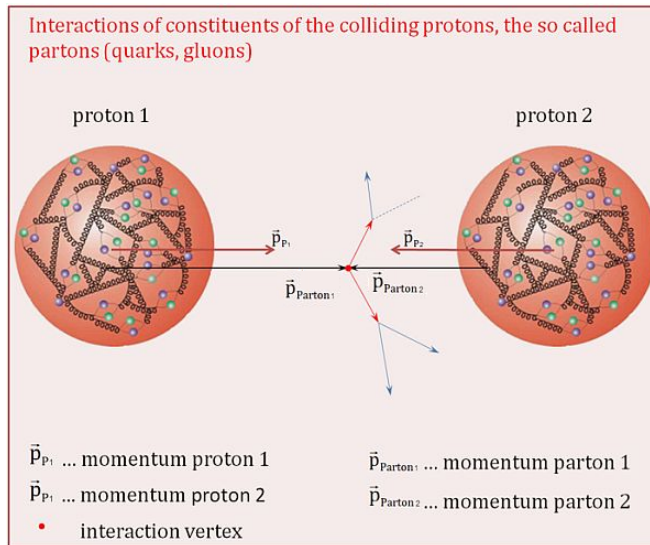


Figure 1.10: Proton-proton collision. Protons are composed of 3 valence quarks, a sea of quarks and gluons; therefore in a proton-proton collision, quarks and gluons are those who collide. [39].

811

812 Protons are composed of quarks and these quarks are bound by gluons; however,
 813 what is commonly called the quark content of the proton makes reference to the
 814 valence quarks. In fact, a proton is not just a rigid entity with three balls in it all
 815 tied up with springs, but the gluons exchanged by the valence quarks tend to split

816 spontaneously into quark-antiquark pairs or more gluons, creating *sea of quarks and*
 817 *gluons* as represented in Figure 1.10.

818 In a proton-proton (pp) collision, the proton's constituents, quarks and gluons, are
 819 those that collide. The pp cross section depends on the momentum of the colliding
 820 particles, reason for which it is needed to know how the momentum is distributed
 821 inside the proton. Quarks and gluons are known as partons, hence, the functions
 822 that describe how the proton momentum is distributed among partons inside it are
 823 called *parton distribution functions (PDFs)*; PDFs are determined from experimental
 824 data obtained in experiments where the internal structure of hadrons is tested, and
 825 depend on the momentum transfer Q and the fraction of momentum x carried by an
 826 specific parton. Figure 1.11 shows the proton PDFs ($xf(x, Q^2)$) for two values of Q .

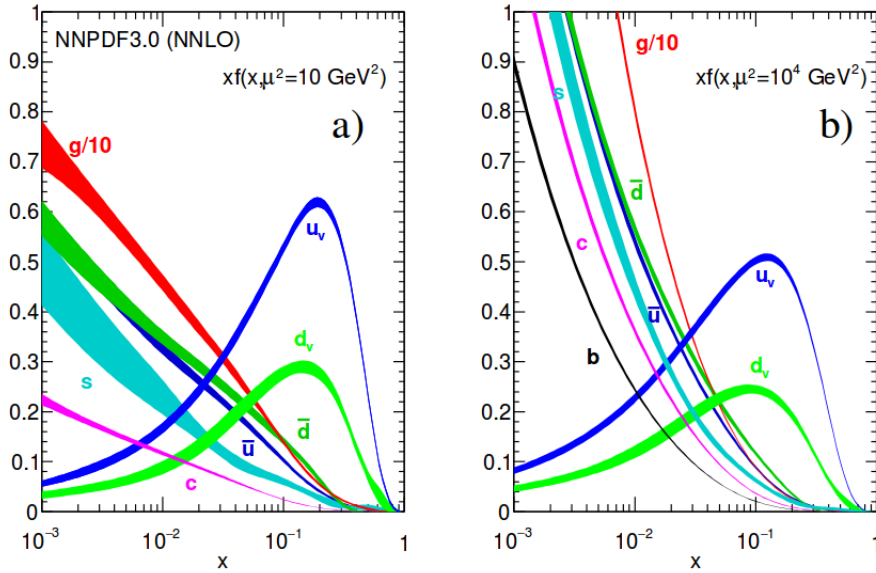


Figure 1.11: Proton PDFs for two values of Q^2 : left. $\mu^2 = Q^2 = 10 \text{ GeV}^2$, right. $\mu^2 = Q^2 = 10^4 \text{ GeV}^2$. u_v and d_v correspond to the u and d valence quarks, $s, c, b, \bar{u}, \bar{d}$ correspond to sea quarks, and g corresponds to gluons. Note that gluons carry a high fraction of the proton's momentum. [9]

827 In physics, a common approach to study complex systems consists of starting
 828 with a simpler version of them, for which a well known description is available, and

adding an additional *perturbation* which represents a small deviation from the known behavior. If the perturbation is small enough, the physical quantities associated with the perturbed system are expressed as a series of corrections to those of the simpler system. The perturbation series corresponds to an expansion in power series of a small parameter, therefore, the more terms are considered in the series (the higher order in the perturbation series), the more precise is the description of the complex system. If the perturbation does not get progressively smaller, the strategy cannot be applied and new methods have to be employed.

High energy systems, like the Higgs production at LHC explored in this thesis, usually can be treated perturbatively with the expansion made in terms of the coupling constants. The overview presented here will be oriented specifically to the Higgs boson production mechanisms in pp collisions at LHC.

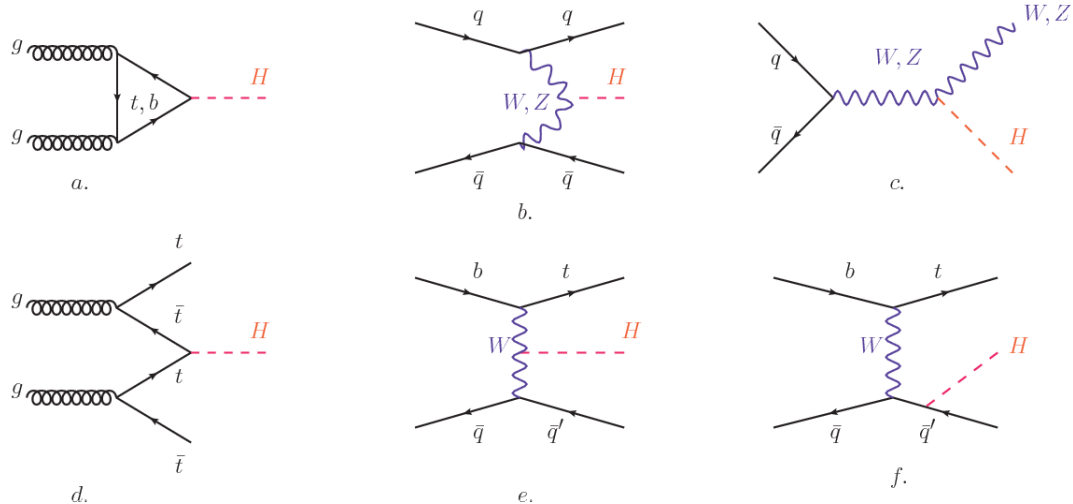


Figure 1.12: Main Higgs boson production mechanism Feynman diagrams. a. gluon-gluon fusion, b. vector boson fusion (VBF), c. Higgs-strahlung, d. Associated production with a top or bottom quark pair, e-f. associated production with a single top quark.

Figure 1.12 shows the Feynman diagrams for the leading order (first order) Higgs production processes at LHC; note that in these diagrams the incoming particles are not the protons themselves but the partons from the protons that actually participate

in the interaction, hence, theorists typically calculate the cross section for the parton interaction, and then convolute that cross section with the information from the PDFs to get a production cross section that is actually measured in experiments. The cross section for Higgs production as a function of the center of mass-energy (\sqrt{s}) for pp collisions is showed in Figure 1.13 left. The tags NLO (next to leading order), NNLO (next to next to leading order) and N3LO (next to next to next to leading order) make reference to the order at which the perturbation series have been considered while the tags QCD and EW correspond to the strong and electroweak coupling constants respectively.

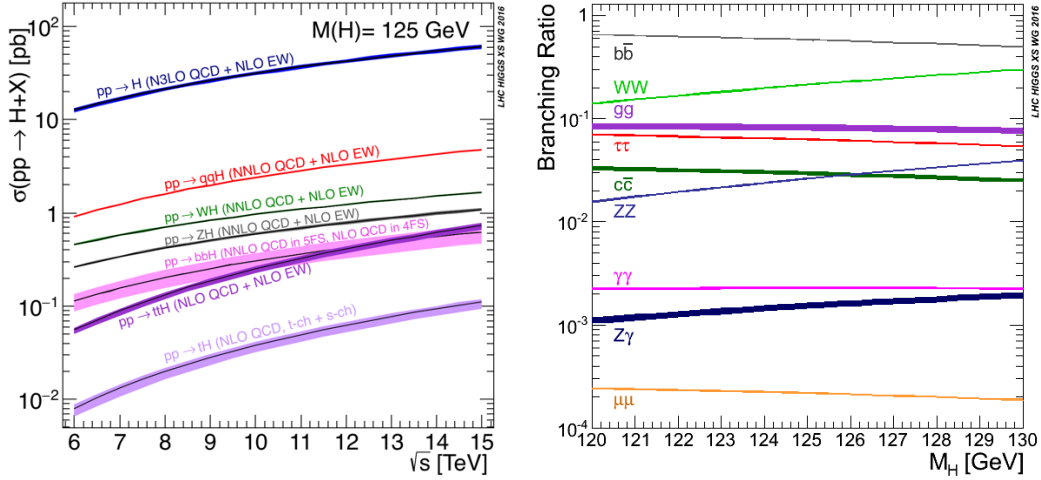


Figure 1.13: Higgs boson production cross sections (left) and decay branching ratios (right) for the main mechanisms. The VBF is indicated as qqH [40].

The main production mechanism is the gluon fusion (Figure 1.12a and $pp \rightarrow H$ in Figure 1.13) given that gluons carry the highest fraction of momentum of the protons in pp colliders (as shown in Figure ??). Since the Higgs boson does not couple to gluons, the mechanism proceeds through the exchange of a virtual top-quark loop. Note that in this process the Higgs boson is produced alone, turning out to be problematic for some Higgs decays, because such absence of anything produced in

859 association with the Higgs represent a trouble for triggering, however, this mechanism
 860 is experimentally clean when combined with the two-photon or the four-lepton decay
 861 channels (see Section 1.3.7).

862 Vector boson fusion (Figure 1.12b and $pp \rightarrow qqH$ in Figure 1.13) has the second
 863 largest production cross section. The scattering of two fermions is mediated by a weak
 864 gauge boson which later emits a Higgs boson. In the final state, the two fermions tend
 865 to be located in the central region of the detector; this kind of features are generally
 866 used as a signature when analyzing the datasets provided by the experiments⁷.

867 In the Higgs-strahlung mechanism (Figure 1.12c and $pp \rightarrow WH, pp \rightarrow ZH$ in
 868 Figure 1.13) two fermions annihilate to form a weak gauge boson. If the initial
 869 fermions have enough energy, the emergent boson might emit a Higgs boson.

870 The associated production with a top or bottom quark pair and the associated
 871 production with a single top quark (Figure 1.12d-f and $pp \rightarrow bbH, pp \rightarrow t\bar{t}H, pp \rightarrow tH$
 872 in Figure 1.13) have a smaller cross section than the main three mechanisms above,
 873 but they provide a good opportunity to test the Higgs-top coupling. The analysis
 874 reported in this thesis is developed using these production mechanisms. A detailed
 875 description of the tH mechanism will be given in Section 1.5.

876 1.3.7 Higgs boson decay channels

877 When a particle can decay through several modes, also known as channels, the prob-
 878 ability of decaying through a given channel is quantified by the *branching ratio (BR)*
 879 of the decay channel; thus, the BR is defined as the ratio of number of decays go-
 880 ing through that given channel to the total number of decays. In regard to the
 881 Higgs boson decay, the BR can be predicted with accuracy once the Higgs mass is
 882 known [41, 42]. In Figure 1.13 right, a plot of the BR as a function of the Higgs mass

⁷ More details about how to identify events of interest in this analysis will be given in chapter 6.

883 is presented; the largest predicted BR corresponds to the $b\bar{b}$ pair decay channel (see
 884 Table 1.9) given that it is the heaviest particle pair whose on-shell⁸ production is
 885 kinematically allowed in the decay.

Decay channel	Branching ratio	Rel. uncertainty
$H \rightarrow b\bar{b}$	5.84×10^{-1}	+3.2% – 3.3%
$H \rightarrow W^+W^-$	2.14×10^{-1}	+4.3% – 4.2%
$H \rightarrow \tau^+\tau^-$	6.27×10^{-2}	+5.7% – 5.7%
$H \rightarrow ZZ$	2.62×10^{-2}	+4.3% – 4.1%
$H \rightarrow \gamma\gamma$	2.27×10^{-3}	+5.0% – 4.9%
$H \rightarrow Z\gamma$	1.53×10^{-3}	+9.0% – 8.9%
$H \rightarrow \mu^+\mu^-$	2.18×10^{-4}	+6.0% – 5.9%

Table 1.9: Predicted branching ratios and the relative uncertainty for some decay channels of a SM Higgs boson with $m_H = 125\text{GeV}/c^2$ [9]; the uncertainties are driven by theoretical uncertainties for the different Higgs boson partial widths and by parametric uncertainties associated to the strong coupling and the masses of the quarks which are the input parameters. Further details on these calculations can be found in Reference [43]

886

887 Decays to other lepton and quark pairs, like electron, strange, up, and down
 888 quark pairs not listed in the table, are also possible but their likelihood is too small
 889 to measure since they are very lightweight, hence, their interaction with the Higgs
 890 boson is very weak. On other hand, the decay to top quark pairs is heavily suppressed
 891 due to the top quark mass ($\approx 173\text{ GeV}/c^2$).

892 Decays to gluons proceed indirectly through a virtual top quark loop while the
 893 decays to photons proceed through a virtual W boson loop, therefore, their branching
 894 ratio is smaller compared to direct interaction decays. Same is true for the decay to
 895 a photon and a Z boson.

⁸ In general, on-shell or real particles are those which satisfy the energy-momentum relation ($E^2 - |\vec{p}|^2 c^2 = m^2 c^4$); off-shell or virtual particles does not satisfy it which is possible under the uncertainty principle of quantum mechanics. Usually, virtual particles correspond to internal propagators in Feynman diagrams.

896 In the case of decays to pairs of W and Z bosons, the decay proceed with one of
 897 the bosons being on-shell and the other being off-shell. The likelihood of the process
 898 diminish depending on how far off-shell are the virtual particles involved, hence, the
 899 branching ratio for W boson pairs is bigger than for Z boson pairs since Z boson mass
 900 is bigger than W boson mass.

901 Note that the decay to a pair of virtual top quarks is possible, but the probability
 902 is way too small.

903 **1.4 Experimental status of the anomalous
 904 Higgs-fermion coupling**

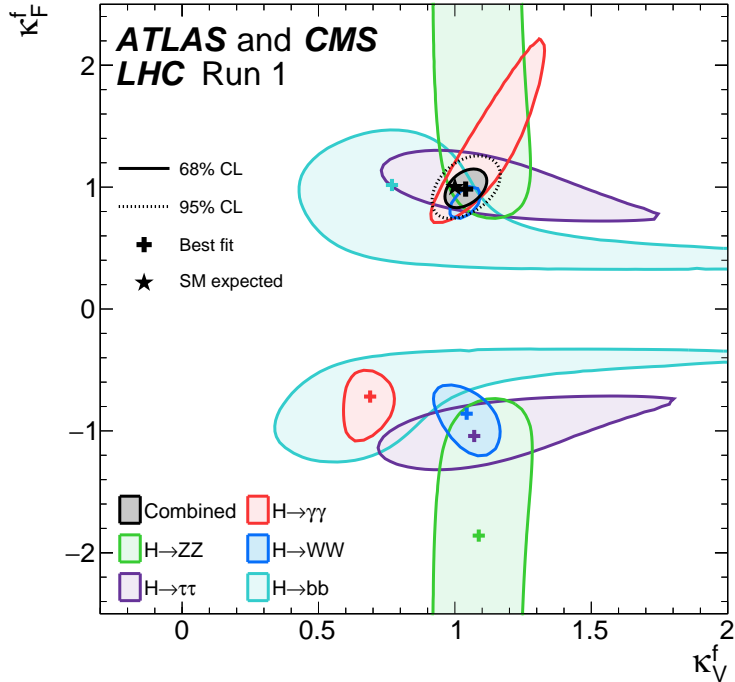


Figure 1.14: Combination of the ATLAS and CMS fits for coupling modifiers $\kappa_t - \kappa_V$; also shown the individual decay channels combination and their global combination. No assumptions have been made on the sign of the coupling modifiers [44].

905 ATLAS and CMS have performed analyses of the anomalous Higgs-fermion cou-
 906 pling by making likelihood scans for the two coupling modifiers, κ_f and κ_V , under
 907 the assumption that $\kappa_Z = \kappa_W \equiv \kappa_V$ and $\kappa_t = \kappa_\tau = \kappa_b \equiv \kappa_f$. Figure 1.14 shows the
 908 result of the combination of ATLAS and CMS fits; also the individual decay channels
 909 combination and the global combination results are shown. Note that from this plot
 910 there is limited information on the sign of the coupling since the only information
 911 available about the sign of the coupling comes from decays rather than production.

912 While all the channels are compatible for positive values of the modifiers, for
 913 negative values of κ_f there is no compatibility. The best fit for individual channels
 914 is compatible with negative values of κ_f except for the $H \rightarrow bb$ channel. The best
 915 fit for the combination yields $\kappa_f \geq 0$, in contrast to the yields from the individual
 916 channels; the reason of this yield resides in the $H \rightarrow \gamma\gamma$ coupling. $H \rightarrow \gamma\gamma$ decay
 917 proceeds through a loop of either top quarks or W bosons, hence, this channel is
 918 sensitive to κ_t thanks to the interference of these two amplitude contributions; under
 919 the assumption that no beyond SM particles take part in the loops, a flipped sign
 920 of κ_t will increase the $H \rightarrow \gamma\gamma$ branching fraction by a factor of ~ 2.4 which is not
 921 supported by measurements; thus, this large asymmetry between the positive and
 922 negative coupling ratios in the $H \rightarrow \gamma\gamma$ channel drives the yield of the global fit and
 923 would mean that the anomalous H-t coupling is excluded as stated in Reference [44],
 924 but there is a caveat, this exclusion holds only if no new particles contribute to the
 925 loop in the main diagram for that decay.

926 Although the $H \rightarrow bb$ channel is expected to be the most sensitive channel and
 927 its best fit value of κ_t is positive, and then the global fit yield is still supported,
 928 the contributions from all the other decay channels, small compared to the $H \rightarrow bb$,
 929 indicate that the anomalous H-t coupling cannot be excluded completely, motivating
 930 to look at tH processes which can help with both, the limited information on the sign

931 of the H-t coupling and the access to information from the Higgs boson production
 932 rather than from its decays.

933 It will be shown in Section 1.5 that the same interference effect enhance the
 934 tH production rate and could reveal evidence of direct production of heavy new par-
 935 ticles as predicted in composite and little Higgs models [45], or new physics related
 936 to Higgs boson mediated flavor changing neutral currents [46] as well as probes the
 937 CP-violating phase of the H-t coupling [47, 48].

938 **1.5 Associated production of a Higgs boson and a 939 single top quark**

940 The production of Higgs boson in association with a top quark has been extensively
 941 studied [47, 49–52]. While measurements of the main Higgs production mechanisms
 942 rates are sensitive to the strength of the Higgs coupling to W boson or top quark,
 943 they are not sensitive to the relative sign between the two couplings. In this thesis,
 944 the Higgs boson production mechanism explored is the associated production with a
 945 single top quark (tH) which offers sensitivity to the relative sign of the Higgs couplings
 946 to W boson and to top quark. The description given here is based on Reference [51]

A process where two incoming particles interact and produce a final state with two particles can proceed in three called channels (see, for instance, Figure 1.15 omitting the red line). The t-channel represents processes where an intermediate particle is emitted by one of the incoming particles and absorbed by the other. The s-channel represents processes where the two incoming particles merge into an intermediate particle which eventually will split into the particles in the final state. The third channel, u-channel, is similar to the t-channel but the two outgoing particles interchange their

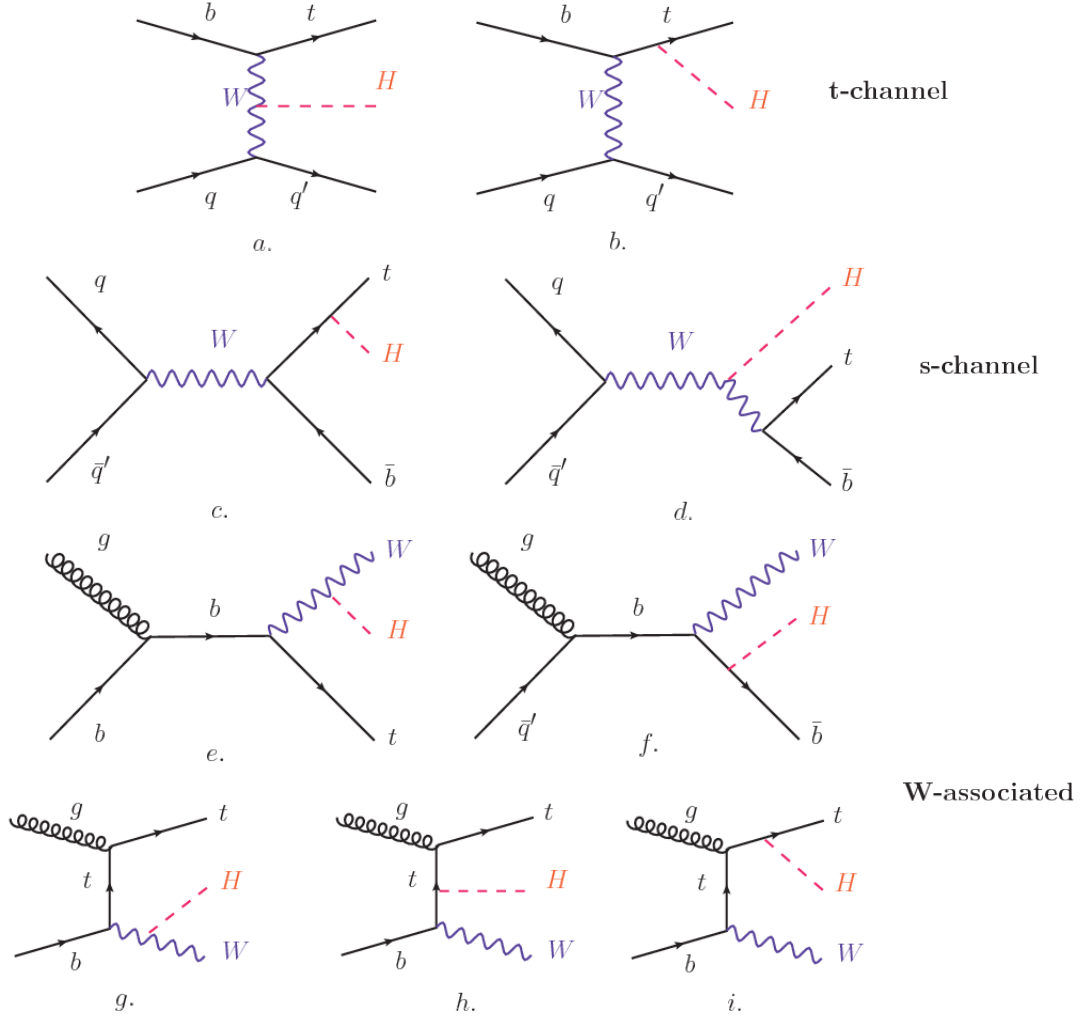


Figure 1.15: Associated Higgs boson production with a top quark mechanism Feynman diagrams. a.,b. t-channel (tHq), c.,d. s-channel (tHb), e-i. W-associated.

roles. These three channels are connected to the so-called Mandelstam variables

$$s = (p_1 + p_2)^2 = (p'_1 + p'_2)^2 \rightarrow \text{square of the center mass-energy.} \quad (1.58)$$

$$t = (p_1 - p'_1)^2 = (p'_2 - p_2)^2 \rightarrow \text{square of the four-momentum transfer.} \quad (1.59)$$

$$u = (p_1 - p'_2)^2 = (p'_1 - p_2)^2 \rightarrow \text{square of the crossed four-momentum transfer.} \quad (1.60)$$

$$s + t + u = m_1^2 + m_2^2 + m'_1{}^2 + m'_2{}^2 \quad (1.61)$$

which relate the momentum, energy and the angles of the incoming and outgoing particles in an scattering process of two particles to two particles. The importance of the Mandelstam variables reside in that they form a minimum set of variables needed to describe the kinematics of this scattering process; they are Lorentz invariant which makes them very useful when doing calculations.

The tH production, where Higgs boson can be radiated either from the top quark or from the W boson, is represented by the leading order Feynman diagrams in Figure 1.15. The cross section for the tH process is calculated, as usual, summing over the contributions from the different Feynman diagrams; therefore it depends on the interference between the contributions. In the SM, the interference for t-channel (tHq process) and W-associated (tHW process) production is destructive [49] resulting in the small cross sections presented in Table 1.10.

tH production channel	Cross section (fb)
t-channel ($pp \rightarrow tHq$)	$70.79^{+2.99}_{-4.80}$
W-associated ($pp \rightarrow tHW$)	$15.61^{+0.83}_{-1.04}$
s-channel($pp \rightarrow tHb$)	$2.87^{+0.09}_{-0.08}$

Table 1.10: Predicted SM cross sections for tH production at $\sqrt{s} = 13$ TeV [53, 54].

959

The s-channel contribution can be neglected. It will be shown that a deviation from the SM destructive interference would result in an enhancement of the tH cross section compared to that in SM, which could be used to get information about the sign of the Higgs-top coupling [51, 52]. In order to describe tH production processes, Feynman diagram 1.15b will be considered; there, the W boson is radiated by a quark in the proton and eventually it will interact with the b quark. In the high energy regime, the effective W approximation [55] is used to describe the process as the

967 emission of an approximately on-shell W and its hard scattering with the b quark;
 968 i.e. $Wb \rightarrow th$. The scattering amplitude for the process is given by

$$\mathcal{A} = \frac{g}{\sqrt{2}} \left[(\kappa_t - \kappa_V) \frac{m_t \sqrt{s}}{m_W v} A \left(\frac{t}{s}, \varphi; \xi_t, \xi_b \right) + \left(\kappa_V \frac{2m_W s}{v t} + (2\kappa_t - \kappa_V) \frac{m_t^2}{m_W v} \right) B \left(\frac{t}{s}, \varphi; \xi_t, \xi_b \right) \right], \quad (1.62)$$

969 where $\kappa_V \equiv g_{HVV}/g_{HVV}^{SM}$ and $\kappa_t \equiv g_{Ht}/g_{Ht}^{SM} = y_t/y_t^{SM}$ are scaling factors that quantify
 970 possible deviations of the couplings from the SM values, Higgs-Vector boson (H-
 971 W) and Higgs-top (H-t) respectively, from the SM couplings; $s = (p_W + p_b)^2$, $t =$
 972 $(p_W - p_H)^2$, φ is the Higgs azimuthal angle around the z axis taken parallel to the
 973 direction of motion of the incoming W; A and B are functions describing the weak
 974 interaction in terms of the chiral states (ξ_t, ξ_b) of the quarks b and t . Terms that
 975 vanish in the high energy limit have been neglected as well as the Higgs and b quark
 976 masses⁹.

977 The scattering amplitude grows with energy like \sqrt{s} for $\kappa_V \neq \kappa_t$, in contrast to
 978 the SM ($\kappa_t = \kappa_V = 1$), where the first term in 1.62 cancels out and the amplitude
 979 is constant for large s ; therefore, a deviation from the SM predictions represents an
 980 enhancement in the tHq cross section. In particular, for a SM H-W coupling and a
 981 H-t coupling of inverted sign with respect to the SM ($\kappa_V = -\kappa_t = 1$) the tHq cross
 982 section is enhanced by a factor greater 10 as seen in the Figure 1.16 taken from
 983 Reference [51]; Reference [56] has reported similar enhancement results.

984 A similar analysis is valid for the W-associated channel but, in that case, the in-
 985 terference is more complicated since there are more than two contributions and an ad-
 986 ditional interference with the production of Higgs boson and a top pair process($t\bar{t}H$).
 987 The calculations are made using the so-called Diagram Removal (DR) technique where

⁹ A detailed explanation of the structure and approximations used to derive \mathcal{A} can be found in Reference [51]

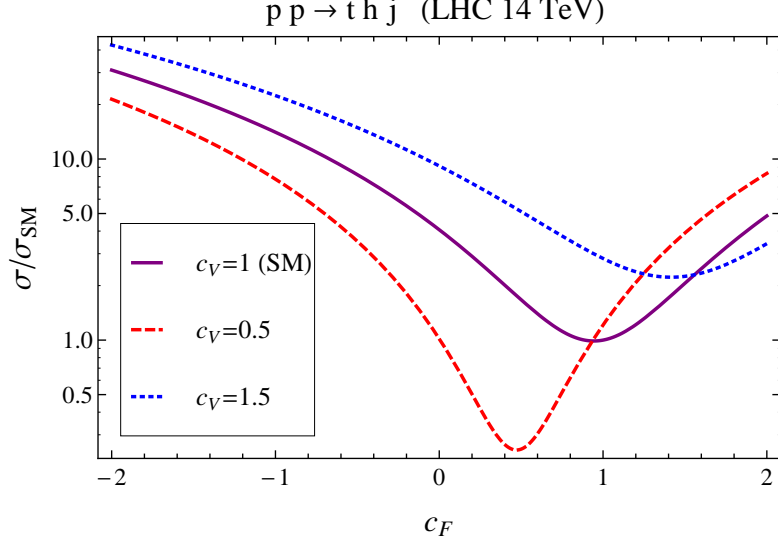


Figure 1.16: Cross section for tHq process as a function of κ_t , normalized to the SM, for three values of κ_V . In the plot c_f refers to the Higgs-fermion coupling which is dominated by the H-t coupling and represented here by κ_t . Solid, dashed and dotted lines correspond to $c_V \rightarrow \kappa_V = 1, 0.5, 1.5$ respectively. Note that for the SM ($\kappa_V = \kappa_t = 1$), the destructive effect of the interference is maximal.

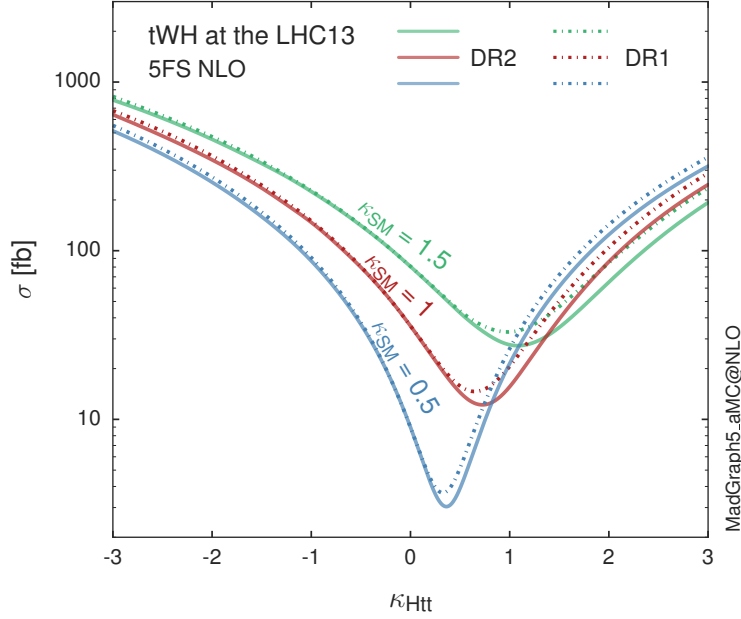


Figure 1.17: Cross section for tHW process as a function of κ_{Htt} , for three values of κ_{SM} at $\sqrt{s} = 13$ TeV. $\kappa_{Htt}^2 = \sigma_{Htt}/\sigma_{Htt}^{SM}$ is a simple re-scaling of the SM Higgs interactions.

interfering diagrams are removed (or added) from the calculations in order to evaluate the impact of the removed contributions. DR1 was defined to neglect $t\bar{t}H$ interference while DR2 was defined to take $t\bar{t}H$ interference into account [48]. As shown in Figure 1.17, the tHW cross section is enhanced from about 15 fb (SM: $\kappa_{Htt} = 1$) to about 150 fb ($\kappa_{Htt} = -1$). Differences between curves for DR1 and DR2 help to gauge the impact of the interference with $t\bar{t}H$. Results of the calculations of the tHq and tHW cross sections at $\sqrt{s} = 13$ TeV can be found in Reference [57] and a summary of the results is presented in Table 1.11.

	\sqrt{s} TeV	$\kappa_t = 1$	$\kappa_t = -1$
$\sigma^{LO}(tHq)(fb)$ [51]	8	≈ 17.4	≈ 252.7
	14	≈ 80.4	≈ 1042
$\sigma^{NLO}(tHq)(fb)$ [51]	8	$18.28^{+0.42}_{-0.38}$	$233.8^{+4.6}_{-0.0}$
	14	$88.2^{+1.7}_{-0.0}$	$982.8^{+28}_{-0.0}$
$\sigma^{LO}(tHq)(fb)$ [56]	14	≈ 71.8	≈ 893
$\sigma^{LO}(tHW)(fb)$ [56]	14	≈ 16.0	≈ 139
$\sigma^{NLO}(tHq)(fb)$ [57]	8	$18.69^{+8.62\%}_{-17.13\%}$	-
	13	$74.25^{+7.48\%}_{-15.35\%}$	$848^{+7.37\%}_{-13.70\%}$
	14	$90.10^{+7.34\%}_{-15.13\%}$	$1011^{+7.24\%}_{-13.39\%}$
$\sigma^{LO}(tHW)(fb)$ [48]	13	$15.77^{+15.91\%}_{-15.76\%}$	-
$\sigma^{NLO}DR1(tHW)(fb)$ [48]	13	$21.72^{+6.52\%}_{-5.24\%}$	≈ 150
$\sigma^{NLO}DR2(tHW)(fb)$ [48]	13	$16.28^{+7.34\%}_{-15.13\%}$	≈ 150

Table 1.11: Predicted enhancement of the tHq and tHW cross sections at LHC for $\kappa_V = 1$ and $\kappa_t = \pm 1$ at LO and NLO; the cross section enhancement of more than a factor of 10 is due to the flipping in the sign of the H-t coupling with respect to the SM one.

996

997 1.6 CP-mixing in tH processes

998 In addition to the sensitivity to sign of the H-t coupling, the tHq and tHW processes
999 have been proposed as a tool to investigate the possibility of a H-t coupling that does

1000 not conserve CP [47, 48, 58].

1001 In this thesis, the sensitivity of tH processes to CP-mixing is also studied on the
 1002 basis of References [47, 48] using the effective field theory framework where a generic
 1003 particle (X_0) of spin-0 and a general CP violating interaction with the top quark
 1004 (Htt coupling), can couple to scalar and pseudo-scalar fermionic densities. The H-W
 1005 interaction is assumed to be SM-like. The Lagrangian modeling the H-t interaction
 1006 is given by

$$\mathcal{L}_0^t = -\bar{\psi}_t (c_\alpha \kappa_{Htt} g_{Htt} + i s_\alpha \kappa_{Att} g_{Att} \gamma_5) \psi_t X_0, \quad (1.63)$$

1007 where α is the CP-mixing phase, $c_\alpha \equiv \cos \alpha$ and $s_\alpha \equiv \sin \alpha$, κ_{Htt} and κ_{Att} are real
 1008 dimensionless re-scaling parameters¹⁰ used to parametrize the magnitude of the CP-
 1009 violating and CP-conserving parts of the amplitude. The model defines $g_{Htt} =$
 1010 $g_{Att} = m_t/v = y_t/\sqrt{2}$ with $v \sim 246$ GeV the Higgs vacuum expectation value. In
 1011 this parametrization, three special cases can be recovered

1012 • CP-even coupling $\rightarrow \alpha = 0^\circ$

1013 • CP-odd coupling $\rightarrow \alpha = 90^\circ$

1014 • SM coupling $\rightarrow \alpha = 0^\circ$ and $\kappa_{Htt} = 1$

1015 The loop induced X_0 coupling to gluons can also be described in terms of the
 1016 parametrization above, according to

$$\mathcal{L}_0^g = -\frac{1}{4} (c_\alpha \kappa_{Hgg} g_{Hgg} G_{\mu\nu}^a G^{a,\mu\nu} + s_\alpha \kappa_{Agg} g_{Agg} G_{\mu\nu}^a \tilde{G}^{a,\mu\nu}) X_0. \quad (1.64)$$

1017 where $g_{Hgg} = -\alpha_s/3\pi v$ and $g_{Agg} = \alpha_s/2\pi v$ and $G_{\mu\nu}$ is the gluon field strength tensors.

1018 Under the assumption that the top quark dominates the gluon-fusion process at LHC

¹⁰ analog to κ_t and κ_V

1019 energies, $\kappa_{Hgg} \rightarrow \kappa_{Htt}$ and $\kappa_{Agg} \rightarrow \kappa_{Att}$, so that the ratio between the gluon-gluon
 1020 fusion cross section for X_0 and for the SM Higgs prediction can be written as

$$\frac{\sigma_{NLO}^{gg \rightarrow X_0}}{\sigma_{NLO,SM}^{gg \rightarrow H}} = c_\alpha^2 \kappa_{Htt}^2 + s_\alpha^2 \left(\kappa_{Att} \frac{g_{Agg}}{g_{Hgg}} \right)^2. \quad (1.65)$$

1021 If the re-scaling parameters are set to

$$\kappa_{Htt} = 1, \quad \kappa_{Att} = \left| \frac{g_{Hgg}}{g_{Agg}} \right| = \frac{2}{3}. \quad (1.66)$$

1022 the gluon-fusion SM cross section is reproduced for every value of the CP-mixing
 1023 angle α ; therefore, by imposing that condition to the Lagrangian density 1.63, the
 1024 CP-mixing angle is not constrained by current data. Figure 1.18 shows the NLO cross
 1025 sections for t-channel tX_0 (blue) and $t\bar{t}X_0$ (red) associated production processes as a
 1026 function of the CP-mixing angle α . X_0 is a generic spin-0 particle with top quark
 1027 CP-violating coupling. Re-scaling factors κ_{Htt} and κ_{Att} have been set to reproduce
 1028 the SM gluon-fusion cross sections.

1029 It is interesting to notice that the tX_0 cross section is enhanced, by a factor of
 1030 about 10, when a continuous rotation in the scalar-pseudoscalar plane is applied; this
 1031 enhancement is similar to the enhancement produced when the H-t coupling is flipped
 1032 in sign with respect to the SM ($y_t = -y_{t,SM}$ in the plot), as showed in Section 1.5. In
 1033 contrast, the degeneracy in the $t\bar{t}X_0$ cross section is still present given that it depends
 1034 quadratically on the H-t coupling, but more interesting is to notice that $t\bar{t}X_0$ cross
 1035 section is exceeded by tX_0 cross section after $\alpha \sim 60^\circ$.

1036 A similar parametrization can be used to investigate the tHW process sensitivity
 1037 to CP-violating H-t coupling. As said in 1.5, the interference in the W-associated
 1038 channel is more complicated because there are more than two contributions and also
 1039 there is interference with the $t\bar{t}H$ production process.

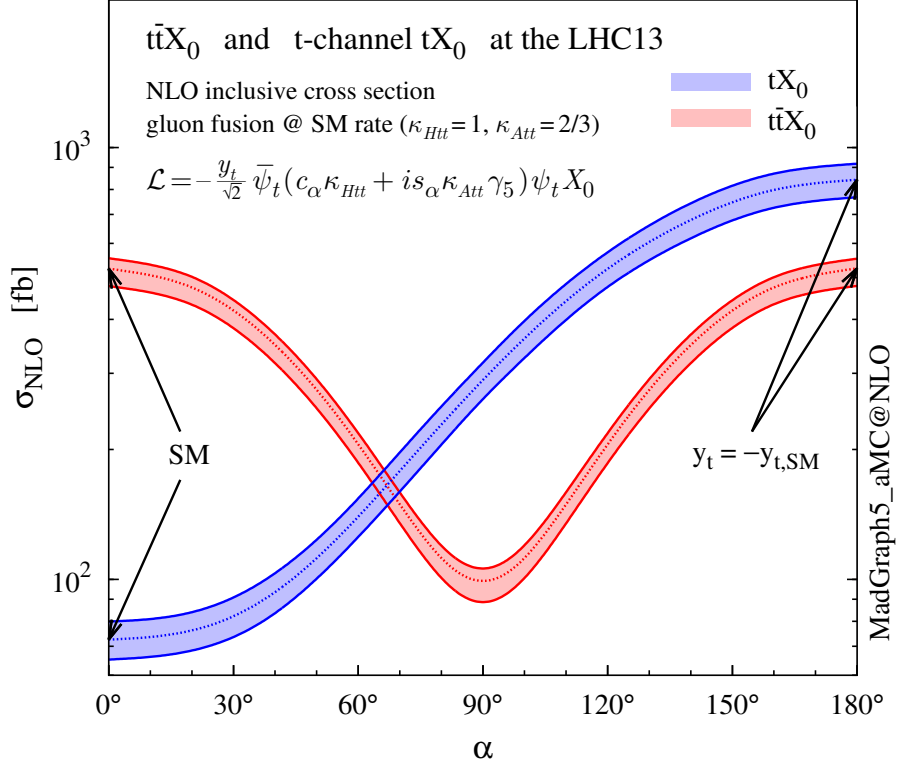


Figure 1.18: NLO cross sections for t-channel tX_0 (blue) and $t\bar{t}X_0$ (red) associated production processes as a function of the CP-mixing angle α . X_0 is a generic spin-0 particle with top quark CP-violating coupling [47].

1040 Figure 1.19 shows the NLO cross sections for t-channel tX_0 (blue), $t\bar{t}X_0$ (red)
 1041 associated production and for the combined $tWX_0+t\bar{t}X_0+interference$ (orange) as
 1042 a function of the CP-mixing angle. It is clear that the effect of the interference in the
 1043 combined case is the lifting of the degeneracy present in the $t\bar{t}X_0$ production. The
 1044 constructive interference enhances the cross section from about 500 fb at SM ($\alpha = 0$)
 1045 to about 600 fb ($\alpha = 180^\circ \rightarrow y_t = -y_{t,SM}$).

1046 An analysis combining tHq and tHW processes will be made in this thesis taking
 1047 advantage of the sensitivity improvement.

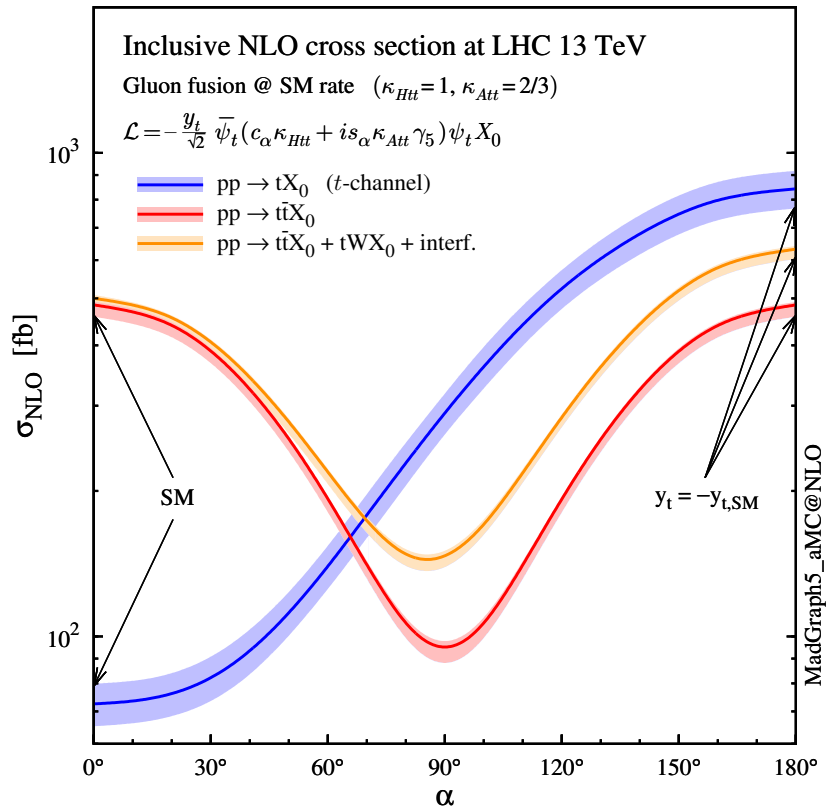


Figure 1.19: NLO cross sections for t-channel tX_0 (blue), $t\bar{t}X_0$ (red) associated production processes and combined $tWX_0 + t\bar{t}X_0$ (including interference) production as a function of the CP-mixing angle α [47].

₁₀₄₈ **Chapter 2**

₁₀₄₉ **The CMS experiment at the LHC**

₁₀₅₀ **2.1 Introduction**

₁₀₅₁ Located on the Swiss-French border, the European Council for Nuclear Research
₁₀₅₂ (CERN) is the largest scientific organization leading particle physics research. About
₁₀₅₃ 13000 people in a broad range of roles including users, students, scientists, engineers,
₁₀₅₄ among others, contribute to the data taking and analysis, with the goal of unveiling
₁₀₅₅ the secrets of nature and revealing the fundamental structure of the universe. CERN
₁₀₅₆ is also the home of the Large Hadron Collider (LHC), the largest particle accelerator
₁₀₅₇ around the world, where protons (or heavy ions) traveling close to the speed of light,
₁₀₅₈ are made to collide. These collisions open a window to investigate how particles (and
₁₀₅₉ their constituents if they are composite) interact with each other, providing clues
₁₀₆₀ about the laws of nature. This chapter presents an overview of the LHC structure
₁₀₆₁ and operation. A detailed description of the CMS detector is offered, given that the
₁₀₆₂ data used in this thesis have been taken with this detector.

1063 2.2 The LHC

1064 With 27 km of circumference, the LHC is currently the most powerful circular accelerator
 1065 in the world. It is installed in the same tunnel where the Large Electron-Positron
 1066 (LEP) collider was located, taking advantage of the existing infrastructure. The LHC
 1067 is part of the CERN's accelerator complex composed of several successive accelerat-
 1068 ing stages before the particles are injected into the LHC ring where they reach their
 1069 maximum energy (see Figure 2.1).

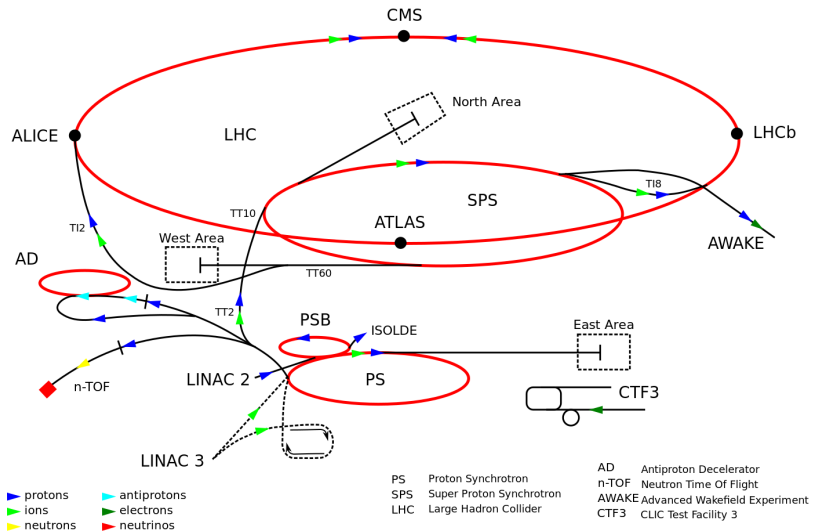


Figure 2.1: CERN accelerator complex. Blue arrows show the path followed by protons along the acceleration process [61].

1070 The LHC runs in three collision modes depending on the particles being acceler-
 1071 ated

- 1072 • Proton-Proton collisions (pp) for multiple physics experiments.
- 1073 • Lead-Lead collisions ($Pb-Pb$) for heavy ion experiments.
- 1074 • Proton-Lead collisions ($p-Pb$) for quark-gluon plasma experiments.

1075 In this thesis only pp collisions will be considered.

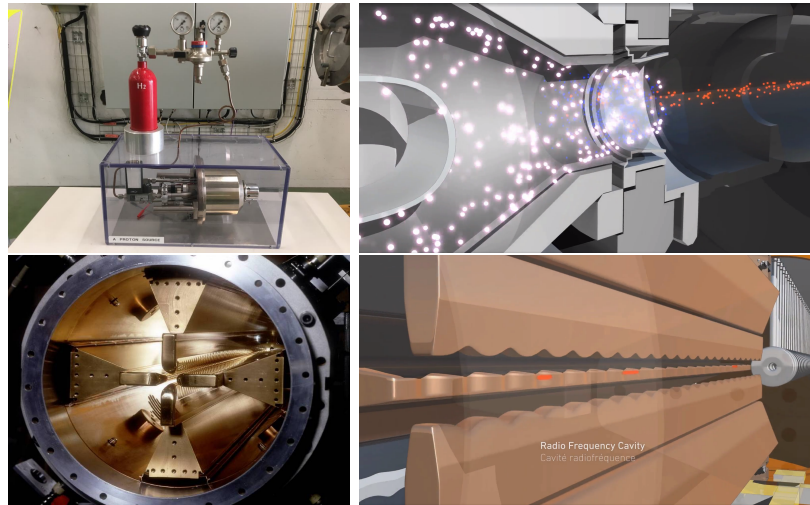


Figure 2.2: LHC protons source and the first acceleration stage. Top: the bottle contains hydrogen gas which is injected into the metal cylinder (white dots) to be broken down into electrons (blue dots) and protons (red dots); Bottom: the obtained protons are directed towards the radio frequency quadrupole which perform the first acceleration, focus the beam and create the bunches of protons. Left images are real pictures while right images are drawings [65, 66].

1076 Collection of protons starts with hydrogen atoms taken from a bottle, containing
 1077 hydrogen gas, and injecting them in a metal cylinder; hydrogen atoms are broken
 1078 down into electrons and protons by an intense electric field (see Figure 2.2 top).
 1079 The resulting protons leave the metal cylinder towards a radio frequency quadrupole
 1080 (RFQ) that focus the beam, accelerates the protons and creates the packets of protons
 1081 called bunches. In the RFQ, an electric field is generated by a RF wave at a frequency
 1082 that matches the resonance frequency of the cavity where the electrodes are contained.
 1083 The beam of protons traveling on the RFQ axis experiences an alternating electric
 1084 field gradient that generates the focusing forces.

1085 In order to accelerate the protons, a longitudinal time-varying electric field com-
 1086 ponent is added to the system; it is done by giving the electrodes a sine-like profile as
 1087 shown in Figure 2.2 bottom. By matching the speed and phase of the protons with
 1088 the longitudinal electric field the bunching is performed; protons synchronized with

1089 the RFQ (synchronous protons) do not feel an accelerating force, but those protons in
 1090 the beam that have more (or less) energy than the synchronous proton (asynchronous
 1091 protons) will feel a decelerating (accelerating) force; therefore, asynchronous protons
 1092 will oscillate around the synchronous ones forming bunches of protons [63]. From the
 1093 RFQ protons emerge with energy 750 keV in bunches of about 1.15×10^{11} protons [64].

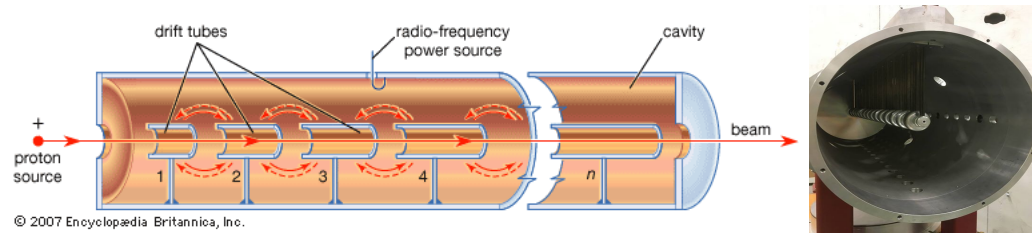


Figure 2.3: Left: drawing of the LINAC2 accelerating system at CERN. Electric fields generated by radio frequency (RF) create acceleration and deceleration zones inside the cavity; deceleration zones are blocked by drift tubes where quadrupole magnets focus the proton beam. Right: picture of a real RF cavity [67].

1094 Proton bunches coming from the RFQ go to the linear accelerator 2 (LINAC2)
 1095 where they are accelerated to reach 50 MeV energy. In the LINAC2 stage, acceleration
 1096 is performed using electric fields generated by radio frequency which create zones
 1097 of acceleration and deceleration as shown in Figure 2.3. In the deceleration zones,
 1098 the electric field is blocked using drift tubes where protons are free to drift while
 1099 quadrupole magnets focus the beam.

1100 The beam coming from LINAC2 is injected into the proton synchrotron booster
 1101 (PSB) to reach 1.4 GeV in energy. The next acceleration is provided at the proton
 1102 synchrotron (PS) up to 26 GeV, followed by the injection into the super proton
 1103 synchrotron (SPS) where protons are accelerated to 450 GeV. Finally, protons are
 1104 injected into the LHC where they are accelerated to the target energy of 6.5 TeV.

1105 PSB, PS, SPS and LHC accelerate protons using the same RF acceleration tech-
 1106 nique described before.

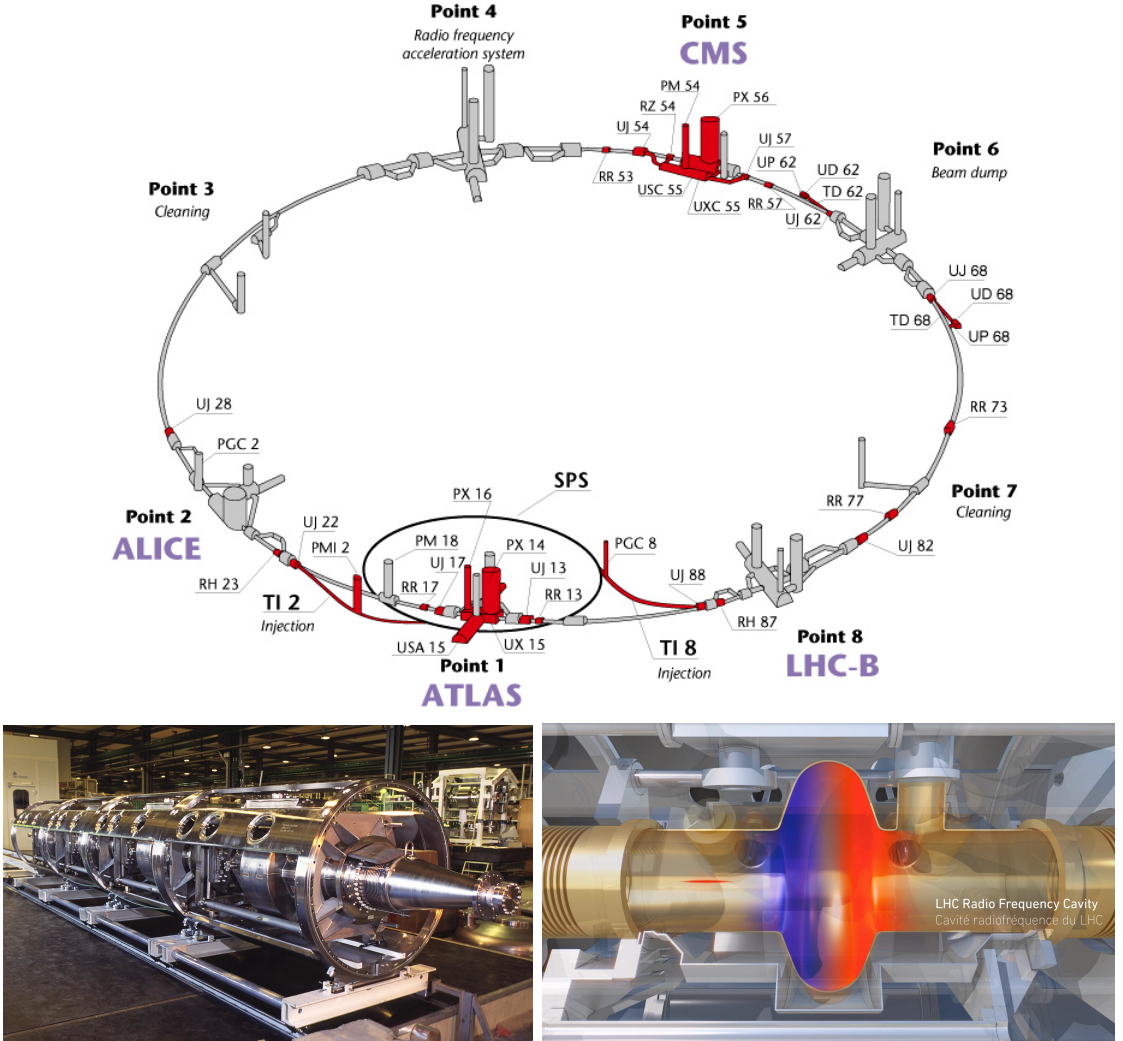


Figure 2.4: Top: LHC layout. The red zones indicate the infrastructure additions to the LEP installations, built to accommodate the ATLAS and CMS experiments which exceed the size of the former experiments located there [62]. Bottom: LHC RF cavities. A module (left picture) accommodates 4 cavities, each like the one in the right drawing, that accelerate protons and preserve the bunch structure of the beam. The color gradient pattern represents the strength of the electric field inside the cavity; red zone corresponds to the maximum of the oscillation electric field while the blue zone corresponds to the minimum. [66, 68]

1107 The LHC has a system of 16 RF cavities located in the so-called point 4, as
 1108 shown in Figure 2.4 top, tuned at a frequency of 400 MHz. The bottom side of
 1109 Figure 2.4 shows a picture of a RF module composed of 4 RF cavities working in a
 1110 superconducting state at 4.5 K; also, a representation of the accelerating electric field

that accelerates the protons in the bunch is shown. The maximum of the oscillating electric field (red region) picks the proton bunches at the entrance of the cavity and keeps accelerating them through the whole cavity. The protons are carefully timed so that in addition to the acceleration effect the bunch structure of the beam is preserved.

While protons are accelerated in one section of the LHC ring, where the RF cavities are located, in the rest of their path they have to be kept in the curved trajectory defined by the LHC ring. Technically, LHC is not a perfect circle; RF, injection, beam dumping, beam cleaning and sections before and after the experimental points where protons collide are all straight sections. In total, there are 8 arcs 2.45 km long each and 8 straight sections 545 m long each. In order to curve the proton's trajectory in the arc sections, superconducting dipole magnets are used.

Inside the LHC ring, there are two proton beams traveling in opposite directions in two separated beam pipes; the beam pipes are kept at ultra-high vacuum ($\sim 10^{-9}$ Pa) to ensure that there are no particles that interact with the proton beams. The superconducting dipole magnets used in LHC are made of a NbTi alloy, capable of transporting currents of about 12000 A when cooled at a temperature below 2K using liquid helium (see Figure 2.5).

Protons in the arc sections of LHC feel a centripetal force exerted by the dipole magnets; the magnitude of magnetic field needed to keep the protons in the LHC curved trayectomy can be found assuming that protons travel at $v \approx c$, using the standard values for proton mass and charge and the LHC radius, as

$$F_m = \frac{mv^2}{r} = qBv \rightarrow B = 8.33T \quad (2.1)$$

which is about 100000 times the Earth's magnetic field. A representation of the

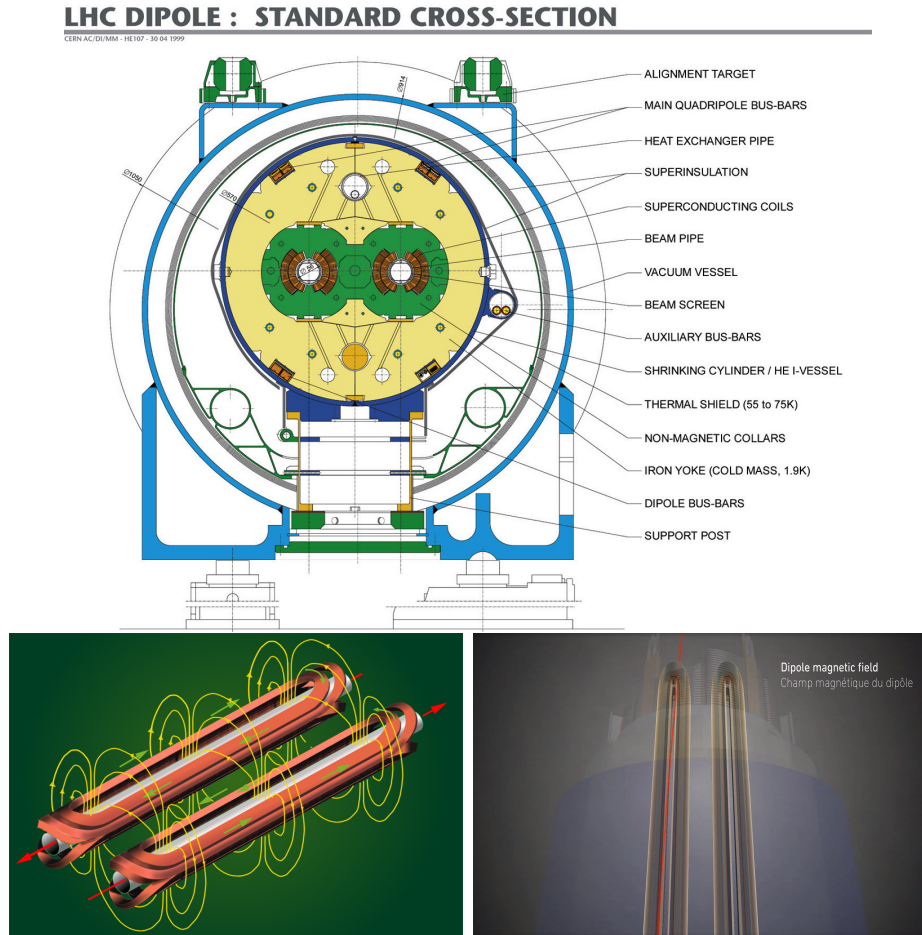


Figure 2.5: Top: LHC dipole magnet transverse view; cooling, shielding and mechanical support are indicated. Bottom left: Magnetic field generated by the dipole magnets; note that the direction of the field inside one beam pipe is opposite with respect to the other beam pipe which guarantee that both proton beams are curved in the same direction towards the center of the ring. The effect of the dipole magnetic field on the proton beam is represented on the bottom right side [66, 69, 70].

1134 magnetic field generated by the dipole magnets is shown on the bottom left side of
 1135 Figure 2.5. The bending effect of the magnetic field on the proton beam is shown on
 1136 the bottom right side of Figure 2.5. Note that the dipole magnets are not curved;
 1137 the arc section of the LHC ring is composed of straight dipole magnets of about 15
 1138 m. In total there are 1232 dipole magnets along the LHC ring.
 1139 In addition to the bending of the beam trajectory, the beam has to be focused. The

focusing is performed by quadrupole magnets installed in a different straight section; in total 858 quadrupole magnets are installed along the LHC ring. Other effects like electromagnetic interaction among bunches, interaction with electron clouds from the beam pipe, the gravitational force on the protons, differences in energy among protons in the same bunch, among others, are corrected using sextupole and other magnetic multipoles.

The two proton beams inside the LHC ring are made of bunches with a cylindrical shape of about 7.5 cm long and about 1 mm in diameter; when bunches are close to the interaction point (IP), the beam is focused up to a diameter of about 16 μm in order to maximize the probability of collisions between protons. The number of collisions per second is proportional to the cross section of the bunches with the *luminosity* (L) as the proportionality factor, thus, the luminosity can be calculated using

$$L = fn \frac{N_1 N_2}{4\pi\sigma_x\sigma_y} \quad (2.2)$$

where f is the revolution frequency, n is the number of bunches per beam, N_1 and N_2 are the numbers of protons per bunch, σ_x and σ_y are the gaussian transverse sizes of the bunches. With the expected parameters, the LHC expected luminosity is about

$$f = \frac{v}{2\pi r_{LHC}} \approx \frac{3 \times 10^8 \text{ m/s}}{27 \text{ km}} \approx 11.1 \text{ kHz},$$

$$n = 2808$$

$$N_1 = N_2 \sim 1.5 \times 10^{11}$$

$$\sigma_x = \sigma_y = 16 \mu\text{m}$$

1155

$$L = 1.28 \times 10^{34} \text{ cm}^{-2} \text{ s}^{-1} = 1.28 \times 10^{-5} \text{ fb}^{-1} \text{ s}^{-1} \quad (2.3)$$

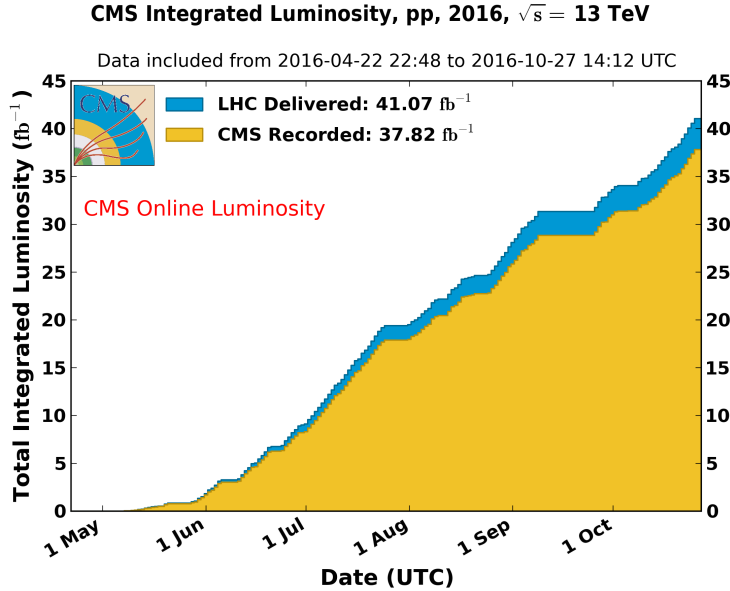


Figure 2.6: Integrated luminosity delivered by LHC and recorded by CMS during 2016. The difference between the delivered and the recorded luminosity is due to fails and issues occurred during the data taking in the CMS experiment [71].

1156 Luminosity is a fundamental aspect of LHC given that the bigger luminosity the
1157 bigger number of collisions, which means that for processes with a very small cross
1158 section the number of expected occurrences is increased and so the chances of being
1159 detected. The integrated luminosity, collected by the CMS experiment during 2016
1160 is shown in Figure 2.6; the data analyzed in this thesis corresponds to an integrated
1161 luminosity of 35.9 fb^{-1} at a center of mass-energy $\sqrt{s} = 13 \text{ TeV}$.

1162 One way to increase L is increasing the number of bunches in the beam. Cur-
1163 rently, the separation between two consecutive bunches in the beam is 7.5 m which
1164 corresponds to a time separation of 25 ns. In the full LHC ring the allowed number
1165 of bunches is $n = 27\text{km}/7.5\text{m} = 3600$; however, there are some gaps in the bunch pat-
1166 tern intended for preparing the dumping and injection of the beam, thus, the proton
1167 beams are composed of 2808 bunches.

1168 Once the proton beams reach the desired energy, they are brought to cross each

other producing pp collisions. The bunch crossing happens in precise places where the four LHC experiments are located, as seen in the top of Figure 2.7. In 2008 pp collisions of $\sqrt{s} = 7$ TeV were performed; the energy was increased to 8 TeV in 2012 and to 13 TeV in 2015.

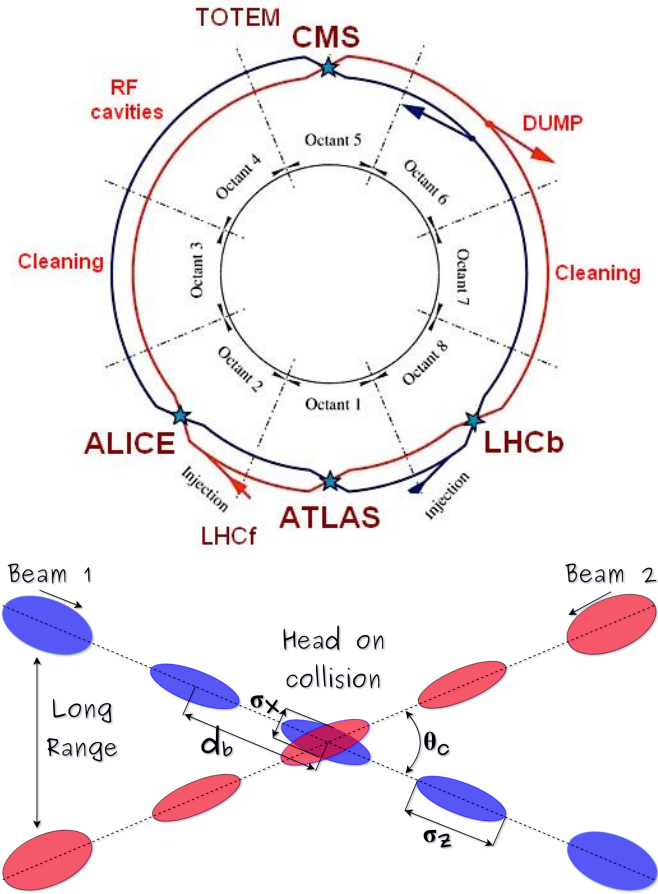


Figure 2.7: Top: LHC interaction points. Bunch crossing occurs where the LHC experiments are located [72]. Sections indicated as cleaning are dedicated to collimate the beam in order to protect the LHC ring from collisions with protons in very spreaded bunches. Bottom: bunch crossing scheme. Since the bunch crossing is not perfectly head-on, the luminosity is reduced in a factor of 17%; adapted from Reference [86].

The CMS and ATLAS experiments are multi-purpose experiments, hence, they are enabled to explore physics in any of the LHC collision modes. LHCb experiment is optimized to explore bottom quark physics, while ALICE is optimized for heavy

1176 ion collisions searches; TOTEM and LHCf are dedicated to forward physics studies;
 1177 MoEDAL (not indicated in the Figure) is intended for monopole or massive pseudo
 1178 stable particles searches.

1179 At the IP there are two interesting details that need to be addressed. The first
 1180 one is that the bunch crossing does not occur head-on but at a small crossing angle θ_c
 1181 (280 μ rad in CMS and ATLAS) as shown in the bottom side of Figure 2.7, affecting
 1182 the overlapping between bunches; the consequence is a reduction of about 17% in
 1183 the luminosity (represented by a factor not included in eqn. 2.2). The second one
 1184 is the occurrence of multiple pp collisions in the same bunch crossing; this effect is
 1185 called *pileup* (PU). A fairly simple estimation of the PU follows from estimating the
 1186 probability of collision between two protons, one from each of the bunches in the
 1187 course of collision; it depends roughly on the ratio of proton size and the cross section
 1188 of the bunch in the IP, i.e.,

$$P(pp\text{-}collision) \sim \frac{d_{proton}^2}{\sigma_x \sigma_y} = \frac{(1\text{fm})^2}{(16\mu\text{m})^2} \sim 4 \times 10^{-21} \quad (2.4)$$

1189 however, there are $N = 1.15 \times 10^{11}$ protons in a bunch, thus the estimated number of
 1190 collisions in a bunch crossing is

$$PU = N^2 * P(pp\text{-}collision) \sim 50pp \text{ collision per bunch crossing}, \quad (2.5)$$

1191 about 20 of which are inelastic. A multiple pp collision event in a bunch crossing at
 1192 CMS is shown in Figure 2.8.

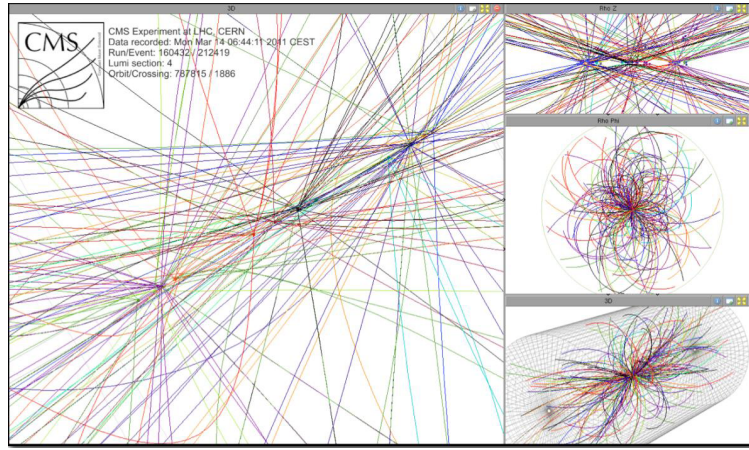


Figure 2.8: Multiple pp collision bunch crossing at CMS. [73].

1193 2.3 The CMS experiment

1194 CMS is a general-purpose detector designed to conduct research in a wide range
 1195 of physics from the standard model to new physics like extra dimensions and dark
 1196 matter. Located at Point 5 in the LHC layout as shown in Figure 2.4, CMS is
 1197 composed of several detection systems distributed in a cylindrical structure; in total,
 1198 CMS weights about 12500 tons in a very compact 21.6 m long and 14.6 m diameter
 1199 cylinder. It was built in 15 separate sections at the ground level and lowered to the
 1200 cavern individually to be assembled. A complete and detailed description of the CMS
 1201 detector and its components is given in Reference [74] on which this section is based.
 1202 Figure 2.9 shows the layout of the CMS detector. The detection system is composed
 1203 of (from the innermost to the outermost)

- 1204 • Pixel detector.
- 1205 • Silicon strip tracker.
- 1206 • Preshower detector.
- 1207 • Electromagnetic calorimeter.

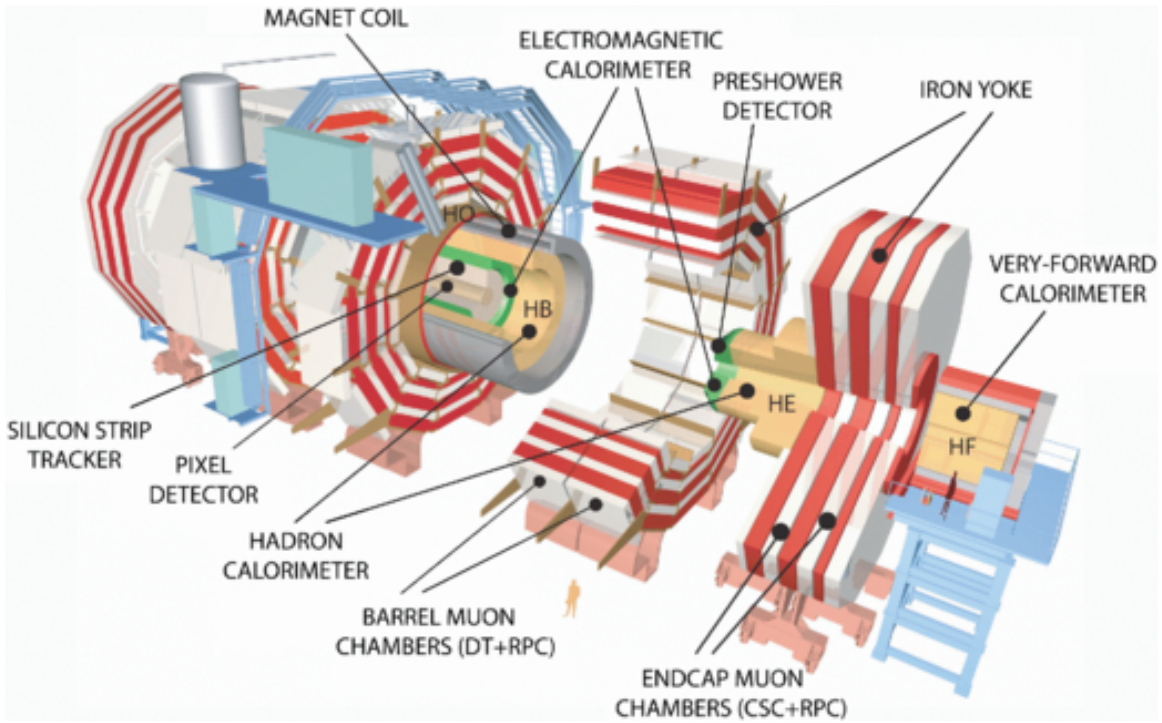


Figure 2.9: Layout of the CMS detector. The several subdetectors are indicated. The central region of the detector is referred as the barrel section while the endcaps are referred as the forward sections. [75].

1208 • Hadronic calorimeter.

1209 • Muon chambers (barrel and endcap)

1210 The central region of the detector is commonly referred as the barrel section while
 1211 the endcaps are referred as the forward sections of the detector; thus, each subdetector
 1212 is composed of a barrel section and a forward section.

1213 When a pp collision happens inside the CMS detector, many different particles are
 1214 produced, but only some of them live long enough to be detected; they are electrons,
 1215 photons, pions, kaons, protons, neutrons and muons; neutrinos are not detected by
 1216 the CMS detector. Thus, the CMS detector was designed to detect those particles and
 1217 measure their properties. Figure 2.10 shows a transverse slice of the CMS detector.
 1218 The silicon tracker (pixel detector + strip tracker) is capable to register the track of

1219 the charged particles traversing it, while calorimeters (electromagnetic and hadronic)
 1220 measure the energy of the particles that are absorbed by their materials. Considering
 1221 the detectable particles, mentioned above, emerging from the IP, a basic description
 1222 of the detection process is as follows.

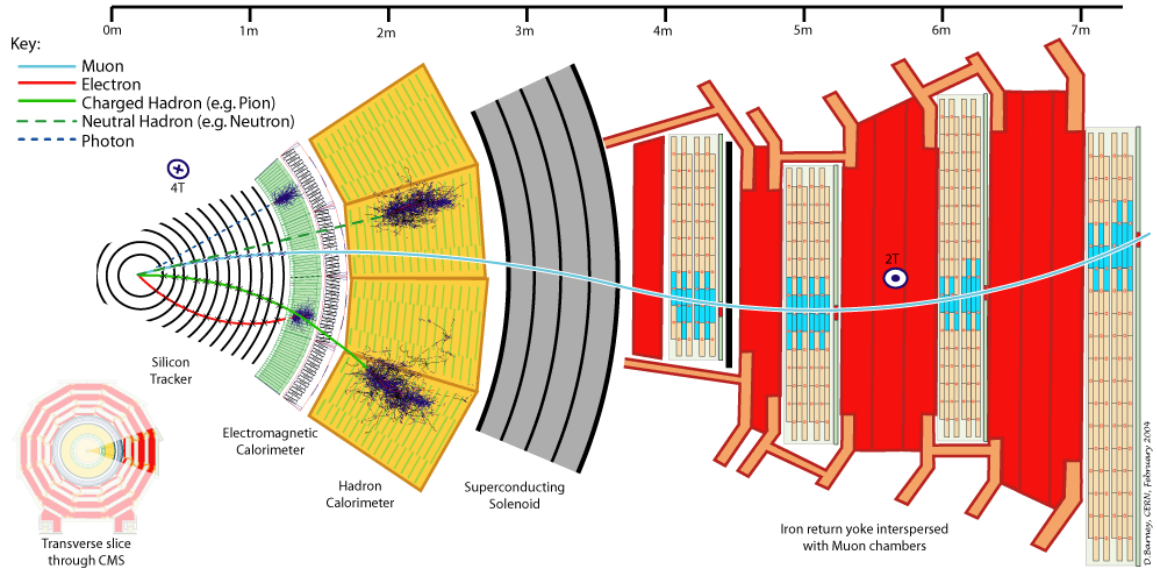


Figure 2.10: CMS detector transverse slice [76].

1223 A muon emerging from the IP, will create a track on the silicon tracker and on
 1224 the muon chambers. The design of the CMS detector is driven by the requirements
 1225 on the identification, momentum resolution and unambiguous charge determination
 1226 of the muons; therefore, a large bending power is provided by the solenoid magnet
 1227 made of superconducting cable capable of generating a 3.8 T magnetic field. The
 1228 muon track is bent twice since the magnetic field inside the solenoid is directed along
 1229 the z -direction but outside its direction is reversed. Muons interact very weakly with
 1230 the calorimeters, therefore, it is not absorbed but escape away from the detector.

1231 An electron emerging from the IP will create a track along the tracker which will
 1232 be bent due to the presence of the magnetic field, later, it will be absorbed in the
 1233 electromagnetic calorimeter where its energy is measured.

1234 A photon will not leave a track because it is neutral, but it will be absorbed in
 1235 the electromagnetic calorimeter.

1236 A neutral hadron, like the neutron, will not leave a track either but it will lose a
 1237 small amount of its energy during its passage through the electromagnetic calorimeter
 1238 and then it will be absorbed in the hadron calorimeter depositing the rest of its energy.

1239 A charged hadron, like the proton or π^\pm , will leave a curved track on the silicon
 1240 tracker, some of its energy in the electromagnetic calorimeter and finally will be
 1241 absorbed in the hadronic calorimeter.

1242 A more detailed description of each detection system will be presented in the
 1243 following sections.

1244 2.3.1 CMS coordinate system

1245 The coordinate system used by CMS is centered on the geometrical center of the
 1246 detector which is the nominal IP as shown in Figure 2.11¹. The z -axis is parallel
 1247 to the beam direction, while the Y -axis pointing vertically upward, and the X -axis
 1248 pointing radially inward toward the center of the LHC.

1249 In addition to the common cartesian and cylindrical coordinate systems, two co-
 1250 ordinates are of particular utility in particle physics: rapidity (y) and pseudorapidity
 1251 (η), defined in connection to the polar angle θ , energy and longitudinal momentum
 1252 component (momentum along the z -axis) according to

$$y = \frac{1}{2} \ln \frac{E + p_z}{E - p_z} \quad \eta = -\ln \left(\tan \frac{\theta}{2} \right) \quad (2.6)$$

1253 Rapidity is related to the angle between the XY -plane and the direction in which
 1254 the products of a collision are emitted; it has the nice property that the difference

¹ Not all the pp interaction occur at the nominal IP because of the bunch lenght, therefore, each pp collision has its own IP location

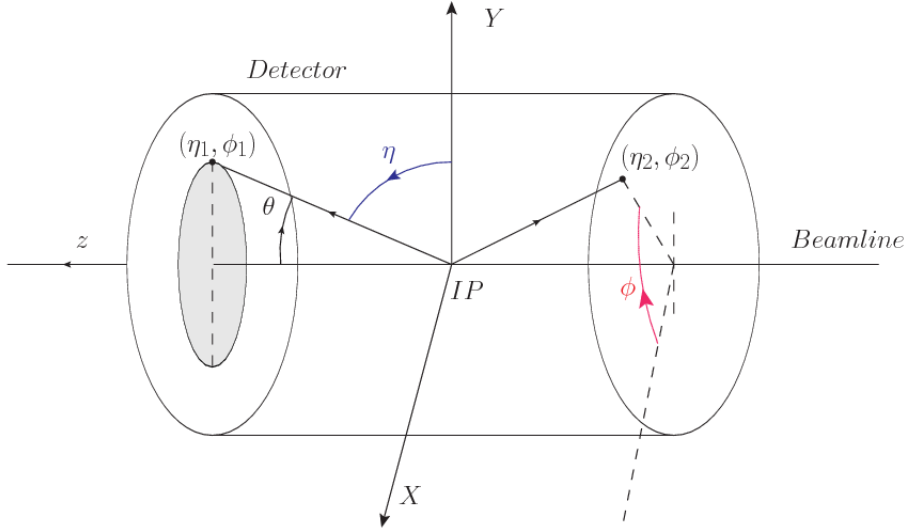


Figure 2.11: CMS detector coordinate system.

1255 between the rapidities of two particles is invariant with respect to Lorentz boosts
 1256 along the z -axis, hence, data analysis becomes more simple when based on rapid-
 1257 ity; however, it is not simple to measure the rapidity of highly relativistic particles,
 1258 as those produced after pp collisions. Under the highly relativistic motion approxi-
 1259 mation, y can be rewritten in terms of the polar angle, concluding that rapidity is
 1260 approximately equal to the pseudorapidity defined above, i.e., $y \approx \eta$. Note that η
 1261 is easier to measure than y given the direct relationship between the former and the
 1262 polar angle.

1263 The angular distance between two objects in the detector (ΔR) is commonly used
 1264 to judge the isolation of those object; it is defined in terms of their coordinates (η_1, ϕ_1) ,
 1265 (η_2, ϕ_2) as

$$\Delta R = \sqrt{(\Delta\eta)^2 - (\Delta\phi)^2} \quad (2.7)$$

1266 2.3.2 Tracking system

1267 The CMS tracking system is designed to provide a precise measurement of the trajectories (*track*) followed by the charged particles created after the pp collisions; also, the
 1268 precise reconstruction of the primary and secondary origins of the tracks (*vertices*) is
 1269 expected in an environment where, each 25 ns, the bunch crossing produces about 20
 1270 inelastic collisions and about 1000 particles.
 1271

1272 Physics requirements guiding the tracking system performance include the precise characterization of events involving gauge bosons, W and Z, and their leptonic
 1273 decays for which an efficient isolated lepton and photon reconstruction is of capital
 1274 importance, given that isolation is required to suppress background events to a level
 1275 that allows observations of interesting processes like Higgs boson decays or beyond
 1276 SM events.

1278 The ability to identify and reconstruct b -jets and B-hadrons within these jets is also
 1279 a fundamental requirement, achieved through the ability to reconstruct accurately
 1280 displaced vertices, given that b -jets are part of the signature of top quark physics, like
 1281 the one treated in this thesis.

1282 An schematic view of the CMS tracking system is shown in Figure 2.12

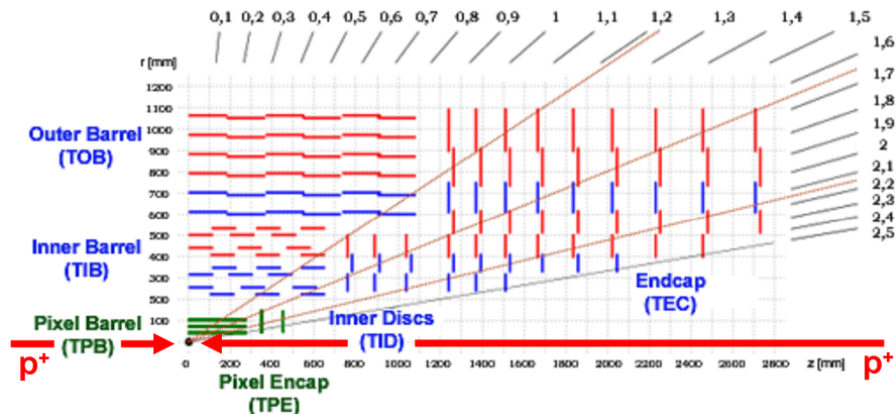


Figure 2.12: CMS tracking system schematic view [78].

1283 In order to satisfy these performance requirements, the tracking system uses two
 1284 different detector subsystems arranged in concentric cylindrical volumes, the pixel
 1285 detector and the silicon strip tracker; the pixel detector is located in the high particle
 1286 density region ($r < 20\text{cm}$) while the silicon strip tracker is located in the medium and
 1287 lower particle density regions $20\text{cm} < r < 116\text{cm}$.

1288 **Pixel detector**

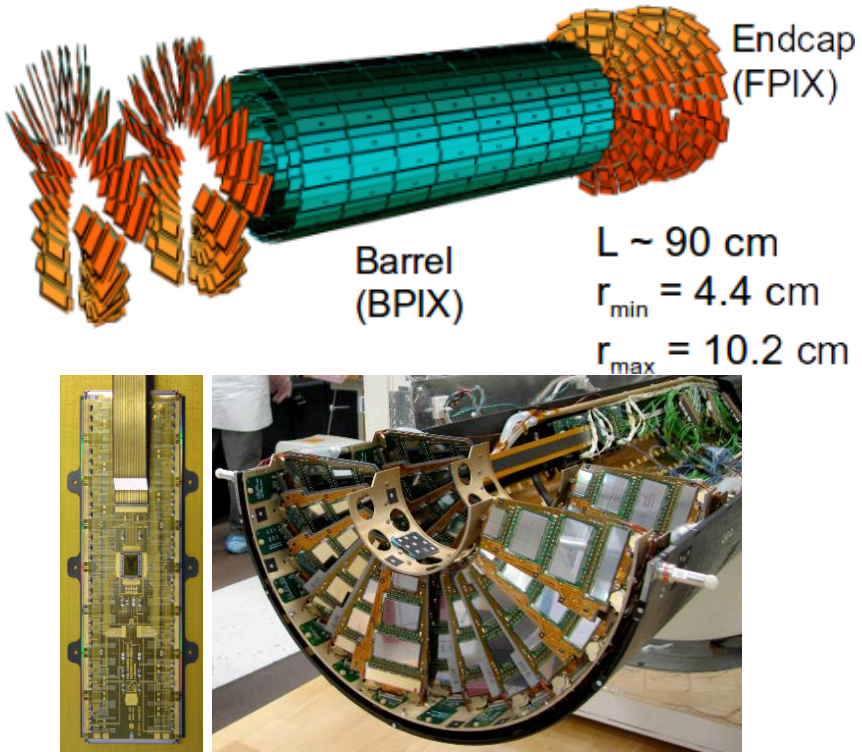


Figure 2.13: CMS pixel detector. Top: schematic view; Bottom: pictures of a barrel(BPIX) module(left) and forward modules(right) [74].

1289 The pixel detector was replaced during the 2016-2017 extended year-end technical
 1290 stop, due to the increasingly challenging operating conditions like the higher particle
 1291 flux and more radiation harsh environment, among others. The new one is responding
 1292 as expected, reinforcing its crucial role in the successful way to fulfill the new LHC

1293 physics objectives after the discovery of the Higgs boson. Since the data sets used
 1294 in this thesis were produced using the previous version of the pixel detector, it will
 1295 be the subject of the description in this section. The last chapter of this thesis is
 1296 dedicated to describe my contribution to the *Forward Pixel Phase 1 upgrade*.

1297 The pixel detector was composed of 1440 silicon pixel detector modules organized
 1298 in three-barrel layers in the central region (BPix) and two disks in the forward region
 1299 (FPix) as shown in the top side of Figure 2.13; it was designed to record efficiently
 1300 and with high precision, up to $20\mu\text{m}$ in the XY -plane and $20\mu\text{m}$ in the z -direction,
 1301 the first three space-points (*hits*) nearest to the IP region in the range $|\eta| \leq 2.5$. The
 1302 first barrel layer was located at a radius of 44 mm from the beamline, while the third
 1303 layer was located at a radius of 102 mm, closer to the strip tracker inner barrel layer
 1304 (see Section 2.3.3) in order to reduce the rate of fake tracks. The high granularity of
 1305 the detector is represented in its about 66 Mpixels, each of size $100 \times 150\mu\text{m}^2$. The
 1306 transverse momentum resolution of tracks can be measured with a resolution of 1-2%
 1307 for muons of $p_T = 100$ GeV.

1308 A charged particle passing through the pixel sensors produce ionization in them,
 1309 giving energy for electrons to be removed from the silicon atoms, hence, creating
 1310 electron-hole pairs. The collection of charges in the pixels generates an electrical
 1311 signal that is read out by an electronic readout chip (ROC); each pixel has its own
 1312 electronics which amplifies the signal. Combining the signal from the pixels activated
 1313 by a traversing particle in the several layers of the detector allows one to reconstruct
 1314 the particle's trajectory in 3D.

1315 Commonly, the charge produced by traversing of a particle is collected by and
 1316 shared among several pixels; by interpolating between pixels, the spatial resolution
 1317 is improved. In the barrel section the charge sharing in the $r\phi$ -plane is due to the
 1318 Lorentz effect. In the forward pixels the charge sharing is enhanced by arranging the

1319 blades in the turbine-like layout as shown in Figure 2.13 bottom left.

1320 2.3.3 Silicon strip tracker

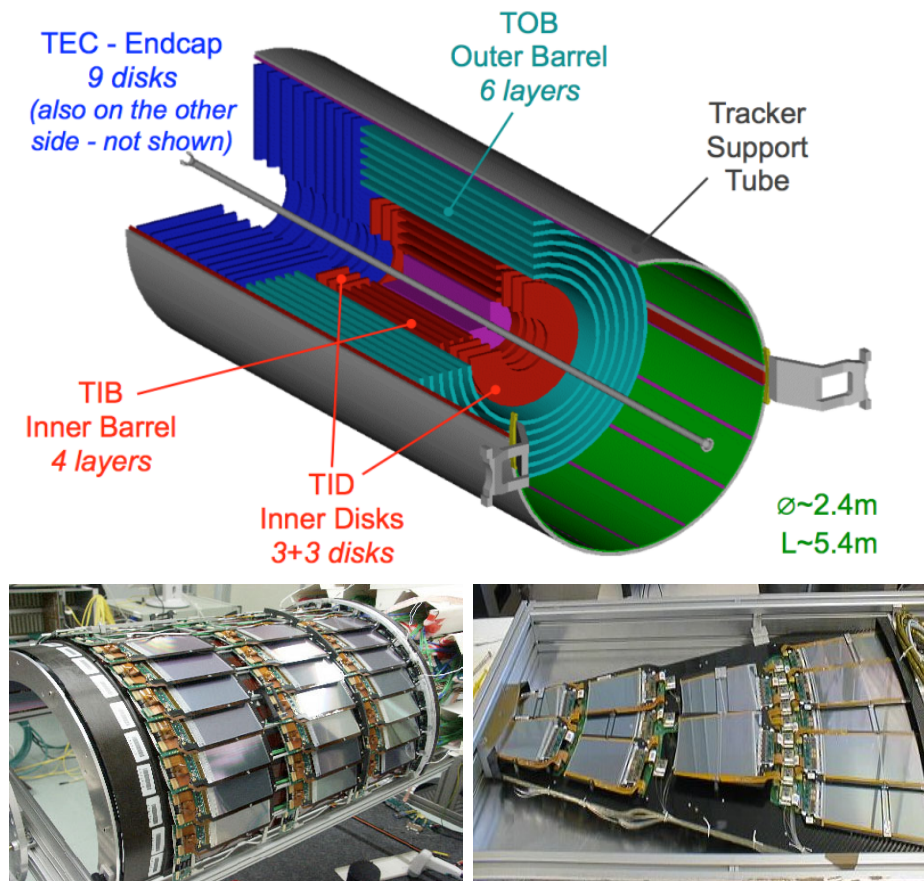


Figure 2.14: Top: CMS Silicon Strip Tracker (SST) schematic view. The SST is composed of the tracker inner barrel (TIB), the tracker inner disks (TID), the tracker outer barrel (TOB) and the tracker endcaps (TEC). Each part is made of silicon strip modules; the modules in blue represent two modules mounted back-to-back and rotated in the plane of the module by a stereo angle of 120 mrad in order to provide a 3-D reconstruction of the hit positions. Bottom: pictures of the TIB (left) and TEC (right) modules [80–82].

1321 The silicon strip tracker (SST) is the second stage in the CMS tracking system.

1322 The top side of Figure 2.14 shows a schematic of the SST. The inner tracker region is

1323 composed of the tracker inner barrel (TIB) and the tracker inner disks (TID) covering

1324 the region $r < 55$ cm and $|z| < 118$ cm. The TIB is composed of 4 layers while the TID

1325 is composed of 3 disks at each end. The silicon sensors in the inner tracker are 320
 1326 μm thick, providing a resolution of about 13-38 μm in the $r\phi$ position measurement.

1327 The modules indicated in blue in the schematic view of Figure 2.14 are two mod-
 1328 ules mounted back-to-back and rotated in the plane of the module by a *stereo* angle
 1329 of 100 mrad; the hits from these two modules, known as *stereo hits*, are combined to
 1330 provide a measurement of the second coordinate (z in the barrel and r on the disks)
 1331 allowing the reconstruction of hit positions in 3-D.

1332 The outer tracker region is composed of the tracker outer barrel (TOB) and the
 1333 tracker endcaps (TEC). The six layers of the TOB offer coverage in the region $r > 55$
 1334 cm and $|z| < 118$ cm, while the 9 disks of the TEC cover the region $124 < |z| < 282$
 1335 cm. The resolution offered by the outer tracker is about 13-38 μm in the $r\phi$ position
 1336 measurement. The inner four TEC disks use silicon sensors 320 μm thick; those in
 1337 the TOB and the outer three TEC disks use silicon sensors of 500 μm thickness. The
 1338 silicon strips run parallel to the z -axis and the distance between strips varies from 80
 1339 μm in the inner TIB layers to 183 μm in the inner TOB layers; in the endcaps the
 1340 wedge-shaped sensors with radial strips, whose pitch range between 81 μm at small
 1341 radii and 205 μm at large radii.

1342 The whole SST has 15148 silicon modules, 9.3 million silicon strips and cover a
 1343 total active area of about 198 m^2 .

1344 2.3.4 Electromagnetic calorimeter

1345 The CMS electromagnetic calorimeter (ECAL) is designed to measure the energy of
 1346 electrons and photons. It is composed of 75848 lead tungstate crystals which have a
 1347 short radiation length (0.89 cm) and fast response, since 80% of the light is emitted
 1348 within 25 ns; however, they are combined with Avalanche photodiodes (APDs) as

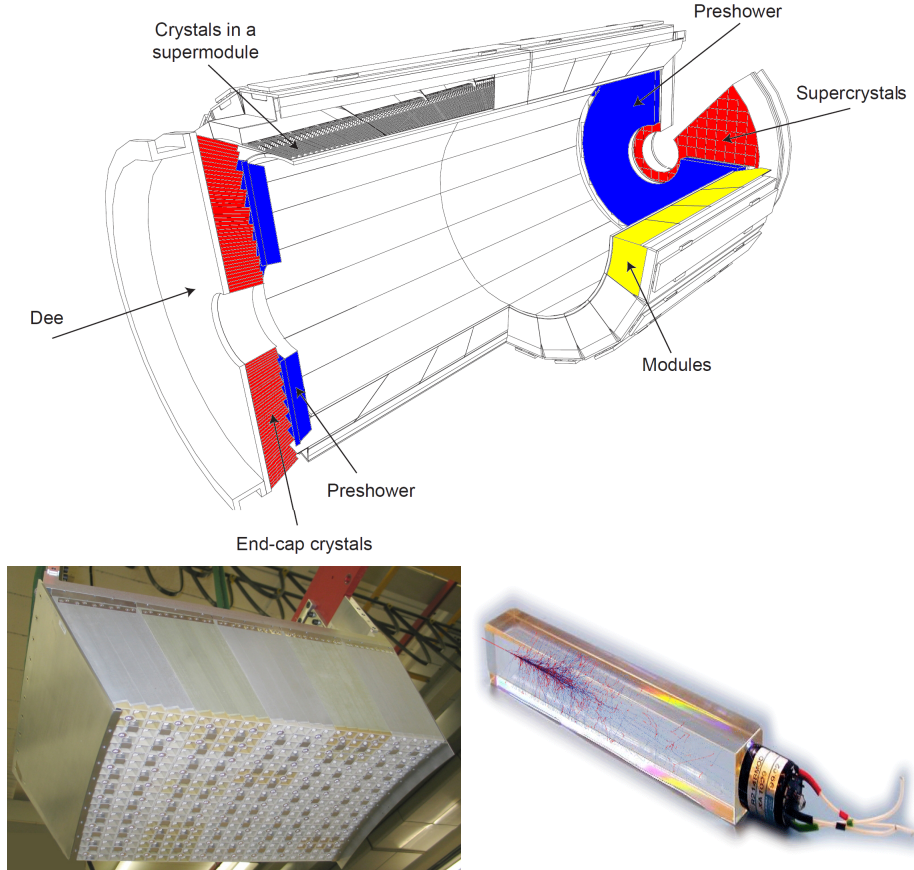


Figure 2.15: Top: CMS ECAL schematic view. Bottom: Module equipped with the crystals (left); ECAL crystal(right) with an artistic representation of an electromagnetic shower [74].

1349 photodetectors given that crystals themselves have a low light yield ($30\gamma/\text{MeV}$). A
 1350 schematic view of the ECAL is shown in Figure 2.15.

1351 Energy is measured when electrons and photons are absorbed by the crystals
 1352 which generates an electromagnetic *shower*, as seen in bottom right picture of the
 1353 Figure 2.15; the shower is seen as a *cluster* of energy which depending on the amount
 1354 of energy deposited can involve several crystals. The ECAL barrel (EB) covers the
 1355 region $|\eta| < 1.479$, using crystals of depth of 23 cm and $2.2 \times 2.2 \text{ cm}^2$ transverse
 1356 section; the ECAL endcap (EE) covers the region $1.479 < |\eta| < 3.0$ using crystals of
 1357 depth 22 cm and transverse section of $2.86 \times 2.86 \text{ cm}^2$; the photodetectors used are

1358 vacuum phototriodes (VPTs). Each EE is divided in two structures called *Dees*.

1359 The preshower detector (ES) is installed in front of the EE and covers the region
 1360 $1.653 < |\eta| < 2.6$. The ES provides a precise measurement of the position of electro-
 1361 magnetic showers, which allows to distinguish electrons and photon signals from π^0
 1362 decay signals. The ES is composed of a layer of lead radiators followed by a layer of
 1363 silicon strip sensors. The lead radiators initiate electromagnetic showers when reached
 1364 by photons and electrons, then, the strip sensors measure the deposited energy and
 1365 the transverse shower profiles. The full ES thickness is 20 cm.

1366 2.3.5 Hadronic calorimeter

1367 Hadrons are not absorbed by the ECAL² but by the hadron calorimeter (HCAL),
 1368 which is made of a combination of alternating brass absorber layers and silicon photo-
 1369 multiplier(SiPM) layers; therefore, particles passing through the scintillator material
 1370 produce showers, as in the ECAL, as a result of the inelastic scattering of the hadrons
 1371 with the detector material. Since the particles are not absorbed in the scintillator,
 1372 their energy is sampled; therefore the total energy is not measured but estimated from
 1373 the energy clusters, which reduces the resolution of the detector. Brass was chosen
 1374 as the absorber material due to its short interaction length ($\lambda_I = 16.42\text{cm}$) and its
 1375 non-magnetivity. Figure 2.16 shows a schematic view of the CMS HCAL.

1376 The HCAL is divided into four sections; the Hadron Barrel (HB), the Hadron
 1377 Outer (HO), the Hadron Endcap (HE) and the Hadron Forward (HF) sections. The
 1378 HB covers the region $0 < |\eta| < 1.4$, while the HE covers the region $1.3 < |\eta| < 3.0$.
 1379 The HF, made of quartz fiber scintillator and steel as absorption material, covers the
 1380 forward region $3.0 < |\eta| < 5.2$. Both the HB and HF are located inside the solenoid.
 1381 The HO is placed outside the magnet as an additional layer of scintillators with the

² Most hadrons are not absorbed, but few low-energy ones might be.

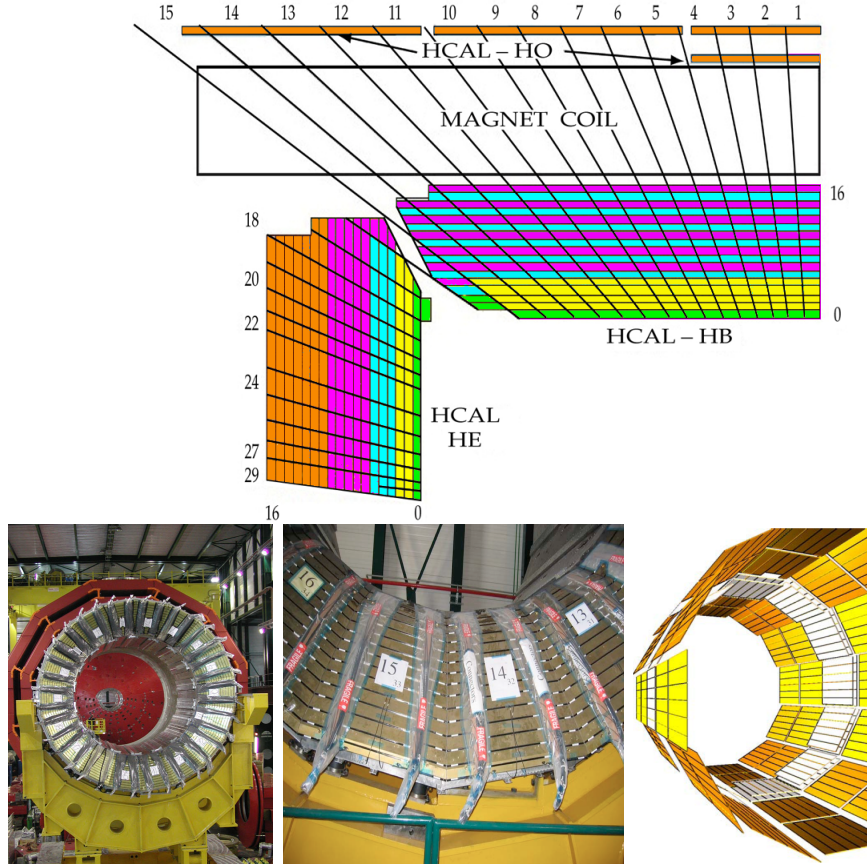


Figure 2.16: Top: CMS HCAL schematic view, the colors indicate the layers that are grouped into the same readout channels. Bottom: picture of a section of the HB; the absorber material is the golden region and scintillators are placed in between the absorber material (left and center). Schematic view of the HO (right). [83,84]

1382 purpose of measure the energy tails of particles passing through the HB and the
 1383 magnet (see Figure 2.16 top and bottom right).

1384 **2.3.6 Superconducting solenoid magnet**

1385 The superconducting magnet installed in the CMS detector is designed to provide
 1386 an intense and highly uniform magnetic field in the central part of the detector.
 1387 In fact, the tracking system takes advantage of the bending power of the magnetic
 1388 field to measure with precision the momentum of the particles that traverse it; the

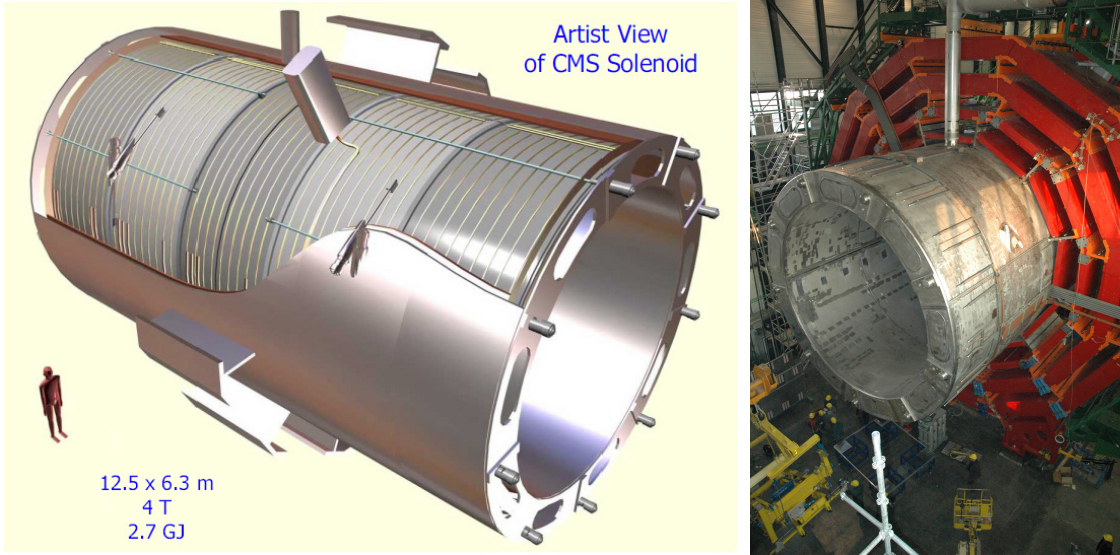


Figure 2.17: Artistic representation of the CMS solenoid magnet(left). The magnet is supported on an iron yoke (right) which also serves as the house of the muon detector and as mechanical support for the whole CMS detector [77].

1389 unambiguous determination of the sign for high momentum muons was a driving
 1390 principle during the design of the magnet. The magnet has a diameter of 6.3 m, a
 1391 length of 12.5 m and a cold mass of 220 t; the generated magnetic field reaches a
 1392 strength of 3.8T. Since it is made of Ni-Tb superconducting cable it has to operate at
 1393 a temperature of 4.7 K by using a helium cryogenic system; the current circulating in
 1394 the cables reaches 18800 A under normal running conditions. The left side of Figure
 1395 2.17 shows an artistic view of the CMS magnet, while the right side shows a transverse
 1396 view of the cold mass where the winding structure is visible.

1397 The yoke (see Figure 2.17), composed of 5 barrel wheels and 6 endcap disks made
 1398 of iron, serves not only as the media for magnetic flux return but also provides housing
 1399 for the muon detector system and structural stability to the full detector.

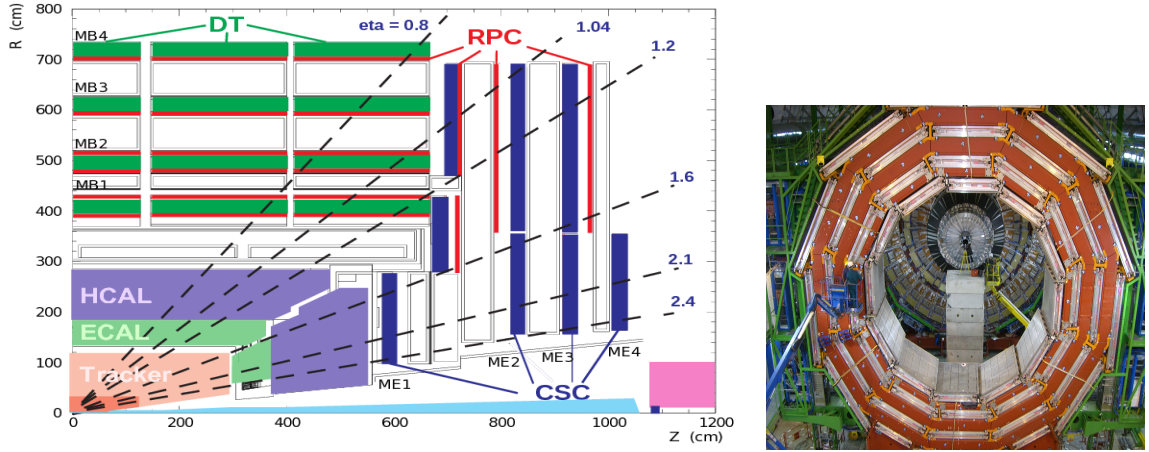


Figure 2.18: Left: CMS muon system schematic view; Right: one of the yoke rings with the muon DTs and RPCs installed; in the back it is possible to see the muon endcap [85].

2.3.7 Muon system

Muons are the only charged particles able to pass through all the CMS detector due to their low ionization energy loss; thus, muons can be separated easily from the high amount of particles produced in a pp collision. Also, muons are expected to be produced in the decay of several new particles; therefore, good detection of muons was one of the leading principles when designing the CMS detector.

The CMS muon detection system (muon spectrometer) is embedded in the return yoke as seen in Figure 2.18. It is composed of three different detector types, the drift tube chambers (DT), cathode strip chambers (CSC), and resistive plate chambers (RPC); DT are located in the central region $\eta < 1.2$ arranged in four layers of drift chambers filled with an Ar/CO₂ gas mixture.

The muon endcaps are made of CSCs covering the region $\eta < 2.4$ and filled with a mixture of Ar/CO₂/CF₄. The reason behind using a different detector type lies on the different conditions in the forward region like the higher muon rate and higher residual magnetic field compared to the central region.

The third type of detector used in the muon system is a set of four disks of RPCs

1416 working in avalanche mode. The RPCs provide good spatial and time resolutions. The
 1417 track of high- p_T muon candidates is built combining information from the tracking
 1418 system and the signal from up to six RPCs and four DT chambers.

1419 The muon tracks are reconstructed from the hits in the several layers of the muon
 1420 system.

1421 **2.3.8 CMS trigger system**

1422 CMS expects pp collisions every 25 ns, i.e., an interaction rate of 40 MHz for which
 1423 it is not possible to store the recorded data in full. In order to handle this high event
 1424 rate data, an online event selection, known as triggering, is performed; triggering
 1425 reduces the event rate to 100 Hz for storage and further offline analysis.

1426 The trigger system starts with a reduction of the event rate to 100 kHz in the
 1427 so-called *the level 1 trigger* (L1). L1 is based on dedicated programmable hardware
 1428 like Field Programmable Gate Arrays (FPGAs) and Application Specific Integrated
 1429 Circuits (ASICs), partly located in the detector itself; another portion is located in
 1430 the CMS underground cavern. Hit pattern information from the muon chambers
 1431 and the energy deposits in the calorimeter are used to decide if an event is accepted
 1432 or rejected, according to selection requirements previously defined, which reflect the
 1433 interesting physics processes. Figure 2.19 shows the L1 trigger architecture.

1434 The second stage in the trigger system is called *the high-level trigger* (HLT); events
 1435 accepted by L1 are passed to HLT in order to make an initial reconstruction of them.
 1436 HLT is software based and runs on a dedicated server farm, using selection algorithms
 1437 and high-level object definitions; the event rate at HLT is reduced to 100 Hz. The
 1438 first HLT stage takes information from the muon detectors and the calorimeters to
 1439 make the initial object reconstruction; in the next HLT stage, information from the

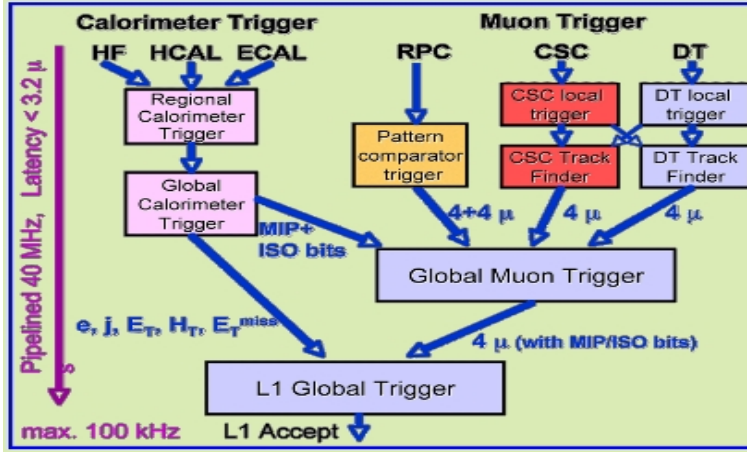


Figure 2.19: CMS Level-1 trigger architecture [86].

pixel and strip detectors is used to do first fast tracking and then full tracking online.

This initial object reconstruction is used in further steps of the trigger system.

Events and preliminary reconstructed physics objects from HLT are sent to be fully reconstructed at the CERN computing center known also as Tier-0 facility. Again, the pixel detector information provides high-quality seeds for the track reconstruction algorithm offline, primary vertex reconstruction, electron and photon identification, muon reconstruction, τ identification, and b-tagging. After full reconstruction, data sets are made available for offline analyses.

2.3.9 CMS computing

Data coming from the experiment have to be stored and made available for further analysis; in order to cope with all the tasks implied in the offline data processing, like transfer, simulation, reconstruction and reprocessing, among others, a large computing power is required. The CMS computing system is based on the distributed architecture concept, where users of the system and physical computer centers are distributed worldwide and interconnected by high-speed networks.

The worldwide LHC computing grid (WLCG) is the mechanism used to provide

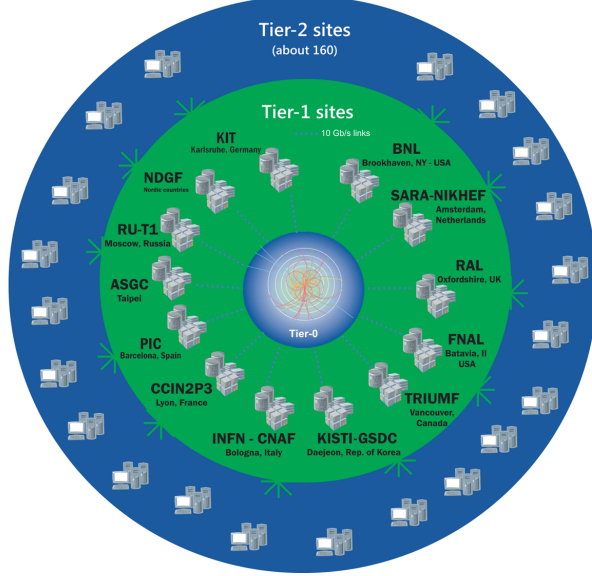


Figure 2.20: WLCG structure. The primary computer centers (Tier-0) are located at CERN (data center) and at the Wigner datacenter in Budapest. Tier-1 is composed of 13 centers and Tier-2 is composed of about 160 centers. [87].

1456 that distributed environment. WLCG is a tiered structure connecting computing
 1457 centers around the world, which provides the necessary storage and computing facil-
 1458 ities. The primary computing centers of the WLCG are located at the CERN and
 1459 the Wigner datacenter in Budapest and are known as Tier-0 as shown in Figure 2.20.
 1460 The main responsibilities for each tier level are [87]

- 1461 • **Tier-0:** initial reconstruction of recorded events and storage of the resulting
 1462 datasets, the distribution of raw data to the Tier-1 centers.
- 1463 • **Tier-1:** provide storage capacity, support for the Grid, safe-keeping of a pro-
 1464 portional share of raw and reconstructed data, large-scale reprocessing and safe-
 1465 keeping of corresponding output, generation of simulated events, distribution
 1466 of data to Tier 2s, safe-keeping of a share of simulated data produced at these
 1467 Tier 2s.
- 1468 • **Tier-2:** store sufficient data and provide adequate computing power for spe-

1469 cific analysis tasks and proportional share of simulated event production and
1470 reconstruction.

1471 Aside from the general computing strategy to manage the huge amount of data
1472 produced by experiments, CMS uses a software framework to perform a variety of
1473 processing, selection and analysis tasks. The central concept of the CMS data model
1474 referred to as *event data model* (EDM) is the *Event*; therefore, an event is the unit
1475 that contains the information from a single bunch crossing, any data derived from
1476 that information like the reconstructed objects, and the details of the derivation.

1477 Events are passed as the input to the *physics modules* that obtain information
1478 from them and create new information; for instance, *event data producers* add new
1479 data into the events, *analyzers* produce an information summary from an event set,
1480 *filters* perform selection and triggering.

1481 CMS uses several event formats with different levels of detail and precision

1482 • **Raw format:** events in this format contain the full recorded information from
1483 the detector as well as trigger decision and other metadata. An extended version
1484 of raw data is used to store information from the CMS Monte Carlo simulation
1485 tools (see Chapter 3). Raw data are stored permanently, occupying about
1486 2MB/event

1487 • **RECO format:** events in this format correspond to raw data that have been
1488 submitted to reconstruction algorithms like primary and secondary vertex re-
1489 construction, particle ID, and track finding. RECO events contain physics ob-
1490 jects and all the information used to reconstruct them; average size is about 0.5
1491 MB/event.

- 1492 • **AOD format:** Analysis Object Data (AOD) is the data format used in the
 1493 physics analyses given that it contains the parameters describing the high-level
 1494 physics objects in addition to enough information to allow a kinematic refitting if
 1495 needed. AOD events are filtered versions of the RECO events to which skimming
 1496 or other filtering have been applied, hence AOD events are subsets of RECO
 1497 events. Requires about 100 kB/event.
- 1498 • **Non-event data** are data needed to interpret and reconstruct events. Some
 1499 of the non-event data used by CMS contains information about the detector
 1500 contraction and condition data like calibrations, alignment, and detector status.

1501 Figure 2.21 shows the data flow scheme between CMS detector and tiers.

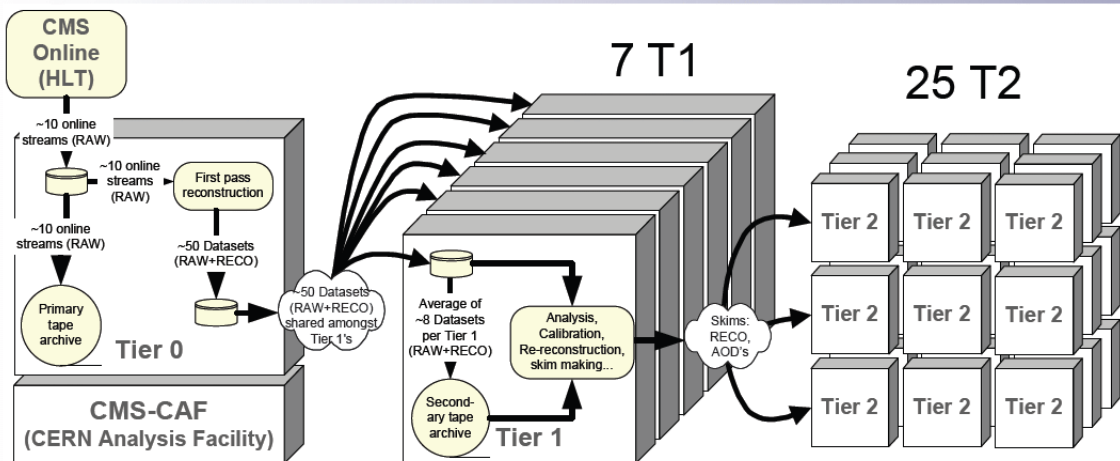


Figure 2.21: Data flow from CMS detector through tiers.

1502 The whole collection of software built as a framework is referred to as *CMSSW*. This
 1503 framework provides the services needed by the simulation, calibration and alignment,
 1504 and reconstruction modules that process event data, so that physicists can perform
 1505 analysis. The CMSSW event processing model is composed of one executable, called
 1506 `cmsRun`, and several plug-in modules which contains all the tools (calibration, recon-

1507 struction algorithms) needed to process an event. The same executable is used for
1508 both detector data and Monte Carlo simulations [88].

1509 **Chapter 3**

1510 **Event generation, simulation and
1511 reconstruction**

1512 The process of analyzing data recorded by the CMS experiment involves several stages
1513 where the data are processed in order to interpret the information provided by all
1514 the detection systems; in those stages, the particles produced after the pp collision
1515 are identified by reconstructing their trajectories and measuring their features. In
1516 addition, the SM provides a set of predictions that have to be compared with the
1517 experimental results; however, in most of the cases, theoretical predictions are not
1518 directly comparable to experimental results due to the diverse source of uncertainties
1519 introduced by the experimental setup and theoretical approximations, among others.

1520 The strategy to face these conditions consists in using statistical methods imple-
1521 mented in computational algorithms to produce numerical results that can be con-
1522 trasted with the experimental results. These computational algorithms are commonly
1523 known as Monte Carlo (MC) methods and, in the case of particle physics, they are
1524 designed to apply the SM rules and produce predictions about the physical observ-
1525 ables measured in the experiments. Since particle physics is governed by quantum

mechanics principles, predictions are not allowed from single events; therefore, a high number of events are *generated* and predictions are produced in the form of statistical distributions for the observables. Effects of the detector presence are included in the predictions by introducing simulations of the detector itself.

This chapter presents a description of the event generation strategy and the tools used to perform the detector simulation and physics objects reconstruction. A comprehensive review of event generators for LHC physics can be found in Reference [89] on which this chapter is based.

3.1 Event generation

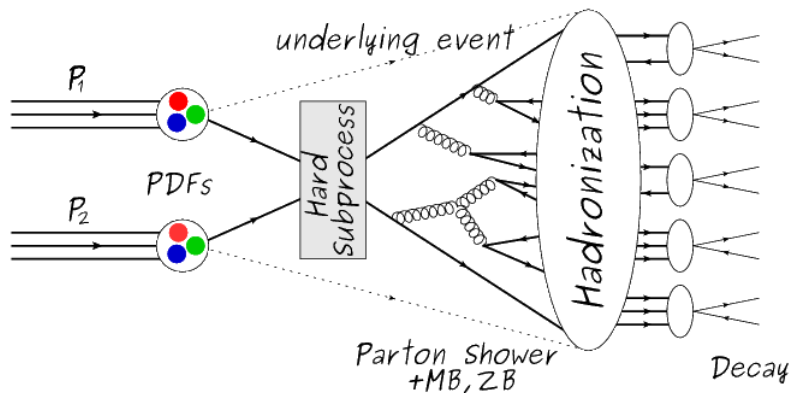


Figure 3.1: Event generation process. The actual interaction is generated in the hard subprocess. The parton shower describes the evolution of the partons from the hard subprocess. Modified from Reference [90].

The event generation is intended to create events that mimic the behavior of actual events produced in collisions; they obey a sequence of steps from the particles collision hard process to the decay process into the final state. Figure 3.1 shows a schematic view of the event generation process; the fact that the full process can be treated as several independent steps is motivated by the QCD factorization theorem.

1540 Generation starts by taking into account the PDFs of the incoming particles.
 1541 Event generators offer the option to chose from several PDF sets depending on the
 1542 particular process under simulation¹; in the following, pp collisions will be consid-
 1543 ered. The *hard subprocess* describes the actual interaction between partons from the
 1544 incoming protons; it is represented by the matrix element connecting the initial and
 1545 final states of the interaction. Normally, the matrix element can be written as a
 1546 sum over Feynman diagrams and consider interferences between terms in the sum-
 1547 mation. During the generation of the hard subprocess, the production cross section
 1548 is calculated.

1549 The order to which the cross section is calculated depends on the order of the Feyn-
 1550 man diagrams involved in the calculation; therefore, radiative corrections are included
 1551 by considering a higher order Feynman diagrams where QCD radiation dominates.
 1552 Currently, cross sections calculated to LO do not offer a satisfactory description of the
 1553 processes, i.e., the results are only reliable for the shape of distributions; therefore,
 1554 NLO calculations have to be performed with the implication that the computing time
 1555 needed is highly increased.

1556 The final parton content of the hard subprocess is subjected to the *parton shower*
 1557 which generates the gluon radiation. Parton shower evolves the partons, i.e., glouns
 1558 split into quark-antiquark pairs and quarks with enough energy radiate gluons giv-
 1559 ing rise to further parton multiplication, following the DGLAP (Dokshitzer-Gribov-
 1560 Lipatov-Altarelli-Parisi) equations. Showering continues until the energy scale is low
 1561 enough to reach the non-perturbative limit.

1562 In the simulation of LHC processes that involve b quarks, like the single top quark
 1563 or Higgs associated production, it is needed to consider that the b quark is heavier
 1564 than the proton; hence, the QCD interaction description is made in two different

¹ Tool in Reference [91] allows to plot different PDF sets under customizable conditions.

1565 schemes [95]

- 1566 • four-flavor (4F) scheme. b quarks appear only in the final state because they
 1567 are heavier than the proton and therefore they can be produced only from the
 1568 splitting of a gluon into pairs or singly in association with a t quark in high
 1569 energy-scale interactions; furthermore, during the simulation, the b -PDFs are set
 1570 to zero. Calculations in this scheme are more complicated due to the presence
 1571 of the second b quark but the full kinematics is considered already at LO and
 1572 therefore the accuracy of the description is better.
- 1573 • five-flavor (5F) scheme. b quarks are considered massless, therefore they can
 1574 appear in both initial and final states since they can now be part of the proton;
 1575 thus, during the simulation b -PDFs are not set to zero. In this scheme, calcu-
 1576 lations are simpler than in the 4F scheme and possible logarithmic divergences
 1577 are absorbed by the PDFs through the DGLAP evolution.

1578 In this thesis, the tHq events are generated using the 4F scheme in order to reduce
 1579 uncertainties, while the tHW events are generated using the 5F scheme to eliminate
 1580 LO interference with $t\bar{t}H$ process [48].

1581 Partons involved in the pp collision are the focus of the simulation, however, the
 1582 rest of the partons inside the incoming protons are also affected because the remnants
 1583 are colored objects; also, multiple parton interactions can occur. The hadronization
 1584 of the remnants and multiple parton interactions are known as *underlying event* and
 1585 it has to be included in the simulation. In addition, multiple pp collisions in the same
 1586 bunch crossing (pile-up mentioned in 2.2) occurs, actually in two forms

- 1587 • *in-time PU* which refers to multiple pp collision in the bunch crossing but that
 1588 are not considered as primary vertices.

1589 • *Out-of-time PU* which refers to overlapping pp collisions from consecutive bunch
 1590 crossings; this can occur due to the time-delays in the detection systems where
 1591 information from one bunch crossing is assigned to the next or previous one.

1592 While the underlying event effects are included in generation using generator-
 1593 specific tools, PU effects are added to the generation by overlaying Minimum-bias (MB)
 1594 and Zero-bias (ZB) events to the generated events. MB events are inelastic events
 1595 selected by using a loose trigger with as little bias as possible, therefore accepting a
 1596 large fraction of the overall inelastic event; ZB events correspond to random events
 1597 recorded by the detector when collisions are likely. MB models in-time PU and ZB
 1598 models out-of-time PU.

1599 The next step in the generation process is called *hadronization*. Since particles
 1600 with a net color charge are not allowed to exits isolated, they have to recombine
 1601 to form bound states. This is precisely the process by which the partons resulting
 1602 from the parton shower arrange themselves as color singlets to form hadrons. At
 1603 this step, the energy-scale is low and the strong coupling constant is large, therefore
 1604 hadronization process is non-perturbative and the evolution of the partons is described
 1605 using phenomenological models. Most of the baryons and mesons produced in the
 1606 hadronization are unstable and hence they will decay in the detector.

1607 The last step in the generation process corresponds to the decay of the unstable
 1608 particles generated during hadronization; it is also simulated in the hadronization
 1609 step, based on the known branching ratios.

1610 **3.2 Monte Carlo Event Generators.**

1611 The event generation described in the previous section has been implemented in
 1612 several software packages for which a brief description is given.

- 1613 • **PYTHIA 8.** It is a program designed to perform the generation of high energy
 1614 physics events which describes the collisions between particles such as electrons
 1615 and protons. Several theories and models are implemented in it, in order to
 1616 describe physical aspects like hard and soft interaction, parton distributions,
 1617 initial and final-state parton showers, multiple parton interactions, beam rem-
 1618 nants, hadronization² and particle decay. Thanks to extensive testing, several
 1619 optimized parametrizations, known as *tunings*, have been defined in order to
 1620 improve the description of actual collisions to a high degree of precision; for
 1621 analysis at $\sqrt{s} = 13$ TeV, the underline event CUETP8M1 tune is employed [97].
 1622 The calculation of the matrix element is performed at LO which is not enough
 1623 for the current required level of precision; therefore, pythia is often used for
 1624 parton shower, hadronization and decays, while other event generators are used
 1625 to generate the matrix element at NLO.
- 1626 • **MadGraph5_aMC@NLO.** MadGraph is a matrix element generator which
 1627 calculates the amplitudes for all contributing Feynman diagrams of a given
 1628 process but does not provide a parton shower while MC@NLO incorporates
 1629 NLO QCD matrix elements consistently into a parton shower framework; thus,
 1630 MadGraph5_aMC@NLO, as a merger of the two event generators MadGraph5
 1631 and aMC@NLO, is an event generator capable to calculate tree-level and NLO
 1632 cross sections and perform the matching of those with the parton shower. It is
 1633 one of the most frequently used matrix element generators; however, it has the
 1634 particular feature of the presence of negative event weights which reduce the
 1635 number of events used to reproduce the properties of the objects generated [98].
- 1636 • **POWHEG.** It is an NLO matrix element generator where the hardest emis-

² based in the Lund string model [96]

1637 sion of color charged particles is generated in such a way that the negative event
 1638 weights issue of MadGraph5_aMC@NLO is overcome; however, the method re-
 1639 quires an interface with p_T -ordered parton shower or a parton shower generator
 1640 where this highest emission can be vetoed in order to avoid double counting of
 1641 this highest-energetic emission. PYTHIA is a commonly matched to POWHEG
 1642 event generator [100].

1643 Events resulting from the whole generation process are known as MC events.

1644 **3.3 CMS detector simulation.**

1645 After generation, MC events contain the physics of the collisions but they are not
 1646 ready to be compared to the events recorded by the experiment since these recorded
 1647 events correspond to the response of the detection systems to the interaction with
 1648 the particles traversing them. The simulation of the CMS detector has to be applied
 1649 on top of the event generation; it is simulated with a MC toolkit for the simulation
 1650 of particles passing through matter called Geant4 which is also able to simulate the
 1651 electronic signals that would be measured by all detectors inside CMS.

1652 The simulation takes the generated particles contained in the MC events as input,
 1653 makes them pass through the simulated geometry, and models physics processes that
 1654 particles experience during their passage through matter. The full set of results from
 1655 particle-matter interactions corresponds to the simulated hit which contains informa-
 1656 tion about the energy loss, momentum and position. Particles of the input event are
 1657 called *primary*, while the particles originating from GEANT4-modeled interactions of
 1658 a primary particle with matter are called a *secondary*. Simulated hits are the input
 1659 of subsequent modules that emulate the response of the detector readout system and

1660 triggers. The output from the emulated detection systems and triggers is known as
 1661 digitization [101, 102].

1662 The modeling of the CMS detector corresponds to the accurate modeling of the
 1663 interaction among particles, the detector material, and the magnetic field. This
 1664 simulation procedure includes the following standard steps

1665 • Modeling of the Interaction Region.

1666 • Modeling of the particle passage through the hierarchy of volumes that compose
 1667 CMS detector and of the accompanying physics processes.

1668 • Modeling of the effect of multiple interactions per beam crossing and/or the
 1669 effect of events overlay (Pile-Up simulation).

1670 • Modeling of the detector's electronics response, signal shape, noise, calibration
 1671 constants (digitization).

1672 In addition to the full simulation, i.e., a detailed detector simulation, a faster
 1673 simulation (FastSim) have been developed, that may be used where much larger
 1674 statistics are required. In FastSim, detector material effects are parametrized and
 1675 included in the hits; those hits are used as input of the same higher-level algorithms³
 1676 used to analyze the recorded events. In this way, comparisons between fast and full
 1677 simulations can be performed [104].

1678 After the full detector simulation, the output events can be directly compared
 1679 to events actually recorded in the CMS detector. The collection of MC events that
 1680 reproduces the expected physics for a given process is known as MC sample.

³ track fitting, calorimeter clustering, b tagging, electron identification, jet reconstruction and calibration, trigger algorithms which will be considered in the next sections

1681 **3.4 Event reconstruction.**

1682 The CMS experiment use the *particle-flow event reconstruction algorithm (PF)* to do
1683 the reconstruction of particles produced in pp collisions. Next sections will present
1684 a basic description of the *Elements* used by PF (tracker tracks, energy clusters, and
1685 muon tracks), based in the References [105, 106] where more detailed descriptions can
1686 be found.

1687 **3.4.1 Particle-Flow Algorithm.**

1688 Each of the several sub detection systems of the CMS detector is dedicated to identify
1689 an specific type of particles, i.e., photons and electrons are absorbed by the ECAL
1690 and their reconstruction is based on ECAL information; hadrons are reconstructed
1691 from clusters in the HCAL while muons are reconstructed from hits in the muon
1692 chambers. PF is designed to correlate signals from all the detector layers (tracks and
1693 energy clusters) in order to reconstruct and identify each final state particle and its
1694 properties as sketched in Figure 3.2.

1695 For instance, a charged hadron is identified by a geometrical connection, known
1696 as *link*, between one or more calorimeter clusters and a track in the tracker, provided
1697 there are no hits in the muon system; combining several measurements allows a better
1698 determination of the energy and charge sign of the charged hadron.

1699 **Charged-particle track reconstruction.**

1700 The strategy used by PF in order to reconstruct tracks is called *Iterative Tracking*
1701 which occurs in four steps

- 1702 • Seed generation where initial track candidates are found by looking for a combi-
1703 nation of hits in the pixel detector, strip tracker, and muon chambers. In total

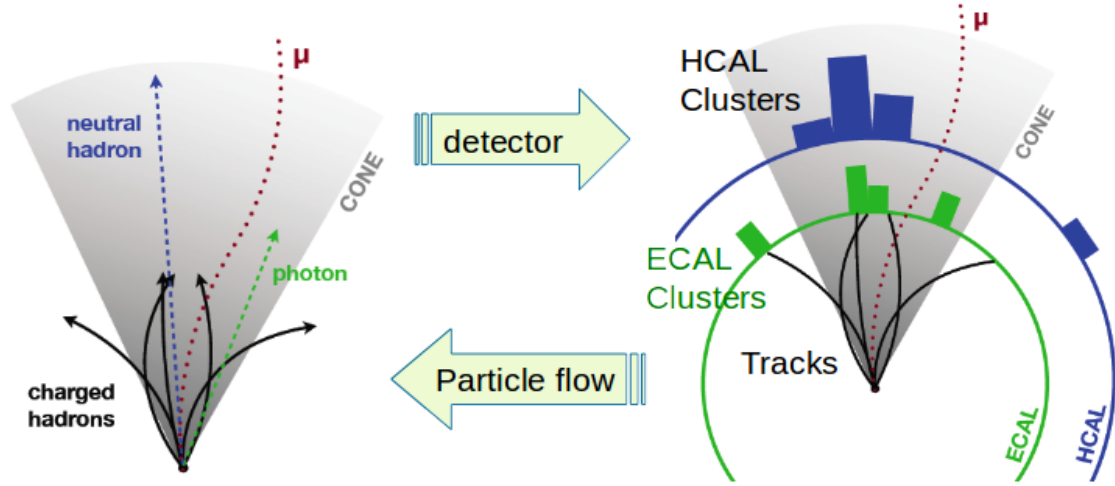


Figure 3.2: Particle flow algorithm. Information from the several CMS detection systems is provided as input to the algorithm which then combines it to identify and reconstruct all the particles in the final state and their properties. Reconstruction of simulated events is also performed by providing information from MC samples, detector and trigger simulation [107].

1704 ten iterations are performed, each one with a different seeding requirement.
 1705 Seeds are used to estimate the trajectory parameters and uncertainties at the
 1706 time of the full track reconstruction. Seeds are also considered track candidates.

- 1707 • Track finding using a tracking software known as Combinatorial Track Finder
 1708 (CTF) [108]. The seed trajectories are extrapolated along the expected flight
 1709 path of a charged particle, in agreement to the trajectory parameters obtained
 1710 in the first step, in an attempt to find additional hits that can be assigned to
 1711 the track candidates.
- 1712 • Track-fitting where the found tracks are passed as input to a module which
 1713 provides the best estimate of the parameters of each trajectory.
- 1714 • Track selection where track candidates are submitted to a selection which dis-
 1715 cards those that fail a set of defined quality criteria.

1716 Iterations differ in the seeding configuration and the final track selection as elab-

1717 orated in References [105, 106]. In the first iteration, high p_T tracks and tracks pro-
 1718 duced near to the interaction region are identified and those hits are masked thereby
 1719 reducing the combinatorial complexity. Next, iterations search for more complicated
 1720 tracks, like low p_T tracks and tracks from b hadron decays, which tend to be displaced
 1721 from the interaction region.

1722 **Vertex reconstruction.**

1723 During the track reconstruction, an extrapolation toward to the calorimeters is per-
 1724 formed in order to match energy deposits; that extrapolation is performed also toward
 1725 the beamline in order to find the origin of the track known as *vertex*. The vertex re-
 1726 construction is performed by selecting from the available reconstructed tracks, those
 1727 that are consistent with being originated in the interaction region where pp collisions
 1728 are produced. The selection involves a requirement on the number of tracker (pixel
 1729 and strip) hits and the goodness of the track fit.

1730 Selected tracks are clustered using a *deterministic annealing algorithm* (DA)⁴. A
 1731 set of candidate vertices and their associated tracks, resulting from the DA, are then
 1732 fitted with an *adaptive vertex fitter* (AVF) to produce the best estimate of the vertices
 1733 locations.

1734 The p_T of the tracks associated to a reconstructed vertex is added, squared and
 1735 used to organize the vertices; the vertex with the highest squared sum is designated
 1736 as the *primary vertex* (*PV*) while the rest are designated as PU vertices.

1737 **Calorimeter clustering.**

1738 After traversing the CMS tracker system, electrons, photons and hadrons deposit their
 1739 energy in the ECAL and HCAL cells. The PF clustering algorithm aims to provide

⁴ DA algorithm and AVF are described in detail in References [110, 111]

1740 a high detection efficiency even for low-energy particles and an efficient distinction
 1741 between close energy deposits. The clustering runs independently in the ECAL barrel
 1742 and endcaps, HCAL barrel and endcaps, and the two preshower layers, following two
 1743 steps

- 1744 • cells with an energy larger than a given seed threshold and larger than the energy
 1745 of the neighboring cells are identified as cluster seeds. The neighbor cells are
 1746 those that either share a side with the cluster seed candidate, or the eight closest
 1747 cells including cells that only share a corner with the seed candidate.
- 1748 • cells with at least a corner in common with a cell already in the cluster seed
 1749 and with an energy above a cell threshold are grouped into topological clusters.

1750 Clusters formed in this way are known as *particle-flow clusters*. With this cluster-
 1751 ing strategy, it is possible to detect and measure the energy and direction of photons
 1752 and neutral hadrons as well as differentiate these neutral particles from the charged
 1753 hadron energy deposits. In cases involving charged hadrons for which the track pa-
 1754 rameters are not determined accurately, for instance, low-quality and high- p_T tracks,
 1755 clustering helps in the energy measurements.

1756 Electron track reconstruction.

1757 Although the charged-particle track reconstruction described above works for elec-
 1758 trons, they lose a significant fraction of their energy via bremsstrahlung photon radi-
 1759 ation before reaching the ECAL; thus, the reconstruction performance depends on the
 1760 ability to measure also the radiated energy. The reconstruction strategy, in this case,
 1761 requires information from the tracking system and from the ECAL. Bremsstrahlung
 1762 photons are emitted at similar η values to that of the electron but at different values
 1763 of ϕ ; therefore, the radiated energy can be recovered by grouping ECAL clusters in a

1764 η window over a range of ϕ around the electron direction. The group is called ECAL
 1765 supercluster.

1766 Electron candidates from the track-seeding and ECAL super clustering are merged
 1767 into a single collection which is submitted to a full electron tracking fit with a
 1768 Gaussian-sum filter (GSF) [109]. The electron track and its associated ECAL su-
 1769 percluster form a *particle-flow electron*.

1770 Muon track reconstruction.

1771 Given that the CMS detector is equipped with a muon spectrometer capable to iden-
 1772 tify and measure the momentum of the muons traversing it, the muon reconstruction
 1773 is not specific to PF; therefore, three different muon types are defined

- 1774 ● *Standalone muon.* A clustering on the DTs or CSCs hits is performed to form
 1775 track segments; those segments are used as seeds for the reconstruction in the
 1776 muon spectrometer. All DTs, CSCs, and RPCs hits along the muon trajectory
 1777 are combined and fitted to form the full track. The fitting output is called a
 1778 *standalone-muon track*.
- 1779 ● *Tracker muon.* Each track in the inner tracker with p_T larger than 0.5 GeV and
 1780 a total momentum p larger than 2.5 GeV is extrapolated to the muon system.
 1781 A *tracker muon track* corresponds to a extrapolated track that matches at least
 1782 one muon segment.
- 1783 ● *Global muon.* When tracks in the inner tracker (inner tracks) and standalone-
 1784 muon tracks are matched and turn out being compatibles, their hits are com-
 1785 bined and fitted to form a *global-muon track*.

1786 Global muons sharing the same inner track with tracker muons are merged into
 1787 a single candidate. PF muon identification uses the muon energy deposits in ECAL,
 1788 HCAL, and HO associated with the muon track to improve the muon identification.

1789 **Particle identification and reconstruction.**

1790 PF elements are connected by a linker algorithm that tests the connection between any
 1791 pair of elements; if they are found to be linked, a geometrical distance that quantifies
 1792 the quality of the link is assigned. Two elements may be linked indirectly through
 1793 common elements. Linked elements form *PF blocks* and each PF block may contain
 1794 elements originating in one or more particles. Links can be established between
 1795 tracks, between calorimeter clusters, and between tracks and calorimeter clusters.
 1796 The identification and reconstruction start with a PF block and proceed as follows

- 1797 • Muons. An *isolated global muon* is identified by evaluating the presence of
 inner track and energy deposits close to the global muon track in the (η, ϕ)
 plane, i.e., in a particular point of the global muon track, inner tracks and
 energy deposits are sought within a radius of $\Delta R = 0.3$ (see eqn. 2.7) from the
 muon track; if they exist and the p_T of the found track added to the E_T of the
 found energy deposit does not exceed 10% of the muon p_T then the global muon
 is an isolated global muon. This isolation condition is stringent enough to reject
 hadrons misidentified as muons.

1805 *Non-isolated global muons* are identified using additional selection requirements
 1806 on the number of track segments in the muon system and energy deposits along
 1807 the muon track. Muons inside jets are identified with more stringent criteria
 1808 in isolation and momentum as described in Reference [112]. The PF elements
 1809 associated with an identified muon are masked from the PF block.

- 1810 ● Electrons are identified and reconstructed as described above plus some addi-
 1811 tional requirements on fourteen variables like the amount of energy radiated,
 1812 the distance between the extrapolated track position at the ECAL and the po-
 1813 sition of the associated ECAL supercluster, among others, which are combined
 1814 in an specialized multivariate analysis strategy that improves the electron iden-
 1815 tification. Tracks and clusters used to identify and reconstruct electrons are
 1816 masked in the PF block.

- 1817 ● Isolated photons are identified from ECAL superclusters with E_T larger than 10
 1818 GeV, for which the energy deposited at a distance of 0.15, from the supercluster
 1819 position on the (η, ϕ) plane, does not exceed 10% of the supercluster energy;
 1820 note that this is an isolation requirement. In addition, there must not be links
 1821 to tracks. Clusters involved in the identification and reconstruction are masked
 1822 in the PF block.

- 1823 ● Bremsstrahlung photons and prompt photons tend to convert to electron-positron
 1824 pairs inside the tracker, therefore, a dedicated finder algorithm is used to link
 1825 tracks that seem to originate from a photon conversion; in case those two tracks
 1826 are compatible with the direction of a bremsstrahlung photon, they are also
 1827 linked to the original electron track. Photon conversion tracks are also masked
 1828 in the PF block.

- 1829 ● The remaining elements in the PF block are used to identify hadrons. In the
 1830 region $|\eta| \leq 2.5$, neutral hadrons are identified with HCAL clusters not linked
 1831 to any track while photons from neutral pion decays are identified with ECAL
 1832 clusters without links to tracks. In the region $|\eta| > 2.5$ ECAL clusters linked to
 1833 HCAL clusters are identified with a charged or neutral hadron shower; ECAL
 1834 clusters with no links are identified with photons. HCAL clusters not used yet,

1835 are linked to one or more unlinked tracks and to an unlinked ECAL in order to
 1836 reconstruct charged-hadrons or a combination of photons and neutral hadrons
 1837 according to certain conditions on the calibrated calorimetric energy.

- 1838 • Charged-particle tracks may be liked together when they converge to a *sec-*
 1839 *ondary vertex (SV)* displaced from the IP where the PV and PU vertices are
 1840 reconstructed; at least three tracks are needed in that case, of which at most
 1841 one has to be an incoming track with hits in tracker region between a PV and
 1842 the SV.

1843 The linker algorithm, as well as the whole PF algorithm, has been validated and
 1844 commissioned; results from that validation are presented in the Reference [105].

1845 **Jet reconstruction.**

1846 Quarks and gluons may be produced in the pp collisions, therefore, their hadronization
 1847 will be seen in the detector as a shower of hadrons and their decay products in the
 1848 form of a *jet*. Two classes of clustering algorithms have been developed based in
 1849 their jet definition [113]:

- 1850 • Iterative cone algorithms (IC). Jets are defined in terms of circles of fixed radius
 1851 R in the $\eta\text{-}\phi$ plane, known as *stable cones*, for which the sum of the momenta
 1852 of all the particles within the cone points in the same direction as the center
 1853 of the circle. The seed of the iteration is the hardest non-isolated particle in
 1854 the event, then, the resulting momentum direction is assigned as the new cone
 1855 direction and a new iteration starts; iteration process stops when the cone if
 1856 found to be stable.

1857 • Sequential recombination algorithms. The distance between non-isolated par-
 1858 ticles is calculated; if that distance is below a threshold, these particles are
 1859 recombined into a new object. The sequence is repeated until the separation
 1860 between the recombined object and any other particle is above certain thresh-
 1861 old; the recombined object is called a jet and the algorithm starts again with
 1862 the remaining particles.

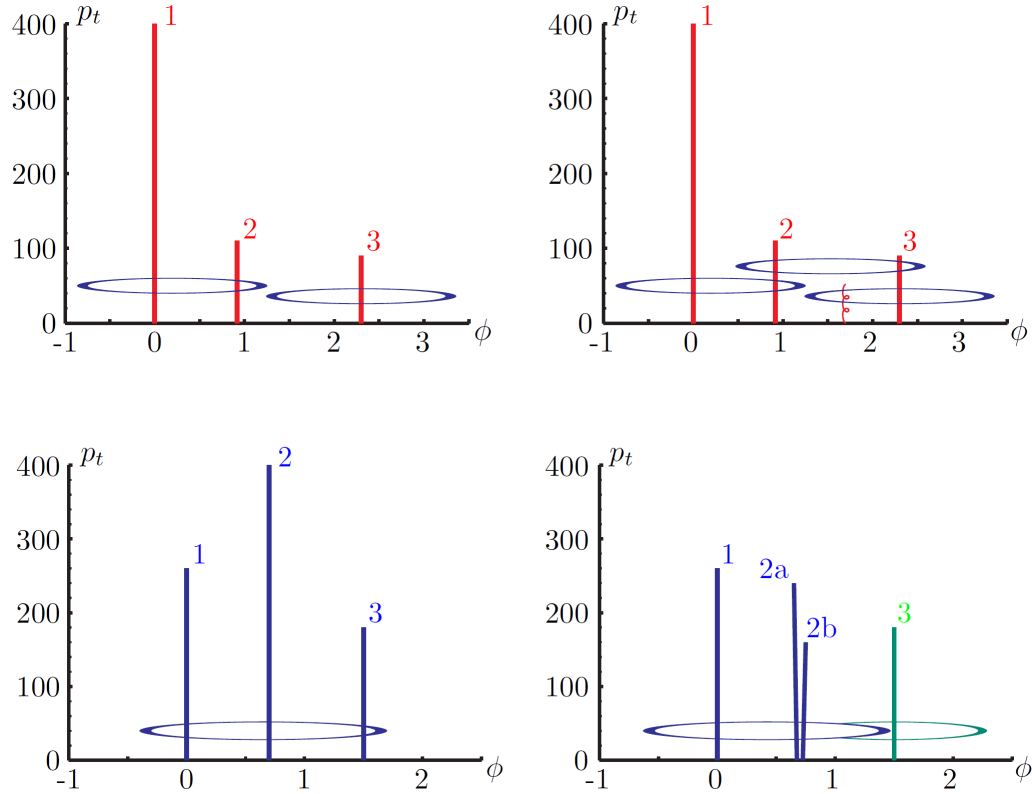


Figure 3.3: Stable cones identification using IC algorithms [113].

1863 Two conditions are of particular importance for the clustering algorithms, *infrared*
 1864 and *collinear (IRC) safety*. In order to explain the concept of infrared (IR) safety,
 1865 consider an event with three hard particles as shown in the top left side of Figure 3.3,
 1866 two stable cones are found and then two jets are identified; if a soft gluon is added, as
 1867 shown in the top right side of Figure 3.3, three stable cones are found and the three

1868 hard particles are now clustered into a single jet. If the addition of soft particles
 1869 change the outcome of the clustering, then it is said that the algorithm is IR unsafe.
 1870 Soft radiation is highly likely in perturbative QCD, which dominates the physics of
 1871 the jets, and then IR unsafe effect leads to divergences [113].

1872 The concept of collinear safety can also be explained considering a three hard
 1873 particles event, as shown in the bottom left side of Figure 3.3, where one stable cone
 1874 containing all three particles is found and one jet is identified; if the hardest particle
 1875 is split into two collinear particles (2a and 2b) in the bottom right side of Figure 3.3,
 1876 then the clustering results in a different jet identification and the algorithm is said
 1877 to be collinear unsafe. The collinear unsafe effect leads to divergences in jet cross
 1878 section calculations [114].

1879 It has been determined that IC algorithms are IRC unsafe, and therefore, they
 1880 have to be replaced by algorithms that not only provide the finite perturbative results
 1881 from theoretical computations, but also that are not highly dependent on underlying
 1882 event and pileup effects which leads to significant corrections [113].

1883 The sequential recombination algorithms arise as the IRC safe alternative used by
 1884 the CMS experiment; in particular the anti- k_t algorithm which is a generalization of
 1885 the previously existing k_t [115] and Cambridge/Aachen [116] jet clustering algorithms.

1886 The anti- k_t algorithm is used to perform the jet reconstruction by clustering those
 1887 PF particles within a cone (see Figure 3.4); previously, isolated electrons, isolated
 1888 muons, and charged particles associated with other interaction vertices are excluded
 1889 from the clustering.

1890 The anti- k_t algorithm proceeds in a sequential recombination of PF particles; the
 1891 distance between particles i and j (d_{ij}) and the distance between particles and the
 1892 beam are defined as

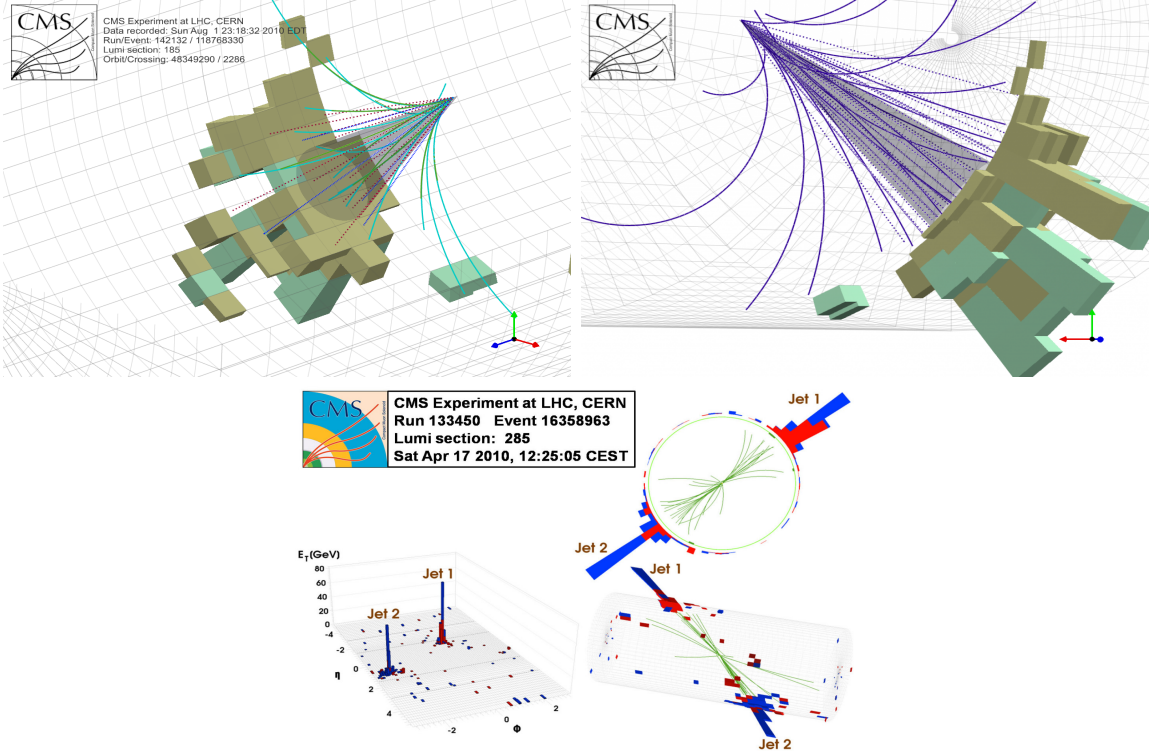


Figure 3.4: Jet reconstruction performed by the anti- k_t algorithm. Top: Two different views of a CMS recorded event are presented. Continuous lines correspond to tracks left by charged particles in the tracker while dotted lines are the imaginary paths followed by neutral particles. The green cubes represent the ECAL cells while the blue ones represent the HCAL cells; in both cases, the height of the cube represent the amount of energy deposited in the cells [117]. Bottom: Reconstruction of a recorded event with two jets [118].

$$d_{ij} = \min\left(\frac{1}{k_{ti}^2}, \frac{1}{k_{tj}^2}\right) \frac{\Delta_{ij}^2}{R^2}$$

$$d_{iB} = \frac{1}{k_{ti}^2} \quad (3.1)$$

1893 where $\Delta_{ij}^2 = (y_i - y_j)^2 + (\phi_i - \phi_j)^2$, k_{ti} , y_i and ϕ_i are the transverse momentum, ra-
1894 pidity and azimuth of particle i respectively and R is the called jet radius. For all
1895 the remaining PF particles, after removing the isolated ones, d_{ij} and d_{iB} are calcu-

lated⁵ and the smallest is identified; if it is a d_{ij} , particles i and j are replaced with
 a new object whose momentum is the vectorial sum of the combined particles. If the
 smallest distance is a d_{iB} the clustering process ends, the object i (which at this stage
 should be a combination of several PF particles) is declared as a *Particle-flow-jet* (PF
 jet) and all the associated PF particles are removed from the detector. The clustering
 process is repeated until no PF particles remain. R is a free parameter that can be
 adjusted according to the specific analysis conditions; usually, two values are used,
 $R=0.4$ and $R=0.5$, giving the name to the so-called AK4-jet and AK5-jet respectively.

An advantage of the anti- k_t algorithm over other clustering algorithms is the regularity of the boundaries of the resulting jets. For all known IRC safe algorithms,
 soft radiation can introduce irregularities in the boundaries of the final jets; however,
 anti- k_t algorithm is soft-resilient, meaning that jets shape is not affected by soft radiation,
 which is a valuable property considering that knowing the typical shape of jets
 makes experimental calibration of jets more simple. In addition, that soft-resilience
 is expected to simplify certain theoretical calculations and reduce the momentum-
 resolution loss caused by underlying-event (UE) and pileup contamination [114].

The effect of the UE and pileup contamination over a jet identification, can be
 seen as if soft events are added to the jet; for instance, if a soft event representing UE
 or pileup is added to an event for which a set of jets J have been identified, and the
 clustering is rerun on that new extended event, the outcome will be different in two
 aspects: jets will contain some additional soft energy and the distribution of particles
 in jets may have change; that effect is called *back-reaction*. The back-reaction effect in
 the anti- k_t algorithm is suppressed not by the amount of momentum added to the jet
 but by the jet transverse momentum $p_{T,J}$, which means that this strong suppression
 leads to a smaller correction due to EU and pileup effect [114].

⁵ Notice that this is a combinatorial calculation.

1921 **Jet energy Corrections**

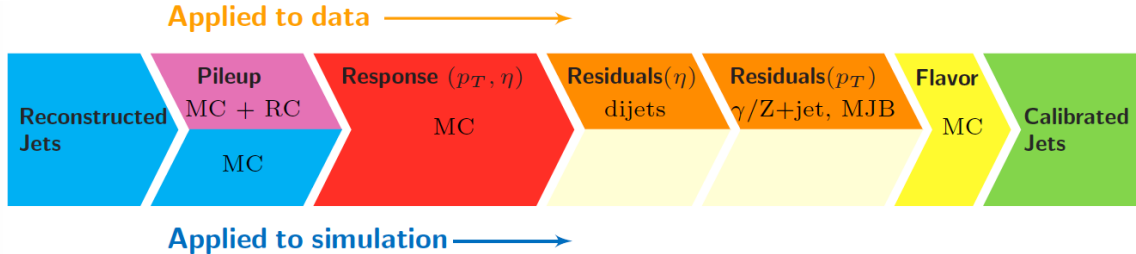


Figure 3.5: Jet energy correction diagram. Correction levels are applied sequentially in the indicated fixed order [120].

1922 Even though jets can be reconstructed efficiently, there are some effects that are
 1923 not included in the reconstruction and that lead to discrepancies between the re-
 1924 constructed results and the predicted results; in order to overcome these discrep-
 1925 ancies, a factorized model has been designed in the form of jet energy corrections
 1926 (JEC) [119, 120] applied sequentially as shown in the diagram of Figure 3.5.

1927 At each level, the jet four-momentum is multiplied by a scaling factor based on
 1928 jet properties, i.e., η , flavor, etc.

- 1929 • Level 1 correction removes the energy coming from pile-up. The scale factor is
 1930 determined using a MC sample of QCD dijet (2 jets) events with and without
 1931 pileup overlay; it is parametrized in terms of the offset energy density ρ , jet
 1932 area A , jet η and jet p_T . Different corrections are applied to data and MC due
 1933 to the detector simulation.
- 1934 • MC-truth correction accounts for differences between the reconstructed jet en-
 1935 ergy and the MC particle-level energy. The correction is determined on a QCD
 1936 dijet MC sample and is parametrized in terms of the jet p_T and η .
- 1937 • Residuals correct remaining small differences within jet response in data and
 1938 MC. The Residuals η -dependent correction compares jets of similar p_T in the

1939 barrel reference region. The Residuals p_T -dependent correct the jet absolute
 1940 scale (JES vs p_T).

- 1941 • Jet-flavor corrections are derived in the same way as MC-truth corrections but
 1942 using QCD pure flavor samples.

1943 ***b*-tagging of jets.**

1944 A particular feature of the hadrons containing bottom quarks (*b*-hadrons) is that
 1945 their lifetime is long enough to travel some distance before decaying, but it is not as
 1946 long as those of light quark hadrons; therefore, when looking at the hadrons produced
 1947 in pp collisions, *b*-hadrons decay typically inside the tracker rather than reaching the
 1948 calorimeters as some light-hadrons do. As a result, a *b*-hadron decay gives rise to a
 1949 displaced vertex (secondary vertex) with respect to the primary vertex as shown in
 1950 Figure 3.6; the SV displacement is in the order of a few millimeters. A jet resulting
 1951 from the decay of a *b*-hadron is called *b* jet; other jets are called light jets.

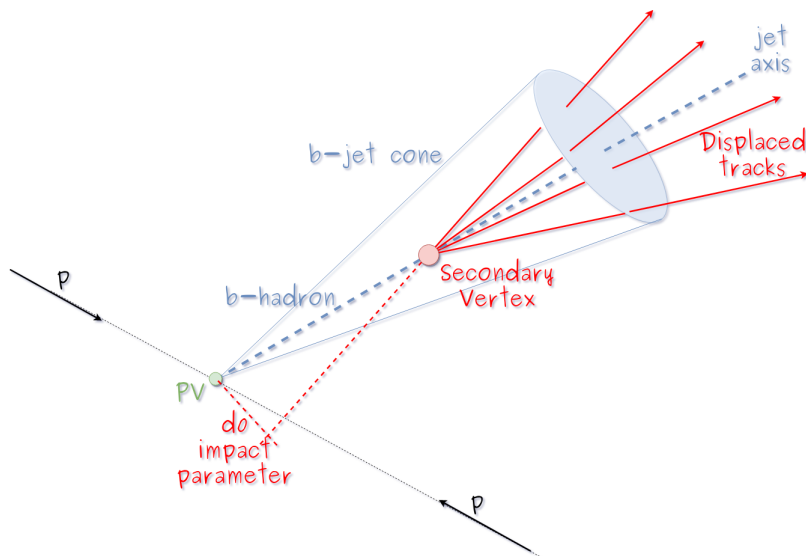


Figure 3.6: Secondary vertex in a *b*-hadron decay.

1952 Several methods to identify *b*-jets (*b*-tagging) have been developed; the method

1953 used in this thesis is known as *Combined Secondary Vertex* algorithm in its second
 1954 version (CSVv2) [121]. By using information of the impact parameter, the recon-
 1955 structed secondary vertices, and the jet kinematics as input in a multivariate analysis
 1956 that combines the discrimination power of each variable in one global discrimina-
 1957 tor variable, three working points (references): loose, medium and tight, are defined
 1958 which quantify the probabilities of mistag jets from light quarks as jets from b quarks;
 1959 10, 1 and 0.1 % respectively. Although the mistagging probability decreases with the
 1960 working point strength, the efficiency to correctly tag b -jets also decreases as 83, 69
 1961 and 49 % for the respective working point; therefore, a balance needs to be achieved
 1962 according to the specific requirements of the analysis.

1963 3.4.1.1 Missing transverse energy.

1964 The fact that proton bunches carry momentum along the z -axis implies that for
 1965 each event it is expected that the momentum in the transverse plane is balanced.
 1966 Imbalances are quantified by the missing transverse energy (MET) and are attributed
 1967 to several sources including particles escaping undetected through the beam pipe,
 1968 neutrinos produced in weak interactions processes which do not interact with the
 1969 detector and thus escaping without leaving a sign, or even undiscovered particles
 1970 predicted by models beyond the SM.

1971 The PF algorithm assigns the negative sum of the momenta of all reconstructed
 1972 PF particles to the *particle-flow MET* according to

$$\vec{E}_T = - \sum_i \vec{p}_{T,i} \quad (3.2)$$

1973 JEC are propagated to the calculation of the \vec{E}_T as described in the Reference [122].

1974 3.4.2 Event reconstruction examples

1975 Figures 3.7-3.9 show the results of the reconstruction performed on 3 recorded events.

1976 Descriptions are taken directly from the source.

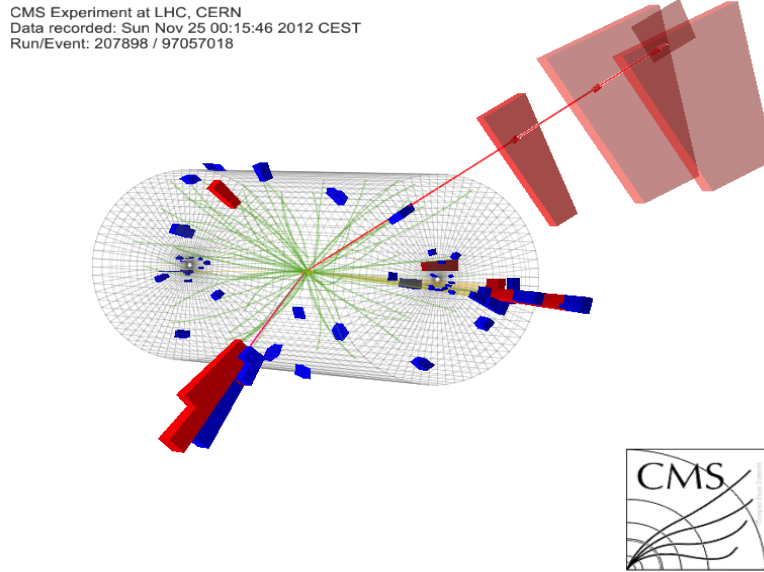


Figure 3.7: HIG-13-004 Event 1 reconstruction results; “HIG-13-004 Event 1: Event recorded with the CMS detector in 2012 at a proton-proton center-of-mass energy of 8 TeV. The event shows characteristics expected from the decay of the SM Higgs boson to a pair of τ leptons. Such an event is characterized by the production of two forward-going jets, seen here in opposite endcaps. One of the τ decays to a muon (red lines on the right) and neutrinos, while the other τ decays into a charged hadron and a neutrino.” [123].

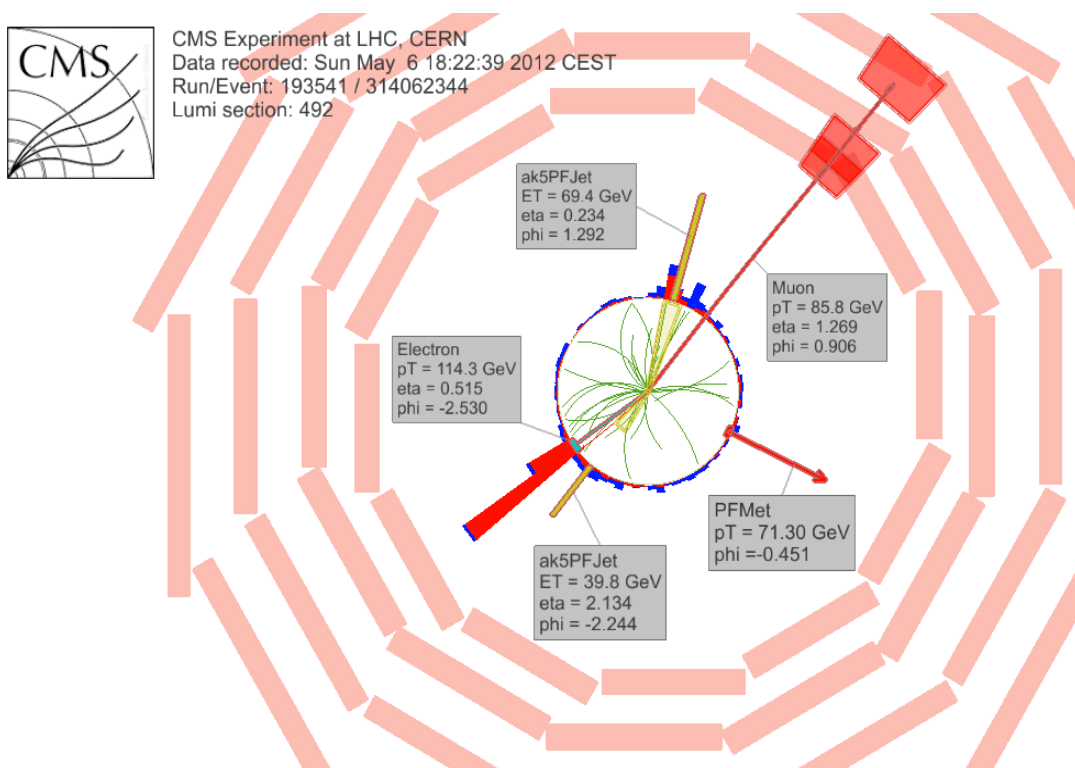


Figure 3.8: $e\mu$ event reconstruction results; “An $e\mu$ event candidate selected in 8 TeV data, as seen from the direction of the proton beams. The kinematics of the main objects used in the event selection are highlighted: two isolated leptons and two particle-flow jets. The reconstructed missing transverse energy is also displayed for reference” [124].

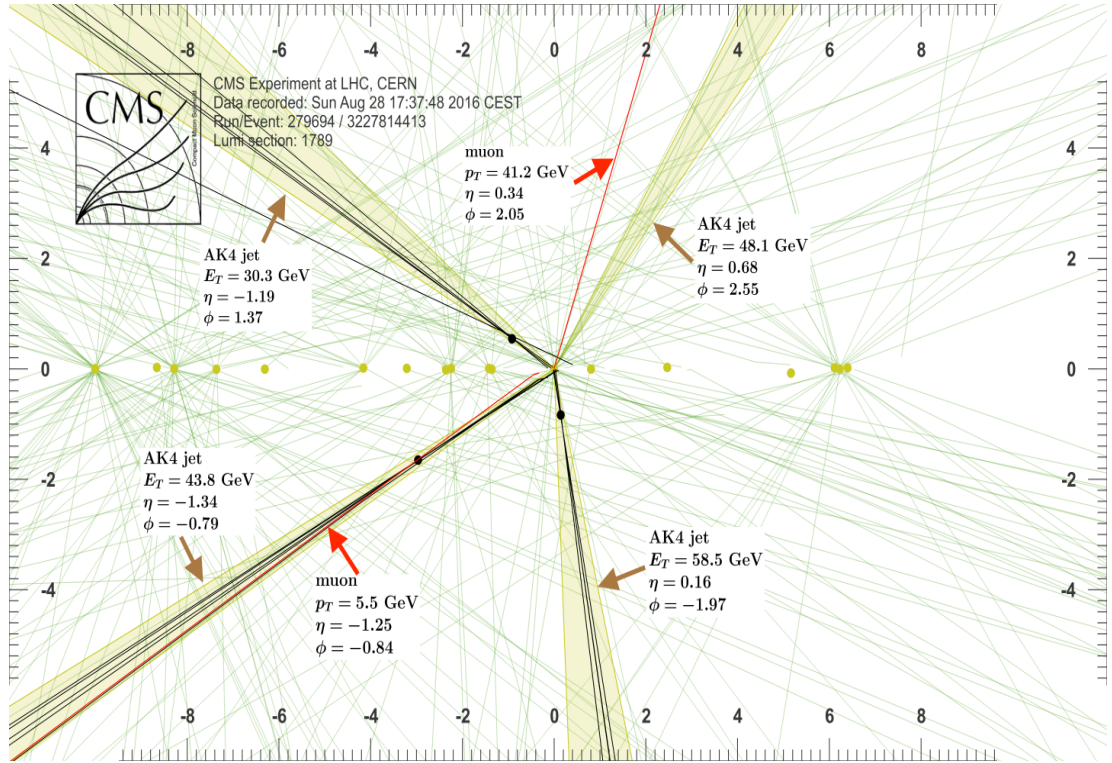


Figure 3.9: Recorded event reconstruction results; “Recorded event (ρ - z projection) with three jets with $p_T > 30$ GeV with one displaced muon track in 2016 data collected at 13 TeV. Each of the three jets has a displaced reconstructed vertex. The jet with $p_T(j) = 43.8$ GeV, $\eta(j) = -1.34$, $\phi(j) = -0.79$ contains muon with $p_T(\mu) = 5.5$ GeV, $\eta(\mu) = -1.25$, $\phi(\mu) = -0.84$. Event contains reconstructed isolated muon with $p_T(\mu) = 41.2$ GeV, $\eta(\mu) = 0.34$, $\phi(\mu) = 2.05$ and MET with $p_T = 72.5$ GeV, $\phi = -0.32$. Jet candidates for a b -jet from top quark leptonic and hadronic decays are tagged by CSVv2T algorithm. One of the other two jets is tagged by CharmT algorithm. Tracks with $p_T > 0.5$ GeV are shown. The number of reconstructed primary vertices is 18. Reconstructed $m_T(W)$ is 101.8 GeV. Beam spot position correction is applied. Reconstructed primary vertices are shown in yellow color, while reconstructed displaced vertices and associated tracks are presented in black color. Dimensions are given in cm” [125].

₁₉₇₇ **Chapter 5**

₁₉₇₈ **Statistical methods**

₁₉₇₉ In the course of analyzing the data sets provided by the CMS experiment and used in
₁₉₈₀ this thesis, several statistical tools have been employed; in this chapter, a description
₁₉₈₁ of these tools will be presented, starting with the general statement of the multivariate
₁₉₈₂ analysis methods, followed by the particularities of the Boosted Decision Trees (BDT)
₁₉₈₃ method and its application to the classification problem. Statistical inference methods
₁₉₈₄ used will also be presented. This chapter is based mainly on References [126–128].

₁₉₈₅ **5.1 Multivariate analysis**

₁₉₈₆ Multivariate data analysis (MVA) makes use of the statistical techniques developed to
₁₉₈₇ analyze more than one variable at once, taking into account all the correlations among
₁₉₈₈ variables. MVA is employed in a variety of fields like consumer and market research,
₁₉₈₉ quality control and process optimization. Using MVA it is possible to identify the
₁₉₉₀ dominant patterns in a data sample, like groups, outliers and trends, and determine
₁₉₉₁ to which group a set of values belong; in the particle physics context, MVA methods
₁₉₉₂ are used to perform the selection of certain type of events from a large data set.

1993 Processes with small cross section, such as the tHq process ($\sigma_{SM}(\sqrt{s} = 13\text{TeV}) =$
 1994 70.96 fb), are hard to detect in the presence of the processes with larger cross sections,
 1995 $\sigma_{SM}^{t\bar{t}}(\sqrt{s} = 13\text{TeV}) = 823.44$ fb for instance; therefore, only a small fraction of the data
 1996 contains events of interest (signal), the major part is signal-like events, which mimic
 1997 signal characteristics but belong to different processes, so they are a background to
 1998 the process of interest. This implies that it is not possible to say with certainty
 1999 that a given event is a signal or a background and statistical methods should be
 2000 involved. In that sense, the challenge can be formulated as one where a set of events
 2001 have to be classified according to certain special features; these features correspond
 2002 to the measurements of several parameters like energy or momentum, organized in a
 2003 set of *input variables*. The measurements for each event can be written in a vector
 2004 $\mathbf{x} = (x_1, \dots, x_n)$ for which

- 2005 • $f(\mathbf{x}|s)$ is the probability density (*likelihood function*) that \mathbf{x} is the set of mea-
 2006 sured values given that the event is a signal event (signal hypothesis).
- 2007 • $f(\mathbf{x}|b)$ is the probability density (*likelihood function*) that \mathbf{x} is the set of mea-
 2008 sured values given that the event is a background event (background hypothe-
 2009 sis).

2010 Figure 5.1 shows three ways to perform a classification of events for which mea-
 2011 surements of two properties, i.e., two input variables x_1 and x_2 , have been performed;
 2012 blue circles represent signal events while red triangles represent background events.
 2013 The classification on the left is *cut-based* requiring $x_1 < c_1$ and $x_2 < c_2$; usually the
 2014 cut values (c_1 and c_2) are chosen according to some knowledge about the event pro-
 2015 cess. In the middle plot, the classification is performed using a linear function of
 2016 the input variables, hence the boundary is a straight line, while in the right plot the

2017 the relationship between input variables is not linear thus the boundary is not linear
 2018 either.

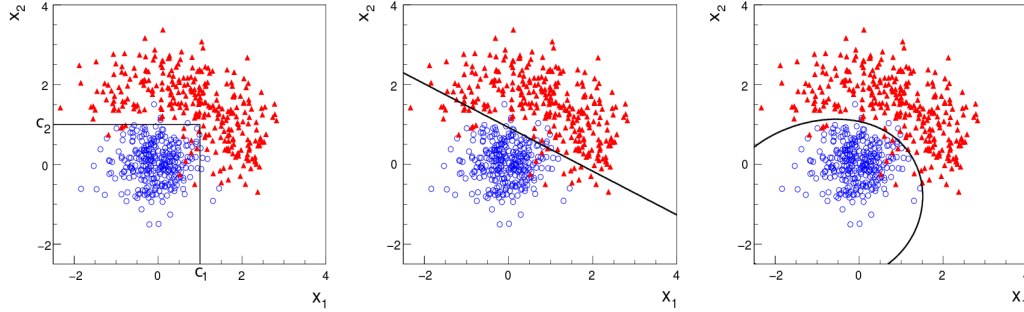


Figure 5.1: Scatter plots-MVA event classification. Distribution of two input variables x_1 and x_2 measured for a set of events; blue circles represent signal events and red triangles represent background events. The classification is based on cuts (left), linear boundary (center), and nonlinear boundary (right) [126]

2019 In general, the boundary can be parametrized in terms of the input variables such
 2020 that the cut is set on the parametrization instead of on the variables, i.e., $y(\mathbf{x}) = y_{cut}$
 2021 with y_{cut} being a constant; thus, the acceptance or rejection of an event is based on
 2022 which side of the boundary the event is located. If $y(\mathbf{x})$, usually called *test statistic*,
 2023 has functional form, it can be used to determine the probability distribution functions
 2024 $p(y|s)$ and $p(y|b)$ and then perform a test statistic with a single cut on the scalar
 2025 variable y .

2026 Figure 5.2 shows an example of what would be the probability distribution func-
 2027 tions under the signal and background hypotheses for a scalar test statistic with a cut
 2028 on the classifier y . Note that the tails of the distributions indicate that some signal
 2029 events fall in the rejection region and some background events fall on the acceptance
 2030 region; therefore, it is convenient to define the *efficiency* with which events of a given
 2031 type are accepted. The signal and background efficiencies are given by

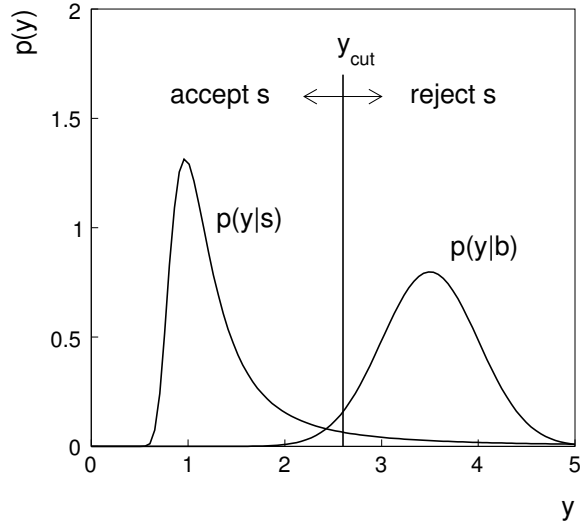


Figure 5.2: Distributions of the scalar test statistic $y(\mathbf{x})$ under the signal and background hypotheses. [126]

$$\varepsilon_s = P(\text{accept event}|s) = \int_A f(\mathbf{x}|s) d\mathbf{x} = \int_{-\infty}^{y_{cut}} p(y|s) dy , \quad (5.1)$$

$$\varepsilon_b = P(\text{accept event}|b) = \int_A f(\mathbf{x}|b) d\mathbf{x} = \int_{-\infty}^{y_{cut}} p(y|b) dy , \quad (5.2)$$

where A is the acceptance region. If the background hypothesis is the *null hypothesis* (H_0), the signal hypothesis would be *alternative hypothesis* (H_1); in this context, the background efficiency corresponds to the significance level of the test (α) and describes the misidentification probability, while the signal efficiency corresponds to the power of the test ($1-\beta$)¹ and describes the probability of rejecting the background hypothesis if the signal hypothesis is true. What is sought in an analysis is to maximize the power of the test relative to the significance level, i.e., set a selection with the largest possible selection efficiency and the smallest possible misidentification probability.

¹ β is the fraction of signal events that fall out of the acceptance region

2040 **5.1.1 Decision trees**

2041 For this thesis, the implementation of the MVA strategy, described above, is per-
 2042 formed through decision trees by using the TMVA software package [127] included
 2043 in the ROOT analysis framework [129]. In a simple picture, a decision tree classifies
 2044 events according to their input variables values by setting a cut on each input variable
 2045 and checking which events are on which side of the cut, just as proposed in the MVA
 2046 strategy, but in addition, as a machine learning algorithm, decision trees offer the
 2047 possibility to be trained and then perform the classification efficiently.

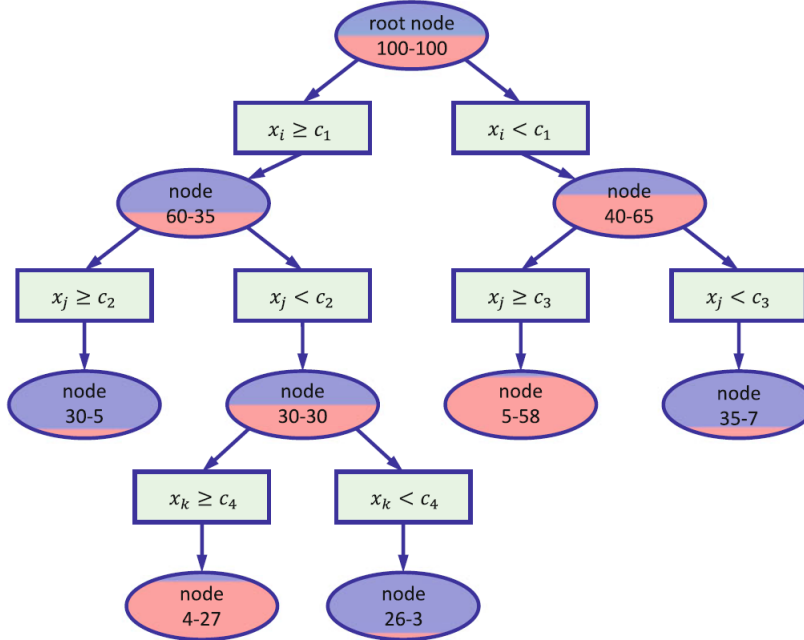


Figure 5.3: Example of a decision tree. Each node is fed with a MC sample mixing signal and background events (left-right numbers); nodes colors represent the relative number of signal/background events [128].

2048 The training or growing of a decision tree is the process where the rules for clas-
 2049 sifying events are defined; this process is represented in Figure 5.3 and consists of
 2050 several steps:

- 2051 • take MC samples of signal and background events and split them into two parts

2052 each; the first parts will be used in the decision tree training, while the second
 2053 parts will be used for testing the final classifier obtained from the training.
 2054 Each event has associated a set of input variables $\mathbf{x} = (x_1, \dots, x_n)$ which serve
 2055 to distinguish between signal and background events. The training sample is
 2056 taken in at the *root node*.

- 2057 • Pick one variable, say x_i .
- 2058 • Pick one value of x_i , each event has its own value of x_i , and split the training
 2059 sample into two subsamples B_1 and B_2 ; B_1 contains events for which $x_i < c_1$
 2060 while B_2 contains the rest of the training events;
- 2061 • scan all possible values of x_i and find the splitting value that provides the *best*
 2062 classification², i.e., B_1 is mostly made of signal events while B_2 is mostly made
 2063 of background events.
- 2064 • It is possible that variables other than the picked one produce a better classi-
 2065 fication, hence, all the variables have to be evaluated. Pick the next variable,
 2066 say x_j , and repeat the scan over its possible values.
- 2067 • At the end, all the variables and their values will have been scanned, the *best*
 2068 variable and splitting value will have been identified, say x_1, c_1 , and there will
 2069 be two nodes fed with the subsamples B_1 and B_2 .

2070 Nodes are further split by repeating the decision process until a given number of
 2071 final nodes is obtained, nodes are largely dominated by either signal or background
 2072 events, or nodes have too few events to continue. Final nodes are called *leaves* and
 2073 they are classified as signal or background leaves according to the class of the majority
 2074 of events in them. Each *branch* in the tree corresponds to a sequence of cuts.

² Quality of the classification will be treated in the next paragraph.

2075 The quality of the classification at each node is evaluated through a separation
 2076 criteria; there are several of them but the *Gini Index* (G) is the one used in the
 2077 decision trees trained for the analysis in this thesis. G is written in terms of the
 2078 purity (P), i.e., the fraction of signal events in the samples after the separation is
 2079 made; it is given by

$$G = P(1 - P) \quad (5.3)$$

2080 note that $P=0.5$ at the root node while $G=0$ for pure leaves. For a node A split into
 2081 two nodes B_1 and B_2 the G gain is

$$\Delta G = G(A) - G(B_1) - G(B_2). \quad (5.4)$$

2082 The *best* classification corresponds to that for which the gain of G is maximized;
 2083 hence, the scanning over all the variables in an event and their values is of great
 2084 importance.

2085 In order to provide a numerical output for the classification, events in a sig-
 2086 nal(background) leaf are assigned a score of 1(-1) each, defining in this way the
 2087 decision tree *classifier/weak learner* as

$$f(\mathbf{x}) = \begin{cases} 1 & \mathbf{x} \text{ in signal region,} \\ -1 & \mathbf{x} \text{ in background region.} \end{cases}$$

2088 Figure 5.4 shows an example of the classification of a sample of events, containing
 2089 two variables, performed by a decision tree.

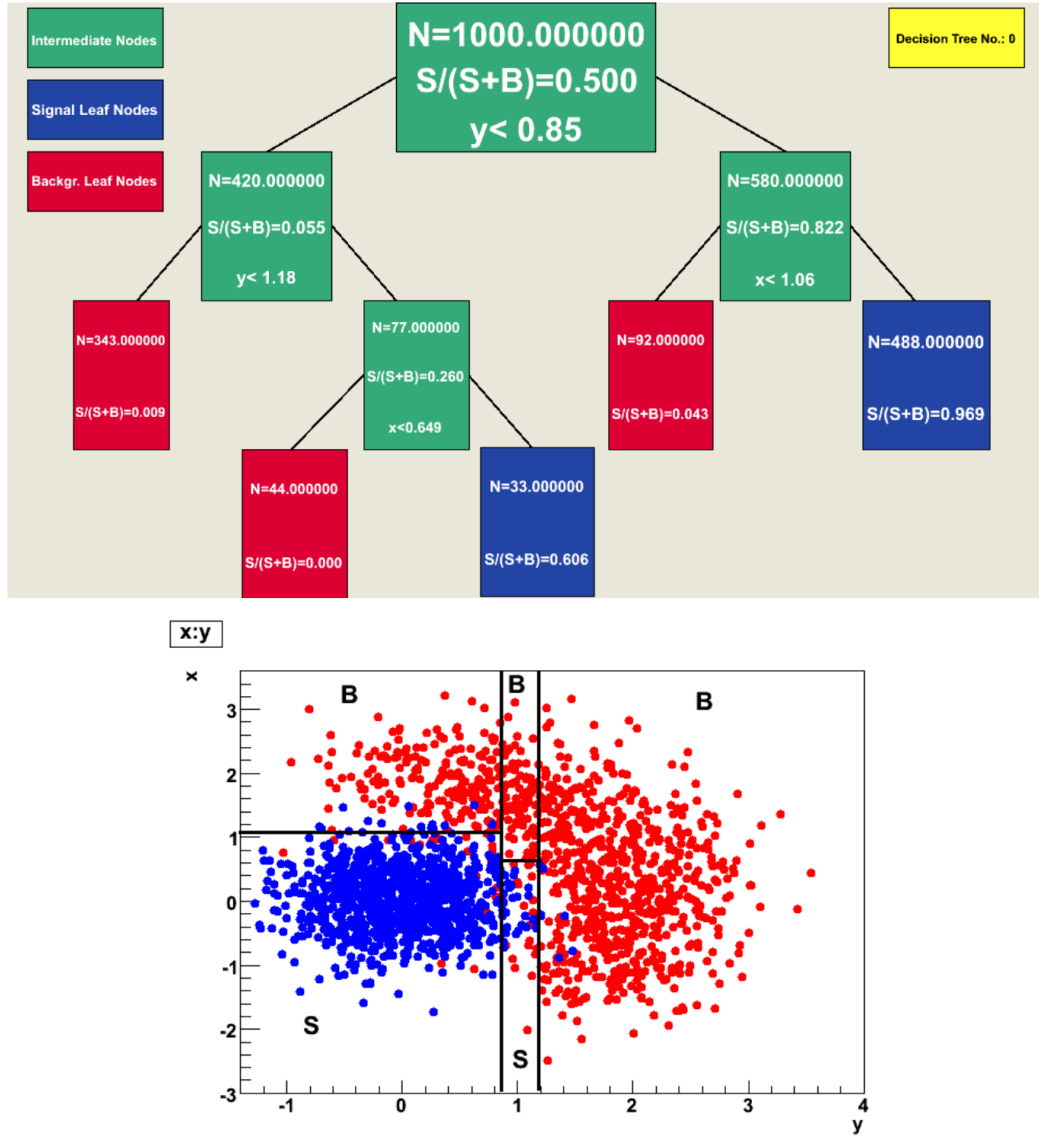


Figure 5.4: Example of a decision tree output. Each leaf, blue for signal events and red for background events, is represented by a region in the variables phase space [130].

2090 5.1.2 Boosted decision trees (BDT).

2091 Event misclassification occurs when a training event ends up in the wrong leaf, i.e., a
 2092 signal event ends up in a background leaf or a background event ends up in a signal
 2093 leaf. A way to correct it is to assign a weight to the misclassified events and train
 2094 a second tree using the reweighted events; the event reweighting is performed by a

boosting algorithm in such a way that when used in the training of a new decision tree the *boosted events* get correctly classified. The process is repeated iteratively adding a new tree to the forest and creating a set of classifiers, which are combined to create the next classifier; the final classifier offers more stability³ and has a smaller misclassification rate than any individual ones. The resulting tree collection is known as a *boosted decision tree (BDT)*.

Thus, purity of the sample is generalized to

$$P = \frac{\sum_s w_s}{\sum_s w_s + \sum_b w_b} \quad (5.5)$$

where w_s and w_b are the weights of the signal and background events respectively; the Gini index is also generalized

$$G = \left(\sum_i^n w_i \right) P(1 - P) \quad (5.6)$$

with n the number of events in the node. The final score of an event, after passing through the forest, is calculated as the renormalized sum of all the individual (possibly weighted) scores; thus, high(low) score implies that the event is most likely signal(background).

The boosting procedure, implemented in the *Gradient boosting* algorithm used in this thesis, produces a classifier $F(\mathbf{x})$ which is the weighted sum of the individual classifiers obtained after each iteration, i.e.,

$$F(\mathbf{x}) = \sum_{m=1}^M \beta_m f(\mathbf{x}; a_m) \quad (5.7)$$

where M is the number of trees in the forest. The *loss function* $L(F, y)$ represents the

³ Decision trees suffer from sensitivity to statistical fluctuations in the training sample which may lead to very different results with a small change in the training samples.

2112 deviation between the classifier $F(\mathbf{x})$ response and the true value y obtained from the
 2113 training sample (1 for signal events and -1 for background event), according to

$$L(F, y) = \ln(1 + e^{-2F(\mathbf{x})y}) \quad (5.8)$$

2114 thus, the reweighting is employed to ensure the minimization of the loss function; a
 2115 more detailed description of the minimization procedure can be found in Reference
 2116 [131]. The final classifier output is later used as a final discrimination variable, labeled
 2117 as *BDT output/response*.

2118 5.1.3 Overtraining

2119 Decision trees offer the possibility to have as many nodes as desired in order to
 2120 reduce the misclassification to zero (in theory); however, when a classifier is too much
 2121 adjusted to a particular training sample, the classifier's response to a slightly different
 2122 sample may leads to a completely different classification results; this effect is known
 2123 as *overtraining*.

2124 An alternative to reduce the overtraining in BDTs consists in pruning the tree
 2125 by removing statistically insignificant nodes after the tree growing is completed but
 2126 this option is not available for BDTs with gradient boosting in the TMVA-toolkit,
 2127 therefore, the overtraining has to be reduced by tuning the algorithm, number of
 2128 nodes, minimum number of events in the leaves, etc. The overtraining can be evaluated
 2129 by comparing the responses of the classifier when running over the training and
 2130 test samples.

2131 5.1.4 Variable ranking

2132 BDTs have a couple of particular advantages related to the input variables; they are
 2133 relatively insensitive to the number of input variables used in the vector \mathbf{x} . The
 2134 ranking of the BDT input variables is determined by counting the number of times a
 2135 variable is used to split decision tree nodes; in addition, the separation gain-squared
 2136 achieved in the splitting and the number of events in the node are accounted by
 2137 applying a weighting to that number. Thus, those variables with small or no power
 2138 to separate signal and background events are rarely chosen to split the nodes, i.e., are
 2139 effectively ignored.

2140 In addition, variables correlations play an important role for some MVA methods
 2141 like the Fisher discriminant algorithm in which the first step consist of performing a
 2142 linear transformation to a phase space where the correlations between variables are
 2143 removed; in the case of BDT algorithm, correlations do not affect the performance.

2144 5.1.5 BDT output example

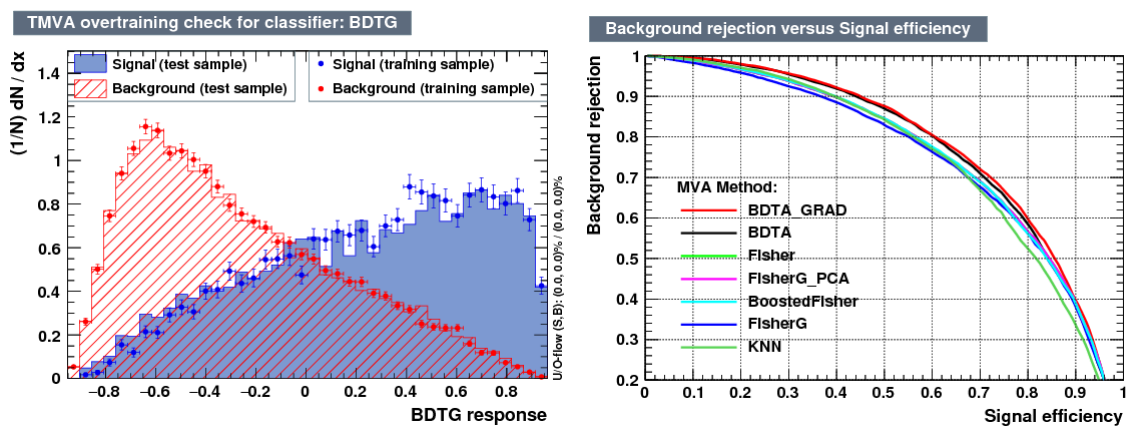


Figure 5.5: Left: Output distributions for the gradient boosted decision tree (BDTG) classifier using a sample of signal ($pp \rightarrow tHq$) and background ($pp \rightarrow tt$) events. Right: Background rejection vs signal efficiency (ROC curves) for various MVA classifiers running over the same sample used to produce the plot on the left.

2145 The left side of figure 5.5 shows the BDT output distributions for signal ($pp \rightarrow$
 2146 tHq) and background ($pp \rightarrow t\bar{t}$) events; this plot is the equivalent to the one showed
 2147 in Figure 5.2. A forest with 800 trees, maximum depth per tree = 3, and gradient
 2148 boosting have been used as training parameters. The BDTG classifier offers a good
 2149 separation power. There is a small overtraining in the signal distribution, while the
 2150 background distribution is very well predicted which might indicate that the sample
 2151 is composed of more background than signal events.

2152 The right side of figure 5.5 shows the background rejection vs signal efficiency
 2153 curves for several combinations of MVA classifiers-boosting algorithms running over
 2154 the same MC sample; these curves are known as ROC curves and give an indication
 2155 of the performance of the classifier. In this particular example, the best performance
 2156 is achieved with the BDTG classifier (BDTA_GRAD), which motivate its use in this
 2157 thesis.

2158 **5.2 Statistical inference**

2159 Once events are classified, the next step consists of finding the parameters that define
 2160 the likelihood functions $f(\mathbf{x}|s)$, $f(\mathbf{x}|b)$ for signal and background events respectively.
 2161 In general, likelihood functions depend not only on the measurements but also on
 2162 parameters (θ_m) that define their shapes; the process of estimating these *unknown*
 2163 *parameters* and their uncertainties from the experimental data is called *inference*.

2164 The statistical inference tools used in this analysis are implemented in the RooFit
 2165 toolkit [132] and COMBINE package [133] included in the CMSSW software frame-
 2166 work.

2167 **5.2.1 Nuisance parameters**

2168 The unknown parameter vector θ is made of two types of parameters: those pa-
 2169 rameters that provide information about the physical observables of interest for the
 2170 experiment or *parameters of interest*, and the *nuisance parameters* that are not of
 2171 direct interest for the experiment but that need to be included in the analysis in
 2172 order to achieve a satisfactory description of the data; they represent effects of the
 2173 detector response like the finite resolutions of the detection systems, miscalibrations,
 2174 and in general any source of uncertainty introduced in the analysis.

2175 Nuisance parameters can be estimated from experimental data; for instance, data
 2176 samples from a test beam are usually employed for calibration purposes. In cases
 2177 where experimental samples are not availables, the estimation of nuisance parameters
 2178 makes use of dedicated simulation programs to provide the required samples.

2179 The estimation of the unknown parameters involves certain deviations from their
 2180 true values, hence, the measurement of the nuisance parameter is written in terms
 2181 of an estimated value, also called central value, $\hat{\theta}$ and its uncertainty $\delta\theta$ using the
 2182 notation

$$\theta = \hat{\theta} \pm \delta\theta \quad (5.9)$$

2183 where the interval $[\hat{\theta} - \delta\theta, \hat{\theta} + \delta\theta]$ is called *confidence interval*; it is usually interpreted,
 2184 in the limit of infinite number of experiments, as the interval where the true value
 2185 of the unknown parameter θ is contained with a probability of 0.6827 (if no other
 2186 convention is stated); this interval represents the area under a Gaussian distribution
 2187 in the interval $\pm 1\sigma$.

2188 The uncertainties associated with nuisance parameters produce *systematic uncer-*
 2189 *tainties* in the final measurement, while the uncertainties related only to fluctuations

2190 in data and that affect the determination of parameters of interest produce *statistical*
 2191 *uncertainties*.

2192 **5.2.2 Maximum likelihood estimation method**

2193 The estimation of the unknown parameters that are in best agreement with the ob-
 2194 served data is performed through a function of the data sample that returns the
 2195 estimate of those parameters; that function is called an *estimator*. Estimators are
 2196 usually constructed using mathematical expressions encoded in algorithms.

2197 In this thesis, the estimator used is the likelihood function $f(\mathbf{x}|\boldsymbol{\theta})$ ⁴ which depends
 2198 on a set of measured variables \mathbf{x} and a set of unknown parameters $\boldsymbol{\theta}$. The likelihood
 2199 function for N events in a sample is the combination of all the individual likelihood
 2200 functions, i.e.,

$$L(\boldsymbol{\theta}) = \prod_{i=1}^N f(\mathbf{x}^i|\boldsymbol{\theta}) = \prod_{i=1}^N f(x_1^i, \dots, x_n^i; \theta_1, \dots, \theta_m) \quad (5.10)$$

2201 and the estimation method used is the *Maximum Likelihood Estimation* method
 2202 (MLE); it is based on the combined likelihood function defined by eqn. 5.10 and
 2203 the procedure seeks for the parameter set that corresponds to the maximum value of
 2204 the combined likelihood function, i.e., the *maximum likelihood estimator* of the un-
 2205 known parameter vector $\boldsymbol{\theta}$ is the function that produces the vector of *best estimators*
 2206 $\hat{\boldsymbol{\theta}}$ for which the likelihood function $L(\boldsymbol{\theta})$ evaluated at the measured \mathbf{x} is maximum.

2207 Usually, the logarithm of the likelihood function is used in numerical algorithm
 2208 implementations in order to avoid underflow the numerical precision of the computers
 2209 due to the product of low likelihoods. In addition, it is common to minimize the
 2210 negative logarithm of the likelihood function, therefore, the negative log-likelihood

⁴ analogue to the likelihood functions described in previous sections

2211 function is

$$F(\boldsymbol{\theta}) = -\ln L(\boldsymbol{\theta}) = -\sum_{i=1}^N f(\mathbf{x}^i | \boldsymbol{\theta}). \quad (5.11)$$

2212 The minimization process is performed by the software MINUIT [134] imple-
 2213 mented in the ROOT analysis framework. In case of data samples with large number
 2214 of measurements, the computational resources necessary to calculate the likelihood
 2215 function are too big; therefore, the parameter estimation is performed using binned
 2216 distributions of the variables of interest for which the *binned likelihood function* is
 2217 given by

$$L(\mathbf{x}|r, \boldsymbol{\theta}) = \prod_{i=1} \frac{(r \cdot s_i(\boldsymbol{\theta}) + b_i(\boldsymbol{\theta}))^{n_i}}{n_i!} e^{-r \cdot s_i(\boldsymbol{\theta}) - b_i(\boldsymbol{\theta})} \prod_{j=1} \frac{1}{\sqrt{2\pi}\sigma_{\theta_j}^2} e^{-(\theta_j - \theta_{0,j})^2/2\sigma_{\theta_j}^2}, \quad (5.12)$$

2218 with s_i and b_i the expected number of signal and background yields for the bin i , n_i
 2219 is the observed number of events in the bin i and $r = \sigma/\sigma_{SM}$ is the signal strength.
 2220 Note that the number of entries per bin follows a Poisson distribution. The effect
 2221 of the nuisance parameters have been included in the likelihood function through
 2222 the multiplication by a Gaussian distribution that models the nuisance. The three
 2223 parameters, r , s_i and b_i are jointly fitted to estimate the value of r .

2224 5.3 Upper limits

2225 In this analysis, two hypotheses are considered; the background only hypothesis
 2226 ($H_0(b)$) and the signal plus background hypothesis ($H_1(s+b)$), i.e., the sample of
 2227 events is composed of background only events ($r=0$) or it is a mixture of signal plus
 2228 background events ($r=1$). The exclusion of one hypothesis against the other means
 2229 that the observed data sample better agrees with H_0 or rather with H_1 . In order
 2230 to discriminate these hypotheses, a test statistic is constructed on the basis of the

2231 likelihood function evaluated for each of the hypothesis.

2232 The *Neyman-Pearson* lemma [135] states that the test statistic that provides the
 2233 maximum power for H_1 for a given significance level (background misidentification
 2234 probability α), is given by the ratio of the likelihood functions $L(\mathbf{x}|H_1)$ and $L(\mathbf{x}|H_0)$;
 2235 however, in order to use that definition it is necessary to know the true likelihood
 2236 functions, which in practice is not always possible. Approximate functions obtained
 2237 by numerical methods, like the BDT method described above, have to be used, so
 2238 that the *profile likelihood* test statistic is defined by

$$\lambda(\mathbf{r}) = \frac{L(\mathbf{x}|r, \hat{\boldsymbol{\theta}}(r))}{L(\mathbf{x}|\hat{r}, \hat{\boldsymbol{\theta}})}, \quad (5.13)$$

2239 where, \hat{r} and $\hat{\boldsymbol{\theta}}$ maximize the likelihood function, and $\hat{\boldsymbol{\theta}}$ maximizes the likelihood
 2240 function for a given value of the signal strength modifier r . In practice, the test
 2241 statistic t_r

$$t_r = -2\ln\lambda(r) \quad (5.14)$$

2242 is used to evaluate the presence of signal in the sample, since the minimum of t_r at
 2243 $r = \hat{r}$ suggests the presence of signal with signal strength \hat{r} . The uncertainty interval
 2244 for r is determined by the values of r for which $t_r = +1$.

2245 The expected probability density function (p.d.f) $f(t_r|r, \boldsymbol{\theta})$ of the test statistic t_r
 2246 can be obtained numerically by generating MC samples where one hypothesis, $H_0(b)$
 2247 or $H_1(s+b)$, is assumed; thus, MC samples contain the possible values of t_r obtained
 2248 from *pseudo-experiments* as shown in Figure 5.6. The probability that t_r takes a value
 2249 equal or greater than the observed value ($t_{r,obs}$) when a signal with a signal modifier
 2250 r is present in the data sample, is called the *p-value* of the observation; it can be
 2251 calculated using

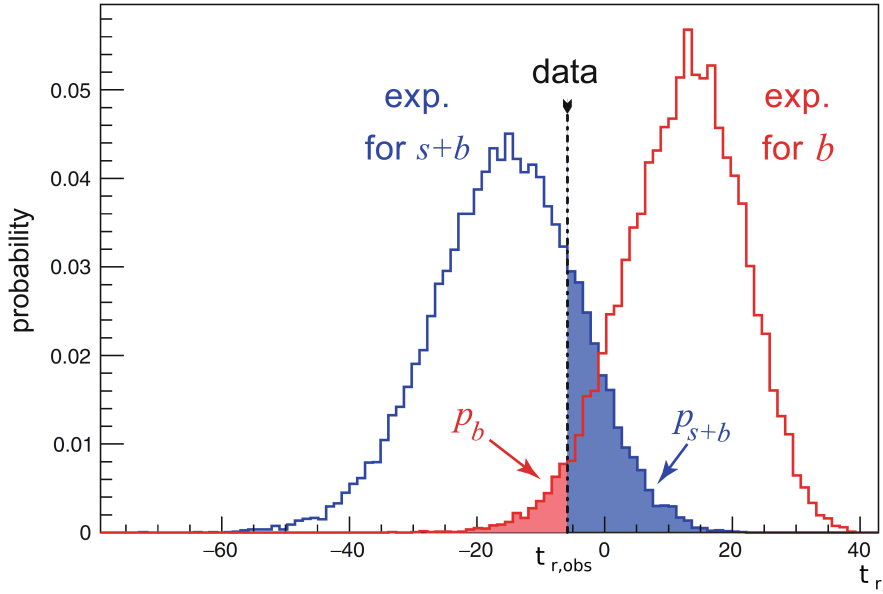


Figure 5.6: t_r p.d.f. from MC pseudo experiments assuming H_0 (red) and H_1 (blue). The black dashed line shows the value of the test statistic as measured from data. Adapted from Reference [128].

$$p_r = \int_{t_{r,obs}}^{\infty} f(t'_r | r, \boldsymbol{\theta}) dt'_r, \quad (5.15)$$

thus, $p_r < 0.05$ means that, for that particular value of r , H_1 could be excluded at 95% Confidence Level (CL). The corresponding background-only p-value is given by

$$1 - p_b = \int_{t_{r,obs}}^{\infty} f(t'_r | 0, \boldsymbol{\theta}) dt'_r, \quad (5.16)$$

If the t_r p.d.f.s for both hypotheses are well separated, as shown in the top side of Figure 5.7, the experiment is sensitive to the presence of signal in the sample. If the signal presence is small, both p.d.f.s will be largely overlapped (bottom of Figure ??) and either the signal hypothesis could be rejected with not enough justification because the experiment is not sensitive to the signal or a fluctuation of the background could be misinterpreted as presence of signal with the corresponding rejection of the

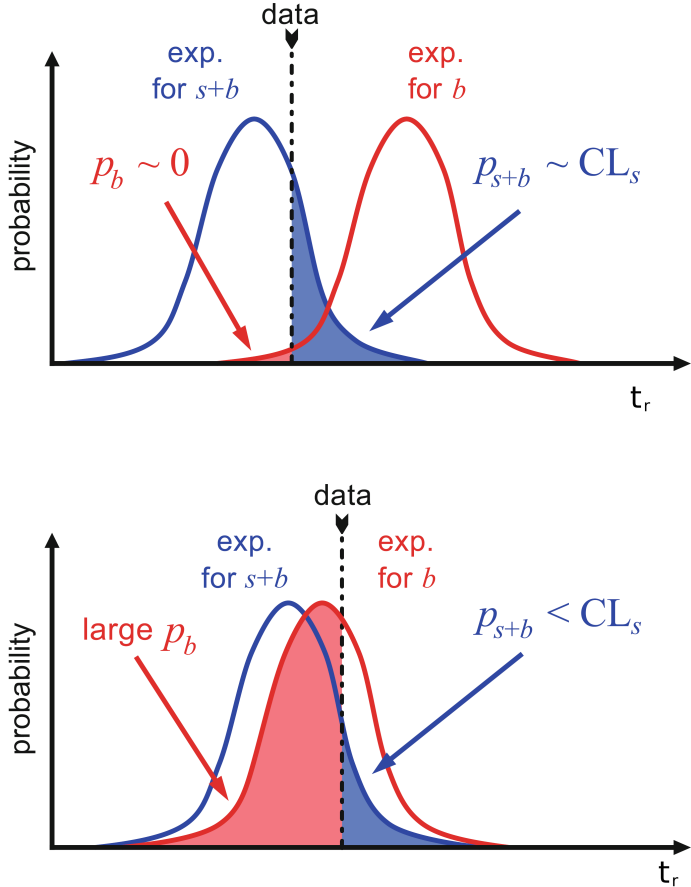


Figure 5.7: CL_s limit illustration. When the test statistic p.d.f. for the two hypotheses H_0 and H_1 are well separated (top) and when they are largely overlapped (bottom). Adapted from Reference [128].

background-only hypothesis. These issues are corrected by using the modified p-value [136]

$$p'_r = \frac{p_r}{1 - p_b} \equiv CL_s. \quad (5.17)$$

If H_1 is true, then p_b is small, $CL_s \simeq p_r$ and H_0 is rejected; if there is large overlap and a statistical fluctuation cause that p_b is large, then both numerator and denominator in Eqn. 5.17 become small but CL_s would allow the rejection of H_1 even if there is poor sensitivity to signal.

2266 The upper limit of the parameter of interest r^{up} is determined by excluding the
 2267 range of values of r for which $CL_s(r, \theta)$ is lower than the confidence level desired,
 2268 normally 90% or 95%, e.g, scanning over r and finding the value for which $p_r'^{up} =$
 2269 0.05. The expected upper limit can be calculated using pseudo-experiments based on
 2270 the background-only hypothesis and obtaining a distribution for r_{ps}^{up} ; the median of
 2271 that distribution corresponds to the expected upper limit, while the $\pm 1\sigma$ and $\pm 2\sigma$
 2272 deviations correspond to the values of the distribution that defines the 68% and 95%
 2273 of the area under the distribution centered in the median. It is usual to present all
 2274 the information about the expected and observed limits in the so-called *Brazilian-flag*
 2275 *plot* as the one showed in Figure 5.8. The solid line represent the observed CL_s

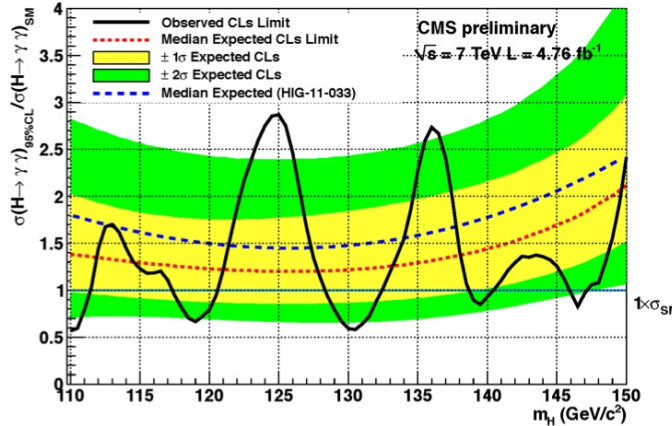


Figure 5.8: Brazilian flag plot of CMS experiment limits for Higgs boson decaying to photons [137].

2276 5.4 Asymptotic limits

2277 As said before, the complexity of the likelihood functions, the construction of test
 2278 statistics, and the calculation of the limits and their uncertainties is not always man-
 2279 ageable and requires extensive computational resources; in order to overcome those
 2280 issues, asymptotic approximations for likelihood-based test statistics, like the ones

described in previous sections, have been developed [138, 139] using Wilks' theorem.
Asymptotic approximations replace the construction of the test statistics p.d.f.s using
MC pseudo-experiments, with the approximate calculation of the test statistics p.d.f.s
by employing the so-called *Asimov dataset*.

The Asimov dataset is defined as the dataset that produce the true values of the
nuisance parameters when it is used to evaluate the estimators for all the parameters;
it is obtained by setting the values of the variables in the dataset to their expected
values [139].

Limits calculated by using the asymptotic approximation and the Asimov dataset
are know as *asymptotic limits*.

2291 Chapter 6

2292 **Search for production of a Higgs
2293 boson and a single top quark in
2294 multilepton final states in pp
2295 collisions at $\sqrt{s} = 13$ TeV**

2296 6.1 Introduction

2297 The Higgs boson discovery, supported on experimental observations and theoretical
2298 predictions made about the SM, gives the clue of the way in that elementary particles
2299 acquire mass through the Higgs mechanism; therefore, knowing the Higgs mass, the
2300 Higgs-vector boson and Higgs-fermion couplings can be determined. In order to test
2301 the Higgs-top coupling, several measurements have been performed, as stated in the
2302 chapter 1, but they are limited in sensitivity to measure the square of the coupling.
2303 The production of a Higgs boson in association with a single top quark (tH) not
2304 only offers access to the sign of the coupling, but also, to the CP phase of the Higgs

2305 couplings.

2306 This chapter presents the search for the associated production of a Higgs boson
 2307 and a single top quark (tHq) events, focusing on leptonic signatures provided by the
 2308 Higgs decay modes to WW , ZZ , and $\tau\tau$; the 13 TeV dataset produced in 2016, which
 2309 corresponds to an integrated luminosity of 35.9fb^{-1} , is used.

2310 As shown in Section 1.5, the SM cross section of tHq process is driven by a
 2311 destructive interference between two contributions (see Figure 1.15), where the Higgs
 2312 couples to either the W boson or the top quark; however, if the sign of the Higgs-
 2313 top coupling is flipped with respect to the SM prediction, a large enhancement of
 2314 the cross section occurs, making this analysis sensitive to such deviation. A second
 2315 process, where the Higgs boson and top quark are accompanied by a W boson (tHW)
 2316 has similar behavior, albeit with a weaker interference pattern and lower contribution
 2317 to the cross section, therefore, a combination of both processes would increase the
 2318 sensitivity to the sign of the coupling; in this analysis both contributions are combined
 2319 and referred as tH channel. A third contribution comes from $t\bar{t}H$ process. The purpose
 2320 of this analysis is to investigate the exclusion of the presence of the $tH + t\bar{t}H$ processes
 2321 under the assumption of the anomalous Higgs-top coupling modifier ($\kappa_t = -1$). The
 2322 analysis exploits signatures with two leptons of the same sign ($2lss$) channel and three
 2323 leptons ($3l$) channel in the final state.

2324 Constraints on the sign of the Higgs-top coupling (y_t) have been derived from the
 2325 decay rate of Higgs boson to photon pairs [50] and from the cross section for associated
 2326 production of Higgs and Z bosons via gluon fusion [141], with recent results disfavoring
 2327 negative signs of the coupling [44, 59, 142], although the negative sign coupling have
 2328 not been completely excluded.

2329 The analysis presented here, expands previous analyses performed at 8 TeV [143,
 2330 144] and searches for associated production of $t\bar{t}$ pair and a Higgs boson in the multi-

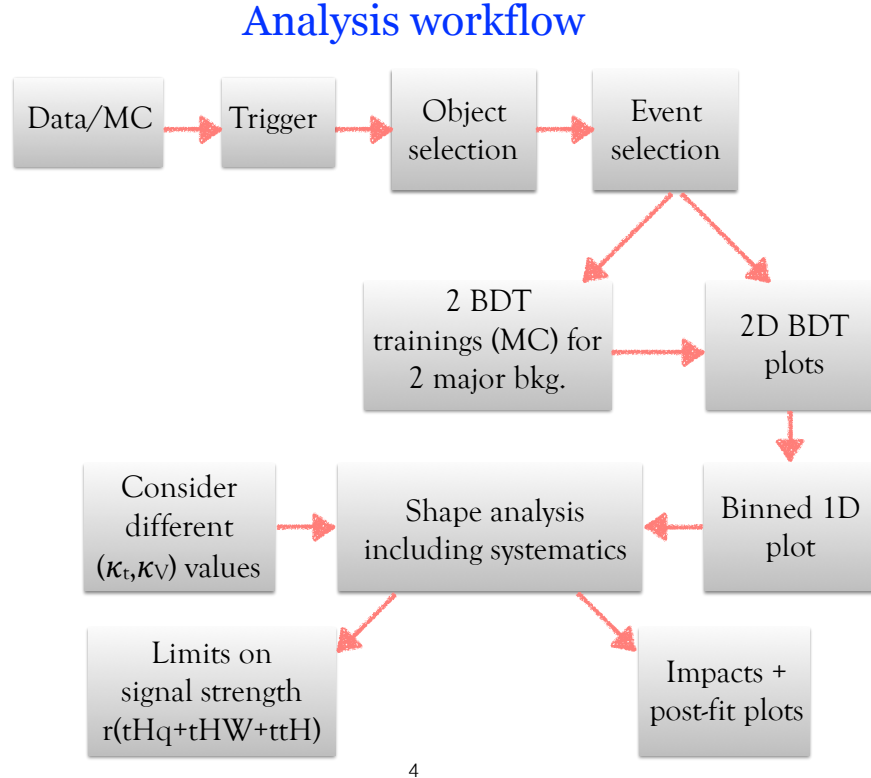
2331 lepton final state channel [145]; it also complements searches in other decay channels
 2332 targeting $H \rightarrow b\bar{b}$ [146].

2333 The first sections present the characteristic tHq signature as well as the expected
 2334 backgrounds. The MC samples, data sets, and the physics object definitions are
 2335 then defined. Following, the background predictions, the signal extraction, and the
 2336 statistical treatment of the selected events as well as the systematic uncertainties are
 2337 described. The final section present the results for the exclusion limits as a function
 2338 of the ratio of κ_t and the dimensionless modifier of the Higgs-vector boson coupling
 2339 κ_V .

2340 The analysis is designed to efficiently identify and select prompt leptons from on-
 2341 shell W and Z boson decays and to reject non-prompt leptons from b quark decays
 2342 and spurious lepton signatures from hadronic jets. Events are then selected in the
 2343 $2lss$ and $3l$ channels, and are required to contain hadronic jets, some of which must
 2344 be consistent with b quark hadronization. Finally, the signal yield is extracted by
 2345 simultaneously fitting the output of two dedicated multivariate discriminants, trained
 2346 to separate the tHq signal from the two dominant backgrounds, in all categories. The
 2347 fit result is then used to set an upper limit on the combined $t\bar{t}H + tH$ production
 2348 cross section, as a function of the relative coupling strengths of Higgs-top quark and
 2349 Higgs-Vector boson. Figure 6.1 shows an schematic overview of the analysis strategy
 2350 workflow.

2351 With respect to the 8 TeV analysis, the object selections have been adjusted for
 2352 the updated LHC running conditions at 13 TeV, the lepton identification has been
 2353 improved, and more powerful multivariate analysis techniques are used for the signal
 2354 extraction.

2355 The analysis has been made public by CMS as a Physics Analysis Summary [147]
 2356 combining the result for the three lepton and two lepton same-sign channels; the



4

Figure 6.1: A schematic overview of the analysis workflow. Based on sets of optimized physics object definitions and selection criteria, signal and background events in a data sample are discriminated. The discrimination is performed by a BDT, previously trained using MC samples of the dominant backgrounds, using discriminant variables based on the b -jet multiplicity, the activity in the forward region of the detector, and the kinematic properties of leptons. The CL_s limits on the combined $t\bar{t}H + tH$ production cross section, as a function of the relative coupling strengths are calculated.

2357 content present in this chapter is based on that document and on References [145,149]
 2358 unless other Reference is stated. Currently, an effort to turn the analysis into a paper
 2359 combining the multilepton and $H \rightarrow b\bar{b}$ is ongoing.

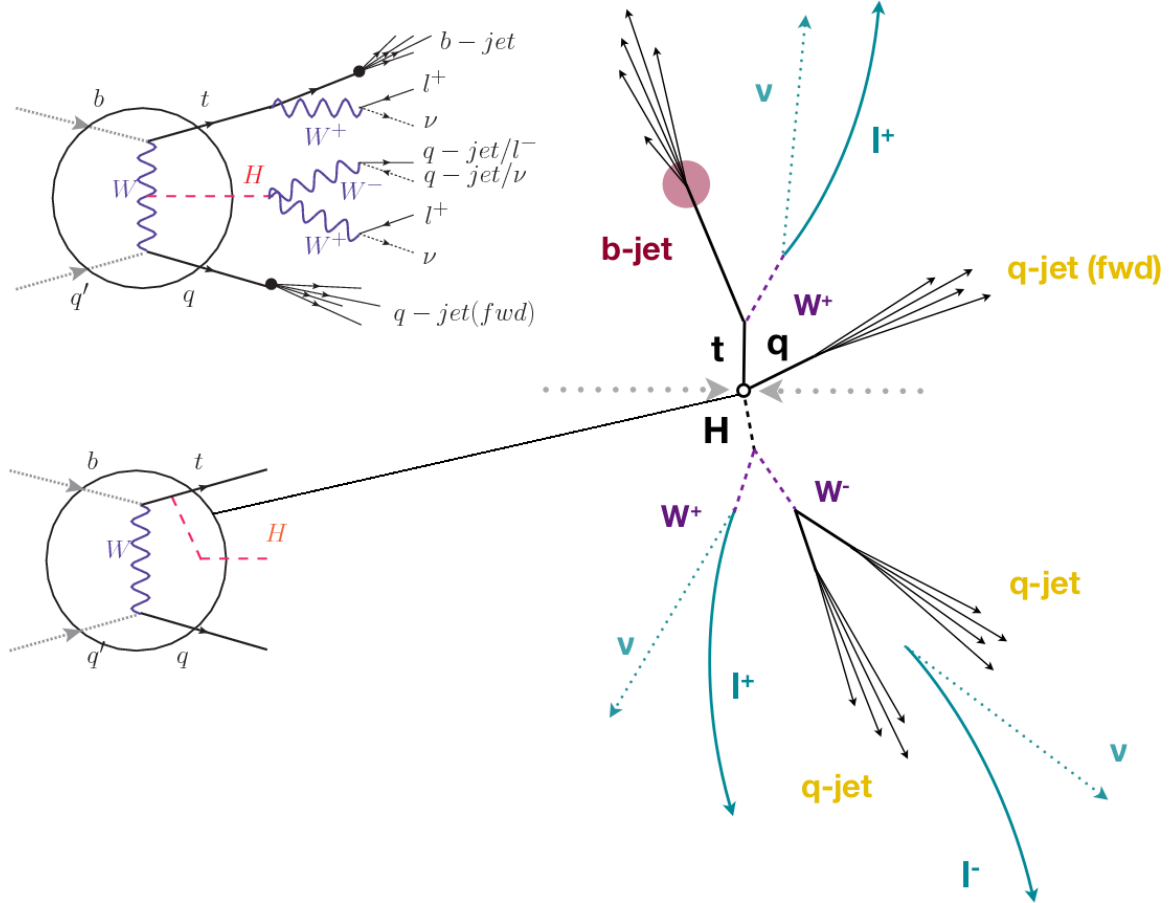


Figure 6.2: tHq event signature. Left: Feynman diagram including the whole evolution up to the final state for the case of the Higgs boson emitted by the W boson (top); Feynman diagram for the case where the Higgs boson is emitted by the top quark. Right: Schematic view as it would be seen in the detector; the circle in the Feynman diagrams on the left corresponds to the circle in the center of the schematic view as indicated by the line connecting them. In the $2lss$ channel, one of the W bosons from the Higgs boson decays to two light-quark jets while in the $3l$ channel both W bosons decay to leptons.

2360 6.2 tHq signature

2361 In order to select events of tHq process, its features are translated into a set of
 2362 selection rules; Figure 6.2 shows the Feynman diagram and an schematic view of the
 2363 tHq process from the pp collision to the final state configuration. A single top quark
 2364 is produced accompanied by a light quark, denoted as q ; this light quark is produced

2365 predominantly in the forward region of the detector. The Higgs boson can be either
 2366 emitted by the exchanged W boson or directly by the singly produced top quark.

2367 Due to their high masses/short lifetimes, top quark and Higgs boson decay after
 2368 their production within the detector. The Higgs boson is required to decay into a W
 2369 boson pair¹. The top quark almost always decays into a bottom quark and a W boson,
 2370 as encoded in the CMK matrix. The W bosons are required to decay leptonically
 2371 either all the three in the $3l$ channel or the pair with equal electrical charge in the
 2372 $2lss$ channel case; τ leptons are not reconstructed separately and only their leptonic
 2373 decays into either electrons or muons are considered in this analysis.

2374 In summary, the signal process is characterized by a the final state with

2375 • one light-flavored forward jet,

2376 • one central b-jet,

2377 • $2lss$ channel → two leptons of the same sign, two neutrinos and two light (often
 2378 soft) jets,

2379 • $3l$ channel → three leptons, three neutrinos and no central light-flavored jets,

2380 The presence of neutrinos is inferred from the presence of MET.

2381 6.3 Background processes

2382 The background processes are those that can mimic the signal signature or at least
 2383 can be reconstructed as that as a result of certain circumstances. The backgrounds
 2384 can be classified as

¹ ZZ and $\tau\tau$ decays are also include in the analysis but they are not separately reconstructed

- 2385 • irreducible backgrounds: where genuine prompt leptons are produced in on-
 2386 shell W and Z boson decays; they can be reliably estimated directly from MC
 2387 simulated events, using higher-order cross sections or data control regions for
 2388 the overall normalization.

- 2389 • reducible backgrounds: where at least one of the leptons is *non-prompt*, i.e.,
 2390 produced within a hadronic jet; genuine leptons from heavy flavor decays and
 2391 misreconstructed jets, also known as *mis-ID leptons* or *fake leptons*, are consid-
 2392 ered non-prompt leptons. These non-prompt leptons leave tracks and hits in
 2393 the detection systems as would a prompt lepton, but correlating those hits with
 2394 nearby jets could be a way of removing them. The misassignment of electron
 2395 charge in processes like $t\bar{t}$ or Drell-Yan, represent an additional source of back-
 2396 ground, but it is relevant only for the $2lss$ channel. Reducible backgrounds are
 2397 not well predicted by simulation, hence, they are estimated using data-driven
 2398 methods.

2399 The main sources of background events for tHq process are $t\bar{t}$ process and $t\bar{t} +$
 2400 $X(X = W, Z, \gamma)$ processes, the latter regarded together as $t\bar{t}V$ process. Figure 6.3
 2401 shows the signature for $t\bar{t}$ and $t\bar{t}W$ processes.

2402 The largest contribution to irreducible backgrounds comes from $t\bar{t}W$ and $t\bar{t}Z$ processes
 2403 for which the number of ($b-$)jets (($b-$)jet multiplicity) is higher than that of the sig-
 2404 nal events, while for other contributing background events, WZ , ZZ , and rare SM
 2405 processes like $W^\pm W^\pm qq$, $t\bar{t}t\bar{t}$, tZq , tZW , WWW , WWZ , WZZ , ZZZ , the ($b-$)jet
 2406 multiplicity is lower compared to that of the signal events. None of the irreducible
 2407 backgrounds present activity in the forward region of the detector.

2408 On the side of the reducible backgrounds, the largest contribution comes from the
 2409 $t\bar{t}$ events which have a very similar signature to the signal events but does no present

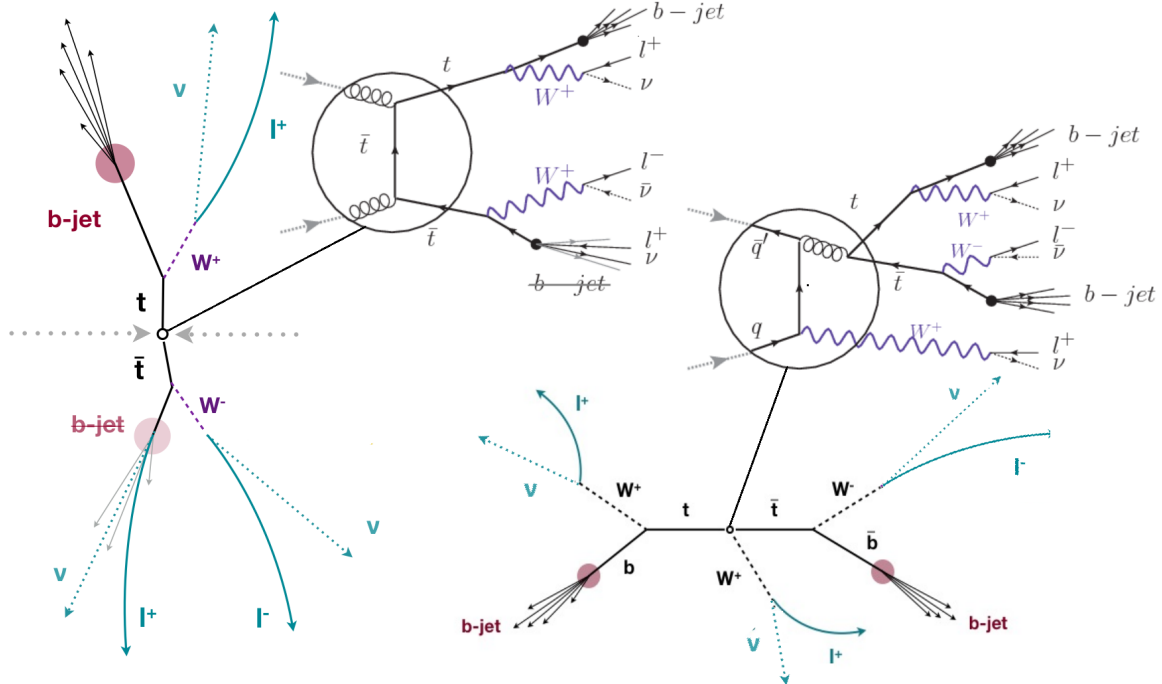


Figure 6.3: $t\bar{t}$ (left) and $t\bar{t}W$ (right) events signature as they would be seen in the detector; the Feynman diagrams including the whole evolution up to the final state are also showed. The $t\bar{t}$ process signature is very similar to that of the signal process with one fake lepton and no forward activity. The $t\bar{t}W$ process present a higher b-jet multiplicity compared to the signal process, a prompt lepton and no forward activity.

2410 activity in the forward region of the detector either; A particular feature of the $t\bar{t}$
 2411 events is their charge-symmetry, which is also a difference with respect to the signal
 2412 events.

2413 6.4 Data and MC Samples

2414 6.4.1 Full 2016 data set

2415 The data set used in this analysis was collected by the CMS experiment during 2016
 2416 at while running at $\sqrt{s} = 13\text{TeV}$ and corresponds to a total integrated luminosity
 2417 of 35.9fb^{-1} . Only periods when the CMS magnet was on were considered when

2418 selecting the data samples; that corresponds to the 23Sep2016 (Run B to G) and
 2419 PromptReco (Run H) versions of the datasets.

2420 Multilepton final states with either two same-sign leptons or three leptons tar-
 2421 get the case where the Higgs boson decays to a pair of W bosons, τ leptons, or Z
 2422 bosons, and where the top quark decays leptonically, hence, the SingleElectron,
 2423 SingleMuon, DoubleEG, MuonEG, DoubleMuon dataset (see Table A.1) compose the
 2424 full dataset. The certified luminosity sections are selected using the golden JSON file
 2425 defined by the CMS experiment [148].

2426 6.4.2 Triggers

2427 The events considered are those online-reconstructed events triggered by one, two, or
 2428 three leptons. Single-lepton triggers are included in order to boost the acceptance
 2429 of events where the p_T of the sub-leading lepton falls below the threshold of the
 2430 double-lepton triggers. The trigger efficiency is increased by including double-lepton
 2431 triggers in the $3l$ category, and single-lepton triggers in all categories; it is possible
 2432 given the logical “or” of the trigger decisions of all the individual triggers in a given
 2433 category. Table A.2 shows the lowest-threshold non-prescaled triggers present in the
 2434 High-Level Trigger (HLT) menus for both Monte-Carlo and data in 2016.

2435 Trigger efficiency scale factors

2436 Trigger efficiency describes the ability of events to pass the trigger requirements. It
 2437 is measured in simulated events using generator information given that there is no
 2438 trigger bias with the MC sample. Measuring the trigger efficiency in data requires a
 2439 more elaborated procedure; first, select a set of events collected by a trigger that is
 2440 uncorrelated with the lepton triggers such that the selected events form an unbiased

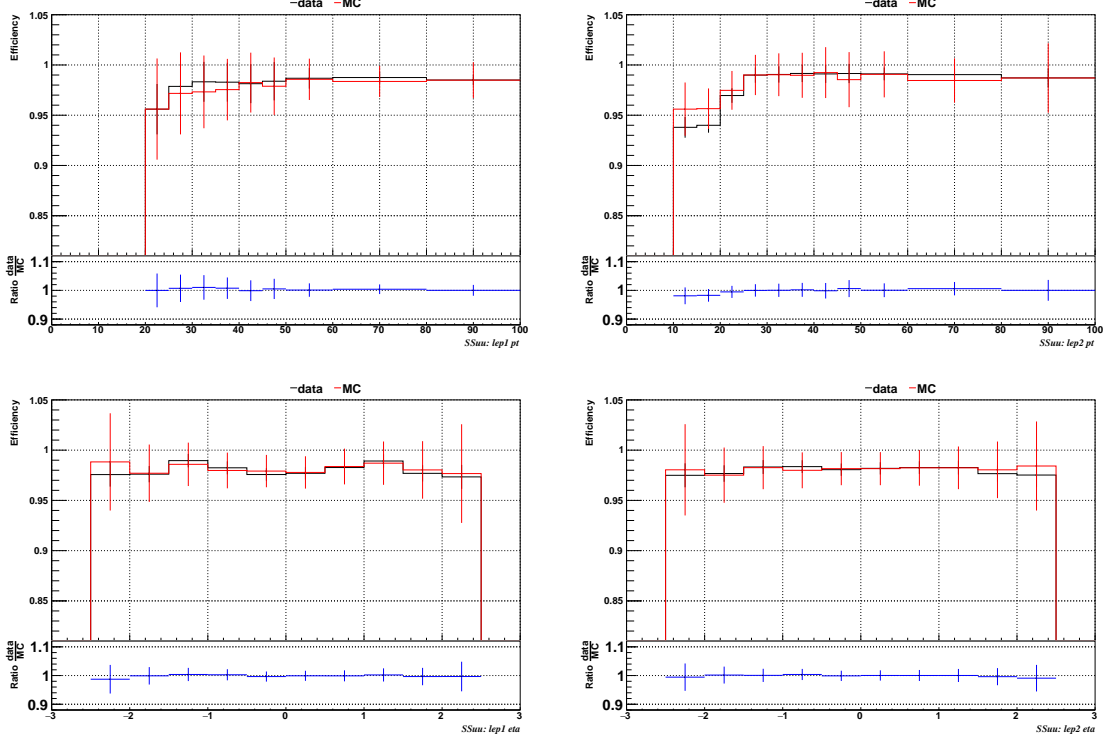


Figure 6.4: Comparison between data and MC trigger efficiencies in the same-sign $\mu\mu$ category, as a function of the p_T and η of the leading lepton (left) and the sub-leading lepton (right) [149].

sample. In this analysis, that uncorrelated trigger is a MET trigger. Second step is looking for candidate events with exactly two good leptons (exactly three good leptons for the $3l$ channel). Finally, measure the efficiency for the candidate events to pass the logical “or” of triggers being considered in a given event category as defined in Table A.2.

Comparisons between the data and MC efficiencies for each category, showed in Figures 6.4, 6.5, and 6.6, reveal that they are in good agreement; the difference is corrected by applying scale factors derived from the ratio between both efficiencies.

Applied flat scale factors in each category are shown in Table 6.1; they have been inherited from Reference [149].

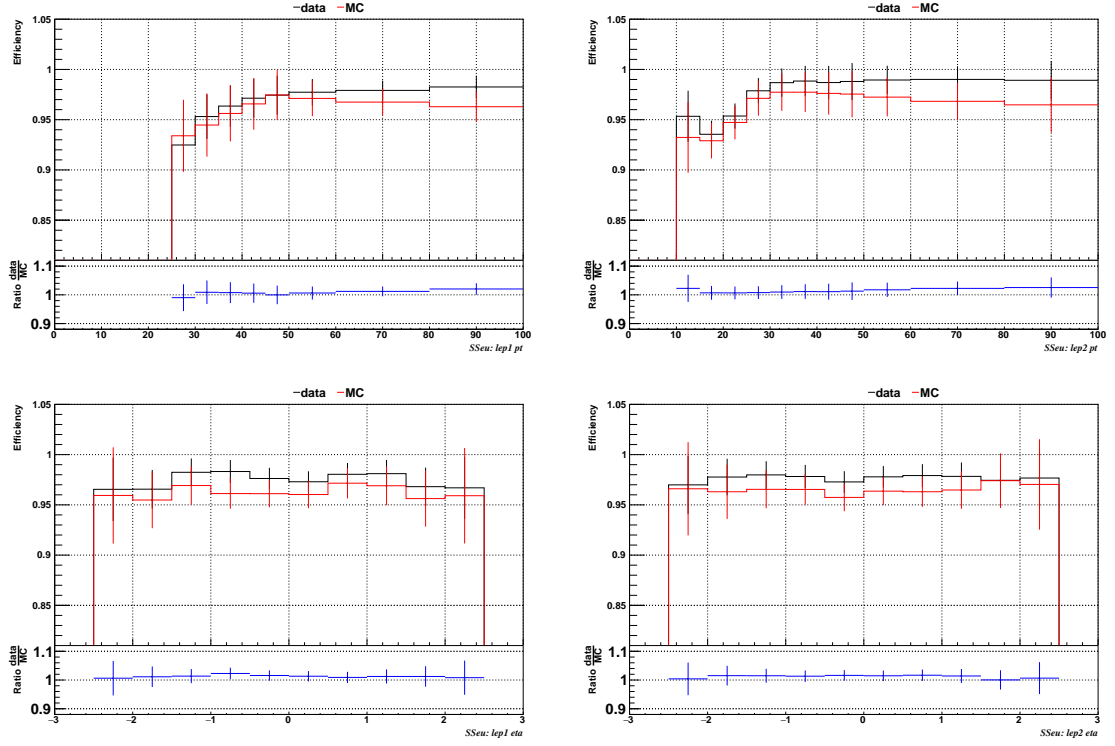


Figure 6.5: Comparison between data and MC trigger efficiencies in the same-sign $e\mu$ category as a function of the p_T and η of the leading lepton (left) and the sub-leading lepton (right) [149].

Category	Scale Factor
ee	1.01 ± 0.02
$e\mu$	1.01 ± 0.01
$\mu\mu$	1.00 ± 0.01
3l	1.00 ± 0.03

Table 6.1: Trigger efficiency scale factors and associated uncertainties, shown here rounded to the nearest percent.

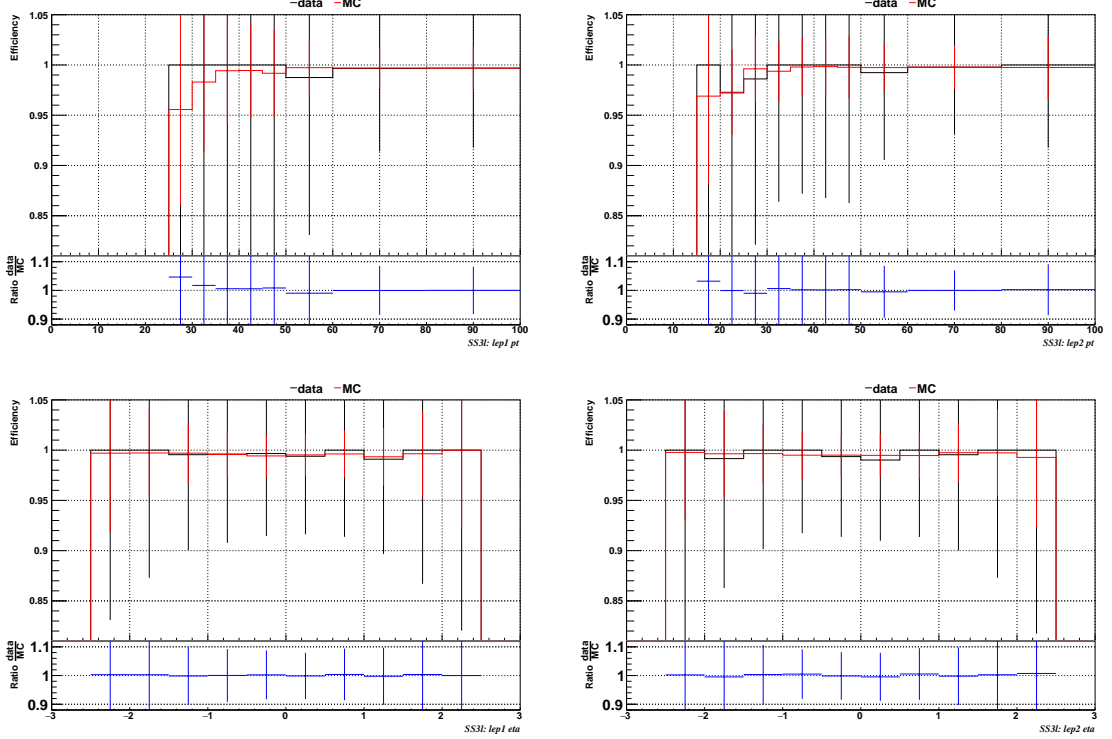


Figure 6.6: Comparison between data and MC trigger efficiencies in the $3l$ category, as a function of the p_T and η of the leading lepton (left) and the sub-leading lepton (right) [149].

2451 6.4.3 MC samples

2452 Current event generators allow for adjusting the kinematics of the generated events,
 2453 based on an event-wise reweighting; in this way, several generation parameters phase
 2454 spaces can be explored according to the experimental interests. The signal samples
 2455 used in this analysis were generated in such a way that not only the case $\kappa_t = -1$, but
 2456 an extended range of κ_t and κ_V values may be investigated.

2457 tHq and tHW cross section in the κ_t - κ_V phase space are shown in Figure 6.7. As
 2458 said in section 3.1, the tHq sample was generated using the 4F scheme which provides
 2459 a better description of the additional b quark from the initial gluon splitting, while the
 2460 tHW sample was generated using the 5F scheme in order to remove its interference
 2461 with $t\bar{t}H$ at LO.

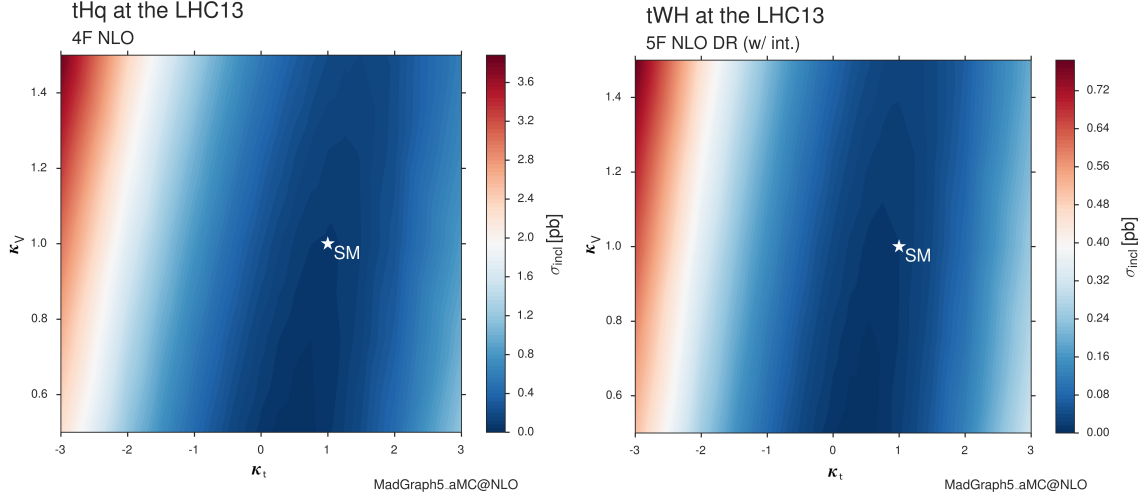


Figure 6.7: tHq and tHW cross section in the κ_t - κ_V phase space [150].

2462 MC signal samples

2463 The two signal samples, tHq and tHW , correspond to the `RunIISummer16MiniAODv2`
 2464 campaign produced with `CMSSW_80X`; they were produced with `MG5_aMC@NLO`
 2465 (version 5.2.2.3), in LO order mode at $\sqrt{s} = 13$ TeV, and are normalized to NLO cross
 2466 sections (see Table 6.2). The Higgs boson is assumed to be SM-like except for the
 2467 values of its couplings to the top quark and W boson. Each sample was generated
 2468 with a set of event weights corresponding to 51 different values of (κ_t, κ_V) couplings,
 2469 accessible in terms of LHE event weights as shown in Table A.3; however, the main
 2470 interest is the $(\kappa_t = -1, \kappa_V = 1)$ case.

Sample	σ [pb]	BF
<code>/THQ_Hincl_13TeV-madgraph-pythia8_TuneCUETP8M1/</code>	0.7927	0.324
<code>/THW_Hincl_13TeV-madgraph-pythia8_TuneCUETP8M1/</code>	0.1472	1.0
<code>/tthJetToNonbb_M125_13TeV_amcatnloFXFX_madspin_pythia8_mWCutfix/</code>	0.2151	1.0

Table 6.2: MC signal samples used in this analysis; cross section and branching fraction are also listed [150].

2471 The $t\bar{t}H$ sample was produced using `AMC@NLO` interfaced to `PYTHIA 8` for
 2472 the parton shower, and is scaled to NLO cross sections. The $t\bar{t}H$ cross section depends

2473 quadratically on κ_t ; however, in contrast to the tHq and tHW samples, the scaling
 2474 is not performed during the sample generation process but in the analysis code since
 2475 it was decided to include the $t\bar{t}H$ process as part of the signal in the course of the
 2476 analysis.

2477 **MC background samples**

2478 Several MC generators were used to generate the samples of the background processes.
 2479 The dominant background sources ($t\bar{t}$, $t\bar{t}W$, $t\bar{t}Z$) were produced using AMC@NLO
 2480 interfaced to PYTHIA8, and are scaled to NLO cross sections. Other minor back-
 2481 ground processes are simulated using POWHEG interfaced to PYTHIA, or bare
 2482 PYTHIA as stated in the sample names in Table A.4. Pileup interactions are in-
 2483 cluded in the simulation in order to reflect the observed multiplicity in data; the
 2484 simulated events are weighted according to the actual pileup in data, estimated from
 2485 the measured bunch-to-bunch instantaneous luminosity and the total inelastic cross
 2486 section, 69.2 mb. All events are finally passed through a full simulation of the CMS
 2487 detector based on GEANT4, and reconstructed using the same algorithms as used for
 2488 the data.

2489 **6.5 Object Identification**

2490 In this section, the specific definitions of the physical objects in terms of the numerical
 2491 values assigned to the reconstruction parameters are presented; thus, the provided
 2492 details summarize and complement the descriptions presented in previous chapters.
 2493 The object reconstruction and selection strategy used in this thesis is inherited from
 2494 the analyses in References [145, 149], thus, the information in this section is extracted
 2495 from those documents unless other References are stated.

2496 6.5.1 Lepton reconstruction and identification

2497 Two types of leptons are defined in this analysis: *signal leptons* are those coming from
 2498 W, Z and τ decays which usually are isolated from other particles; *background leptons*
 2499 are defined as leptons produced in b -jet hadron decays, light-jets misidentification,
 2500 and photon conversions.

2501 The process of reconstruction and identification of electron and muon candidates
 2502 was described in chapter3, hence, the identification variables used in order to retain
 2503 the highest possible efficiency for signal leptons while maximizing the rejection of
 2504 background leptons are listed and described in the following sections ².

2505 The identification variables include not only observables related directly to the re-
 2506 constructed leptons themselves, but also to the clustered energy deposits and charged
 2507 particles in a cone around the lepton direction (jet-related variables); an initial loose
 2508 preselection of leptons candidates is performed and then an MVA discriminator, re-
 2509 ferred to as *lepton MVA* discriminator, is used to distinguish signal leptons from
 2510 background leptons.

2511 Muons

2512 The Physics Objects Groups (POG) at CMS, are in charge of studying and defining
 2513 the set of selection criteria applied on the course of reconstruction and identification
 2514 of particles. These selection criteria are implemented in the CMS framework in the
 2515 form of several object identification working points according to the strength of the
 2516 requirements.

2517 The muon candidates are reconstructed by combining information from the tracker
 2518 system and the muon detection system of CMS detector and the POG defined three

² the studies performed to optimize the identification are far from the scope of this thesis, therefore, only general descriptions are provided

2519 working points for muon identification *MuonID* [153];

- 2520 • *POG Loose Muon ID* is a particle identified as a muon by the PF event re-
 2521 construction and also reconstructed either as a global-muon or as an arbitrated
 2522 tracker-muon. This identification criteria is designed to be highly efficient for
 2523 prompt muons and for muons from heavy and light quark decays; it can be com-
 2524 plemented by applying impact parameter cuts in analyses with prompt muon
 2525 signals.
- 2526 • *POG Medium Muon ID* is a Loose muon with additional track-quality and
 2527 muon-quality (spatial matching between the individual measurements in the
 2528 tracker and the muon system) requirements. This identification criteria is de-
 2529 signed to be highly efficient in the separation of the muons coming from decay
 2530 in flight of heavy quarks and muons coming from B meson decays as well as
 2531 prompt muons. An additional category *MVA Prompt ID* is defined in this iden-
 2532 tification criteria directed to discriminated muons from B mesons and prompt
 2533 muons (from W,Z and τ decays). The Medium ID provides the same fake rate as
 2534 the Tight Muon ID but a higher efficiency on prompt and B-decays muons. [154]
- 2535 • *POG Tight Muon ID* is a global muon with additional muon-quality require-
 2536 ments Tight Muon ID selects a subset of the PF muons.

2537 Only muons within the muon system acceptance $|\eta| < 2.4$ and minimum p_T of 5
 2538 GeV are considered.

2539 **Electrons**

2540 Electrons are reconstructed using information from the tracker and from the electro-
 2541 magnetic calorimeter and identified by an MVA algorithm (*MVA eID* discriminant)

2542 using the shape of the calorimetric shower variables like the shape in η and ϕ , the clus-
 2543 ter circularity, widths along η and ϕ ; track-cluster matching variables like E_{tot}/p_{in} ,
 2544 E_{Ele}/p_{out} , $\Delta\eta_{in}$, $\Delta\eta_{out}$, $\Delta\phi_{in}$, $1/E - 1/p$; and track quality variables like χ^2 of the
 2545 GSF tracks, the number of hits used by the GSF filter [155].

2546 A loose selection based on η -dependent cuts on this discriminant is used to prese-
 2547 lect electron candidates, the full shape of the discriminant is used in the lepton MVA
 2548 selection to separate signal leptons from background leptons (described in Section
 2549 6.5.1).

2550 In order to reject electrons from photon conversions, electron candidates with
 2551 missing hits in the pixel tracker layers or matched to a conversion secondary vertex
 2552 are discarded. Electrons are selected for the analysis if they have $p_T > 7$ GeV and
 2553 are located within the tracker system acceptance region ($|\eta| < 2.5$).

2554 **Lepton vertexing and pile-up rejection**

2555 The impact parameter in the transverse plane d_0 , impact parameter along the z -
 2556 axis d_z , and the impact parameter significance in the detector space SIP_{3D} , are
 2557 considered to perform the identification and rejection of pile-up, misreconstructed
 2558 tracks, and background leptons from b-hadron decays; pile-up and misreconstructed
 2559 track mitigation is achieved by imposing loose cuts on the impact parameter variables.
 2560 The full shape of the those variables is used in a lepton MVA classifier to achieve the
 2561 best separation between the signal and the background leptons.

2562 **Lepton isolation**

2563 PF is able to recognize leptons from two different sources: on one side, leptons from
 2564 the decays of heavy particles, such as W and Z bosons, which are normally isolated
 2565 in space from the hadronic activity in the event; on the other side, leptons from the

2566 decays of hadrons and jets misidentified as leptons, which are not isolated as the
 2567 former. For highly boosted systems, like the lepton and the b -jet generated in the
 2568 semileptonic decay of a boosted top, the decay products tend to be more closer and
 2569 sometimes they even overlap; thus, the PF standard definition of isolation in terms of
 2570 the separation between the lepton candidates and other PF objects in the η - ϕ plane,

$$\Delta R = \sqrt{(\eta^l - \eta^i)^2 + (\phi^l - \phi^i)^2} < 0.3 \quad (6.1)$$

2571 which considers all the neutral, charged hadrons and photons in a cone around the
 2572 leptons, is refocused to the local isolation of the leptons through the mini-isolation
 2573 I_{mini} [156] defined as the sum of particle flow candidates p_T within a cone around
 2574 the lepton, corrected for the effects of pileup and divided by the lepton p_T

$$I_{mini} = \frac{\sum_R p_T(h^\pm) - \max\left(0, \sum_R p_T(h^0) + p_T(\gamma) - \rho \mathcal{A}\left(\frac{R}{0.3}\right)^2\right)}{p_T(l)} \quad (6.2)$$

2575 where ρ is the pileup energy density, h^\pm, h^0, γ, l , represent the charged hadron, neutral
 2576 hadrons, photons, and the lepton, respectively. The radius R of the cone depends on
 2577 the p_T of the lepton according to

$$R = \frac{10\text{GeV}}{\min(\max(p_T(l), 50\text{GeV}), 200\text{GeV})}, \quad (6.3)$$

2578 The p_T dependence of the cone size allows for greater signal efficiency. Setting a
 2579 cut on I_{mini} below a given threshold ensures that the lepton is locally isolated, even
 2580 in boosted systems. The effect of pileup is mitigated using the so-called effective area
 2581 correction \mathcal{A} listed in Table 6.3.

2582 A loose cut on I_{mini} is applied to pre-select the muon and electron candidates;

$ \eta $ range	$\mathcal{A}(e)$ neutral/charged	$A(\mu)$ neutral/charged
0.0 - 0.8	0.1607 / 0.0188	0.1322 / 0.0191
0.8 - 1.3	0.1579 / 0.0188	0.1137 / 0.0170
1.3 - 2.0	0.1120 / 0.0135	0.0883 / 0.0146
2.0 - 2.2	0.1228 / 0.0135	0.0865 / 0.0111
2.2 - 2.5	0.2156 / 0.0105	0.1214 / 0.0091

Table 6.3: Effective areas, for electrons and muons used to mitigate the effect of pileup by using the so-called effective area correction.

however, the full shape is used in the lepton MVA discriminator when performing the signal lepton selection.

Jet-related variables

In order to reject misidentified leptons from b -jets, mostly coming from $t\bar{t}$ +jets, Drell-Yan+jets, and W +jets events, the vertexing and isolation described in previous sections are complemented with additional variables related to the closest reconstructed jet to the lepton, i.e., the PF jets reconstructed³ around the leptons with $\Delta R = \sqrt{(\eta^l - \eta^{jet})^2 + (\phi^l - \phi^{jet})^2} < 0.5$. The identification variables used in the lepton MVA discriminator are the ratio p_T^l/p_T^{jet} , the CSV b-tagging discriminator value of the jet, the number of charged tracks of the jet, and the relative p_T given by

$$p_T^{rel} = \frac{(\vec{p}_{jet} - \vec{p}_l) \cdot \vec{p}_l}{||\vec{p}_{jet} - \vec{p}_l||}. \quad (6.4)$$

LeptonMVA discriminator

Electrons and muons passing the basic selection process described above are referred to as *loose leptons*. Additional discrimination between signal leptons and background leptons is crucial considering that the rate of $t\bar{t}$ production is much larger than the signal, hence, an overwhelming background from $t\bar{t}$ production. To maximally ex-

³ charged hadrons from PU vertices are not removed prior to the jet clustering.

2598 ploit the available information in each event to that end, the dedicated lepton MVA
 2599 discriminator, based on a boosted decision tree (BDT) algorithm, has been built so
 2600 that all the identification variables can be used together.

2601 The lepton MVA discriminator training is performed using simulated signal Loose
 2602 leptons from the $t\bar{t}H$ MC sample and fake leptons from the $t\bar{t}$ + jets MC sample,
 2603 separately for muons and electrons. The input variables used include vertexing, iso-
 2604 lation and jet-related variables, the p_T and η of the lepton, the electron MVA eID
 2605 discriminator and the muon segment-compatibility variables. An additional require-
 2606 ment known as *tight-charge* requirement, is imposed by comparing two independent
 2607 measurement of the charge, one from the ECAL supercluster and the other from the
 2608 tracker; thus, the consistency in the measurements of the electron charge is ensured
 2609 so that events with a wrong electron charge assignment are rejected; this variable is
 2610 particularly used in the $2lss$ channel to suppress opposite-sign events for which the
 2611 charge of one of the leptons has been mismeasured. The tight-charge requirement for
 2612 muons is represented by the requirement of a consistently well measured track trans-
 2613 verse momentum given by $\Delta p_T/p_T < 0.2$. Leptons are selected for the final analysis
 2614 if they pass a given threshold of the BDT output, and are referred to as *tight leptons*
 2615 in the following.

2616 The validation of the lepton MVA algorithm and the lepton identification variables
 2617 is performed using data in various control regions; the details about that validation
 2618 are not discussed here but can be found in Reference [149].

2619 Selection definitions

2620 Electron and muon object identification is defined in three different sets of selections
 2621 criteria; the *Loose*, *Fakeable Object*, and *Tight* selection. These three levels of selection
 2622 are designed to serve for event level vetoes, the fake rate estimation application region

(see Section 6.7.2), and the final signal selection, respectively. The p_T of fakeable objects is defined as $0.85 \times p_T(\text{jet})$, where the jet is the one associated to the lepton object. This mitigates the dependence of the fake rate on the momentum of the fakeable object and thereby improves the precision of the method.

Tables 6.4 and 6.5 list the full criteria for the different selections of muons and electrons.

Cut	Loose	Fakeable object	Tight
$ \eta < 2.4$	✓	✓	✓
p_T	$> 5\text{GeV}$	$> 15\text{GeV}$	$> 15\text{GeV}$
$ d_{xy} < 0.05$ (cm)	✓	✓	✓
$ d_z < 0.1$ (cm)	✓	✓	✓
$\text{SIP}_{3D} < 8$	✓	✓	✓
$I_{\text{mini}} < 0.4$	✓	✓	✓
is Loose Muon	✓	✓	✓
jet CSV	–	< 0.8484	< 0.8484
is Medium Muon	–	–	✓
tight-charge	–	–	✓
lepMVA > 0.90	–	–	✓

Table 6.4: Requirements on each of the three muon selections. In the cases where the cut values change between the selections, those values are listed in the table. Otherwise, whether the cut is applied is indicated.

In addition to the previously defined requirements for jets, they are required to be separated from any lepton candidates passing the fakeable object selections by $\Delta R > 0.4$.

6.5.2 Lepton selection efficiency

Efficiencies of reconstruction and selecting loose leptons are measured both for muons and electrons using a tag and probe method on both data and MC, using $Z \rightarrow \ell^+ \ell^-$ [157]. The scale factors are derived from the ratio of efficiencies $\varepsilon_i(p_T, \eta)$ measured

Cut	Loose	Fakeable Object	Tight
$ \eta < 2.5$	✓	✓	✓
p_T	$> 7\text{GeV}$	$> 15\text{GeV}$	$> 15\text{GeV}$
$ d_{xy} < 0.05 \text{ (cm)}$	✓	✓	✓
$ d_z < 0.1 \text{ (cm)}$	✓	✓	✓
$\text{SIP}_{3D} < 8$	✓	✓	✓
$I_{\text{mini}} < 0.4$	✓	✓	✓
MVA eID $> (0.0, 0.0, 0.7)$	✓	✓	✓
$\sigma_{in\eta} < (0.011, 0.011, 0.030)$	—	✓	✓
$\text{H/E} < (0.10, 0.10, 0.07)$	—	✓	✓
$\Delta\eta_{in} < (0.01, 0.01, 0.008)$	—	✓	✓
$\Delta\phi_{in} < (0.04, 0.04, 0.07)$	—	✓	✓
$-0.05 < 1/E - 1/p < (0.010, 0.010, 0.005)$	—	✓	✓
p_T^{ratio}	—	$> 0.5^\dagger / -$	—
jet CSV	—	$< 0.3^\dagger / < 0.8484$	< 0.8484
tight-charge	—	—	✓
conversion rejection	—	—	✓
Number of missing hits	< 2	$== 0$	$== 0$
lepton MVA > 0.90	—	—	✓

Table 6.5: Criteria for each of the three electron selections. In cases where the cut values change between selections, those values are listed in the table. Otherwise, whether the cut is applied is indicated. In some cases, the cut values change for different η ranges. These ranges are $0 < |\eta| < 0.8$, $0.8 < |\eta| < 1.479$, and $1.479 < |\eta| < 2.5$ and the respective cut values are given in the form (value₁, value₂, value₃). For the two p_T^{ratio} and CSV rows, the cuts marked with a \dagger are applied to leptons that fail the lepton MVA cut, while the loose cut value is applied to those that pass the lepton MVA cut.

2636 for a given lepton in data/MC, according to

$$\rho(p_T, \eta) = \frac{\varepsilon_{\text{data}}(p_T, \eta)}{\varepsilon_{\text{MC}}(p_T, \eta)}. \quad (6.5)$$

2637 The scale factor for each event is used to correct the weight of the event in the
 2638 full sample; therefore, the full simulation correction is given by the product of all
 2639 the individual scale factors. The scale factors used in this thesis are inherited from
 2640 Reference [149] which in turns inherited them from leptonic SUSY analyses using
 2641 equivalent lepton selections.

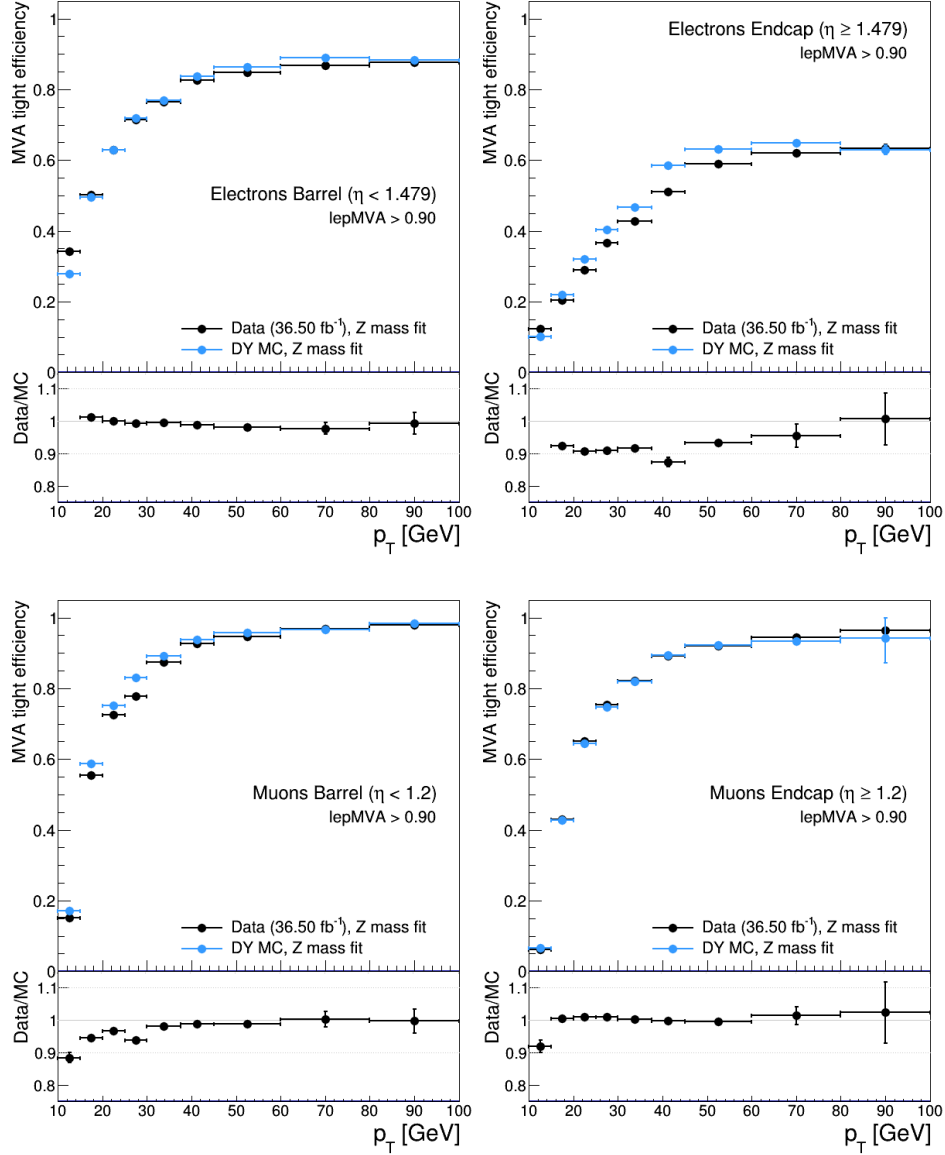


Figure 6.8: Tight vs loose selection efficiencies for electrons (top), and muons (bottom), for the $2lss$ definition, i.e., including the tight-charge requirement.

2642 The efficiency of applying the tight selection as defined in Tables 6.4 and 6.5, on the
 2643 loose leptons are determined by using a tag and probe method on a sample of Drell-
 2644 Yan enriched events. Figures 6.8 and 6.9 show the efficiencies for the $2lss$ channel and
 2645 $3l$ channel respectively. Efficiencies in the $2lss$ channel have been produced including
 2646 the tight-charge requirement, while for the $3l$ channel it is not included. Number

of passed and failed probes are determined from a fit to the invariant mass of the dilepton system. Simulation is corrected using these scale factors; note that they depends on η and p_T .

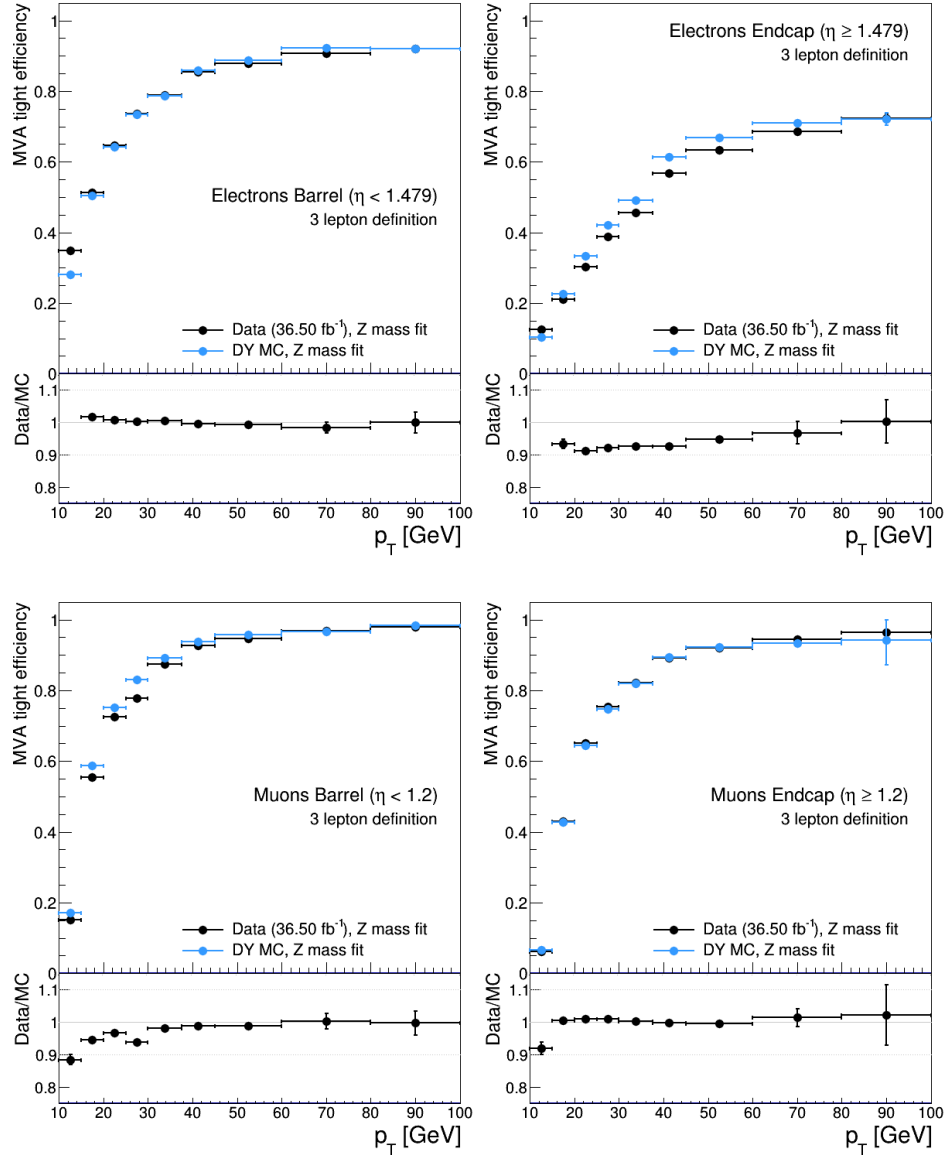


Figure 6.9: Tight vs loose selection efficiencies for electrons (top), and muons (bottom), for the $3l$ channel not including the tight-charge requirement.

2650 **6.5.3 Jets and b -jet tagging**

2651 In this analysis, jets are reconstructed by clustering PF candidates using the anti- k_t
 2652 algorithm with parameter distance $\Delta R = 0.4$; those charged hadrons that are not
 2653 consistent with the selected primary vertex are discarded from the clustering. The
 2654 jet energy is then corrected for the varying response of the detector as a function
 2655 of transverse momentum p_T and pseudorapidity η . Jets are selected for use in the
 2656 analysis only if they have $p_T > 25$ GeV and are separated from any selected leptons
 2657 by $\Delta R > 0.4$.

2658 Jets coming from the primary vertex and jets coming from pile-up vertices are
 2659 distinguished using a MVA discriminator based on the differences in the jet shapes,
 2660 in the relative multiplicity of charged and neutral components, and in the different
 2661 fraction of transverse momentum which is carried by the hardest components. Jet
 2662 tracks are also required to be compatible with the primary vertex.

2663 Jets originated from the hadronization of a b quark are selected using a MVA
 2664 likelihood discriminant which uses track-based lifetime information and reconstructed
 2665 secondary vertices (CSV algorithm). Only jets within the CMS tracker acceptance
 2666 ($\eta < 2.4$) are identified with this tool. Data samples are used to measure the efficiency
 2667 of the b -jet tagging and the probability to misidentify jets from light quarks or gluons;
 2668 in both cases the measurements are parametrized as a function of the jet p_T and η
 2669 and later used to correct differences between the data and MC simulation in the b
 2670 tagging performance, by applying per-jet weights to the simulation, dependent on
 2671 the jet p_T , η , b tagging discriminator, and flavor (from simulation truth) [151]. The
 2672 per-event weight is taken as the product of the per-jet weights, including those of the
 2673 jets associated to the leptons. The weights are derived on $t\bar{t}$ and Z+jets events.

2674 Two working points are defined, based on the CSV algorithm output: ‘*loose*’ work-

ing point ($\text{CSV} > 0.46$) with a b signal tagging efficiency of about 83% and a mistagging rate of about 8%; and *medium* working point ($\text{CSV} > 0.80$) with b -tagging efficiency of about 69% and mistagging rate of order 1% [152]. Tagging of jets from charm quarks have efficiencies of about 40% and 18% for loose and medium working points respectively. Separate scale factors are applied to jets originating from bottom/charm quarks and from light quarks in simulated events to match the tagging efficiencies measured in the data.

6.5.4 Missing Energy MET

As stated in Section 3.4.1.1, the MET vector is calculated as the negative of the vector sum of transverse momenta of all PF candidates in the event and its magnitude is referred to as E_T^{miss} . Due to pile-up interactions, the performance in determining MET is degraded; in order to correct for that, the energy from the selected jets and leptons that compose the event is assigned to the variable H_T^{miss} . It is calculated in the same way as E_T^{miss} and although it has worse resolution than E_T^{miss} , it is more robust in the sense that it does not rely on the soft part of the event. The event selection uses a linear discriminator based on the two variables given by

$$E_T^{\text{miss}}_{LD} = 0.00397 * E_T^{\text{miss}} + 0.00265 * H_T^{\text{miss}} \quad (6.6)$$

taking advantage of the fact that the correlation between E_T^{miss} and H_T^{miss} is less for events with instrumental missing energy than for events with real missing energy. The working point $E_T^{\text{miss}}_{LD} > 0.2$ was chosen to ensure a good signal efficiency while keeping a good background rejection.

2695 6.6 Event selection

2696 Events are selected considering the features of the signal process and the decay sig-
 2697 nature as described in Section 6.2. At the trigger level, events are selected to contain
 2698 either one, two, or three leptons with minimal p_T thresholds:

- 2699 • single-lepton trigger → 24 GeV for muons and at 27 GeV for electrons
- 2700 • double-lepton triggers → leading and sub-leading leptons: 17 and 8 GeV for
 2701 muons and 23 and 12 GeV for electrons.
- 2702 • three-lepton triggers → threshold on the third hardest lepton in the event: 5
 2703 and 9 GeV for muons and electrons, respectively.

2704 The offline event selection level targets the specific topology of the tHq signal
 2705 with $H \rightarrow WW$ and $t \rightarrow Wb \rightarrow l\nu b$; therefore, the resulting state is composed of three
 2706 W bosons, one b quark, and a light spectator quark at high rapidity. The selection
 2707 criteria for the two channels exploited in this analysis are summarized in Table 6.6.
 2708 This selection includes contributions from $H \rightarrow \tau\tau$ and $H \rightarrow ZZ$ as well.

Same-sign $\ell\ell$ channel	$\ell\ell\ell$ channel
have fired one of the corresponding trigger paths	
No loose leptons with $m_{\ell\ell} < 12\text{GeV}$	
One or more b tagged jets (CSV medium) $ \eta < 2.4$	
One or more non-tagged jets: central → $p_T > 25\text{ GeV}$, $\eta < 2.4$ forward → $p_T > 40\text{ GeV}$, $\eta > 2.4$	
	$E_{T,LD}^{\text{miss}} > 0.2$
Exactly two tight same-sign leptons	Exactly three tight leptons
Lepton $p_T > 25/15\text{GeV}$	Lepton $p_T > 25/15/15\text{GeV}$
Electrons are triple-charge consistent.	No OSSF lepton pair with $ m_{\ell\ell} - m_Z < 15\text{GeV}$
Muon p_T resolution: $\Delta p_T/p_T < 0.2$.	
No ee pair with $ m_{ee} - m_Z < 10\text{GeV}$	

Table 6.6: Summary of event pre-selection.

2709 In the $2lss$ channel, events with additional tight leptons are vetoed as well as those
 2710 for which a loose lepton pair has an invariant mass below 12 GeV. A threshold in p_T of
 2711 the leading and sub-leading leptons is also required. Events where the two electrons
 2712 have invariant mass within 10 GeV of the Z boson mass (Z -*veto*) are discarded in
 2713 order to reject events from DY+jets production with charge misidentified electrons.
 2714 In addition, contribution from the associated production of two W bosons of equal
 2715 charge and two light jets $W^\pm W^\pm qq$ and from same-sign W boson pairs can also be
 2716 produced in double parton scattering (DPS) processes, where each of the colliding
 2717 protons gives two partons, resulting in two hard interactions.

2718 In the $3l$ lepton channel, leptons are required to have respectively $p_T > 25\text{GeV}$, $>$
 2719 15 GeV, and > 15 GeV. Events with an opposite-sign same-flavor lepton combination
 2720 (OSSF) with invariant mass within 15 GeV of the Z boson mass are discarded in order
 2721 to reject events from $WZ + \text{jets}$ production.

2722 6.7 Background modeling and predictions

2723 The dominant background contribution is expected to arise from top quark produc-
 2724 tion processes, either $t\bar{t}$ pair production or in $t\bar{t}$ associated production with a W/Z.
 2725 Processes with production of single top quarks also contribute, mainly in the associ-
 2726 ated production with a Z boson (tZq) or when produced with both a W and a Z boson
 2727 (tZW). Background contamination from diboson processes is strongly suppressed by
 2728 imposing the Z-veto, vetoing additional leptons and requiring b -jets in the event.

2729 The selection criteria in Table 6.6 represent a relatively loose selection that allows
 2730 to maintain a large signal efficiency while suppressing the main backgrounds; thus
 2731 that selection is called *pre-selection*. The events obtained from the pre-selection are
 2732 then used to extract the signal contribution in a second analysis step, using BDT dis-

2733 discriminators against the main backgrounds of $t\bar{t}W/t\bar{t}Z$ and non-prompt leptons from
 2734 $t\bar{t}$. The shape of the discriminator variables is then fit to the observed data distribu-
 2735 tion to estimate the signal and background yields, simultaneously for all channels.

2736 Irreducible backgrounds are reliably estimated from MC simulated events; there-
 2737 fore, in this analysis all backgrounds involving prompt leptons are estimated in this
 2738 way. Reducible backgrounds, like non-prompt lepton backgrounds, are not well pre-
 2739 dicted by simulation, hence, they are estimated using data-driven methods.

2740 6.7.1 $t\bar{t}V$ and diboson backgrounds

2741 Backgrounds from $t\bar{t}W$ and $t\bar{t}Z$ processes are estimated using simulated events, cor-
 2742 rected for data/MC differences and inefficiencies (trigger and lepton selection) in the
 2743 same way as signal events. Their production cross sections are calculated at NLO
 2744 order of QCD and EWK, considering theoretical uncertainties from unknown higher
 2745 orders of 12% for $t\bar{t}W$ and 10% for $t\bar{t}Z$. Additional uncertainties arise from the knowl-
 2746 edge of PDFs and α_s of about 4% each for $t\bar{t}W$ and $t\bar{t}Z$.

2747 The diboson contribution is also estimated from simulated events; however, the
 2748 overall normalization of this process is obtained from a dedicated control region.
 2749 The motivation behind that strategy is that even though the measured inclusive
 2750 cross section for diboson processes (WZ, ZZ) is in good agreement with the NLO
 2751 calculations [149], that agreement is perturbed when leptonic Z decays and hadronic
 2752 jets in the final state are required; those requirements are precisely the ones that
 2753 make the diboson production a background for the tHq signal. Thus, by using a
 2754 dedicated control region dominated by WZ production⁴, the overall normalization is
 2755 constrained.

⁴ ZZ background is strongly reduced by the cut on MET.

2756 The control region is defined by the presence of at least three leptons, of which
 2757 one opposite-sign pair must be compatible with a Z boson decay, i.e., invert the Z-
 2758 veto which makes the control region orthogonal to signal region; the b-jet tagging
 2759 requirements is also inverted with respect to the signal region, i.e., require two not
 2760 b -jets. A scale factor is extracted from the predicted distribution of WZ events in the
 2761 control region, and the observed data, while keeping other processes fixed; this factor
 2762 is used to scale the diboson prediction in the signal selection region. More details
 2763 about the procedure used can be found in Reference [149] from where the scale factor
 2764 is taken.

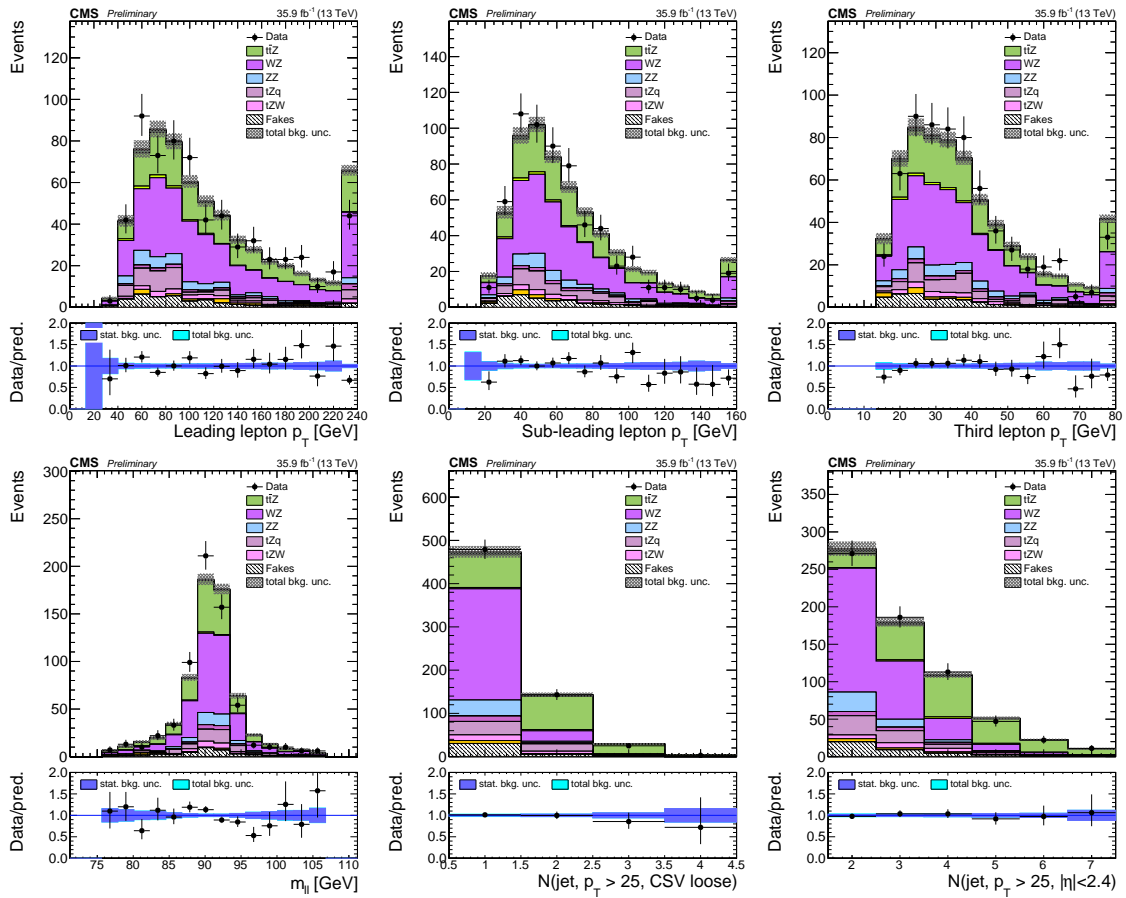


Figure 6.10: Kinematic distributions in the diboson control region.

2765 In order to test the usability of the diboson background scale factor in this analysis,

2766 a Z-enriched control region⁵ was defined by inverting the Z-veto and requiring exactly
 2767 three tight leptons with $p_T > 25/15/15$ GeV, one or more jets passing the CSVv2 loose
 2768 working point and less than four central jets. Figure 6.10 shows the distribution of
 2769 three variables in the diboson control region; the good agreement between MC and
 2770 data motivates the adoption of the diboson background scale factor.

2771 Most of the diboson events passing the signal selection contain jets from light
 2772 quarks and gluons that are incorrectly tagged as b -jets; it makes the estimate mainly
 2773 sensitive to the experimental uncertainty in the mis-tag rate rather than the theore-
 2774 tical uncertainty in the jet flavor composition. The overall uncertainty assigned to
 2775 the diboson prediction is estimated from the statistical uncertainty due to the limited
 2776 sample size in the control region (30%), the residual background in the control region
 2777 (20%), the uncertainties on the b -tagging rate (10-40%), and from the knowledge of
 2778 PDFs and the theoretical uncertainties of the extrapolation (up to 10%).

2779 **6.7.2 Non-prompt and charge mis-ID backgrounds**

2780 The non-prompt lepton background contribution to the final selection is estimated
 2781 using the fake factor method. The main idea of the method is to define a control
 2782 region of events enriched in the background to estimate and determine a factor that
 2783 relates (extrapolates) these events to those in the signal region. The method is data-
 2784 driven in the sense that the control sample is selected from data, and the extrapolation
 2785 factor is measured from data.

2786 In the signal region of this analysis, non-prompt leptons are predominantly pro-
 2787 duced in $t\bar{t}$ events, with a much smaller contribution, from Drell-Yan production;
 2788 therefore, the control region also known as *application region*, is defined by modifying
 2789 the event selection criteria in such a way that most of the events after selection are

⁵ This control region is different to the one used to find the scale factor.

2790 $t\bar{t}$ events and thus the misidentification rate is increased. The application regions
 2791 for electrons and muons are defined by the fakeable object definitions in Tables 6.4
 2792 and 6.5. Since the fakeable definition is a loosened version of the tight definition, in
 2793 the context of fake rates the fakeable definition it becomes the loose selection.

2794 The ratio between the number of events that pass both, the loose and tight se-
 2795 lections, and the number of events that pass the loose selection but fail the tight
 2796 one, corresponds to the *fake factor/fake rate* (f). The measurement of the fake fac-
 2797 tor is made using two background dominated data samples, collected with dedicated
 2798 triggers, as a function of p_T and $|\eta|$ and separately for muons and electrons:

- 2799 • A sample dominated by QCD multijet events, collected using single lepton trig-
 2800 gers at relatively high p_T thresholds. It is used to extract ratios for lepton
 2801 candidates with p_T above 30 GeV.
- 2802 • A sample dominated by $Z + \text{jets}$ events, where the two high p_T leptons resulting
 2803 from the Z decay are used to trigger the events without biasing the p_T spectrum
 2804 of a third lepton at low transverse momentum. It is used to determine the ratios
 2805 for low p_T leptons.

2806 Processes like $W + \text{jets}$, $Z + \text{jets}$, WZ and ZZ produce prompt leptons that
 2807 contaminate the samples; thus, they are suppressed by vetoing additional leptons in
 2808 the selection, and the residual contamination is then subtracted using the transverse
 2809 mass as a discriminating variable.

2810 The extrapolation from the application region to the signal region is performed
 2811 by weighting the events in the application region using the fake factor according to
 2812 the following rules:

- 2813 • events with one lepton failing the tight criteria are weighted with the factor
 2814 $\frac{f}{(1-f)}$ for the estimate to the signal region.
- 2815 • events with two leptons (i,j) failing the tight criteria are weighted with the factor
 2816 $-\frac{f_i f_j}{(1-f_i)(1-f_j)}$ for the estimate to the signal region.
- 2817 • events with three leptons (i,j,k) failing the tight criteria are weighted with the
 2818 factor $\frac{f_i f_j f_k}{(1-f_i)(1-f_j)(1-f_k)}$ for the estimate to the signal region.

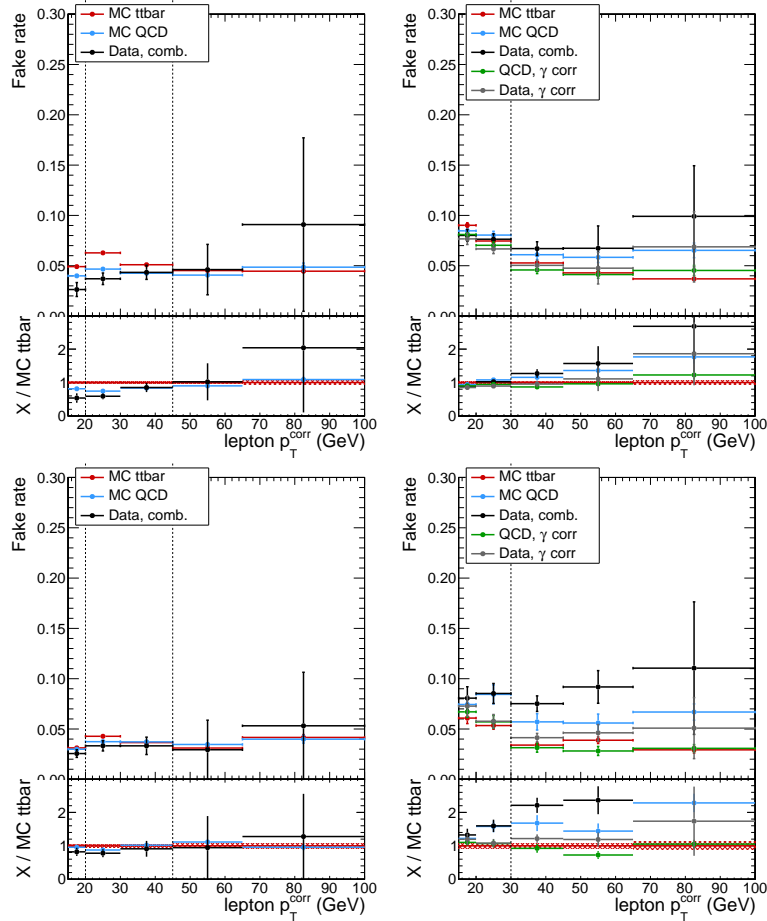


Figure 6.11: Fake rate measurement in events in data for muons (left column) and electrons (right column). Predictions from simulated events in the measurement region (blue) and from non-prompt leptons in $t\bar{t}$ (red) are included for comparison. Top row is for $|\eta| < 2.5$ and bottom row for $|\eta| > 2.5$.

2819 Figure 6.11 shows the fake rates for electrons and muons used in this analysis
 2820 which were taken from the studies in Reference [149].

2821 The resulting prediction of the event yield in the signal selection carries an uncer-
 2822 tainty of 30-50% which is composed of the statistical uncertainty in the measurement
 2823 of the fake rates due to prescaling of lepton triggers, the uncertainty in the subtraction
 2824 of residual prompt leptons from the control region, and from testing the closure of the
 2825 method in simulated background events; hence, it is one of the dominant limitations
 2826 on the performance of multilepton analyses in general and this analysis in particular.

2827 Finally, an additional source of background arises in the $2lss$ channel from events
 2828 with an originally opposite-sign lepton pair for which the charge of one of the leptons
 2829 is misidentified (*charge mis-ID*); usually this happens because of the conversion of
 2830 hard bremsstrahlung photons emitted from the initial lepton, hence, it is more likely
 2831 to happen for electrons than for muons.

2832 The charge mis-ID background is estimated from the yield of opposite-sign event
 2833 in the signal region by measuring the charge mis-ID probability in same-sign and
 2834 opposite-sign events compatible with a Z boson decay, in several bins of p_T and η ,
 2835 and weighting events with opposite-sign leptons in the signal selection.

Data	$10 \leq p_T < 25$ GeV	$25 \leq p_T < 50$ GeV	$50 \text{ GeV} \leq p_T$
$0 \leq \eta < 1.48$	0.0442 ± 0.0011	0.0179 ± 0.0004	0.0262 ± 0.0020
$1.48 \leq \eta < 2.5$	0.1329 ± 0.0066	0.1898 ± 0.0014	0.3067 ± 0.0113
<hr/>			
MC			
$0 \leq \eta < 1.48$	0.0378 ± 0.0016	0.0222 ± 0.0003	0.0233 ± 0.0015
$1.48 \leq \eta < 2.5$	0.0956 ± 0.0044	0.2108 ± 0.0027	0.3157 ± 0.0018

Table 6.7: Electron charge mis-ID probabilities (in percent), determined in data (top) and Drell-Yan MC (bottom) [149].

2836 The charge mis-ID probability is found to be negligible for this analysis for muons,
 2837 whereas for electrons it ranges from about 0.02% in the barrel section ($|\eta| < 1.48$)

2838 up to about 0.35% in the detector endcaps ($1.48 < |\eta| < 2.5$). as shown in Table 6.7
 2839 and Figure 6.12.

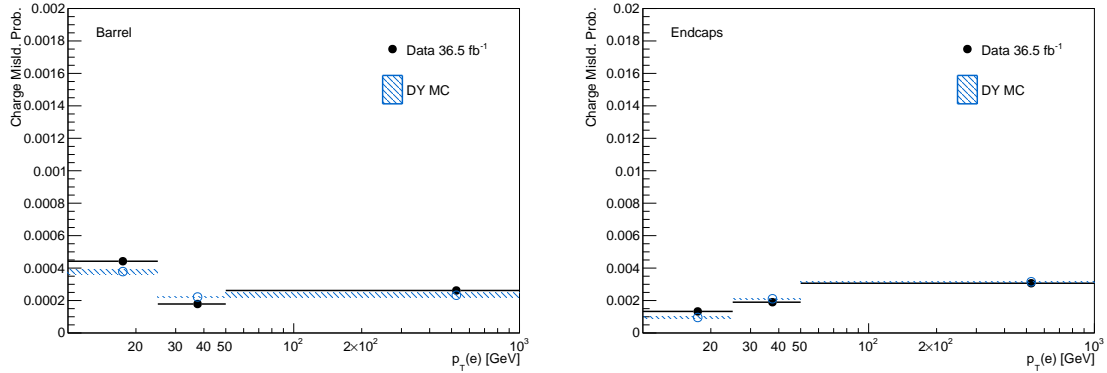


Figure 6.12: Electron charge mis-ID probabilities as a function of p_T for $|\eta| < 2.5$ (left) and $|\eta| < 2.5$ (right) [149].

2840 The contribution from charge mis-ID electrons in signal selection of this analysis
 2841 comes mainly from $t\bar{t}$ and Drell-Yan events. The systematic uncertainty of the nor-
 2842 malization of the charge mis-id. estimate is evaluated at about 30%, arising from a
 2843 slight disagreement of the mis-ID. probability between data and simulation. Given
 2844 that it only affects the $e\mu$ channel, its impact on the final sensitivity is very limited.

2845 6.8 Pre-selection yields

2846 The expected and observed event yields of the pre-selection are shown in Table 6.8;
 2847 Figure 6.13 shows the distributions of some relevant kinematic variables, normalized
 2848 to the cross section of the respective processes and to the integrated luminosity. The
 2849 remaining variables distributions are shown in Appendix B.1.

2850 For the tH and $t\bar{t}H$ processes, the largest contribution comes from Higgs decays
 2851 to WW (about 75%), followed by $\tau\tau$ (about 20%) and ZZ (about 5%). Other Higgs

	3ℓ	$\mu^\pm\mu^\pm$	$e^\pm\mu^\pm$	$e^\pm e^\pm$
$t\bar{t}W$	22.50 ± 0.35	68.03 ± 0.61	97.00 ± 0.71	29.63 ± 0.39
$t\bar{t}Z/\gamma^*$	32.80 ± 1.79	25.89 ± 1.12	64.82 ± 2.42	28.74 ± 1.70
WZ	8.22 ± 0.86	15.07 ± 1.19	26.25 ± 1.57	9.31 ± 0.93
ZZ	1.62 ± 0.33	1.16 ± 0.29	2.86 ± 0.45	1.09 ± 0.27
$W^\pm W^\pm qq$	—	3.96 ± 0.52	6.99 ± 0.69	2.19 ± 0.37
$W^\pm W^\pm(\text{DPS})$	—	2.48 ± 0.42	4.17 ± 0.54	0.81 ± 0.24
VVV	0.42 ± 0.16	2.99 ± 0.34	4.85 ± 0.43	1.19 ± 0.21
ttt	1.84 ± 0.44	2.32 ± 0.45	4.06 ± 0.57	0.89 ± 0.31
tZq	3.92 ± 1.48	5.77 ± 2.24	10.73 ± 3.03	7.56 ± 1.72
tZW	1.70 ± 0.12	2.13 ± 0.13	3.91 ± 0.18	1.13 ± 0.10
γ conversions	7.43 ± 1.94	—	23.81 ± 6.04	9.87 ± 4.17
Non-prompt	25.61 ± 1.26	80.94 ± 2.02	135.34 ± 2.83	47.72 ± 1.79
Charge mis-ID	—	—	58.50 ± 0.31	44.52 ± 0.31
All backgrounds	106.05 ± 3.45	210.74 ± 3.61	443.30 ± 8.01	184.65 ± 5.29
tHq ($\kappa_t = -1.0$)	7.48 ± 0.14	18.48 ± 0.22	27.41 ± 0.27	8.47 ± 0.15
tHW ($\kappa_V = -1.0$)	7.38 ± 0.16	7.72 ± 0.17	11.23 ± 0.20	3.66 ± 0.11
$t\bar{t}H$	18.29 ± 0.41	24.18 ± 0.48	35.21 ± 0.58	11.07 ± 0.32
Data ($35.9 fb^{-1}$)	127	280	525	208

Table 6.8: Expected and observed yields for $35.9 fb^{-1}$ after the pre-selection in all final states. Uncertainties are statistical only.

2852 production modes contribute negligible event yields (< 5% of the $tH+t\bar{t}H$ yield) as
 2853 shown in Table 6.9.

2854 A significant fraction of selected data events (about 50% in the dilepton channels,
 2855 and about 80% in the trilepton channel) also passes the selection used in the dedicated
 2856 search for tH in multilepton channels [149]. This is particularly important when
 2857 considering a possible combination of the measurements from both studies. More
 2858 details about the overlap between this both analyses are presented in Appendix E.

2859 6.9 Signal discrimination

2860 The production cross section for the signal processes tHq , tHW , and $t\bar{t}H$ is only
 2861 about 600 fb (the enhancement provided by inverted couplings, $\kappa_t = -1$ almost double

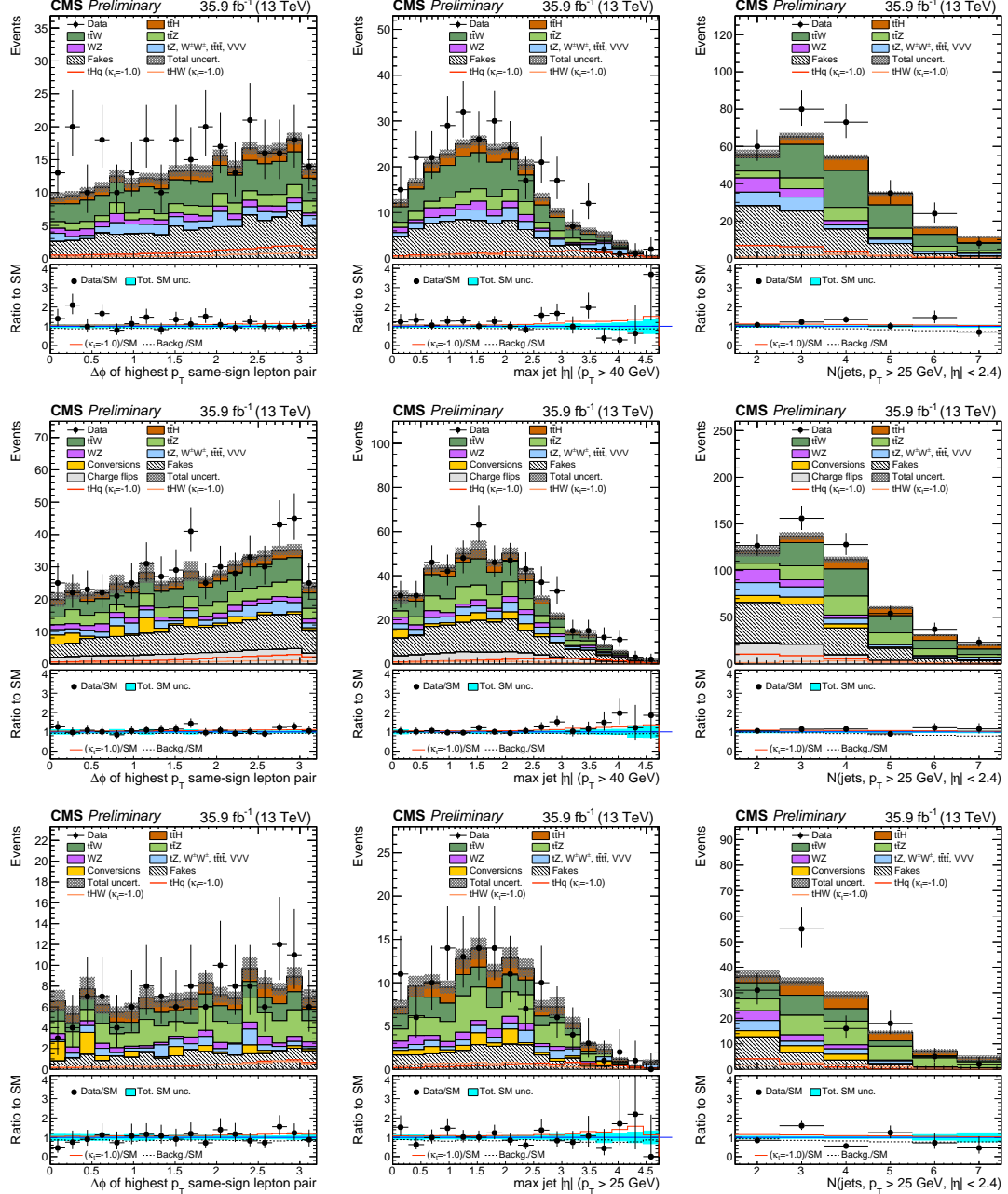


Figure 6.13: Distributions of discriminating variables for the event pre-selection for the same-sign $\mu^{\pm}\mu^{\pm}$ channel (top row), the same-sign $e^{\pm}\mu^{\pm}$ channel (middle row) and three lepton channel (bottom row), normalized to 35.9 fb^{-1} , before fitting the signal discriminant to the observed data. Uncertainties are statistical and unconstrained (pre-fit) normalization systematics. The shape of the two tH signals for $\kappa_t = -1.0$ is shown, normalized to their respective cross sections for $\kappa_t = -1.0, \kappa_V = 1.0$.

	3ℓ	$\mu^\pm\mu^\pm$		
tHq (Inclusive)	6.57	100.0%	17.38	100.0%
$tHq(H \rightarrow WW)$	4.84	73.9%	13.33	76.9%
$tHq(H \rightarrow \tau\tau)$	1.04	15.9%	3.62	20.6%
$tHq(H \rightarrow ZZ)$	0.48	7.2%	0.37	2.2%
$tHq(H \rightarrow \mu\mu)$	0.21	3.0%	0.04	0.2%
$tHq(H \rightarrow \gamma\gamma)$	< 0.01	0.1%	0.02	0.1%
$tHq(H \rightarrow bb)$	< 0.01	< 0.1%	0.01	< 0.1%
tHW (Inclusive)	7.32	100.0%	7.62	100.0%
$tHW(H \rightarrow WW)$	5.50	76.9%	5.60	74.1%
$tHW(H \rightarrow \tau\tau)$	1.40	20.6%	1.81	23.1%
$tHW(H \rightarrow ZZ)$	0.31	2.2%	0.21	2.7%
$tHW(H \rightarrow \mu\mu)$	0.12	0.2%	0.01	0.1%
$tHW(H \rightarrow \gamma\gamma)$	< 0.01	< 0.1%	< 0.01	< 0.1%
$tHW(H \rightarrow bb)$	< 0.01	< 0.1%	< 0.01	< 0.1%

Table 6.9: Signal yields split by decay channels of the Higgs boson. Forward jet p_T cut at 25 GeV.

it), resulting in a small signal to background ratio even for a tight selection. A multivariate method is hence employed to train discriminators to separate tH signal events from the dominant background events.

6.9.1 MVA classifiers evaluation

Several MVA classifier algorithms were evaluated in order to determine the most appropriate method for this analysis⁶. The comparison is based on the performance of the classifiers, encoded in the plot of the background rejection as a function of the signal efficiency (ROC curve). The top row of Figure 6.14 shows the ROC curves for the several methods evaluated; two separated training were performed in the $3l$ channel: against $t\bar{t}$ (right) and $t\bar{t}V$ (left) processes.

⁶ The choice of the tested algorithms was based on the recommendations provided by the official TMVA user guide, the experience from previous analyses and considering the expertise of the members of the tHq and $t\bar{t}H$ analyses groups. Only the BDT classifier is described in this thesis and a detailed description of all available methods can be found in Reference [127]

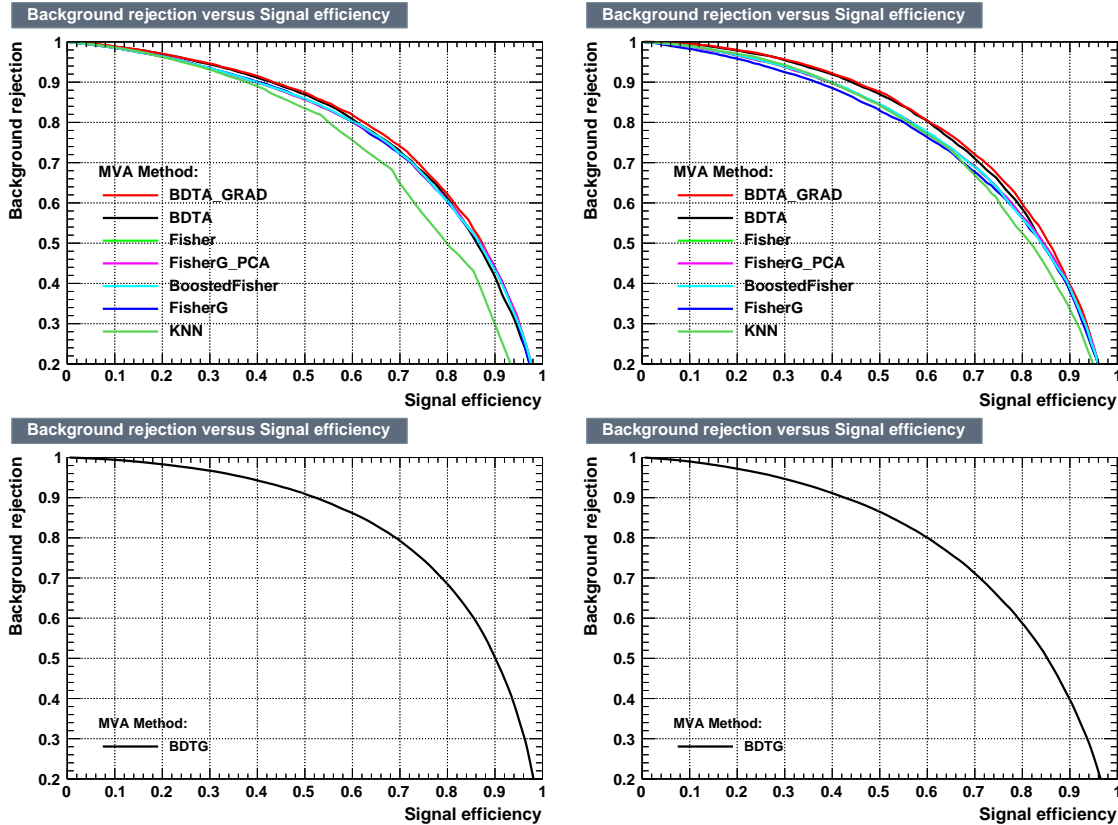


Figure 6.14: Top: Background rejection vs signal efficiency (ROC curves) for various MVA classifiers in the $3l$ channel for training against $t\bar{V}$ (left) and $t\bar{t}$ (right). Bottom: background rejection vs signal efficiency (ROC curve) in the $2lss$ channel for a single discriminator: BDTG, against $t\bar{V}$ (left) and $t\bar{t}$ (right).

2872 In both cases, the gradient boosted decision tree $BDTG$ ($BDTA_GRAD$ in the
 2873 plot) classifier offers the best results, followed by the adaptive BDT classifier ($BDTA$);
 2874 the several Fisher classifiers tested, which differ in their parameters and/or boosting
 2875 method, they offer similar performance among them, while the k-Nearest Neighbour
 2876 (kNN) classifier performance is below the rest of the classifiers. The corresponding
 2877 ROC curves and in the $2lss$ channel for trainings against $t\bar{V}$ (left) and $t\bar{t}$ (right)
 2878 processes are shown in the bottom row of Figure 6.14; the BDTG performance is
 2879 similar to that in the $3l$ channel.

2880 **6.9.2 Discriminating variables**

2881 The classifier chosen to separate the tHq signal from the main backgrounds is the
 2882 BDTG classifier, trained on simulated signal and background events. The samples
 2883 used in the training are the tHq sample in Table 6.2, the samples in the third section
 2884 of table A.4 and the samples marked with an * in the same table.

2885 As explained in Section 5.1.1, a set of discriminating variables are given as input to
 2886 the BDTG which combines the individual discrimination power of each input variable
 2887 to produce a discriminator with the maximum discrimination power. Table 6.10 lists
 2888 the input variables used in the BDTG trainings for this analysis. The same set of
 2889 input variables was used to produce the plots for MVA classifiers evaluation.

Variable name	Description
nJet25	Number of jets with $p_T > 25$ GeV, $ \eta < 2.4$
nJetEta1	Number of jets with $ \eta > 1.0$, non-CSV-loose
MaxEtaJet25	Max. $ \eta $ of any (non-CSV-loose) jet with $p_T > 25$ GeV
detaFwdJetClosestLep	$\Delta\eta$ forward light jet and closest lepton
detaFwdJetBJet	$\Delta\eta$ forward light jet and hardest CSV loose jet
detaFwdJet2BJet	$\Delta\eta$ forward light jet and second hardest CSV loose jet
Lep3Pt/Lep2Pt	p_T of the 3 rd lepton (2 nd for ss2l)
totCharge	Sum of lepton charges
minDRll	Min ΔR any two leptons
dphiHighestPtSSPair	$\Delta\phi$ of highest p_T same-sign lepton pair

Table 6.10: BDTG input variables. First section lists variables related to jet multiplicities; second section lists variables related to forward jet activity, and third section lists variables related to lepton kinematics.

2890 Plots in Figure 6.15 shows the BDTG input variables distributions for the signal
 2891 and background samples, in the 3 l channels.

2892 All the input variables have some discrimination power, however, that power is
 2893 bigger for some of them; for instance, the third lepton p_T plot (top left in Figure 6.15)
 2894 shows some discrimination power against WZ and VVV backgrounds for which there
 2895 is a peak around 30 GeV while tHq peak around 18 GeV; although the discrimination

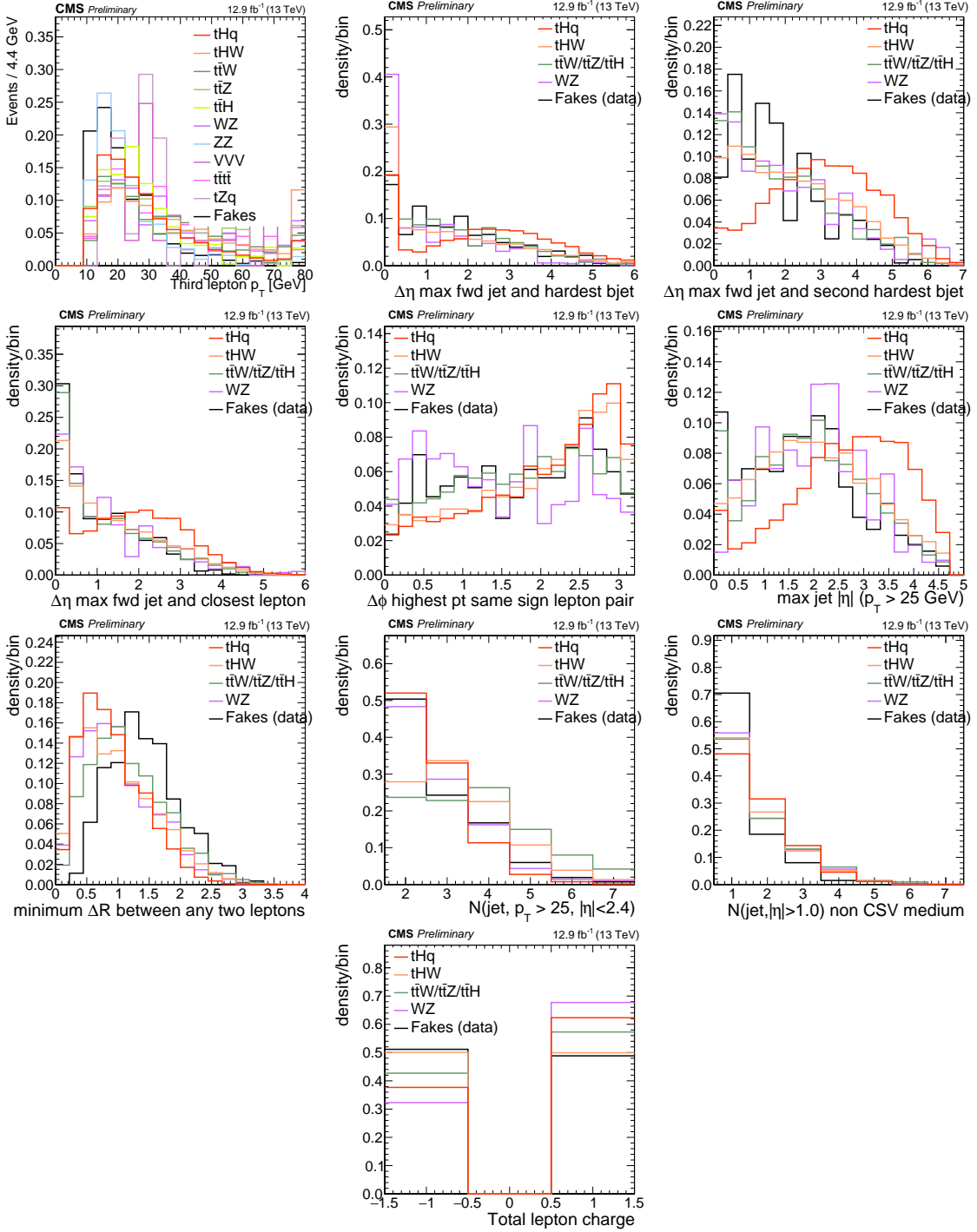


Figure 6.15: Distributions of the BDTG classifier input variables (not normalized) for signal discrimination in the $3l$ channel.

power does not cover all the backgrounds, it counts for the final discriminator. A similar situation can be seen in the plot for the number of jets (row three, column two); $t\bar{t}W$, $t\bar{t}Z$ and $t\bar{t}H$ processes tend to have more jets compared to the tHq process. The discrimination power is more evident in other plots like in the plot of the maximum $|\eta|$ of the jets in the event (row two, column three). The same or equivalent input variables are found to be performing well for both $3l$ and $2lss$ channels. Figure B.4 shows the corresponding input variables distribution plots for the $2lss$ channel.

Discrimination power from BDTG classifier

The Discrimination power of the input variables can also be evaluated from the BDTG training, exclusively for the training samples, i.e., dominant backgrounds ($t\bar{t}$ and $t\bar{t}V$); the training samples are submitted to the selection cuts on Table 6.6.

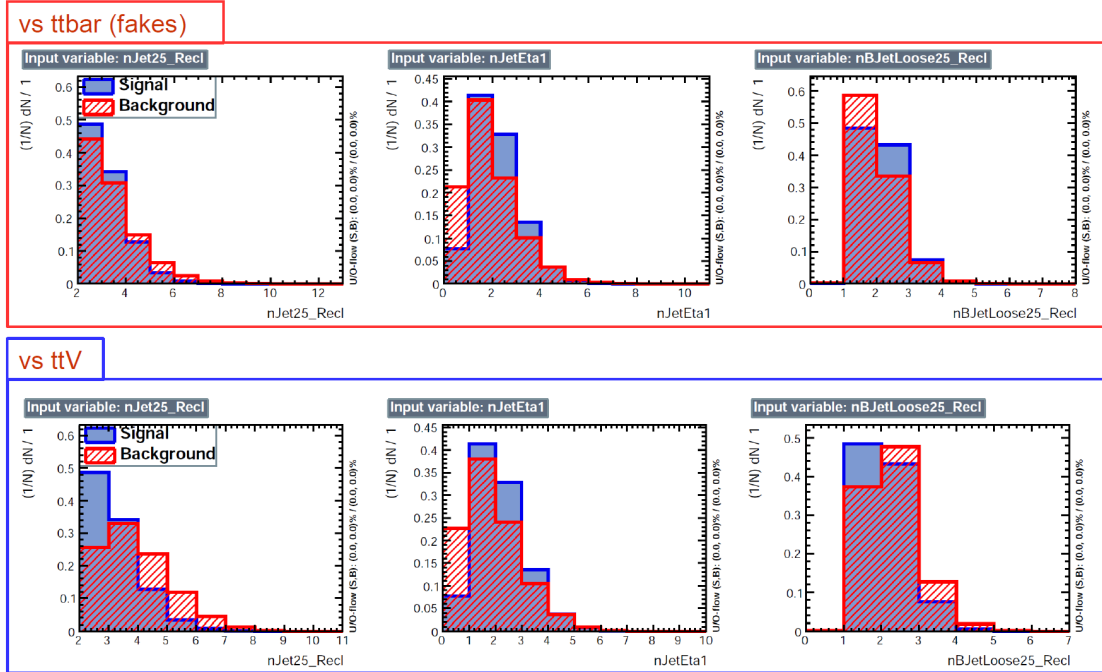


Figure 6.16: BDT input variables as seen by BDTG classifier for the $3l$ channel, tHq signal(blue) discriminated against $t\bar{t}V$ background (red).

Figure 6.16 shows the comparison between input variables for the two trainings in the $3l$ channel; it reveals that some variables show opposite behavior for the two background sources, which results in potentially screening the discrimination power if they were to be used in a single discriminant, i.e., if the training would join $t\bar{t}$ and $t\bar{t}V$. For some other variables the distributions are similar in both background cases. In contrast to the distributions in Figure 6.15 only the dominant backgrounds are included; however, the discrimination power agrees among plots.

Figures in the Appendix B.5, B.6, B.7, and B.8 show the input variables distributions for the $2lss$ and $3l$ channel as seen by the BDTG classifier.

Input variables correlations

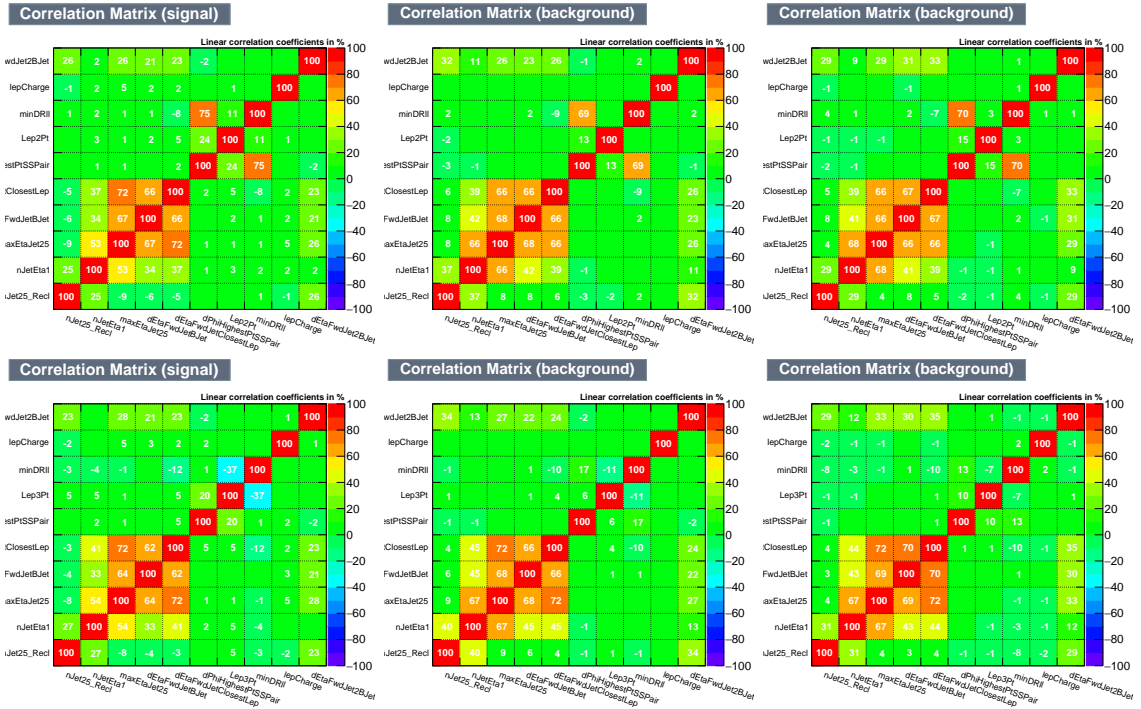


Figure 6.17: Signal (left), $t\bar{t}$ background (middle), and $t\bar{t}V$ background (right.) correlation matrices for the input variables in the BDTG classifier for the $2lss$ (top) and $3l$ (bottom) channels.

From Table 6.10, it is clear that the input variables are correlated to some extend.

2918 These correlations play an important role for some MVA methods like the Fisher
 2919 discriminant method in which the first step consist of performing a linear transfor-
 2920 mation to an phase space where the correlations between variables are removed. In
 2921 the case of BDT, correlations do not affect the performance. Figure 6.17 shows the
 2922 linear correlation coefficients for signal and background for the two training cases (the
 2923 signal values are identical by construction). As expected, strong correlations appears
 2924 for variables related to the forward jet activity.

2925 6.9.3 BDTG classifiers response

2926 After the training stage, the BDTG classifier is tested to ensure its ability to discrim-
 2927 inate between simulated signal and background events. The BDTG classifier output
 2928 distributions for signal and backgrounds in the $3l$ channel are shown in Figure 6.18.
 2929 As expected, a good discrimination power is obtained using default discriminator
 2930 parameter values; some overtraining is also visible.

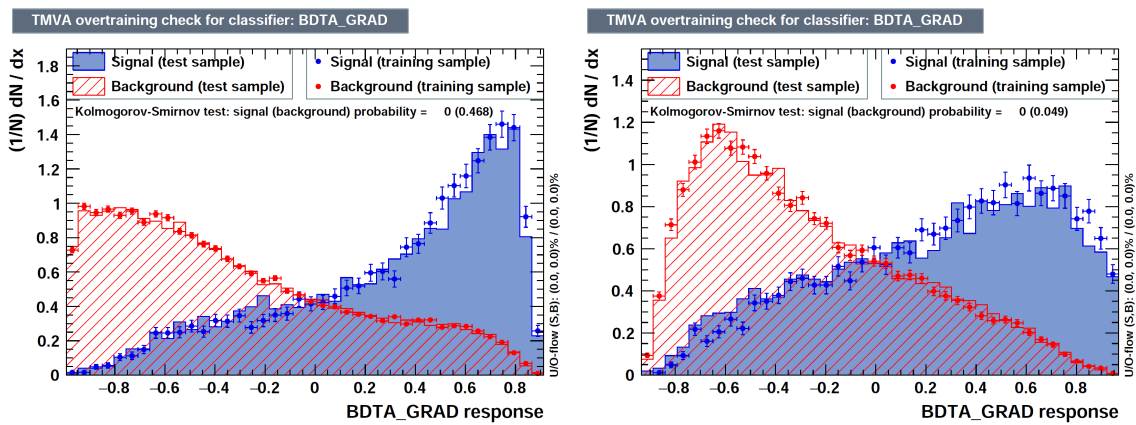


Figure 6.18: BDTG classifier output for trainings against $t\bar{t}V$ (left) and $t\bar{t}$ (right). Default BDTG parameters have been used.

2931 In order to explore further optimization in the BDTG performance, several changes
 2932 from the default BDTG parameters were tested; Table 6.11 list the set of parameters
 2933 found to be most discriminant with minimal overtraining as shown in Figure 6.19.

TMVA.Types.kBDT		
Option	Default	Used
NTrees	200	800
BoostType	AdaBoost	Grad
Shrinkage	1	0.1
nCuts	20	50
MaxDepth	3	

Table 6.11: Configuration used in the final BDTG training. Parameters not listed were not tested.

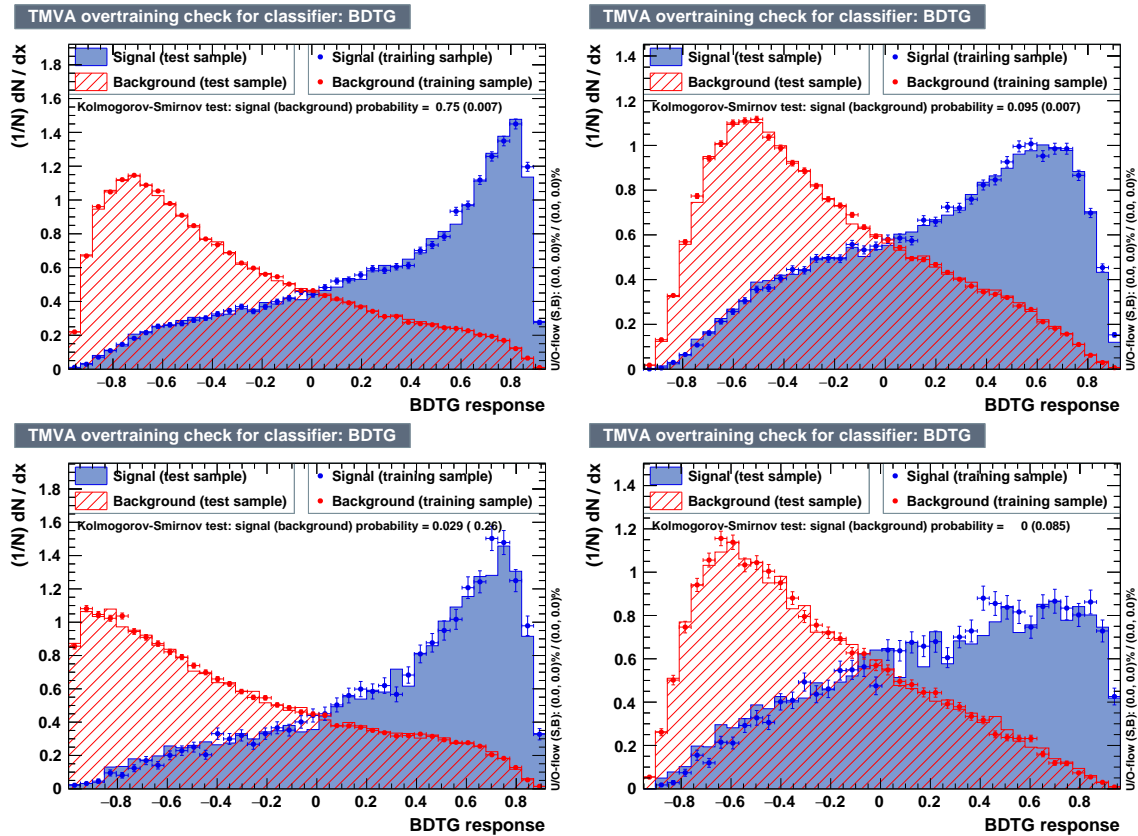


Figure 6.19: BDTG classifiers output for training against $t\bar{t}V$ (left) and $t\bar{t}$ (right) for $2lss$ channel(top) and $3l$ channel (bottom) .

2934 The ranking of the input variables by their importance in the classification process
 2935 is shown in Table 6.12; for both trainings the rankings show almost the same 5
 2936 variables in the first places.

$t\bar{t}$ training		
Rank	Variable	
1	minDRll	dEtaFwdJetBJet
2	dEtaFwdJetClosestLep	Lep3Pt
3	dEtaFwdJetBJet	maxEtaJet25
4	dPhiHighestPtSSPair	dEtaFwdJet2BJet
5	Lep3Pt	dEtaFwdJetClosestLep
6	maxEtaJet25	minDRll
7	dEtaFwdJet2BJet	dPhiHighestPtSSPair
8	nJetEta1	nJet25_Recl
9	nJet25_Recl	nJetEta1
10	lepCharge	lepCharge
$t\bar{t}V$ training		
Rank	Variable	
1	dEtaFwdJetClosestLep	maxEtaJet25
2	minDRll	dEtaFwdJet2BJet
3	maxEtaJet25	dEtaFwdJetBJet
4	dPhiHighestPtSSPair	Lep2Pt
5	Lep2Pt	dEtaFwdJetClosestLep
6	dEtaFwdJetBJet	minDRll
7	dEtaFwdJet2BJet	nJet25_Recl
8	nJetEta1	dPhiHighestPtSSPair
9	nJet25	nJetEta1
10	lepCharge	lepCharge

Table 6.12: Input variables ranking for BDTG classifiers for the trainings in the $2lss$ channel (first section) and $3l$ channel (second section). For both trainings the rankings show almost the same 5 variables in the first places.

2937 6.9.4 Additional discriminating variables

2938 Given that the forward jet in background processes could be originated from pileup,
 2939 two additional discriminating variables accounting for that were tested. These addi-
 2940 tional variables describe the forward jet momentum (fwdJetPt25) and the forward jet
 2941 identification(fwdJetPUID); their distributions in the $3l$ channel are shown in Fig-
 2942 ure 6.20. The forward jet identification distribution show that for both, signal and
 2943 background, jets are mostly originated in the primary vertex.

2944 The testing was performed by including in the BDTG input one variable at a time,
 2945 so the discrimination power of each variable can be evaluated individually, and then
 2946 both simultaneously. fwdJetPUID was ranked in the last place in importance (11) in
 2947 both training ($t\bar{t}V$ and $t\bar{t}$) while fwdJetPt25 was ranked 3 in the $t\bar{t}V$ training and 7 in

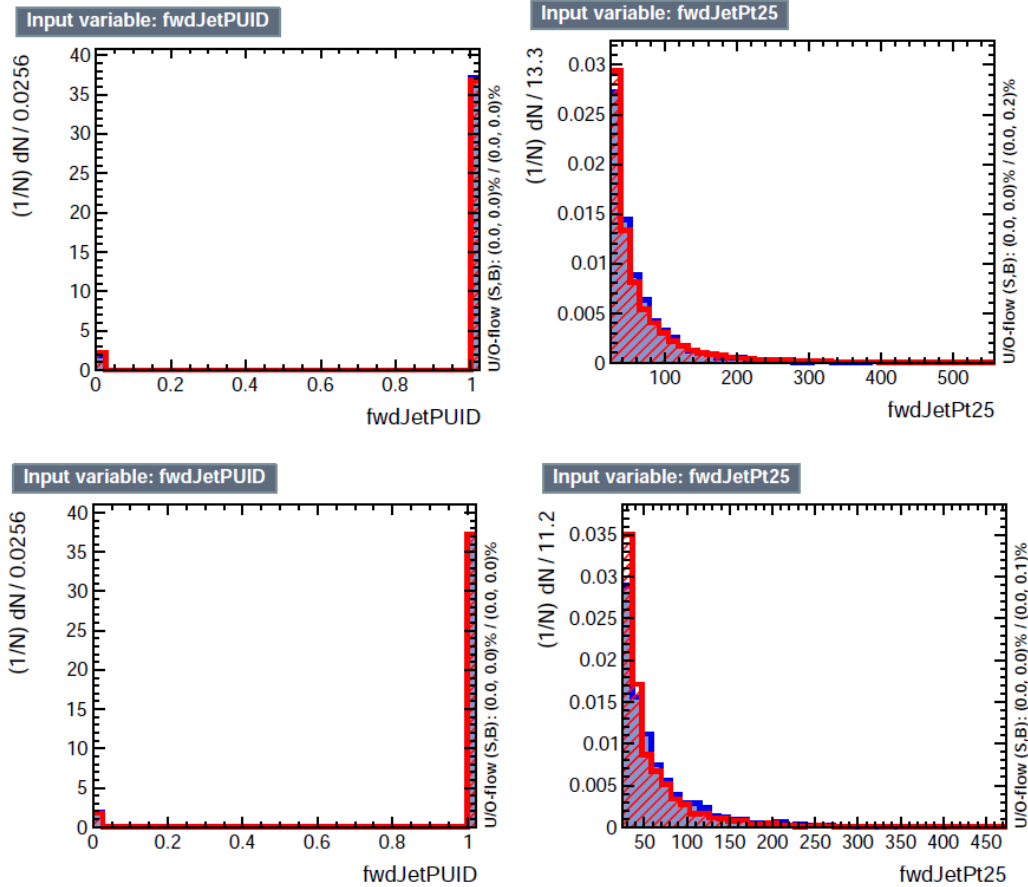


Figure 6.20: Additional discriminating variables distributions for $t\bar{t}V$ training (top row) and $t\bar{t}$ training (bottom row) in the $3l$ channel. The origin of the jets in the forward jet identification distribution is tagged as 0 for *pileup jets* while *primary vertex jets* are tagged as 1.

2948 the $t\bar{t}$ training. When training using 12 variables, `fwdJetPt25` was ranked 5 and 7 in
 2949 the $t\bar{t}V$ and $t\bar{t}$ trainings respectively, while `fwdJetPUID` was ranked 12 in both cases.
 2950 The improvement in the discrimination performance provided by the additional
 2951 variables is about 1%, so it was decided not to include them in the procedure. Table
 2952 6.13 show the ROC-integral for all the testing cases performed.

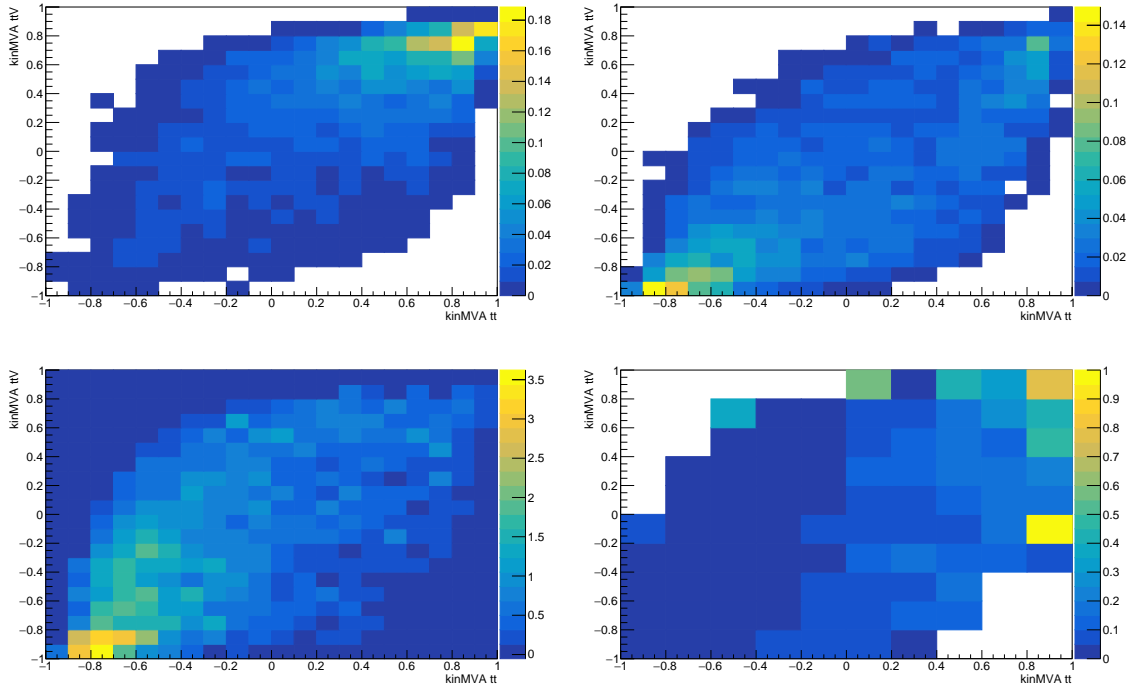


Figure 6.21: BDT classifier output planes (training vs $t\bar{t}$ on x-axis and vs $t\bar{t}V$ on y-axis) for the tHq and tHW signals (top row), and for the combined backgrounds (bottom left). Bottom right: S/B ratio (combining tHq and tHW) in the same plane. Plots are for $3l$ channel.

2953 6.9.5 Signal extraction procedure

2954 Once the two BDTG classifiers, introduced in the previous section, are trained against
 2955 the dominant backgrounds in each channel, they are used to classify the events in the
 2956 samples; their outputs are then used to evaluate the signal cross section limits in a

	ROC-integral	
	$t\bar{t}V$	$t\bar{t}$
base 10 var	0.848	0.777
+ fwdJetPUID	0.849	0.777
+ fwdJetPt25	0.856	0.787
12 var	0.856	0.787

Table 6.13: ROC-integral for all the testing cases performed in the evaluation of the additional variables discriminating power. The improvement in the discrimination performance provided by the additional variables is about 1% .

2957 fit to the classifier shape. Figure 6.21 shows the expected output distributions in a
 2958 2D plane of one training vs. the other, i.e., $t\bar{V}$ vs. $t\bar{t}$. Top row shows the 2D planes
 2959 for tHq and tHW signals, while the bottom left plot shows the corresponding 2D
 2960 plane for the combined backgrounds, which are evaluated as in the final background
 2961 prediction, i.e., these are not the samples used in the BDTG training and this includes
 2962 data-driven backgrounds. The signal (combining of tHq and tHW) to background
 2963 ratio (S/B) is showed in the bottom right plot of Figure 6.21.

2964 Each event is now classified into one of ten 2D-bins according to its position in the
 2965 plane, as shown in Figure 6.22. The number of bins is chosen such that no bins are
 2966 entirely empty for any process. The bin boundary positions and number of bins have
 2967 been studied and optimized with respect to the expected limit on the signal strength
 2968 (see Sec. 6.9.6).

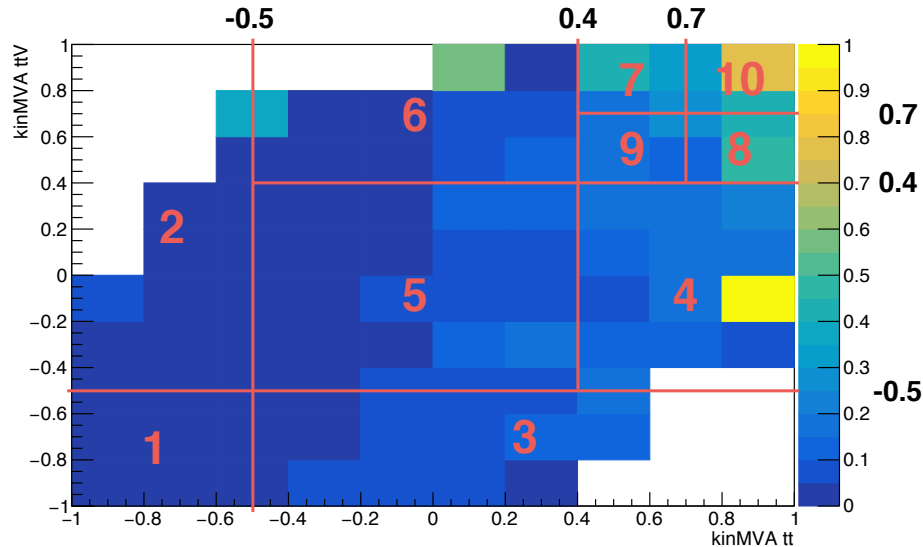


Figure 6.22: Binning overlaid on the S/B ratio map on the plane of classifier outputs.

2969 From this event categorization, a 1D histogram of expected distribution is pro-
 2970 duced for each signal and background process, and fit to the observed data (or the
 2971 Asimov dataset for expected limits).

2972 6.9.6 Binning and selection optimization

2973 The effect of the choice of pre-selection cuts and the number of bins of the 1D his-
 2974 togram on the cross section limit is evaluated by varying the most important cuts and
 2975 re-calculating the limit in each case. In this analysis, the optimization was performed
 2976 in the $3l$ channel, by evaluating the upper limits on the $tHq + tHW$ expected signal
 2977 strength only (without $t\bar{t}H$ component), always evaluated at $\kappa_t = -1.0$, $\kappa_V = 1.0$.

2978 Table 6.14 shows the several variations explored, compared with a baseline; the
 2979 baseline is similar to the selection reported in Table 6.6 but only a loose CSV jet and
 2980 a Z veto of ± 10 GeV are required.

Selection	Variation	Expected limit
Baseline		< 2.93
Loose CSV tags	$\geq 1 \rightarrow \geq 2$	< 3.81
Medium CSV tags	$\geq 0 \rightarrow \geq 1$	< 2.76
Light forward jet η	$\geq 0 \rightarrow \geq 1$	< 2.94
Light forward jet η	$\geq 0 \rightarrow \geq 1.5$	< 3.00
MET > 30 GeV		< 2.91
Z veto ($ m_{\ell\ell} - m_Z $)	$> 10\text{GeV} \rightarrow > 15\text{ GeV}$	< 2.79
One medium CSV + 15 GeV Z veto	combined	< 2.62

Table 6.14: Signal strength limit variation as a function of tighter cuts. The baseline selection corresponds to a looser selection compared to the one reported in Tab. 6.6 where only a CSV-loose b -jet is required, and the Z veto is loosened to ± 10 GeV. The optimal selection determined here corresponds to the baseline plus the two variations in the last row.

2981 The optimal limit is found when requiring a slightly tighter selection with respect
 2982 to the baseline. The optimal selection is reported in Table 6.6.

2983 The signal strength limit also depends on the chosen binning in the 2D plane as
 2984 the S/B ratio varies across the plane, hence, several sizes and binning combinations
 2985 were tested in order to improve the limit. Figure 6.23 shows some of the binning
 2986 combinations tested; in the default combination all the bins have the same size, while

2987 the best limit was found for a set of 10 bins. The bin borders and the resulting limits
 2988 are shown in Table 6.15.

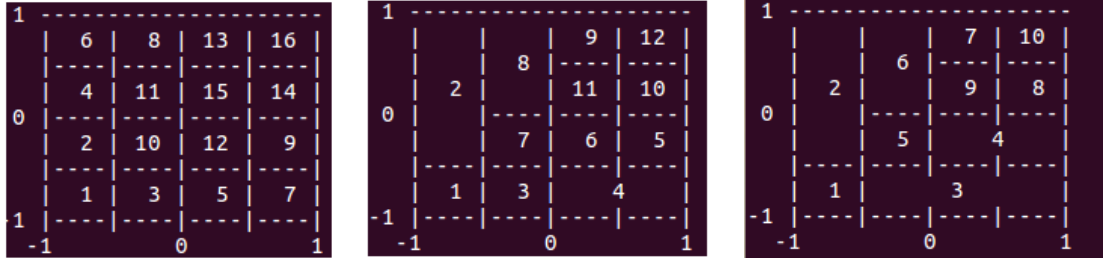


Figure 6.23: Binning combination scheme.

Number of bins	Bin borders						Expected limit
	x_1	x_2	x_3	y_1	y_2	y_3	
16 (default)	-0.5	0.0	0.5	-0.5	0.0	0.5	< 2.91
16	-0.5	0.3	0.7	-0.5	0.3	0.7	< 2.83
10	-0.5	0.0	0.5	-0.5	0.0	0.5	< 2.93
10	-0.5	0.0	0.7	-0.5	0.0	0.7	< 2.86
10	-0.5	0.0	0.7	-0.5	0.0	0.5	< 2.84
10	-0.5	0.0	0.5	-0.5	0.0	0.7	< 2.87
10	-0.5	0.4	0.7	-0.5	0.4	0.7	< 2.81

Table 6.15: Limit variation as a function of bin size. The final bin borders used in the $3l$ channel are indicated in bold.

2989 Combining the optimization of binning and using the tighter pre-selection cuts,

2990 the expected limit in the $3l$ channel alone reaches **r<2.59**.

2991 A similar binning optimization was made for $2lss$ channel, including other binning
 2992 combinations. First, the $3l$ channel binning was used to estimate the expected limit,
 2993 then, bin borders were varied to obtain the best possible expected limit. The bin
 2994 borders and the resulting signal strength limits for the same-sign dimuon channel are
 2995 shown in Table 6.16:

2996 The expected limit was found to be **r<1.69** for optimized bin borders in 10 bins

2997 and optimized pre-selection cuts.

Number of bins	Bin borders						Expected limit
	x_1	x_2	x_3	y_1	y_2	y_3	
16	-0.5	0.4	0.7	-0.5	0.4	0.7	< 1.72
12	-0.5	0.4	0.7	-0.5	0.4	0.7	< 1.72
12	-0.3	0.4	0.7	-0.5	0.4	0.7	< 1.71
12	-0.3	0.3	0.7	-0.5	0.4	0.7	< 1.71
12	-0.3	0.3	0.7	-0.4	0.4	0.7	< 1.70
12	-0.3	0.3	0.7	-0.3	0.4	0.7	< 1.70
12	-0.3	0.3	0.7	-0.3	0.2	0.7	< 1.68
12	-0.3	0.3	0.7	-0.3	0.1	0.7	< 1.70
12	-0.3	0.3	0.7	-0.3	0.2	0.6	< 1.70
10	-0.5	0.4	0.7	-0.5	0.4	0.7	< 1.75
10	-0.3	0.3	0.7	-0.3	0.2	0.6	< 1.69

Table 6.16: Limit variation as a function of bin size in the same-sign dimuon channel. (In bold: the final bin borders used in the $2lss$ channel.)

2998 Two additional binning strategies were tested, however, the obtained limits are
 2999 degraded; they are documented in Appendix C.

3000 6.10 Signal model

3001 It is worth to remind that the main goal of this analysis is to test the compatibility
 3002 of points in the parameter space of Higgs-to-vector boson and Higgs-to-top quark
 3003 couplings. This is achieved by using simulated tHq , tHW , and $t\bar{t}H$ signal events
 3004 which are weighted to reflect the impact of the couplings on kinematic distributions,
 3005 and together with different predictions of the respective production cross sections and
 3006 branching ratios, to produce limits on the cross section for different values of κ_V and
 3007 κ_t . See Section 6.4.3 and Table A.3 for the set of κ_t and κ_V values generated. The
 3008 slight shape-dependence of the BDTG classifier outputs as a function of the couplings
 3009 is showed in Appendix D.

3010 In addition to the (κ_t, κ_V) dependence of the tHq and tHW production cross
 3011 sections, due to interferences, the cross section of $t\bar{t}H$ depends quadratically on κ_t

3012 according to []:

$$\sigma(tHq) = (2.633\kappa_t^2 + 3.578\kappa_V^2 - 5.211\kappa_t\kappa_V) * \sigma_{SM}(tHq), \quad (6.7)$$

$$\sigma(tHW) = (2.909\kappa_t^2 + 2.310\kappa_V^2 - 4.220\kappa_t\kappa_V) * \sigma_{SM}(tHW), \quad (6.8)$$

$$\sigma(t\bar{H}) = \kappa_t^2 * \sigma_{SM}(t\bar{H}). \quad (6.9)$$

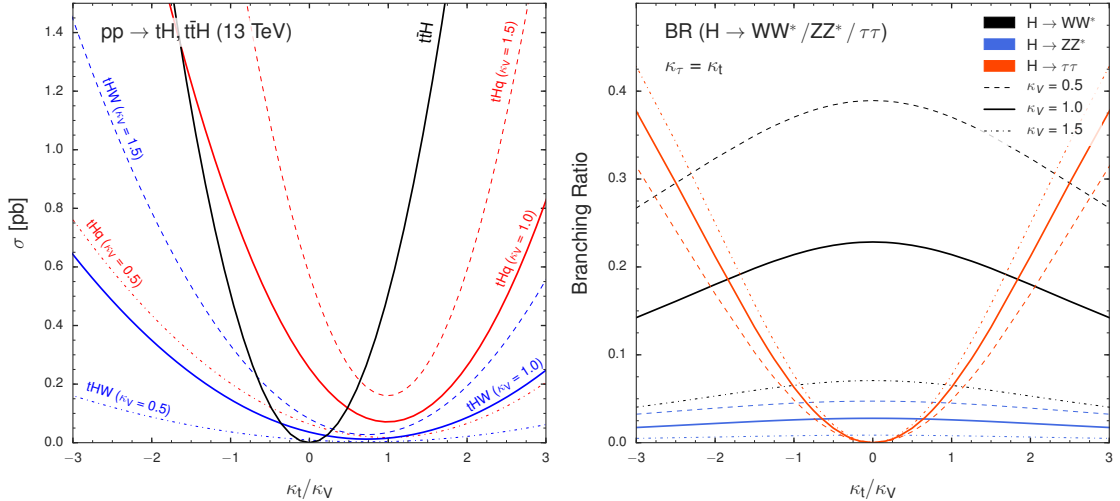


Figure 6.24: Scaling of the tHq , tHW , and $t\bar{H}$ production cross sections (left) and of the $H \rightarrow WW^*$, $H \rightarrow \tau\tau$, and $H \rightarrow ZZ^*$ branching ratios (right), as a function of κ_t/κ_V , for three different values of κ_V .

3013 The Higgs branching fractions to vector bosons depend on κ_V , and the overall
 3014 Higgs decay width depend both on κ_t and κ_V when considering resolved top-quark
 3015 loops in the $H \rightarrow \gamma\gamma$, $H \rightarrow Z\gamma$, and $H \rightarrow gg$ decays. The relative contributions from
 3016 $H \rightarrow WW$, $H \rightarrow ZZ$, and $H \rightarrow \tau\tau$ also changes with changing κ_V .

3017 If the Higgs-to-tau coupling modifier (κ_τ) is assumed to be equal to κ_t , the relative
 3018 fractions of WW , ZZ , and $\tau\tau$ in the event selection will only depend on the ratio of
 3019 κ_t/κ_V ; thus, any limit set at any given value of κ_t/κ_V is valid for all values of κ_t and
 3020 κ_V with that ratio, and could then be compared with theoretical predictions of cross

3021 sections at different values of either modifier. Figure F.1 shows the tHq , tHW and
 3022 $t\bar{t}H$ cross sections(left) and the Higgs boson branching ratios $H \rightarrow WW$, $H \rightarrow ZZ$,
 3023 and $H \rightarrow \tau\tau$ (right) as a function of the κ_t/κ_V ratio.

3024 Thus, this analysis sets an upper limit on the combined cross section times branch-
 3025 ing ratio of tHq , tHW , and $t\bar{t}H$ as a function of the ratio κ_t/κ_V .

3026 Similar interpretation can be made if instead of reporting the limits as a function
 3027 of the κ_t/κ_V ratio, they are reported as a function of the relative strength of Higgs-top
 3028 and Higgs-vector-boson couplings, multiplied by the relative sign

$$f_t = \text{sign}\left(\frac{\kappa_t}{\kappa_V}\right) \times \frac{\kappa_t^2}{\kappa_t^2 + \kappa_V^2}. \quad (6.10)$$

3029 this parameter covers the full space between -1.0 and 1.0 , with the SM expectation
 3030 at 0.5 . Absolute values of 1.0 or 0.0 would correspond to purely Higgs-top and purely
 3031 Higgs-V couplings, respectively.

3032 Table 6.17 shows the points in the κ_t/κ_V and f_t parameter space that are mapped
 3033 by the 51 individual κ_t and κ_V points.

3034 The overall Higgs decay width (modified by both κ_t and κ_V) becomes irrelevant
 3035 if limits are quoted as absolute cross sections rather than multiples of the expected
 3036 cross section (which depends on it).

3037 The 1D histograms of events as categorized in regions of the 2D BDTG plane are
 3038 then used in a maximum likelihood fit of signal and background shapes, where the
 3039 tHq , tHW , and $t\bar{t}H$ signals are floating with a common signal strength modifier r ,
 3040 producing a 95% C.L. upper limit the observed cross section of $tHq + tHW + t\bar{t}H$.

3041 This procedure is done separately for each point (κ_t, κ_V) where the cross sections
 3042 and branching fractions are scaled accordingly in each point. Limits at fixed values of
 3043 κ_t/κ_V are by construction identical. Tables F.1–F.3 and F.4–F.6 in Appendix F show

f_t	κ_t/κ_V	$\kappa_V = 0.5$	$\kappa_V = 1.0$	$\kappa_V = 1.5$
-0.973	-6.000	-3.00		
-0.941	-4.000	-2.00		
-0.900	-3.000	-1.50	-3.00	
-0.862	-2.500	-1.25		
-0.800	-2.000	-1.00	-2.00	-3.00
-0.692	-1.500	-0.75	-1.50	
-0.640	-1.333			-2.00
-0.610	-1.250		-1.25	
-0.500	-1.000	-0.50	-1.00	-1.50
-0.410	-0.833			-1.25
-0.360	-0.750		-0.75	
-0.308	-0.667			-1.00
-0.200	-0.500	-0.25	-0.50	-0.75
-0.100	-0.333			-0.50
-0.059	-0.250		-0.25	
-0.027	-0.167			-0.25
0.000	0.000	0.00	0.00	0.00
0.027	0.167			0.25
0.059	0.250		0.25	
0.100	0.333			0.50
0.200	0.500	0.25	0.50	0.75
0.308	0.667			1.00
0.360	0.750		0.75	
0.410	0.833			1.25
0.500	1.000	0.50	1.00	1.50
0.610	1.250		1.25	
0.640	1.333			2.00
0.692	1.500	0.75	1.50	
0.800	2.000	1.00	2.00	3.00
0.862	2.500	1.25		
0.900	3.000	1.50	3.00	
0.941	4.000	2.00		
0.973	6.000	3.00		

Table 6.17: The 33 distinct values of κ_t/κ_V and f_t as mapped by the 51 κ_t and κ_V points.

3044 the scalings of cross section times branching fraction, as well as branching fractions
 3045 alone for each of the Higgs decay modes and each of the signal components.
 3046 Systematic uncertainties on the signal selection efficiency arise from correction

3047 factors applied to the simulated events to better match the measured detector perfor-
3048 mance and also from theoretical uncertainties in the modeling of the signal process.

3049 Scale factors applied to correct for data/MC differences in the trigger efficiency, lepton
3050 reconstruction and identification performance, and lepton selection efficiency carry a
3051 combined uncertainty of about 5% from jet energy corrections is evaluated by varying
3052 the correction factors within their uncertainty and propagating the effect to the final
3053 result by recalculating all kinematic quantities. Effects on the overall normalization
3054 of event yields and on the shape of kinematic properties are both taken into account.
3055 Jet energy resolution effects have negligible impact on this

3056 analysis. Correction factors for data/MC differences in the b-tagging performance
3057 are applied depending on the pT and \hat{t}_b , and on the flavor of the jet, and their effect
3058 on the signal efficiency is evaluated by varying the factors within their measured
3059 uncertainty and recalculating the overall event scale factors. The uncertainties from
3060 unknown higher orders of tHq and tHW production are estimated from a change
3061 in the Q2 scale of double and half the initial value, evaluated for each point of \hat{t}_b
3062 and \hat{t}_V . The ttH signal component has an uncertainty of about $+5.8/\sqrt{9.2}$ scale
3063 variations and a further 3.6%. Uncertainties related to the choice of PDF set and its scale
3064 are estimated to be about 3.7% tHq and about 4.0%

3065 . Multivariate techniques are used to discriminate the signal from the dominant
3066 backgrounds. The analysis yields a 95% confidence level (C.L.) upper limit on the
3067 combined tH + ttH production cross section times branching ratio of 0.64 pb, with
3068 an expected limit of 0.32 pb, for a scenario with $k_t = \sqrt{1.0}$ and $k_V = 1.0$. Values
3069 of k_t outside the range of $\sqrt{1.25}$ to $\sqrt{1.60}$ are excluded at 95% C.L., assuming k_V
3070 = 1.0.

³⁰⁷¹ **Appendix A**

³⁰⁷² **Datasets and triggers**

Dataset name
/JetHT/Run2016X-23Sep2016-vY/MINIAOD
/HTMHT/Run2016X-23Sep2016-vY/MINIAOD
/MET/Run2016X-23Sep2016-vY/MINIAOD
/SingleElectron/Run2016X-23Sep2016-vY/MINIAOD
/SingleMuon/Run2016X-23Sep2016-vY/MINIAOD
/SinglePhoton/Run2016X-23Sep2016-vY/MINIAOD
/DoubleEG/Run2016X-23Sep2016-vY/MINIAOD
/MuonEG/Run2016X-23Sep2016-vY/MINIAOD
/DoubleMuon/Run2016X-23Sep2016-vY/MINIAOD
/Tau/Run2016B-23Sep2016-v3/MINIAOD
/JetHT/Run2016H-PromptReco-v3/MINIAOD
/HTMHT/Run2016H-PromptReco-v3/MINIAOD
/MET/Run2016H-PromptReco-v3/MINIAOD
/SingleElectron/Run2016H-PromptReco-v3/MINIAOD
/SingleMuon/Run2016H-PromptReco-v3/MINIAOD
/SinglePhoton/Run2016H-PromptReco-v3/MINIAOD
/DoubleEG/Run2016H-PromptReco-v3/MINIAOD
/MuonEG/Run2016H-PromptReco-v3/MINIAOD
/DoubleMuon/Run2016H-PromptReco-v3/MINIAOD

Table A.1: Full 2016 dataset used in the analysis. In the first section of the table are listed the 23Sep2016 samples; in the Run2016X-23Sep-vY label, X:B-G tag the run while Y:1,3 tag the version of the data sample. Second section list the PromptReco version of the dataset.

Same-sign dilepton (==2 muons)
HLT_Mu17_TrkIsoVVL_Mu8_TrkIsoVVL_DZ_v*
HLT_Mu17_TrkIsoVVL_TkMu8_TrkIsoVVL_DZ_v*
HLT_IsoMu22_v*
HLT_IsoTkMu22_v*
HLT_IsoMu22_eta2p1_v*
HLT_IsoTkMu22_eta2p1_v*
HLT_IsoMu24_v*
HLT_IsoTkMu24_v*
Same-sign dilepton (==2 electrons)
HLT_Ele23_Ele12_CaloIdL_TrackIdL_IsoVL_DZ_v*
HLT_Ele27_eta2p1_WP Loose_Gsf_v*
HLT_Ele27_WPTight_Gsf_v*
HLT_Ele25_eta2p1_WPTight_Gsf_v*
Same-sign dilepton (==1 muon, ==1 electron)
HLT_Mu23_TrkIsoVVL_Ele8_CaloIdL_TrackIdL_IsoVL_v*
HLT_Mu8_TrkIsoVVL_Ele23_CaloIdL_TrackIdL_IsoVL_v*
HLT_Mu23_TrkIsoVVL_Ele8_CaloIdL_TrackIdL_IsoVL_DZ_v*
HLT_Mu8_TrkIsoVVL_Ele23_CaloIdL_TrackIdL_IsoVL_DZ_v*
HLT_IsoMu22_v*
HLT_IsoTkMu22_v*
HLT_IsoMu22_eta2p1_v*
HLT_IsoTkMu22_eta2p1_v*
HLT_IsoMu24_v*
HLT_IsoTkMu24_v*
HLT_Ele27_WPTight_Gsf_v*
HLT_Ele25_eta2p1_WPTight_Gsf_v*
HLT_Ele27_eta2p1_WP Loose_Gsf_v*
Three lepton
HLT_DiMu9_Ele9_CaloIdL_TrackIdL_v*
HLT_Mu8_DiEle12_CaloIdL_TrackIdL_v*
HLT_TripleMu_12_10_5_v*
HLT_Ele16_Ele12_Ele8_CaloIdL_TrackIdL_v*
HLT_Mu23_TrkIsoVVL_Ele8_CaloIdL_TrackIdL_IsoVL_v*
HLT_Mu23_TrkIsoVVL_Ele8_CaloIdL_TrackIdL_IsoVL_DZ_v*
HLT_Mu8_TrkIsoVVL_Ele23_CaloIdL_TrackIdL_IsoVL_v*
HLT_Mu8_TrkIsoVVL_Ele23_CaloIdL_TrackIdL_IsoVL_DZ_v*
HLT_Ele23_Ele12_CaloIdL_TrackIdL_IsoVL_DZ_v*
HLT_Mu17_TrkIsoVVL_Mu8_TrkIsoVVL_DZ_v*
HLT_Mu17_TrkIsoVVL_TkMu8_TrkIsoVVL_DZ_v*
HLT_IsoMu22_v*
HLT_IsoTkMu22_v*
HLT_IsoMu22_eta2p1_v*
HLT_IsoTkMu22_eta2p1_v*
HLT_IsoMu24_v*
HLT_IsoTkMu24_v*
HLT_Ele27_WPTight_Gsf_v*
HLT_Ele25_eta2p1_WPTight_Gsf_v*
HLT_Ele27_eta2p1_WP Loose_Gsf_v*

Table A.2: Table of high-level triggers considered in the analysis.

		<i>tHq</i>		<i>tHW</i>		
κ_V	κ_t	sum of weights	cross section [pb]	sum of weights	cross section [pb]	LHE weights
1.0	-3.0	35.700022	2.991	11.030445	0.6409	LHEweight_wgt[446]
1.0	-2.0	20.124298	1.706	5.967205	0.3458	LHEweight_wgt[447]
1.0	-1.5	14.043198	1.205	4.029093	0.2353	LHEweight_wgt[448]
1.0	-1.25	11.429338	0.9869	3.208415	0.1876	LHEweight_wgt[449]
1.0	-1.0		0.7927		0.1472	
1.0	-0.75	7.054998	0.6212	1.863811	0.1102	LHEweight_wgt[450]
1.0	-0.5	5.294518	0.4723	1.339886	0.07979	LHEweight_wgt[451]
1.0	-0.25	3.818499	0.3505	0.914880	0.05518	LHEweight_wgt[452]
1.0	0.0	2.627360	0.2482	0.588902	0.03881	LHEweight_wgt[453]
1.0	0.25	1.719841	0.1694	0.361621	0.02226	LHEweight_wgt[454]
1.0	0.5	1.097202	0.1133	0.233368	0.01444	LHEweight_wgt[455]
1.0	0.75	0.759024	0.08059	0.204034	0.01222	LHEweight_wgt[456]
1.0	1.0	0.705305	0.07096	0.273617	0.01561	LHEweight_wgt[457]
1.0	1.25	0.936047	0.0839	0.442119	0.02481	LHEweight_wgt[458]
1.0	1.5	1.451249	0.1199	0.709538	0.03935	LHEweight_wgt[459]
1.0	2.0	3.335034	0.2602	1.541132	0.08605	LHEweight_wgt[460]
1.0	3.0	10.516125	0.8210	4.391335	0.2465	LHEweight_wgt[461]
1.5	-3.0	45.281492	3.845	13.426212	0.7825	LHEweight_wgt[462]
1.5	-2.0	27.606715	2.371	7.809713	0.4574	LHEweight_wgt[463]
1.5	-1.5	20.476088	1.784	5.594971	0.3290	LHEweight_wgt[464]
1.5	-1.25	17.337465	1.518	4.635978	0.2749	LHEweight_wgt[465]
1.5	-1.0	14.483302	1.287	3.775902	0.2244	LHEweight_wgt[466]
1.5	-0.75	11.913599	1.067	3.014744	0.1799	LHEweight_wgt[467]
1.5	-0.5	9.628357	0.874	2.352505	0.1410	LHEweight_wgt[468]
1.5	-0.25	7.627574	0.702	1.789184	0.1081	LHEweight_wgt[469]
1.5	0.0	5.911882	0.5577	1.324946	0.08056	LHEweight_wgt[470]
1.5	0.25	4.479390	0.4365	0.959295	0.05893	LHEweight_wgt[471]
1.5	0.5	3.331988	0.3343	0.692727	0.04277	LHEweight_wgt[472]
1.5	0.75	2.469046	0.2558	0.525078	0.03263	LHEweight_wgt[473]
1.5	1.0	1.890565	0.2003	0.456347	0.02768	LHEweight_wgt[474]
1.5	1.25	1.596544	0.1689	0.486534	0.02864	LHEweight_wgt[475]
1.5	1.5	1.586983	0.1594	0.615638	0.03509	LHEweight_wgt[476]
1.5	2.0	2.421241	0.2105	1.170602	0.06515	LHEweight_wgt[477]
1.5	3.0	7.503280	0.5889	3.467546	0.1930	LHEweight_wgt[478]
0.5	-3.0	27.432685	2.260	8.929074	0.5136	LHEweight_wgt[479]
0.5	-2.0	13.956013	1.160	4.419093	0.2547	LHEweight_wgt[480]
0.5	-1.5	8.924438	0.7478	2.757611	0.1591	LHEweight_wgt[481]
0.5	-1.25	6.835341	0.5726	2.075247	0.1204	LHEweight_wgt[482]
0.5	-1.0	5.030704	0.4273	1.491801	0.08696	LHEweight_wgt[483]
0.5	-0.75	3.510528	0.2999	1.007273	0.05885	LHEweight_wgt[484]
0.5	-0.5	2.274811	0.1982	0.621663	0.03658	LHEweight_wgt[485]
0.5	-0.25	1.323555	0.1189	0.334972	0.01996	LHEweight_wgt[486]
0.5	0.0	0.656969	0.06223	0.147253	0.008986	LHEweight_wgt[487]
0.5	0.25	0.274423	0.02830	0.058342	0.003608	LHEweight_wgt[488]
0.5	0.5	0.176548	0.01778	0.068404	0.003902	LHEweight_wgt[489]
0.5	0.75	0.363132	0.03008	0.177385	0.009854	LHEweight_wgt[490]
0.5	1.0	0.834177	0.06550	0.385283	0.02145	LHEweight_wgt[491]
0.5	1.25	1.589682	0.1241	0.692099	0.03848	LHEweight_wgt[492]
0.5	1.5	2.629647	0.2047	1.097834	0.06136	LHEweight_wgt[493]
0.5	2.0	5.562958	0.4358	2.206057	0.1246	LHEweight_wgt[494]
0.5	3.0	14.843102	1.177	5.609519	0.3172	LHEweight_wgt[495]

Table A.3: κ_V and κ_t combinations generated for the two signal samples and their NLO cross sections. The *tHq* cross section is multiplied by the branching fraction of the enforced leptonic decay of the top quark (0.324) [150].

Sample	σ [pb]	*
TTWJetsToLNu_TuneCUETP8M1_13TeV-amcatnloFXFX-madspin-pythia8	0.2043	*
TTZToLLNuNu_M-10_TuneCUETP8M1_13TeV-amcatnlo-pythia8	0.2529	*
/store/cmst3/group/susy/gpetrucc/13TeV/u/TTLL_m1to10_L0_NoMS_for76X/	0.0283	
WGToLNuG_TuneCUETP8M1_13TeV-madgraphMLM-pythia8	585.8	
ZGTo2LG_TuneCUETP8M1_13TeV-amcatnloFXFX-pythia8	131.3	
TGJets_TuneCUETP8M1_13TeV_amcatnlo_madspin_pythia8	2.967	
TGJets_TuneCUETP8M1_13TeV_amcatnlo_madspin_pythia8	2.967	
TTGJets_TuneCUETP8M1_13TeV-amcatnloFXFX-madspin-pythia8	3.697	
WpWpJJ_EWK-QCD_TuneCUETP8M1_13TeV-madgraph-pythia8	0.03711	
ZZZ_TuneCUETP8M1_13TeV-amcatnlo-pythia8	0.01398	
WWZ_TuneCUETP8M1_13TeV-amcatnlo-pythia8	0.1651	
WZZ_TuneCUETP8M1_13TeV-amcatnlo-pythia8	0.05565	
WW_DoubleScattering_13TeV-pythia8	1.64	
tZq_ll_4f_13TeV-amcatnlo-pythia8_TuneCUETP8M1	0.0758	
ST_tW1l_5f_L0_13TeV-MadGraph-pythia8	0.01123	
TTTT_TuneCUETP8M1_13TeV-amcatnlo-pythia8	0.009103	
WZTo3LNu_TuneCUETP8M1_13TeV-powheg-pythia8	4.4296	
ZZTo4L_13TeV_powheg_pythia8	1.256	
TTJets_SingleLeptFromTbar_TuneCUETP8M1_13TeV-madgraphMLM-pythia8	182.1754	*
TTJets_SingleLeptFromT_TuneCUETP8M1_13TeV-madgraphMLM-pythia8	182.1754	*
TTJets_DiLept_TuneCUETP8M1_13TeV-madgraphMLM-pythia8	87.3	*
DYJetsToLL_M-10to50_TuneCUETP8M1_13TeV-amcatnloFXFX-pythia8	18610	
DYJetsToLL_M-50_TuneCUETP8M1_13TeV-madgraphMLM-pythia8	6024	
WJetsToLNu_TuneCUETP8M1_13TeV-amcatnloFXFX-pythia8	61526.7	
ST_tW_top_5f_inclusiveDecays_13TeV-powheg-pythia8_TuneCUETP8M1	35.6	
ST_tW_antitop_5f_inclusiveDecays_13TeV-powheg-pythia8_TuneCUETP8M1	35.6	
ST_t-channel_4f_leptonDecays_13TeV-amcatnlo-pythia8_TuneCUETP8M1	70.3144	
ST_t-channel_antitop_4f_leptonDecays_13TeV-powheg-pythia8_TuneCUETP8M1	26.2278	
ST_s-channel_4f_leptonDecays_13TeV-amcatnlo-pythia8_TuneCUETP8M1	3.68064	
WWTo2L2Nu_13TeV-powheg	10.481	
ttWJets_13TeV_madgraphMLM	0.6105	
ttZJets_13TeV_madgraphMLM	0.5297/0.692	

Table A.4: List of background samples used in this analysis (CMSSW 80X). The first section of the table lists the samples used in simulation to extract the final yields and shapes; the second section lists the samples of the processes for which the yields are estimated from data. The MC simulation is used to design the data driven methods and in the derivation of the associated systematic uncertainties. The third section list the leading order $t\bar{t}W$ and $t\bar{t}Z$ samples, which in addition to the ones marked with a *, where used in the BDT training.

³⁰⁷³ **Appendix B**

³⁰⁷⁴ **Additional plots**

³⁰⁷⁵ **B.1 Pre-selection kinematic variables**

³⁰⁷⁶ Figures B.1, B.2 and B.3 show the distributions of some relevant kinematic variables,
³⁰⁷⁷ normalized to the cross section of the respective processes and to the integrated
³⁰⁷⁸ luminosity.

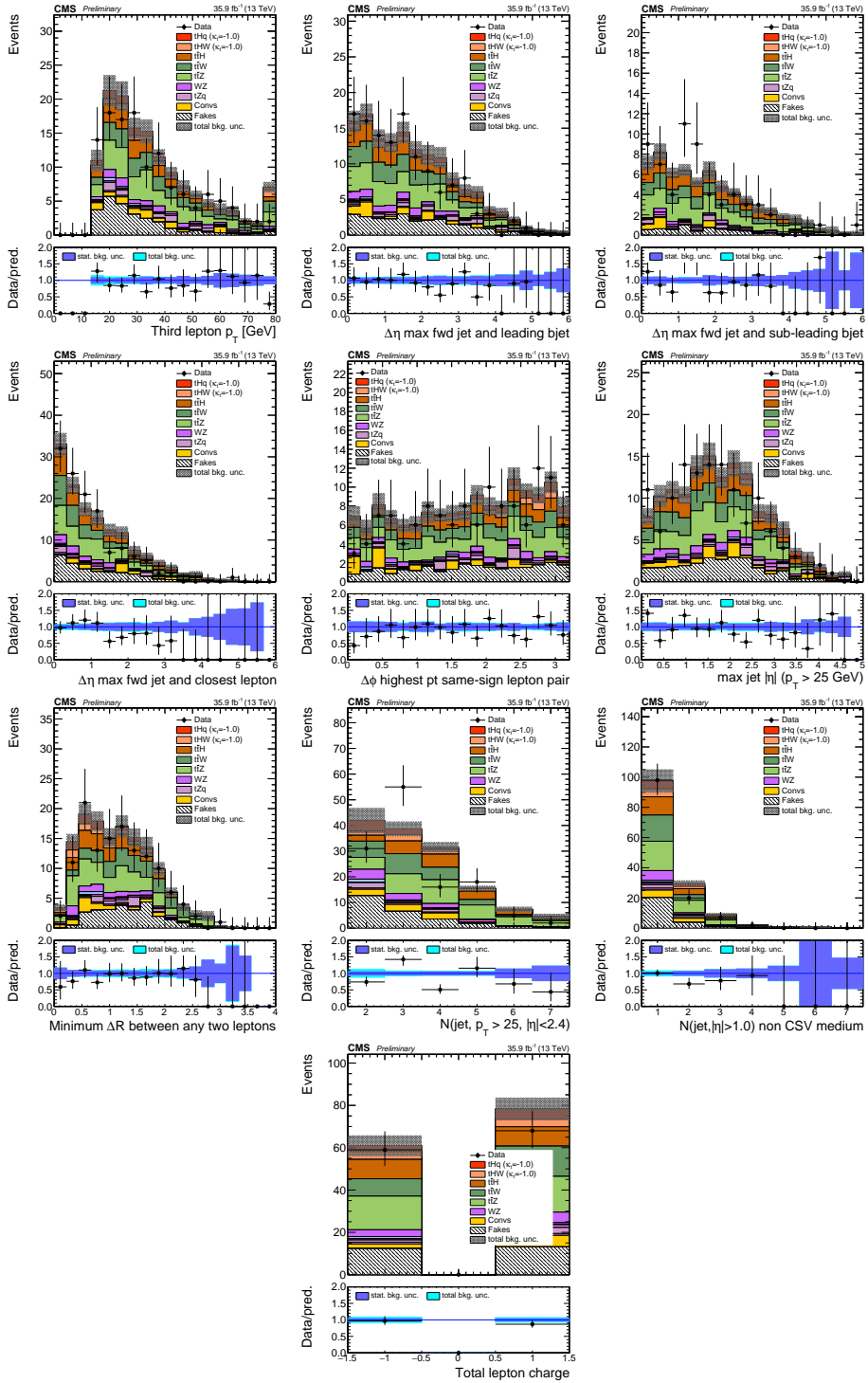


Figure B.1: Distributions of input variables to the BDT for signal discrimination, three lepton channel, normalized to their cross section and to 35.9 fb^{-1} .

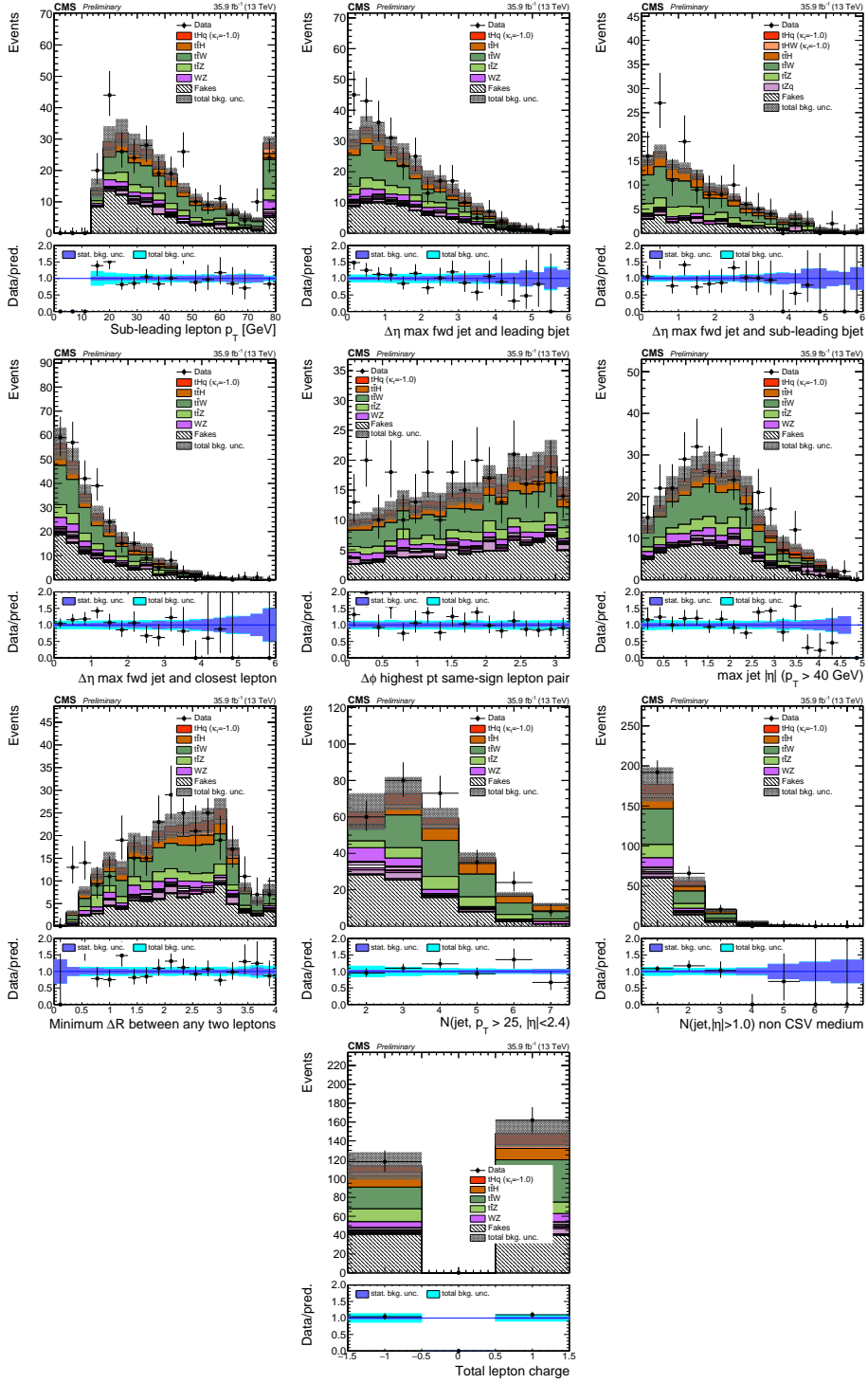


Figure B.2: Distributions of input variables to the BDT for signal discrimination, in $\mu^\pm\mu^\pm$ channel, normalized to their cross section and to 35.9fb^{-1} .

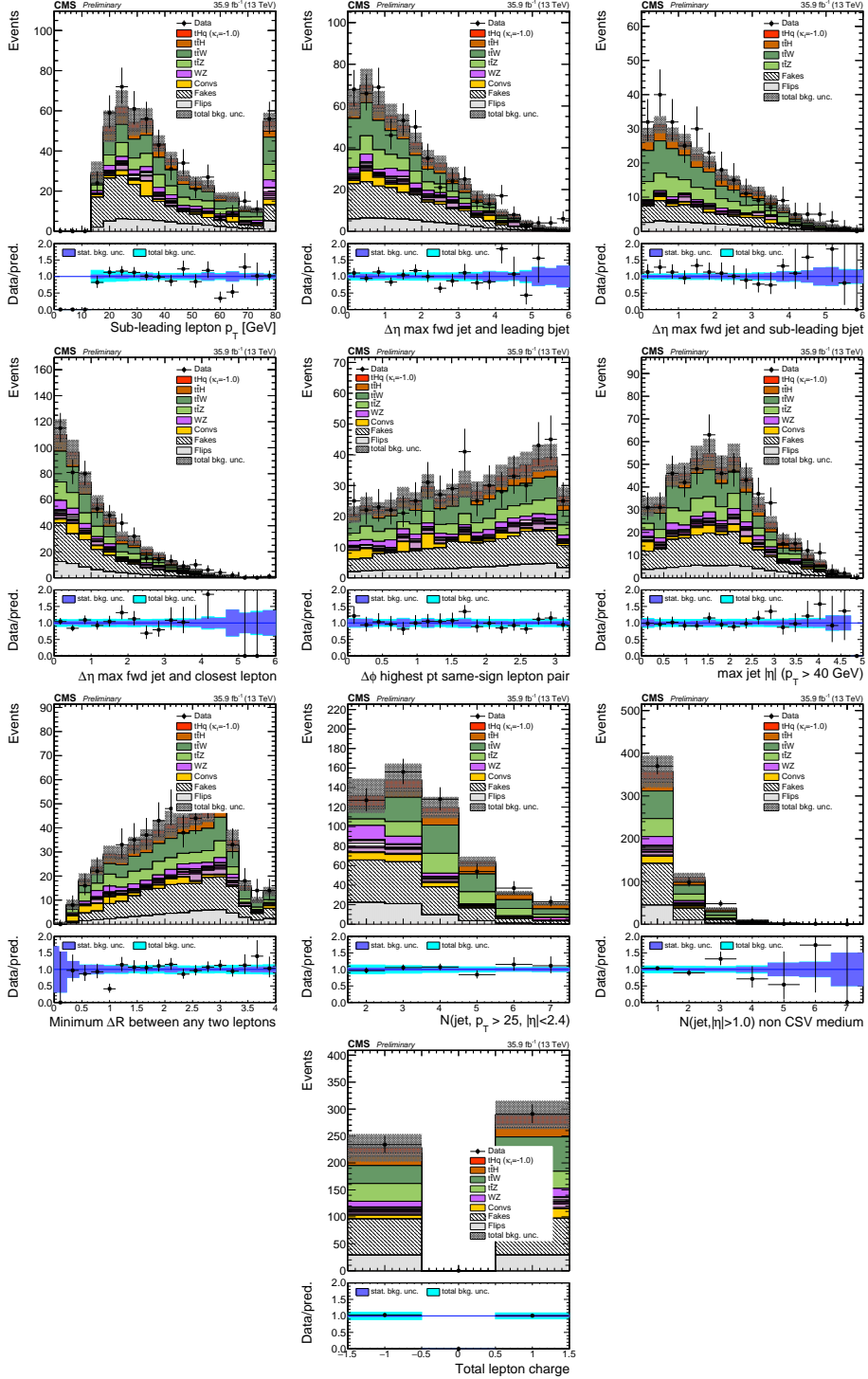


Figure B.3: Distributions of input variables to the BDT for signal discrimination, in $e^\pm\mu^\pm$ channel, normalized to their cross section and to 35.9 fb^{-1} .

3079 **B.2 BDTG input variables for $2lss$ channel**

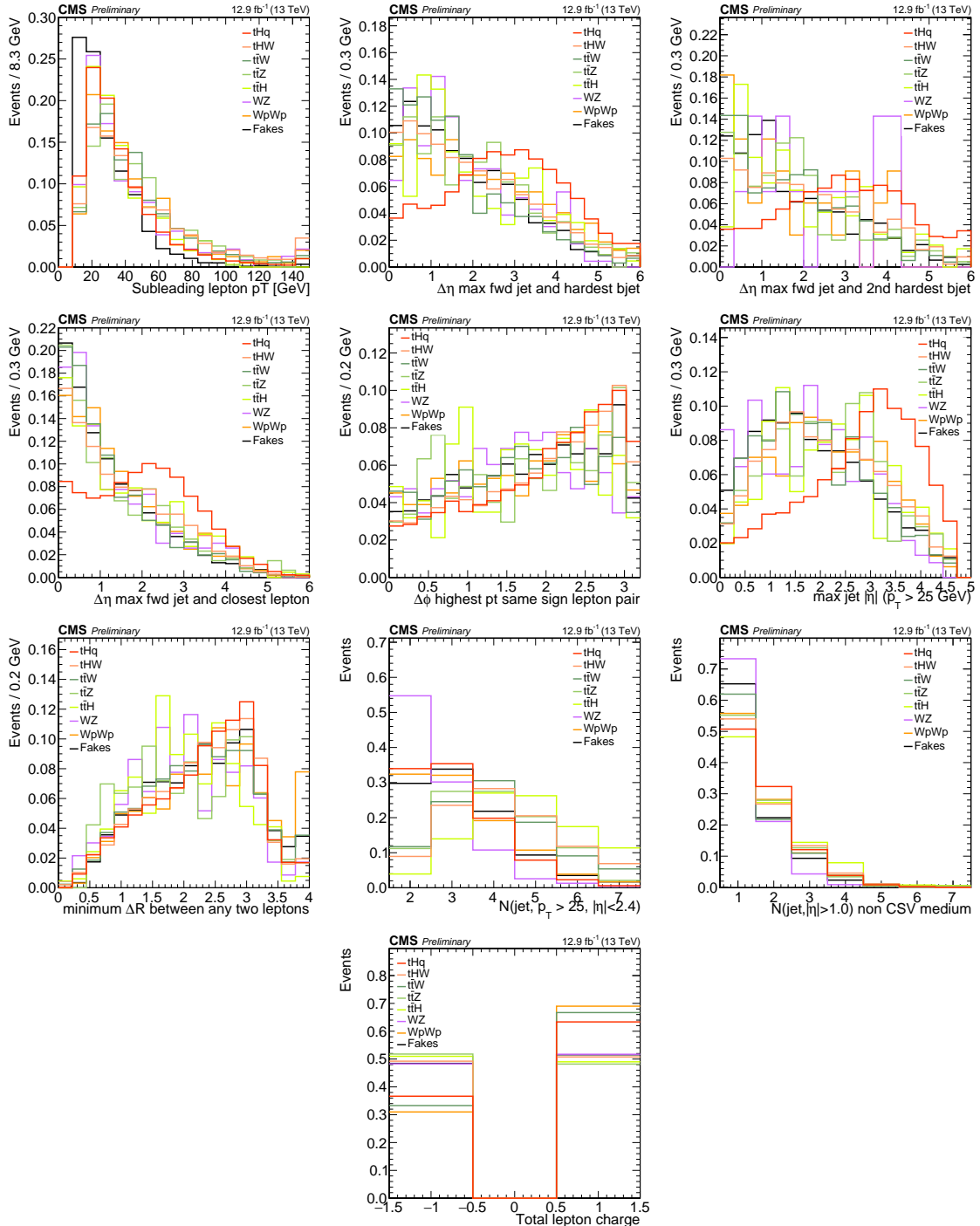


Figure B.4: Distributions of input variables to the BDT for signal discrimination, two lepton same sign channel.

3080 **B.3 Input variables distributions from BDTG**
 3081 classifiers

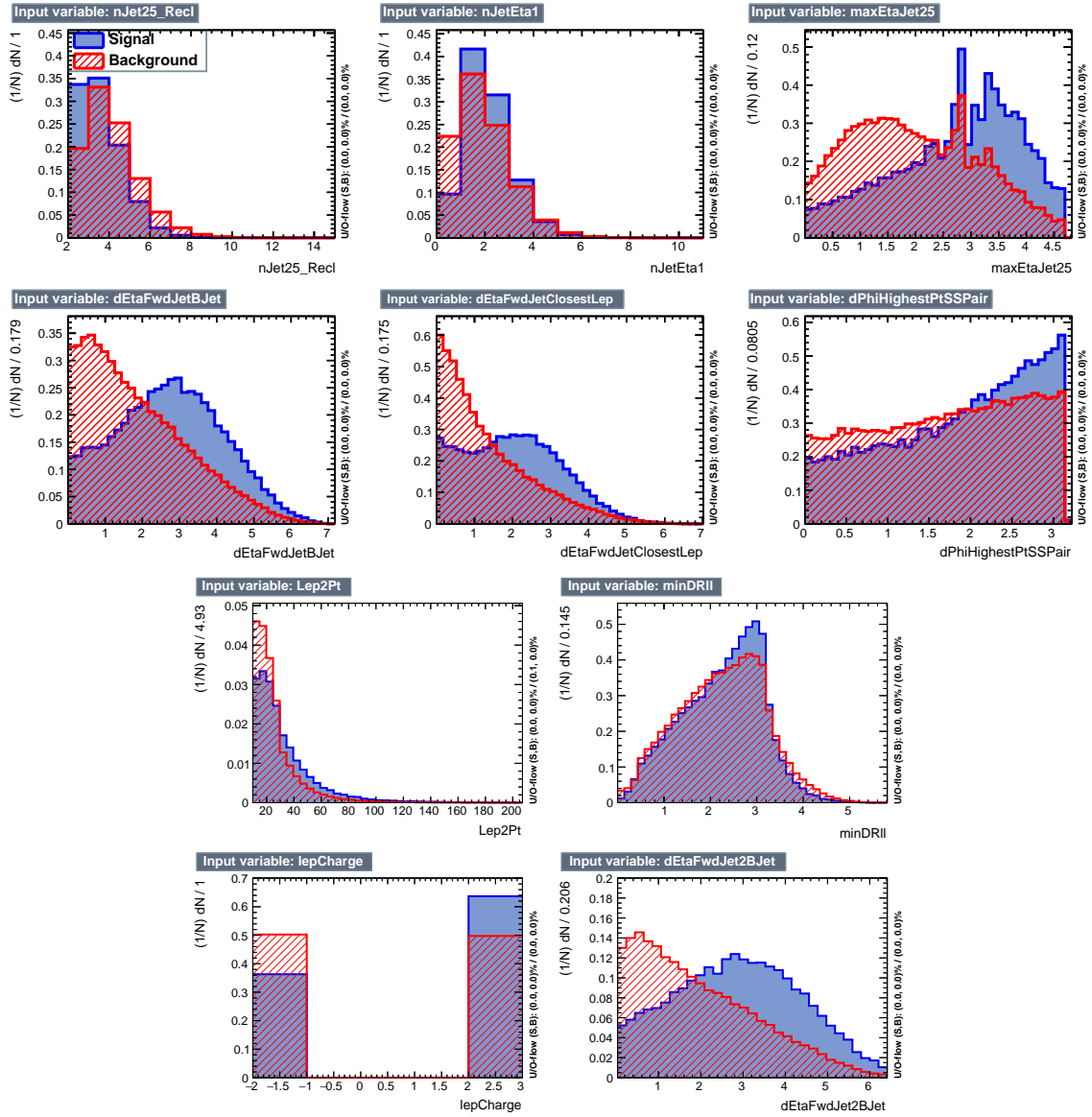


Figure B.5: BDT input variables as seen by BDTG classifier for the $2lss$ channel, tHq signal (blue) discriminated against $t\bar{t}$ background (red).

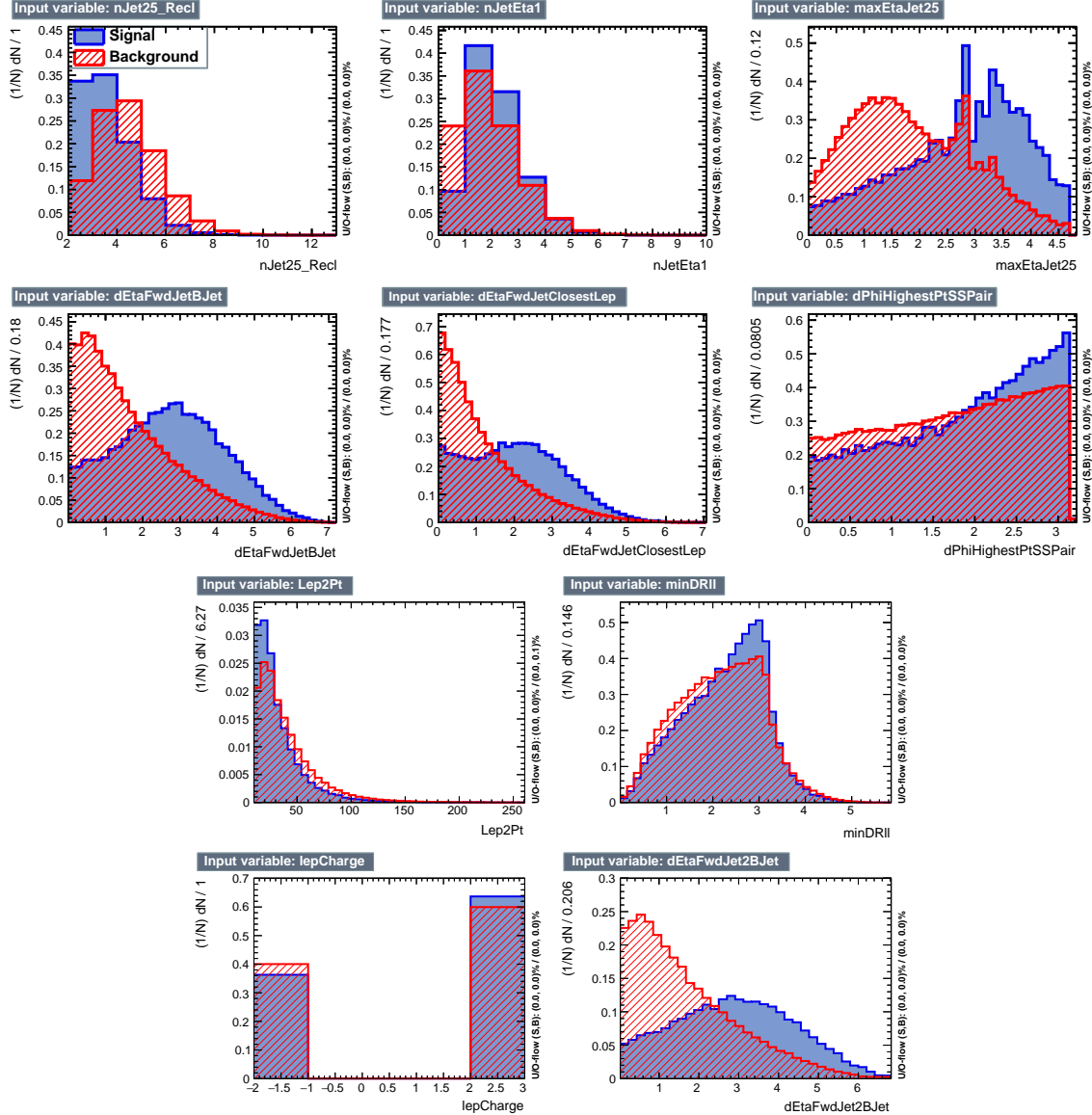


Figure B.6: BDT input variables as seen by BDTG classifier for the $2lss$ channel, tHq signal(blue) discriminated against $t\bar{t}V$ background (red).

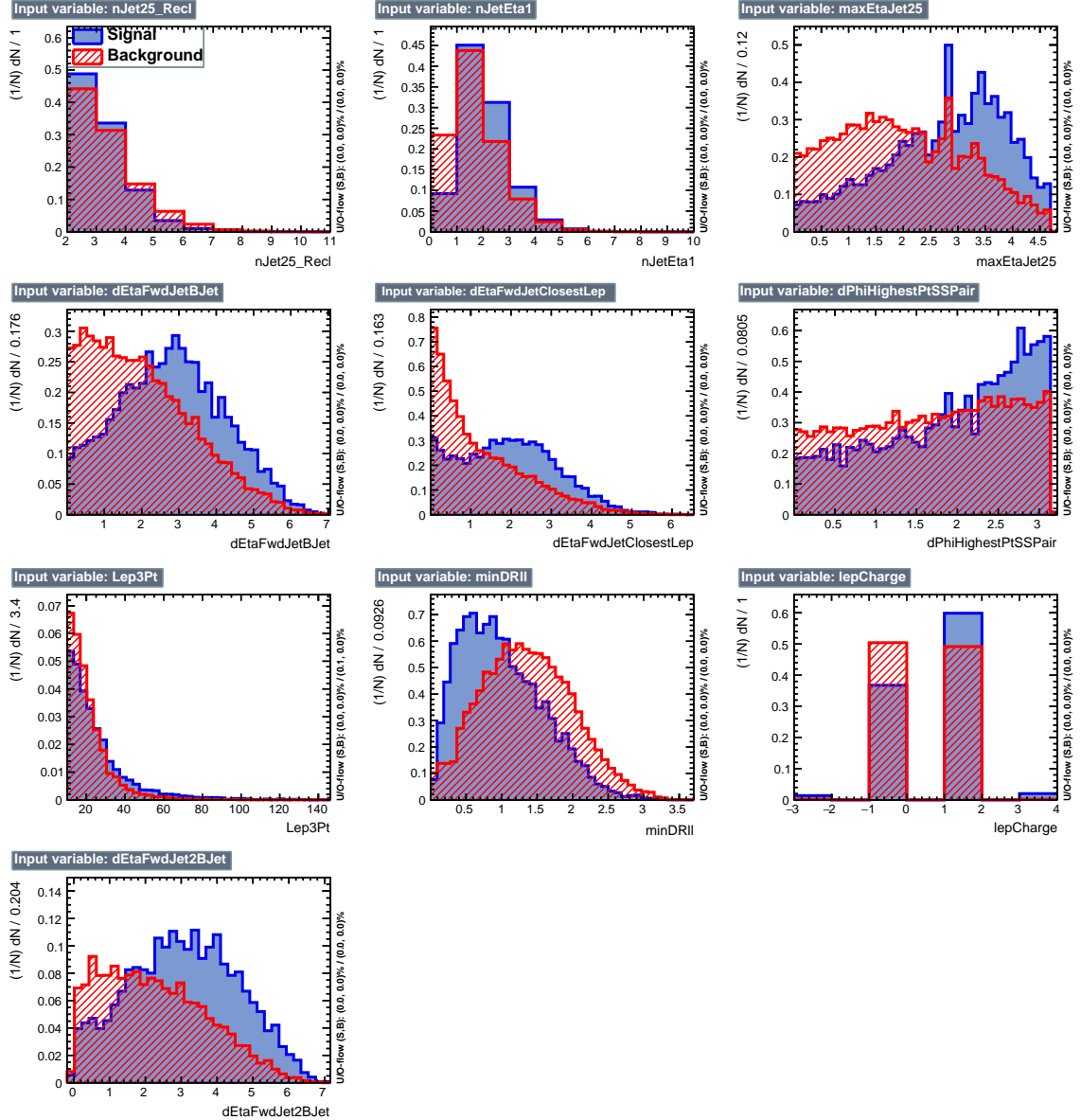


Figure B.7: BDT input variables as seen by BDTG classifier for the $3l$ channel, tHq signal (blue) discriminated against $t\bar{t}$ background (red).

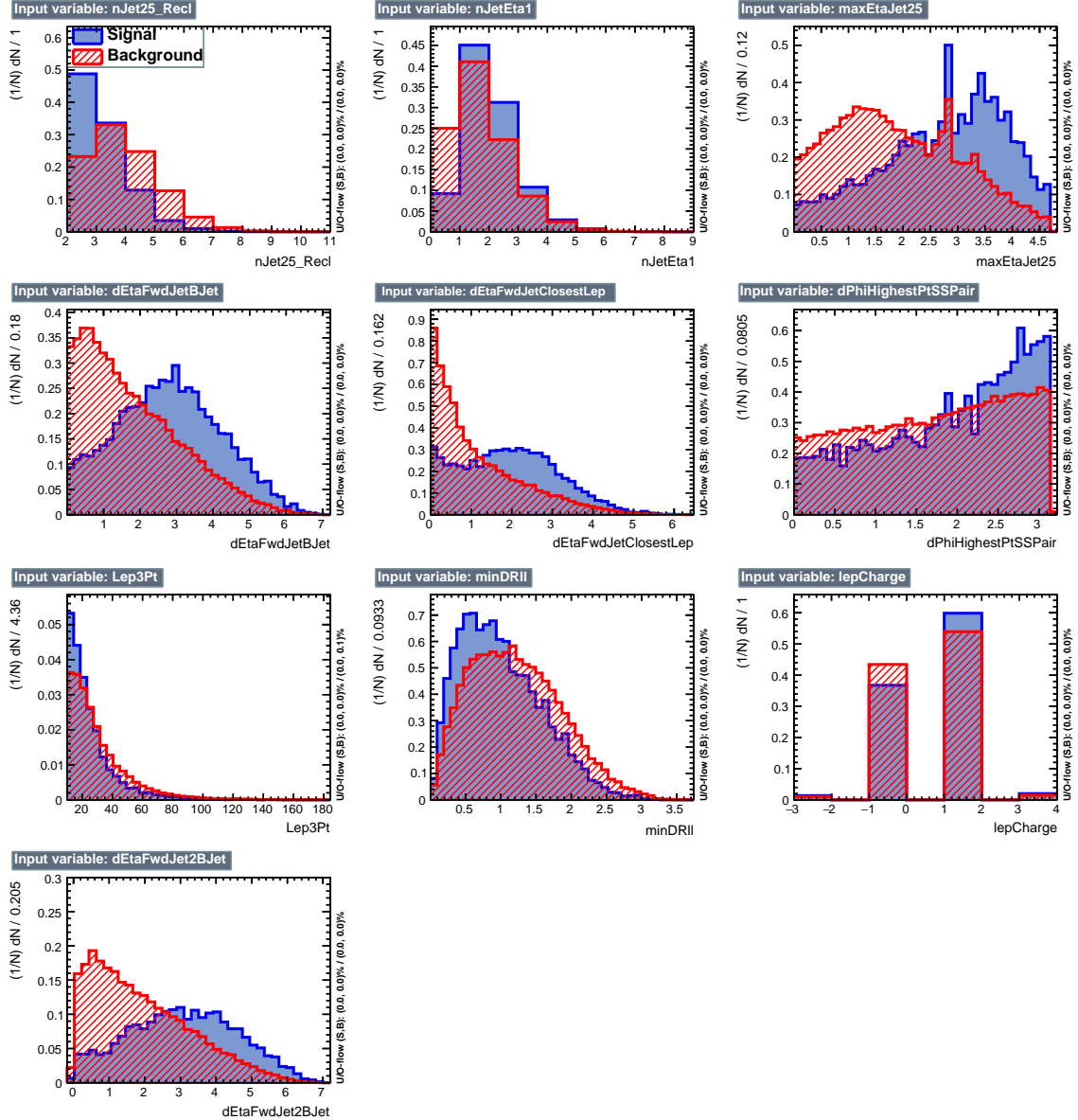


Figure B.8: BDT input variables as seen by BDTG classifier for the $3l$ channel, tHq signal (blue) discriminated against $t\bar{t}V$ background (red).

3082 **Appendix C**

3083 **Other binning strategies**

3084 Two additional strategies of clustering regions in the 2D plane of $BDTG_{tt}$ vs $BDTG_{ttV}$
 3085 into bins were attempted, following studies done and documented in great detail in
 3086 Reference [149]. A brief description is provided in the following.

3087 **Clustering by S/B ratio** In this method, the 2D plane is clustered into a given
 3088 number of bins corresponding to regions where S/B is within a certain range. The
 3089 bin borders are determined such that the number of background events in each bin is
 3090 approximately equal. The resulting regions for $2lss$ and $3l$ events are shown in Figure
 3091 C.1, while the expected distribution of signal and dominant backgrounds are shown
 3092 in Figure C.2.

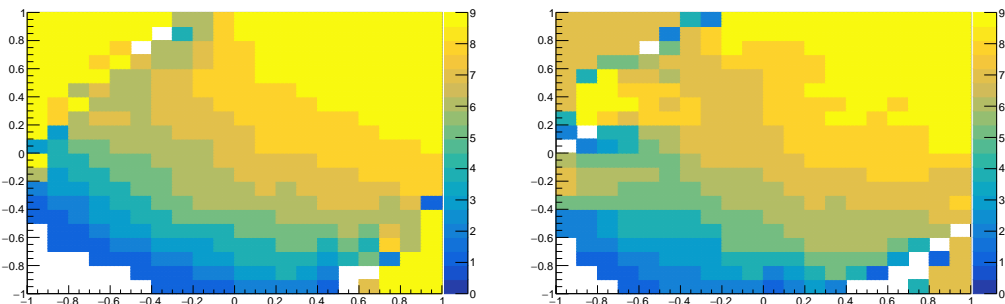


Figure C.1: Binning by S/B regions for $2lss$ (left) and $3l$ (right).

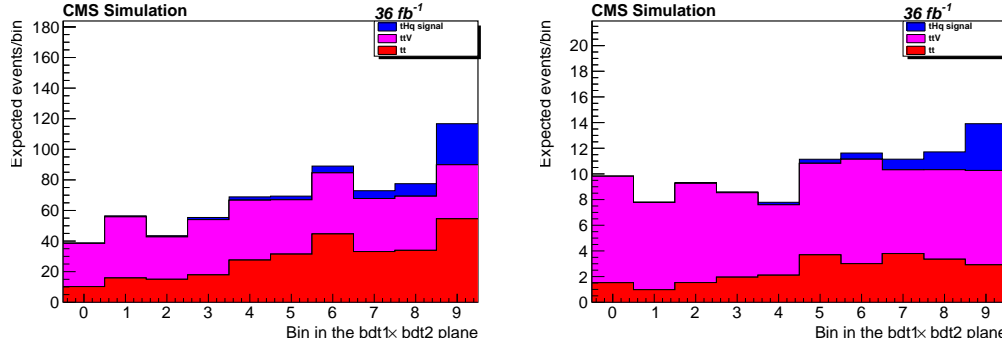


Figure C.2: Final bins (corresponding to S/B regions in the 2D plane) for $2lss$ and $3l$ (right).

Using this method, the resulting limits (for the $\kappa_t = -1, \kappa_V = 1$ scenario) are about 20% worse than with the binning in Section 6.9.6: $\mu^\pm\mu^\pm$ changed from 1.82 to 2.15, $3l$ changed from 1.52 to 1.75.

***k*-Means geometric clustering** This method employs a recursive application of the k -means algorithm (see Appendix D in Reference [149]) to separate the 2D plane into geometric regions. The resulting clustering (using the $t\bar{t}H$ multilepton code on tHq signal and $t\bar{t}$ and $t\bar{t}V$ background events) are shown in Figure C.3. The expected distribution of events for the signal and dominant backgrounds in these bins is shown in Fig. C.4.

Similarly to the S/B ratio binning, the limits using the k -means clustering are significantly worse than those of the bins described before. In the $\mu^\pm\mu^\pm$ channel, the limit deteriorates from 1.82 to 2.05, whereas in $3l$ it changes from 1.58 to 1.78.

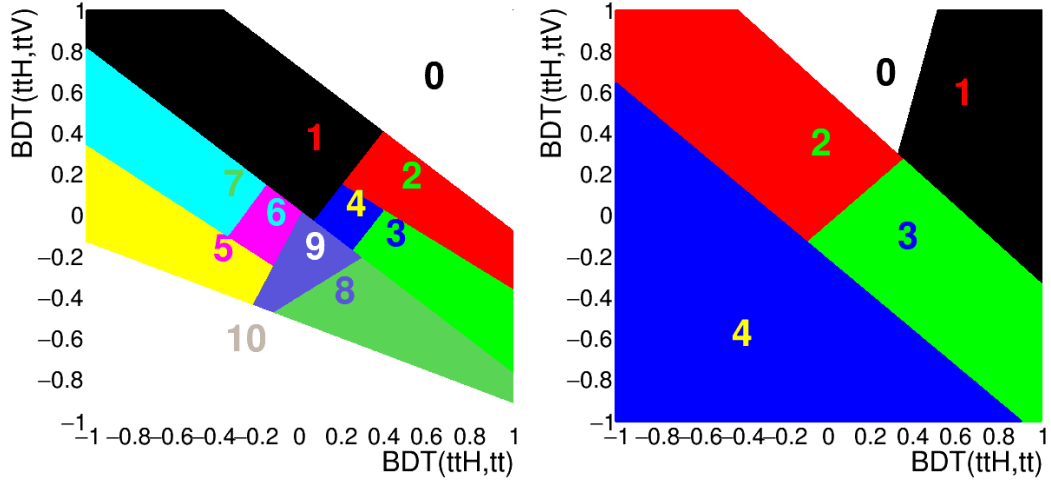


Figure C.3: Binning into geometric regions using a k -means algorithm for $2lss$ (left) and $3l$ (right).

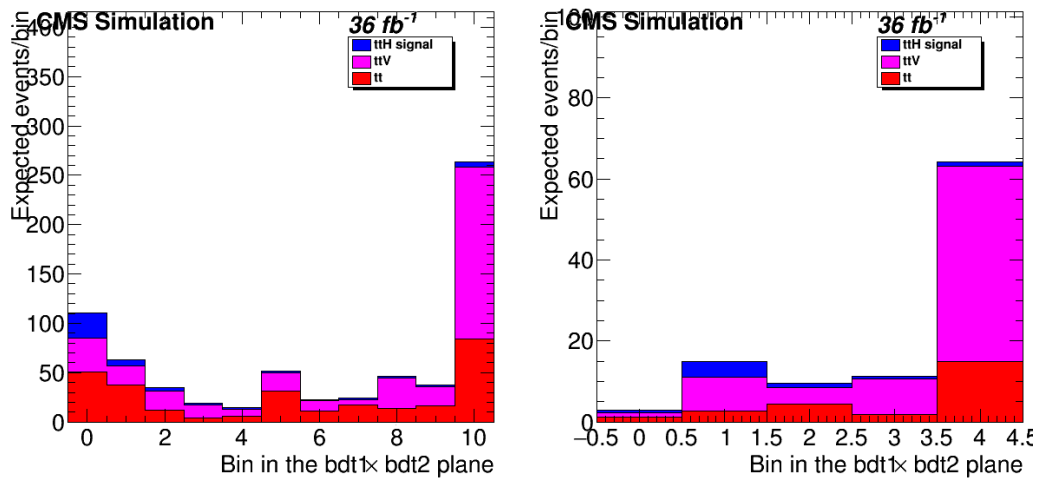


Figure C.4: Final bins using a k -means algorithm for $2lss$ (left) and $3l$ (right). Note that the bin numbering here is such that signal-like bins are lower.

3105 **Appendix D**

3106 **BDTG output variation with κ_V/κ_t**

3107 The BDTG classifier output was described in Section in the $\kappa_t = -1, \kappa_V = 1$ scenario;
3108 the change of BDTG classifiers output shape when varying the κ_V/κ_t coupling sce-
3109 nario is shown in Figure D.1 in the $3l$ channel for five different values of κ_t , with κ_V fixed at 1.0.

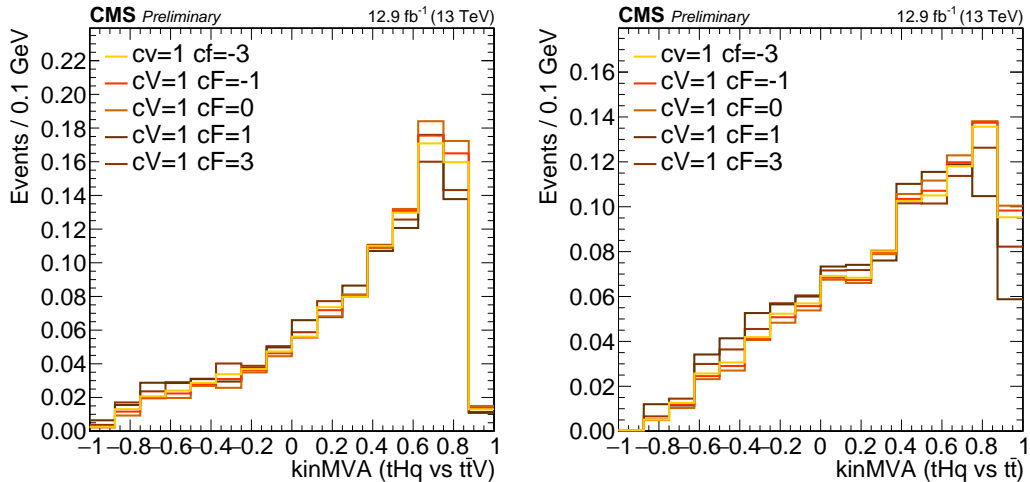


Figure D.1: Change of the BDTG classifiers output when varying κ_t coupling (κ_V is fixed at 1.0). Training vs. $tt\bar{V}$ (right) and vs. $tt\bar{t}$ (left).

3110

3111 Complete this section !!!!!!! ask about this !

3112 Appendix E

3113 tHq - $t\bar{t}H$ overlap

3114 This section provides a quick overview of the differences and commonalities in event
 3115 selections between this analysis and the $t\bar{t}H$ multilepton search [149]. The object
 3116 selections of the two analysis are perfectly synchronized due to shared frameworks
 3117 and samples. The only exception is the usage of forward jets ($|\eta| > 2.4, p_T > 40$ GeV)
 3118 in this analysis. Such jets are not considered in the $t\bar{t}H$ analysis.

3119 Table E.1 gives an overview of the main differences in the event selections. Here,
 3120 $E_T^{miss}_{LD}$ is defined as $E_T^{miss} \times 0.00397 + H_T^{miss} \times 0.00265$. Un-tagged jets in the tHq
 3121 analysis are jets that do not pass the CSV loose working point and are either central
 3122 ($|\eta| < 2.4, p_T > 25$ GeV) or forward ($|\eta| < 2.4, p_T > 40$ GeV). All jets in the $t\bar{t}H$ analysis
 3123 are selected with $p_T > 25$ GeV. Lepton p_T cuts and the trigger selections are identical.

Channel	tHq	$t\bar{t}H$
3l	Z veto, 15bGeV $N_{jets}^{\text{b, med.}} \geq 1$ ≥ 1 un-tagged jet	Z veto, 10 GeV $N_{jets}^{\text{b, med.}} \geq 1$ OR $N_{jets}^{\text{b, loose}} \geq 2$ $E_T^{miss}_{LD} > 0.2$ OR $N_{\text{centrl.}} \geq 4$
2lss	$N_{jets}^{\text{b, med.}} \geq 1$ ≥ 1 un-tagged jet	$N_{jets}^{\text{b, med.}} \geq 1$ OR $N_{jets}^{\text{b, loose}} \geq 2$ $N_{\text{central}} \geq 4$

Table E.1: Differences in event selection between this analysis and the $t\bar{t}H$ multilepton analysis.

3124 Table E.2 shows the total events yields in the individual channels, and the yield
 3125 of shared events between each channel, for the tHq signal sample, the $t\bar{t}H$ signal
 3126 sample, and the data. In the data, for the $3l$ channel, about 80% of events passing
 3127 the tHq selection also pass the $t\bar{t}H$ selection, constituting about 70% of that channel.
 3128 In the $2lss$ channel, about 50% of data events passing the tHq selection also pass the
 3129 $t\bar{t}H$ selection, but these events constitute almost 90% of the $t\bar{t}H$ selection in those
 3130 channels. Similar overlaps are also seen in the tHq and $t\bar{t}H$ signal samples.

3131 There is no migration between different channels and different selections, i.e. no
 3132 events passing the selection of a given tHq channel pass the selection of any other
 3133 channels of $t\bar{t}H$ and vice versa.

tHq sample	tHq	$t\bar{t}H$	Common	(% tHq)	(% $t\bar{t}H$)
$\mu^\pm\mu^\pm$	7400	2353	2166	29.3	92.1
$e^\pm\mu^\pm$	11158	3600	3321	29.8	92.2
$e^\pm e^\pm$	3550	1106	1025	28.9	92.7
$\ell\ell\ell$	3115	2923	2347	75.3	80.3

$t\bar{t}H$ sample	tHq	$t\bar{t}H$	Common	(% tHq)	(% $t\bar{t}H$)
$\mu^\pm\mu^\pm$	32612	28703	26547	81.4	92.5
$e^\pm\mu^\pm$	48088	42521	39164	81.4	92.1
$e^\pm e^\pm$	15476	12869	11896	76.9	92.4
$\ell\ell\ell$	26627	30598	25288	95.0	82.6

Data	tHq	$t\bar{t}H$	Common	(% tHq)	(% $t\bar{t}H$)
$\mu^\pm\mu^\pm$	280	160	140	50.0	87.5
$e^\pm\mu^\pm$	525	280	242	46.1	86.4
$e^\pm e^\pm$	208	90	79	38.0	87.8
$\ell\ell\ell$	126	154	104	82.5	67.5

Table E.2: Individual and shared event yields between this analysis (tHq) and $t\bar{t}H$ multilepton selections.

³¹³⁴ **Appendix F**

³¹³⁵ **Cross sections and Branching**

³¹³⁶ **ratios scalings**

κ_V	κ_t	HWW	HZZ	H $\tau\tau$	H $\mu\mu$	Hbb	Hcc	H $\gamma\gamma$	HZ γ	Hgg
0.5	-6.0	0.0827	0.0827	11.9098	11.9098	0.3308	0.3308	0.3308	0.3308	0.3308
0.5	-4.0	0.1417	0.1417	9.0699	9.0699	0.5669	0.5669	0.5669	0.5669	0.5669
0.5	-3.0	0.1889	0.1889	6.7999	6.7999	0.7555	0.7555	0.7555	0.7555	0.7555
0.5	-2.5	0.2173	0.2173	5.4325	5.4325	0.8692	0.8692	0.8692	0.8692	0.8692
0.5	-2.0	0.2478	0.2478	3.9647	3.9647	0.9912	0.9912	0.9912	0.9912	0.9912
0.5	-1.5	0.2782	0.2782	2.5034	2.5034	1.1126	1.1126	1.1126	1.1126	1.1126
0.5	-1.333	0.2877	0.2877	2.0448	2.0448	1.1508	1.1508	1.1508	1.1508	1.1508
0.5	-1.25	0.2922	0.2922	1.8264	1.8264	1.1689	1.1689	1.1689	1.1689	1.1689
0.5	-1.0	0.3048	0.3048	1.2194	1.2194	1.2194	1.2194	1.2194	1.2194	1.2194
0.5	-0.833	0.3122	0.3122	0.8665	0.8665	1.2487	1.2487	1.2487	1.2487	1.2487
0.5	-0.75	0.3154	0.3154	0.7097	0.7097	1.2617	1.2617	1.2617	1.2617	1.2617
0.5	-0.667	0.3184	0.3184	0.5666	0.5666	1.2736	1.2736	1.2736	1.2736	1.2736
0.5	-0.5	0.3235	0.3235	0.3235	0.3235	1.2938	1.2938	1.2938	1.2938	1.2938
0.5	-0.333	0.3272	0.3272	0.1451	0.1451	1.3087	1.3087	1.3087	1.3087	1.3087
0.5	-0.25	0.3285	0.3285	0.0821	0.0821	1.3139	1.3139	1.3139	1.3139	1.3139
0.5	-0.167	0.3294	0.3294	0.0367	0.0367	1.3177	1.3177	1.3177	1.3177	1.3177
0.5	0.0	0.3302	0.3302	0.0000	0.0000	1.3207	1.3207	1.3207	1.3207	1.3207
0.5	0.167	0.3294	0.3294	0.0367	0.0367	1.3177	1.3177	1.3177	1.3177	1.3177
0.5	0.25	0.3285	0.3285	0.0821	0.0821	1.3139	1.3139	1.3139	1.3139	1.3139
0.5	0.333	0.3272	0.3272	0.1451	0.1451	1.3087	1.3087	1.3087	1.3087	1.3087
0.5	0.5	0.3235	0.3235	0.3235	0.3235	1.2938	1.2938	1.2938	1.2938	1.2938
0.5	0.667	0.3184	0.3184	0.5666	0.5666	1.2736	1.2736	1.2736	1.2736	1.2736
0.5	0.75	0.3154	0.3154	0.7097	0.7097	1.2617	1.2617	1.2617	1.2617	1.2617
0.5	0.833	0.3122	0.3122	0.8665	0.8665	1.2487	1.2487	1.2487	1.2487	1.2487
0.5	1.0	0.3048	0.3048	1.2194	1.2194	1.2194	1.2194	1.2194	1.2194	1.2194
0.5	1.25	0.2922	0.2922	1.8264	1.8264	1.1689	1.1689	1.1689	1.1689	1.1689
0.5	1.333	0.2877	0.2877	2.0448	2.0448	1.1508	1.1508	1.1508	1.1508	1.1508
0.5	1.5	0.2782	0.2782	2.5034	2.5034	1.1126	1.1126	1.1126	1.1126	1.1126
0.5	2.0	0.2478	0.2478	3.9647	3.9647	0.9912	0.9912	0.9912	0.9912	0.9912
0.5	2.5	0.2173	0.2173	5.4325	5.4325	0.8692	0.8692	0.8692	0.8692	0.8692
0.5	3.0	0.1889	0.1889	6.7999	6.7999	0.7555	0.7555	0.7555	0.7555	0.7555
0.5	4.0	0.1417	0.1417	9.0699	9.0699	0.5669	0.5669	0.5669	0.5669	0.5669
0.5	6.0	0.0827	0.0827	11.9098	11.9098	0.3308	0.3308	0.3308	0.3308	0.3308

Table F.1: Scalings of Higgs decay branching ratios vs. κ_t and $\kappa_V = 0.5$ for the resolved model.

κ_V	κ_t	HWW	HZZ	H $\tau\tau$	H $\mu\mu$	Hbb	Hcc	H $\gamma\gamma$	HZ γ	Hgg
1.0	-6.0	0.3122	0.3122	11.2408	11.2408	0.3122	0.3122	0.3122	0.3122	0.3122
1.0	-4.0	0.5144	0.5144	8.2305	8.2305	0.5144	0.5144	0.5144	0.5144	0.5144
1.0	-3.0	0.6651	0.6651	5.9862	5.9862	0.6651	0.6651	0.6651	0.6651	0.6651
1.0	-2.5	0.7517	0.7517	4.6979	4.6979	0.7517	0.7517	0.7517	0.7517	0.7517
1.0	-2.0	0.8412	0.8412	3.3647	3.3647	0.8412	0.8412	0.8412	0.8412	0.8412
1.0	-1.5	0.9271	0.9271	2.0859	2.0859	0.9271	0.9271	0.9271	0.9271	0.9271
1.0	-1.333	0.9534	0.9534	1.6941	1.6941	0.9534	0.9534	0.9534	0.9534	0.9534
1.0	-1.25	0.9658	0.9658	1.5091	1.5091	0.9658	0.9658	0.9658	0.9658	0.9658
1.0	-1.0	1.0000	1.0000	1.0000	1.0000	1.0000	1.0000	1.0000	1.0000	1.0000
1.0	-0.833	1.0196	1.0196	0.7075	0.7075	1.0196	1.0196	1.0196	1.0196	1.0196
1.0	-0.75	1.0283	1.0283	0.5784	0.5784	1.0283	1.0283	1.0283	1.0283	1.0283
1.0	-0.667	1.0362	1.0362	0.4610	0.4610	1.0362	1.0362	1.0362	1.0362	1.0362
1.0	-0.5	1.0495	1.0495	0.2624	0.2624	1.0495	1.0495	1.0495	1.0495	1.0495
1.0	-0.333	1.0593	1.0593	0.1175	0.1175	1.0593	1.0593	1.0593	1.0593	1.0593
1.0	-0.25	1.0627	1.0627	0.0664	0.0664	1.0627	1.0627	1.0627	1.0627	1.0627
1.0	-0.167	1.0652	1.0652	0.0297	0.0297	1.0652	1.0652	1.0652	1.0652	1.0652
1.0	0.0	1.0672	1.0672	0.0000	0.0000	1.0672	1.0672	1.0672	1.0672	1.0672
1.0	0.167	1.0652	1.0652	0.0297	0.0297	1.0652	1.0652	1.0652	1.0652	1.0652
1.0	0.25	1.0627	1.0627	0.0664	0.0664	1.0627	1.0627	1.0627	1.0627	1.0627
1.0	0.333	1.0593	1.0593	0.1175	0.1175	1.0593	1.0593	1.0593	1.0593	1.0593
1.0	0.5	1.0495	1.0495	0.2624	0.2624	1.0495	1.0495	1.0495	1.0495	1.0495
1.0	0.667	1.0362	1.0362	0.4610	0.4610	1.0362	1.0362	1.0362	1.0362	1.0362
1.0	0.75	1.0283	1.0283	0.5784	0.5784	1.0283	1.0283	1.0283	1.0283	1.0283
1.0	0.833	1.0196	1.0196	0.7075	0.7075	1.0196	1.0196	1.0196	1.0196	1.0196
1.0	1.0	1.0000	1.0000	1.0000	1.0000	1.0000	1.0000	1.0000	1.0000	1.0000
1.0	1.25	0.9658	0.9658	1.5091	1.5091	0.9658	0.9658	0.9658	0.9658	0.9658
1.0	1.333	0.9534	0.9534	1.6941	1.6941	0.9534	0.9534	0.9534	0.9534	0.9534
1.0	1.5	0.9271	0.9271	2.0859	2.0859	0.9271	0.9271	0.9271	0.9271	0.9271
1.0	2.0	0.8412	0.8412	3.3647	3.3647	0.8412	0.8412	0.8412	0.8412	0.8412
1.0	2.5	0.7517	0.7517	4.6979	4.6979	0.7517	0.7517	0.7517	0.7517	0.7517
1.0	3.0	0.6651	0.6651	5.9862	5.9862	0.6651	0.6651	0.6651	0.6651	0.6651
1.0	4.0	0.5144	0.5144	8.2305	8.2305	0.5144	0.5144	0.5144	0.5144	0.5144
1.0	6.0	0.3122	0.3122	11.2408	11.2408	0.3122	0.3122	0.3122	0.3122	0.3122

Table F.2: Scalings of Higgs decay branching ratios vs. κ_t and $\kappa_V = 1.0$ for the resolved model.

κ_V	κ_t	HWW	HZZ	H $\tau\tau$	H $\mu\mu$	Hbb	Hcc	H $\gamma\gamma$	HZ γ	Hgg
1.5	-6.0	0.6424	0.6424	10.2785	10.2785	0.2855	0.2855	0.2855	0.2855	0.2855
1.5	-4.0	1.0028	1.0028	7.1307	7.1307	0.4457	0.4457	0.4457	0.4457	0.4457
1.5	-3.0	1.2477	1.2477	4.9909	4.9909	0.5545	0.5545	0.5545	0.5545	0.5545
1.5	-2.5	1.3802	1.3802	3.8338	3.8338	0.6134	0.6134	0.6134	0.6134	0.6134
1.5	-2.0	1.5115	1.5115	2.6870	2.6870	0.6718	0.6718	0.6718	0.6718	0.6718
1.5	-1.5	1.6322	1.6322	1.6322	1.6322	0.7254	0.7254	0.7254	0.7254	0.7254
1.5	-1.333	1.6682	1.6682	1.3175	1.3175	0.7414	0.7414	0.7414	0.7414	0.7414
1.5	-1.25	1.6851	1.6851	1.1702	1.1702	0.7489	0.7489	0.7489	0.7489	0.7489
1.5	-1.0	1.7310	1.7310	0.7693	0.7693	0.7693	0.7693	0.7693	0.7693	0.7693
1.5	-0.833	1.7570	1.7570	0.5419	0.5419	0.7809	0.7809	0.7809	0.7809	0.7809
1.5	-0.75	1.7684	1.7684	0.4421	0.4421	0.7860	0.7860	0.7860	0.7860	0.7860
1.5	-0.667	1.7788	1.7788	0.3517	0.3517	0.7906	0.7906	0.7906	0.7906	0.7906
1.5	-0.5	1.7962	1.7962	0.1996	0.1996	0.7983	0.7983	0.7983	0.7983	0.7983
1.5	-0.333	1.8089	1.8089	0.0891	0.0891	0.8039	0.8039	0.8039	0.8039	0.8039
1.5	-0.25	1.8133	1.8133	0.0504	0.0504	0.8059	0.8059	0.8059	0.8059	0.8059
1.5	-0.167	1.8165	1.8165	0.0225	0.0225	0.8073	0.8073	0.8073	0.8073	0.8073
1.5	0.0	1.8191	1.8191	0.0000	0.0000	0.8085	0.8085	0.8085	0.8085	0.8085
1.5	0.167	1.8165	1.8165	0.0225	0.0225	0.8073	0.8073	0.8073	0.8073	0.8073
1.5	0.25	1.8133	1.8133	0.0504	0.0504	0.8059	0.8059	0.8059	0.8059	0.8059
1.5	0.333	1.8089	1.8089	0.0891	0.0891	0.8039	0.8039	0.8039	0.8039	0.8039
1.5	0.5	1.7962	1.7962	0.1996	0.1996	0.7983	0.7983	0.7983	0.7983	0.7983
1.5	0.667	1.7788	1.7788	0.3517	0.3517	0.7906	0.7906	0.7906	0.7906	0.7906
1.5	0.75	1.7684	1.7684	0.4421	0.4421	0.7860	0.7860	0.7860	0.7860	0.7860
1.5	0.833	1.7570	1.7570	0.5419	0.5419	0.7809	0.7809	0.7809	0.7809	0.7809
1.5	1.0	1.7310	1.7310	0.7693	0.7693	0.7693	0.7693	0.7693	0.7693	0.7693
1.5	1.25	1.6851	1.6851	1.1702	1.1702	0.7489	0.7489	0.7489	0.7489	0.7489
1.5	1.333	1.6682	1.6682	1.3175	1.3175	0.7414	0.7414	0.7414	0.7414	0.7414
1.5	1.5	1.6322	1.6322	1.6322	1.6322	0.7254	0.7254	0.7254	0.7254	0.7254
1.5	2.0	1.5115	1.5115	2.6870	2.6870	0.6718	0.6718	0.6718	0.6718	0.6718
1.5	2.5	1.3802	1.3802	3.8338	3.8338	0.6134	0.6134	0.6134	0.6134	0.6134
1.5	3.0	1.2477	1.2477	4.9909	4.9909	0.5545	0.5545	0.5545	0.5545	0.5545
1.5	4.0	1.0028	1.0028	7.1307	7.1307	0.4457	0.4457	0.4457	0.4457	0.4457
1.5	6.0	0.6424	0.6424	10.2785	10.2785	0.2855	0.2855	0.2855	0.2855	0.2855

Table F.3: Scalings of Higgs decay branching ratios vs. κ_t and $\kappa_V = 1.5$ for the resolved model.

κ_V	κ_t	ttHWW	ttHZZ	ttH $\tau\tau$	tHqWW	tHqZZ	tHq $\tau\tau$	tHWWW	tHWZZ	tHW $\tau\tau$
0.5	-6.0	2.9775	2.9775	428.7530	9.2066	9.2066	1325.7460	9.7660	9.7660	1406.3049
0.5	-4.0	2.2675	2.2675	145.1182	7.5740	7.5740	484.7357	7.8819	7.8819	504.4411
0.5	-3.0	1.7000	1.7000	61.1988	6.1214	6.1214	220.3702	6.2562	6.2562	225.2227
0.5	-2.5	1.3581	1.3581	33.9529	5.1857	5.1857	129.6430	5.2277	5.2277	130.6931
0.5	-2.0	0.9912	0.9912	15.8589	4.1227	4.1227	65.9633	4.0762	4.0762	65.2197
0.5	-1.5	0.6259	0.6259	5.6327	2.9838	2.9838	26.8544	2.8645	2.8645	25.7805
0.5	-1.333	0.5112	0.5112	3.6333	2.6025	2.6025	18.4974	2.4648	2.4648	17.5190
0.5	-1.25	0.4566	0.4566	2.8538	2.4154	2.4154	15.0962	2.2700	2.2700	14.1878
0.5	-1.0	0.3048	0.3048	1.2194	1.8696	1.8696	7.4784	1.7078	1.7078	6.8310
0.5	-0.833	0.2166	0.2166	0.6012	1.5271	1.5271	4.2386	1.3605	1.3605	3.7760
0.5	-0.75	0.1774	0.1774	0.3992	1.3657	1.3657	3.0729	1.1987	1.1987	2.6970
0.5	-0.667	0.1417	0.1417	0.2521	1.2111	1.2111	2.1553	1.0451	1.0451	1.8598
0.5	-0.5	0.0809	0.0809	0.0809	0.9236	0.9236	0.9236	0.7640	0.7640	0.7640
0.5	-0.333	0.0363	0.0363	0.0161	0.6720	0.6720	0.2981	0.5249	0.5249	0.2328
0.5	-0.25	0.0205	0.0205	0.0051	0.5618	0.5618	0.1405	0.4231	0.4231	0.1058
0.5	-0.167	0.0092	0.0092	0.0010	0.4622	0.4622	0.0516	0.3334	0.3334	0.0372
0.5	0.0	0.0000	0.0000	0.0000	0.2953	0.2953	0.0000	0.1909	0.1909	0.0000
0.5	0.167	0.0092	0.0092	0.0010	0.1755	0.1755	0.0196	0.1010	0.1010	0.0113
0.5	0.25	0.0205	0.0205	0.0051	0.1339	0.1339	0.0335	0.0762	0.0762	0.0191
0.5	0.333	0.0363	0.0363	0.0161	0.1043	0.1043	0.0463	0.0647	0.0647	0.0287
0.5	0.5	0.0809	0.0809	0.0809	0.0809	0.0809	0.0809	0.0809	0.0809	0.0809
0.5	0.667	0.1417	0.1417	0.2521	0.1044	0.1044	0.1859	0.1480	0.1480	0.2634
0.5	0.75	0.1774	0.1774	0.3992	0.1329	0.1329	0.2991	0.1993	0.1993	0.4485
0.5	0.833	0.2166	0.2166	0.6012	0.1720	0.1720	0.4775	0.2620	0.2620	0.7272
0.5	1.0	0.3048	0.3048	1.2194	0.2811	0.2811	1.1243	0.4200	0.4200	1.6801
0.5	1.25	0.4566	0.4566	2.8538	0.5119	0.5119	3.1993	0.7270	0.7270	4.5438
0.5	1.333	0.5112	0.5112	3.6333	0.6041	0.6041	4.2939	0.8449	0.8449	6.0051
0.5	1.5	0.6259	0.6259	5.6327	0.8096	0.8096	7.2863	1.1020	1.1020	9.9179
0.5	2.0	0.9912	0.9912	15.8589	1.5402	1.5402	24.6428	1.9827	1.9827	31.7238
0.5	2.5	1.3581	1.3581	33.9529	2.3549	2.3549	58.8716	2.9329	2.9329	73.3233
0.5	3.0	1.7000	1.7000	61.1988	3.1686	3.1686	114.0678	3.8625	3.8625	139.0502
0.5	4.0	2.2675	2.2675	145.1182	4.6200	4.6200	295.6829	5.4873	5.4873	351.1881
0.5	6.0	2.9775	2.9775	428.7530	6.6207	6.6207	953.3740	7.6698	7.6698	1104.4467

Table F.4: Scalings of cross section times BR for the resolved model, for the different $t\bar{t}H$, tHq , tHW signal components and $\kappa_V = 0.5$.

κ_V	κ_t	ttHWW	ttHZZ	ttH $\tau\tau$	tHqWW	tHqZZ	tHq $\tau\tau$	tHWWW	tHWZZ	tHW $\tau\tau$
1.0	-6.0	11.2408	11.2408	404.6686	40.4768	40.4768	1457.1666	41.3681	41.3681	1489.2533
1.0	-4.0	8.2305	8.2305	131.6886	34.2339	34.2339	547.7422	33.8480	33.8480	541.5676
1.0	-3.0	5.9862	5.9862	53.8759	28.5396	28.5396	256.8562	27.3983	27.3983	246.5850
1.0	-2.5	4.6979	4.6979	29.3616	24.8511	24.8511	155.3195	23.3557	23.3557	145.9734
1.0	-2.0	3.3647	3.3647	13.4590	20.6360	20.6360	82.5440	18.8497	18.8497	75.3987
1.0	-1.5	2.0859	2.0859	4.6933	16.0557	16.0557	36.1254	14.0919	14.0919	31.7068
1.0	-1.333	1.6941	1.6941	3.0102	14.4942	14.4942	25.7545	12.5059	12.5059	22.2216
1.0	-1.25	1.5091	1.5091	2.3579	13.7201	13.7201	21.4377	11.7273	11.7273	18.3239
1.0	-1.0	1.0000	1.0000	1.0000	11.4220	11.4220	11.4220	9.4484	9.4484	9.4484
1.0	-0.833	0.7075	0.7075	0.4909	9.9372	9.9372	6.8953	8.0059	8.0059	5.5552
1.0	-0.75	0.5784	0.5784	0.3254	9.2212	9.2212	5.1869	7.3200	7.3200	4.1175
1.0	-0.667	0.4610	0.4610	0.2051	8.5229	8.5229	3.7917	6.6579	6.6579	2.9620
1.0	-0.5	0.2624	0.2624	0.0656	7.1807	7.1807	1.7952	5.4076	5.4076	1.3519
1.0	-0.333	0.1175	0.1175	0.0130	5.9375	5.9375	0.6584	4.2814	4.2814	0.4748
1.0	-0.25	0.0664	0.0664	0.0042	5.3616	5.3616	0.3351	3.7730	3.7730	0.2358
1.0	-0.167	0.0297	0.0297	0.0008	4.8163	4.8163	0.1343	3.3009	3.3009	0.0921
1.0	0.0	0.0000	0.0000	0.0000	3.8183	3.8183	0.0000	2.4676	2.4676	0.0000
1.0	0.167	0.0297	0.0297	0.0008	2.9624	2.9624	0.0826	1.7981	1.7981	0.0501
1.0	0.25	0.0664	0.0664	0.0042	2.5928	2.5928	0.1620	1.5284	1.5284	0.0955
1.0	0.333	0.1175	0.1175	0.0130	2.2612	2.2612	0.2507	1.3014	1.3014	0.1443
1.0	0.5	0.2624	0.2624	0.0656	1.7115	1.7115	0.4279	0.9742	0.9742	0.2435
1.0	0.667	0.4610	0.4610	0.2051	1.3198	1.3198	0.5871	0.8188	0.8188	0.3643
1.0	0.75	0.5784	0.5784	0.3254	1.1834	1.1834	0.6657	0.8042	0.8042	0.4524
1.0	0.833	0.7075	0.7075	0.4909	1.0852	1.0852	0.7530	0.8301	0.8301	0.5760
1.0	1.0	1.0000	1.0000	1.0000	1.0000	1.0000	1.0000	1.0000	1.0000	1.0000
1.0	1.25	1.5091	1.5091	2.3579	1.1380	1.1380	1.7782	1.5278	1.5278	2.3872
1.0	1.333	1.6941	1.6941	3.0102	1.2492	1.2492	2.2197	1.7691	1.7691	3.1434
1.0	1.5	2.0859	2.0859	4.6933	1.5628	1.5628	3.5163	2.3434	2.3434	5.2727
1.0	2.0	3.3647	3.3647	13.4590	3.1023	3.1023	12.4092	4.6362	4.6362	18.5449
1.0	2.5	4.6979	4.6979	29.3616	5.2667	5.2667	32.9167	7.4799	7.4799	46.7493
1.0	3.0	5.9862	5.9862	53.8759	7.7435	7.7435	69.6914	10.5403	10.5403	94.8625
1.0	4.0	8.2305	8.2305	131.6886	12.7892	12.7892	204.6276	16.4642	16.4642	263.4266
1.0	6.0	11.2408	11.2408	404.6686	20.9516	20.9516	754.2573	25.5403	25.5403	919.4497

Table F.5: Scalings of cross section times BR for the resolved model, for the different $t\bar{t}H$, tHq , tHW signal components and $\kappa_V = 1.0$.

κ_V	κ_t	ttHWW	ttHZZ	ttH $\tau\tau$	tHqWW	tHqZZ	tHq $\tau\tau$	tHWWW	tHWZZ	tHW $\tau\tau$
1.5	-6.0	23.1266	23.1266	370.0260	96.1923	96.1923	1539.0768	95.1080	95.1080	1521.7272
1.5	-4.0	16.0441	16.0441	114.0913	81.6690	81.6690	580.7570	77.3512	77.3512	550.0531
1.5	-3.0	11.2295	11.2295	44.9178	68.8703	68.8703	275.4812	62.9086	62.9086	251.6344
1.5	-2.5	8.6261	8.6261	23.9614	60.7939	60.7939	168.8720	54.1622	54.1622	150.4505
1.5	-2.0	6.0458	6.0458	10.7481	51.7152	51.7152	91.9381	44.6227	44.6227	79.3293
1.5	-1.5	3.6725	3.6725	3.6725	41.9469	41.9469	41.9469	34.6991	34.6991	34.6991
1.5	-1.333	2.9643	2.9643	2.3410	38.6171	38.6171	30.4971	31.4016	31.4016	24.7987
1.5	-1.25	2.6330	2.6330	1.8284	36.9629	36.9629	25.6687	29.7807	29.7807	20.6810
1.5	-1.0	1.7310	1.7310	0.7693	32.0233	32.0233	14.2326	25.0144	25.0144	11.1175
1.5	-0.833	1.2192	1.2192	0.3760	28.7953	28.7953	8.8803	21.9653	21.9653	6.7740
1.5	-0.75	0.9948	0.9948	0.2487	27.2234	27.2234	6.8058	20.5014	20.5014	5.1254
1.5	-0.667	0.7914	0.7914	0.1565	25.6778	25.6778	5.0772	19.0767	19.0767	3.7720
1.5	-0.5	0.4491	0.4491	0.0499	22.6628	22.6628	2.5181	16.3435	16.3435	1.8159
1.5	-0.333	0.2006	0.2006	0.0099	19.7986	19.7986	0.9758	13.8117	13.8117	0.6807
1.5	-0.25	0.1133	0.1133	0.0031	18.4397	18.4397	0.5122	12.6364	12.6364	0.3510
1.5	-0.167	0.0507	0.0507	0.0006	17.1281	17.1281	0.2123	11.5203	11.5203	0.1428
1.5	0.0	0.0000	0.0000	0.0000	14.6443	14.6443	0.0000	9.4640	9.4640	0.0000
1.5	0.167	0.0507	0.0507	0.0006	12.3858	12.3858	0.1535	7.6760	7.6760	0.0951
1.5	0.25	0.1133	0.1133	0.0031	11.3529	11.3529	0.3154	6.8916	6.8916	0.1914
1.5	0.333	0.2006	0.2006	0.0099	10.3820	10.3820	0.5117	6.1783	6.1783	0.3045
1.5	0.5	0.4491	0.4491	0.0499	8.6227	8.6227	0.9581	4.9621	4.9621	0.5513
1.5	0.667	0.7914	0.7914	0.1565	7.1299	7.1299	1.4098	4.0411	4.0411	0.7990
1.5	0.75	0.9948	0.9948	0.2487	6.4888	6.4888	1.6222	3.6932	3.6932	0.9233
1.5	0.833	1.2192	1.2192	0.3760	5.9148	5.9148	1.8241	3.4176	3.4176	1.0540
1.5	1.0	1.7310	1.7310	0.7693	4.9627	4.9627	2.2057	3.0782	3.0782	1.3681
1.5	1.25	2.6330	2.6330	1.8284	4.0340	4.0340	2.8014	3.0873	3.0873	2.1440
1.5	1.333	2.9643	2.9643	2.3410	3.8531	3.8531	3.0429	3.2206	3.2206	2.5434
1.5	1.5	3.6725	3.6725	3.6725	3.6725	3.6725	3.6725	3.6725	3.6725	3.6725
1.5	2.0	6.0458	6.0458	10.7481	4.4580	4.4580	7.9254	6.3144	6.3144	11.2255
1.5	2.5	8.6261	8.6261	23.9614	6.8533	6.8533	19.0368	10.4359	10.4359	28.9887
1.5	3.0	11.2295	11.2295	44.9178	10.3536	10.3536	41.4143	15.4728	15.4728	61.8913
1.5	4.0	16.0441	16.0441	114.0913	18.9646	18.9646	134.8595	26.5208	26.5208	188.5926
1.5	6.0	23.1266	23.1266	370.0260	35.9359	35.9359	574.9741	46.2619	46.2619	740.1909

Table F.6: Scalings of cross section times BR for the resolved model, for the different $t\bar{t}H$, tHq , tHW signal components and $\kappa_V = 1.5$.

3137 References

- 3138 [1] J. Schwinger. "Quantum Electrodynamics. I. A Covariant Formulation". Phys-
 3139 ical Review. 74 (10): 1439-61, (1948). <https://doi.org/10.1103/PhysRev.74.1439>
- 3141 [2] R. P. Feynman. "Space-Time Approach to Quantum Electrodynamics". Physical
 3142 Review. 76 (6): 769-89, (1949). <https://doi.org/10.1103/PhysRev.76.769>
- 3143 [3] S. Tomonaga. "On a Relativistically Invariant Formulation of the Quantum
 3144 Theory of Wave Fields". Progress of Theoretical Physics. 1 (2): 27-42, (1946).
 3145 <https://doi.org/10.1143/PTP.1.27>
- 3146 [4] D.J. Griffiths, "Introduction to electrodynamics". 4th ed. Pearson, (2013).
- 3147 [5] F. Mandl, G. Shaw. "Quantum field theory." Chichester, Wiley (2009).
- 3148 [6] F. Halzen, and A.D. Martin, "Quarks and leptons: An introductory course in
 3149 modern particle physics". New York: Wiley, (1984) .
- 3150 [7] File: Standard_Model_of_Elementary_Particle_dark.svg. (2017, June 12)
 3151 Wikimedia Commons, the free media repository. Retrieved November 27, 2017
 3152 from <https://www.collegiate-advanced-electricity.com/single-post/2017/04/10/The-Standard-Model-of-Particle-Physics>.

- 3154 [8] E. Noether, "Invariante Variationsprobleme", Nachrichten von der Gesellschaft
3155 der Wissenschaften zu Göttingen, mathematisch-physikalische Klasse, vol. 1918,
3156 pp. 235-257, (1918).
- 3157 [9] C. Patrignani et al. (Particle Data Group), Chin. Phys. C, 40, 100001 (2016)
3158 and 2017 update.
- 3159 [10] M. Goldhaber, L. Grodzins, A.W. Sunyar "Helicity of Neutrinos", Phys. Rev.
3160 109, 1015 (1958).
- 3161 [11] Palanque-Delabrouille N et al. "Neutrino masses and cosmology with Lyman-
3162 alpha forest power spectrum", JCAP 11 011 (2015).
- 3163 [12] M. Gell-Mann. "A Schematic Model of Baryons and Mesons". Physics Letters.
3164 8 (3): 214-215 (1964).
- 3165 [13] G. Zweig. "An SU(3) Model for Strong Interaction Symmetry and its Breaking"
3166 (PDF). CERN Report No.8182/TH.401 (1964).
- 3167 [14] G. Zweig. "An SU(3) Model for Strong Interaction Symmetry and its Breaking:
3168 II" (PDF). CERN Report No.8419/TH.412(1964).
- 3169 [15] M. Gell-Mann. "The Interpretation of the New Particles as Displaced Charged
3170 Multiplets". Il Nuovo Cimento 4: 848. (1956).
- 3171 [16] T. Nakano, K. Nishijima. "Charge Independence for V-particles". Progress of
3172 Theoretical Physics 10 (5): 581-582. (1953).
- 3173 [17] N. Cabibbo, "Unitary symmetry and leptonic decays" Physical Review Letters,
3174 vol. 10, no. 12, p. 531, (1963).

- 3175 [18] M.Kobayashi, T.Maskawa, “CP-violation in the renormalizable theory of weak
3176 interaction,” Progress of Theoretical Physics, vol. 49, no. 2, pp. 652-657, (1973).
- 3177 [19] File: Weak Decay (flipped).svg. (2017, June 12). Wikimedia Com-
3178 mons, the free media repository. Retrieved November 27, 2017
3179 from [https://commons.wikimedia.org/w/index.php?title=File:
3180 Weak_Decay_\(flipped\)\.svg&oldid=247498592](https://commons.wikimedia.org/w/index.php?title=File:Weak_Decay_(flipped)\.svg&oldid=247498592).
- 3181 [20] Georgia Tech University. Coupling Constants for the Fundamental Forces(2005).
3182 Retrieved January 10, 2018, from [http://hyperphysics.phy-astr.gsu.edu/
3183 hbase/Forces/couple.html#c2](http://hyperphysics.phy-astr.gsu.edu/hbase/Forces/couple.html#c2)
- 3184 [21] M. Strassler. (May 31, 2013).The Strengths of the Known Forces. Retrieved Jan-
3185 uary 10, 2018, from [https://profmattstrassler.com/articles-and-posts/
3186 particle-physics-basics/the-known-forces-of-nature/
3187 the-strength-of-the-known-forces/](https://profmattstrassler.com/articles-and-posts/particle-physics-basics/the-known-forces-of-nature/the-strength-of-the-known-forces/)
- 3188 [22] S.L. Glashow. “Partial symmetries of weak interactions”, Nucl. Phys. 22 579-
3189 588, (1961).
- 3190 [23] A. Salam, J.C. Ward. “Electromagnetic and weak interactions”, Physics Letters
3191 13 168-171, (1964).
- 3192 [24] S. Weinberg, “A model of leptons”, Physical Review Letters, vol. 19, no. 21, p.
3193 1264, (1967).
- 3194 [25] M. Peskin, D. Schroeder, “An introduction to quantum field theory”. Perseus
3195 Books Publishing L.L.C., (1995).
- 3196 [26] A. Pich. “The Standard Model of Electroweak Interactions” <https://arxiv.org/abs/1201.0537>
- 3197

- 3198 [27] G. Arnison et al. (UA1 Collaboration), Phys. Lett. B 122, 103 (1983).
- 3199 [28] M. Banner et al. (UA2 Collaboration), Phys. Lett. B 122, 476 (1983).
- 3200 [29] G. Arnison et al. (UA1 Collaboration), Phys. Lett. B 126, 398 (1983).
- 3201 [30] P. Bagnaia et al. (UA2 Collaboration), Phys. Lett. B 129, 130 (1983).
- 3202 [31] F.Bellaiche. (2012, 2 September). “What’s this Higgs boson anyway?”. Retrieved
3203 from: <https://www.quantum-bits.org/?p=233>
- 3204 [32] M. Endres et al. Nature 487, 454-458 (2012) doi:10.1038/nature11255
- 3205 [33] F. Englert, R. Brout. “Broken Symmetry and the Mass of Gauge
3206 Vector Mesons”. Physical Review Letters. 13 (9): 321-23.(1964)
3207 doi:10.1103/PhysRevLett.13.321
- 3208 [34] P.Higgs. “Broken Symmetries and the Masses of Gauge Bosons”. Physical Re-
3209 view Letters. 13 (16): 508-509,(1964). doi:10.1103/PhysRevLett.13.508.
- 3210 [35] G.Guralnik, C.R. Hagen and T.W.B. Kibble. “Global Conservation Laws
3211 and Massless Particles”. Physical Review Letters. 13 (20): 585-587, (1964).
3212 doi:10.1103/PhysRevLett.13.585.
- 3213 [36] CMS collaboration. “Observation of a new boson at a mass of 125 GeV with
3214 the CMS experiment at the LHC”. Physics Letters B. 716 (1): 30-61 (2012).
3215 arXiv:1207.7235. doi:10.1016/j.physletb.2012.08.021
- 3216 [37] ATLAS collaboration. “Observation of a New Particle in the Search for the Stan-
3217 dard Model Higgs Boson with the ATLAS Detector at the LHC”. Physics Letters
3218 B. 716 (1): 1-29 (2012). arXiv:1207.7214. doi:10.1016/j.physletb.2012.08.020.

- 3219 [38] ATLAS collaboration; CMS collaboration (26 March 2015). “Combined Mea-
 3220 surement of the Higgs Boson Mass in pp Collisions at $\sqrt{s}=7$ and 8 TeV with
 3221 the ATLAS and CMS Experiments”. Physical Review Letters. 114 (19): 191803.
 3222 arXiv:1503.07589. doi:10.1103/PhysRevLett.114.191803.
- 3223 [39] LHC InternationalMasterclasses“When protons collide”. Retrieved from http://atlas.physicsmasterclasses.org/en/zpath_protoncollisions.htm
- 3225 [40] CMS Collaboration, “SM Higgs Branching Ratios and Total Decay Widths (up-
 3226 date in CERN Report4 2016)”. <https://twiki.cern.ch/twiki/bin/view/LHCPhysics/CERNYellowReportPageBR> , last accessed on 17.12.2017.
- 3228 [41] R.Grant V. “Determination of Higgs branching ratios in $H \rightarrow W^+W^- \rightarrow l\nu jj$
 3229 and $H \rightarrow ZZ \rightarrow l^+l^-jj$ channels”. Physics Department, University of Ten-
 3230 nessee (Dated: October 31, 2012). Retrieved from <http://aesop.phys.utk.edu/ph611/2012/projects/Riley.pdf>
- 3232 [42] LHC Higgs Cross Section Working Group, Denner, A., Heinemeyer, S. et al.
 3233 “Standard model Higgs-boson branching ratios with uncertainties”. Eur. Phys.
 3234 J. C (2011) 71: 1753. <https://doi.org/10.1140/epjc/s10052-011-1753-8>
- 3235 [43] D. de Florian et al., LHC Higgs Cross Section Working Group,
 3236 CERNâš2017âš002-M, arXiv:1610.07922[hep-ph] (2016).
- 3237 [44] ATLAS and CMS Collaborations, “Measurements of the Higgs boson produc-
 3238 tion and decay rates and constraints on its couplings from a combined ATLAS
 3239 and CMS analysis of the LHC pp collision data at $\sqrt{s} = 7$ and 8 TeV,” (2016).
 3240 CERN-EP-2016-100, ATLAS-HIGG-2015-07, CMS-HIG-15-002.

- 3241 [45] J. A. Aguilar-Saavedra, R. Benbrik, S. Heinemeyer, and M. Perez-Victoria,
3242 “Handbook of vector-like quarks: Mixing and single production”, Phys. Rev. D
3243 88 (2013) 094010, doi:10.1103/PhysRevD.88.094010, arXiv:1306.0572.
- 3244 [46] A. Greljo, J. F. Kamenik, and J. Kopp, “Disentangling flavor vio-
3245 lation in the top-Higgs sector at the LHC”, JHEP 07 (2014) 046,
3246 doi:10.1007/JHEP07(2014)046, arXiv:1404.1278.
- 3247 [47] F. Demartin, F. Maltoni, K. Mawatari, and M. Zaro, “Higgs production in
3248 association with a single top quark at the LHC,” European Physical Journal C,
3249 vol. 75, p. 267, (2015). doi:10.1140/epjc/s10052-015-3475-9, arXiv:1504.00611.
- 3250 [48] F. Demartin, B. Maier, F. Maltoni, K. Mawatari, and M. Zaro, “tWH associated
3251 production at the LHC”, European Physical Journal C, vol. 77, p. 34, (2017).
3252 arXiv:1607.05862
- 3253 [49] F. Maltoni, K. Paul, T. Stelzer, and S. Willenbrock, “Associated production
3254 of Higgs and single top at hadron colliders”, Phys.Rev. D64 (2001) 094023,
3255 [hep-ph/0106293].
- 3256 [50] S. Biswas, E. Gabrielli, F. Margaroli, and B. Mele, “Direct constraints on the
3257 top-Higgs coupling from the 8 TeV LHC data,” Journal of High Energy Physics,
3258 vol. 07, p. 073, (2013).
- 3259 [51] M. Farina, C. Grojean, F. Maltoni, E. Salvioni, and A. Thamm, “Lifting de-
3260 generacies in Higgs couplings using single top production in association with a
3261 Higgs boson,” Journal of High Energy Physics, vol. 05, p. 022, (2013).
- 3262 [52] T.M. Tait and C.-P. Yuan, “Single top quark production as a window to physics
3263 beyond the standard model”, Phys. Rev. D 63 (2000) 014018 [hep-ph/0007298].

- 3264 [53] CMS Collaboration, “Modelling of the single top-quark production in associa-
3265 tion with the Higgs boson at 13 TeV.” <https://twiki.cern.ch/twiki/bin/viewauth/CMS/SingleTopHiggsGeneration13TeV>, last accessed on 16.01.2018.
3266
- 3267 [54] CMS Collaboration, “SM Higgs production cross sections at $\sqrt{s} =$
3268 13 TeV.” <https://twiki.cern.ch/twiki/bin/view/LHCPhysics/CERNYellowReportPageAt13TeV>, last accessed on 16.01.2018.
3269
- 3270 [55] S. Dawson, The effective W approximation, Nucl. Phys. B 249 (1985) 42.
- 3271 [56] S. Biswas, E. Gabrielli and B. Mele, JHEP 1301 (2013) 088 [arXiv:1211.0499
3272 [hep-ph]].
- 3273 [57] LHC Higgs Cross Section Working Group, “Handbook of LHC Higgs Cross
3274 Sections: 4.Deciphering the Nature of the Higgs Sector”, arXiv:1610.07922.
- 3275 [58] J. Ellis, D. S. Hwang, K. Sakurai, and M. Takeuchi.“Disentangling Higgs-Top
3276 Couplings in Associated Production”, JHEP 1404 (2014) 004, [arXiv:1312.5736].
- 3277 [59] CMS Collaboration, V. Khachatryan et al., “Precise determination of the mass
3278 of the Higgs boson and tests of compatibility of its couplings with the standard
3279 model predictions using proton collisions at 7 and 8 TeV,” arXiv:1412.8662.
- 3280 [60] ATLAS Collaboration, G. Aad et al., “Updated coupling measurements of the
3281 Higgs boson with the ATLAS detector using up to 25 fb^{-1} of proton-proton
3282 collision data”, ATLAS-CONF-2014-009.
- 3283 [61] File:Cern-accelerator-complex.svg. Wikimedia Commons, the free media repos-
3284 itory. Retrieved January, 2018 from <https://commons.wikimedia.org/wiki/File:Cern-accelerator-complex.svg>
3285

- 3286 [62] J.L. Caron , “Layout of the LEP tunnel including future LHC infrastructures.”,
3287 (Nov, 1993). A C Collection. Legacy of AC. Pictures from 1992 to 2002. Re-
3288 trieved from <https://cds.cern.ch/record/841542>
- 3289 [63] M. Vretenar, “The radio-frequency quadrupole”. CERN Yellow Report CERN-
3290 2013-001, pp.207-223 DOI:10.5170/CERN-2013-001.207. arXiv:1303.6762
- 3291 [64] L.Evans. P. Bryant (editors). “LHC Machine”. JINST 3 S08001 (2008).
- 3292 [65] CERN Photographic Service.“Radio-frequency quadrupole, RFQ-1”, March
3293 1983, CERN-AC-8303511. Retrieved from <https://cds.cern.ch/record/615852>.
- 3295 [66] CERN Photographic Service “Animation of CERN’s accelerator network”, 14
3296 October 2013. DOI: 10.17181/cds.1610170 Retrieved from <https://videos.cern.ch/record/1610170>
- 3298 [67] C.Sutton. “Particle accelerator”.Encyclopedia Britannica. July 17,
3299 2013. Retrieved from <https://www.britannica.com/technology/particle-accelerator>.
- 3301 [68] L.Guiraud. “Installation of LHC cavity in vacuum tank.”. July 27 2000. CERN-
3302 AC-0007016. Retrieved from <https://cds.cern.ch/record/41567>.
- 3303 [69] J.L. Caron, “Magnetic field induced by the LHC dipole’s superconducting coils”.
3304 March 1998. AC Collection. Legacy of AC. Pictures from 1992 to 2002. LHC-
3305 PHO-1998-325. Retrieved from <https://cds.cern.ch/record/841511>.
- 3306 [70] AC Team. “Diagram of an LHC dipole magnet”. June 1999. CERN-DI-9906025
3307 retrieved from <https://cds.cern.ch/record/40524>.

- 3308 [71] CMS Collaboration “Public CMS Luminosity Information”. https://twiki.cern.ch/twiki/bin/view/CMSPublic/LumiPublicResults#2016__proton_proton_13_TeV_collis, last accessed 24.01.2018
- 3311 [72] J.L Caron. “LHC Layout” AC Collection. Legacy of AC. Pictures from 1992
3312 to 2002. September 1997, LHC-PHO-1997-060. Retrieved from <https://cds.cern.ch/record/841573>.
- 3314 [73] J.A. Coarasa. “The CMS Online Cluster:Setup, Operation and Maintenance
3315 of an Evolving Cluster”. ISGC 2012, 26 February - 2 March 2012, Academia
3316 Sinica, Taipei, Taiwan.
- 3317 [74] CMS Collaboration. “The CMS experiment at the CERN LHC” JINST 3 S08004
3318 (2008).
- 3319 [75] CMS Collaboration. “CMS detector drawings 2012” CMS-PHO-GEN-2012-002.
3320 Retrieved from <http://cds.cern.ch/record/1433717>.
- 3321 [76] Davis, Siona Ruth. “Interactive Slice of the CMS detector”, Aug. 2016,
3322 CMS-OUTREACH-2016-027, retrieved from <https://cds.cern.ch/record/2205172>
- 3324 [77] R. Breedon. “View through the CMS detector during the cooldown of the
3325 solenoid on February 2006. CMS Collection”, February 2006, CMS-PHO-
3326 OREACH-2005-004, Retrieved from <https://cds.cern.ch/record/930094>.
- 3327 [78] Halyo, V. and LeGresley, P. and Lujan, P. “Massively Parallel Computing and
3328 the Search for Jets and Black Holes at the LHC”, Nucl.Instrum.Meth. A744
3329 (2014) 54-60, DOI: 10.1016/j.nima.2014.01.038”

- 3330 [79] A. Dominguez et. al. “CMS Technical Design Report for the Pixel Detector
3331 Upgrade”, CERN-LHCC-2012-016. CMS-TDR-11.
- 3332 [80] CMS Collaboration. “Description and performance of track and primary-vertex
3333 reconstruction with the CMS tracker,” Journal of Instrumentation, vol. 9, no.
3334 10, p. P10009,(2014).
- 3335 [81] CMS Collaboration and M. Brice. “Images of the CMS Tracker Inner Bar-
3336 rel”, November 2008, CMS-PHO-TRACKER-2008-002. Retrieved from <https://cds.cern.ch/record/1431467>.
- 3338 [82] M. Weber. “The CMS tracker”. 6th international conference on hyperons, charm
3339 and beauty hadrons Chicago, June 28-July 3 2004.
- 3340 [83] CMS Collaboration. “Projected Performance of an Upgraded CMS Detector at
3341 the LHC and HL-LHC: Contribution to the Snowmass Process”. Jul 26, 2013.
3342 arXiv:1307.7135
- 3343 [84] L. Veillet. “End assembly of HB with EB rails and rotation inside SX ”,Jan-
3344 uary 2002. CMS-PHO-HCAL-2002-002. Retrieved from <https://cds.cern.ch/record/42594>.
- 3346 [85] J. Puerta-Pelayo.“First DT+RPC chambers installation round in the UX5 cav-
3347 ern.”. January 2007, CMS-PHO-OREACH-2007-001. Retrieved from <https://cds.cern.ch/record/1019185>
- 3349 [86] X. Cid Vidal and R. Cid Manzano. “CMS Global Muon Trigger” web site:
3350 Taking a closer look at LHC. Retrieved from https://www.lhc-closer.es/taking_a_closer_look_at_lhc/0.lhc_trigger

- 3352 [87] WLCG Project Office, “Documents & Reference - Tiers - Structure,”
 3353 (2014). <http://wlcg.web.cern.ch/documents-reference> , last accessed on
 3354 30.01.2018.
- 3355 [88] CMS Collaboration. “CMSSW Application Framework”, <https://twiki.cern.ch/twiki/bin/view/CMSPublic/WorkBookCMSSWFramework>,
 3356 last accesses 06.02.2018
 3357
- 3358 [89] A. Buckleya, J. Butterworthb, S. Giesekec, et. al. “General-purpose event gen-
 3359 erators for LHC physics”. arXiv:1101.2599v1 [hep-ph] 13 Jan 2011
- 3360 [90] A. Quadt. “Top Quark Physics at Hadron Colliders”. Advances in the Physics
 3361 of Particles and Nuclei. Springer-Verlag Berlin Heidelberg. DOI: 10.1007/978-
 3362 3-540-71060-8 (2007)
- 3363 [91] DurhamHep Data Project, “The Durham HepData Project - PDF Plotter.”
 3364 <http://hepdata.cedar.ac.uk/pdf/pdf3.html> , last accessed on 02.02.2018.
- 3365 [92] G. Altarelli and G. Parisi. “ASYMPTOTIC FREEDOM IN PARTON LAN-
 3366 GUAGE”, Nucl.Phys. B126:298 (1977).
- 3367 [93] Yu.L. Dokshitzer. Sov.Phys. JETP 46:641 (1977)
- 3368 [94] V.N. Gribov, L.N. Lipatov. “Deep inelastic e p scattering in perturbation the-
 3369 ory”, Sov.J.Nucl.Phys. 15:438 (1972)
- 3370 [95] F. Maltoni, G. Ridolfi, and M. Ubiali, “b-initiated processes at the LHC: a
 3371 reappraisal,” Journal of High Energy Physics, vol. 07, p. 022, (2012).
- 3372 [96] B. Andersson, G. Gustafson, G.Ingelman and T. Sjostrand, “Parton fragmen-
 3373 tation and string dynamics”, Physics Reports, Vol. 97, No. 2-3, pp. 31-145,
 3374 1983.

- 3375 [97] CMS Collaboration, “Event generator tunes obtained from underlying event
3376 and multiparton scattering measurements;” European Physical Journal C, vol.
3377 76, no. 3, p. 155, (2016).
- 3378 [98] J. Alwall et. al., “The automated computation of tree-level and next-to-leading
3379 order differential cross sections, and their matching to parton shower simula-
3380 tions,” Journal of High Energy Physics, vol. 07, p. 079, (2014).
- 3381 [99] T. Sjöstrand and P. Z. Skands, “Transverse-momentum-ordered showers and
3382 interleaved multiple interactions,” European Physical Journal C, vol. 39, pp.
3383 129–154, (2005).
- 3384 [100] S. Frixione, P. Nason, and C. Oleari, “Matching NLO QCD computations with
3385 Parton Shower simulations: the POWHEG method,” Journal of High Energy
3386 Physics, vol. 11, p. 070, (2007).
- 3387 [101] S. Agostinelli et al., “GEANT4: A Simulation toolkit,” Nuclear Instruments
3388 and Methods in Physics, vol. A506, pp. 250–303, (2003).
- 3389 [102] J.Allison et.al.,“Recent developments in Geant4”, Nuclear Instruments and
3390 Methods in Physics Research A 835 (2016) 186-225.
- 3391 [103] CMS Collaboration “Full Simulation Offline Guide”, <https://twiki.cern.ch/twiki/bin/view/CMSPublic/SWGuideSimulation>, last accessed 04.02.2018
- 3393 [104] A. Giammanco. “The Fast Simulation of the CMS Experiment” J. Phys.: Conf.
3394 Ser. 513 022012 (2014)
- 3395 [105] A.M. Sirunyan et. al. “Particle-flow reconstruction and global event description
3396 with the CMS detector”, JINST 12 P10003 (2017) <https://doi.org/10.1088/1748-0221/12/10/P10003>.

- 3398 [106] The CMS Collaboration. “ Description and performance of track and pri-
 3399 mary vertex reconstruction with the CMS tracker”. JINST 9 P10009 (2014).
 3400 doi:10.1088/1748-0221/9/10/P10009
- 3401 [107] J. Incandela. “Status of the CMS SM Higgs Search” July 4, 2012. Pdf slides.
 3402 Retrieved from https://indico.cern.ch/event/197461/contributions/1478917/attachments/290954/406673/CMS_4July2012_Final.pdf
- 3404 [108] P. Billoir and S. Qian, “Simultaneous pattern recognition and track fitting by
 3405 the Kalman filtering method”, Nucl. Instrum. Meth. A 294 219. (1990).
- 3406 [109] W. Adam, R. Fruhwirth, A. Strandlie and T. Todorov, “Reconstruction of
 3407 electrons with the Gaussian sum filter in the CMS tracker at LHC”, eConf
 3408 C 0303241 (2003) TULT009 [physics/0306087].
- 3409 [110] K. Rose, “Deterministic Annealing for Clustering, Compression, Classification,
 3410 Regression and related Optimisation Problems”, Proc. IEEE 86 (1998) 2210.
- 3411 [111] R. Fruhwirth, W. Waltenberger and P. Vanlaer, “ Adaptive Vertex Fitting”,
 3412 CMS Note 2007-008 (2007).
- 3413 [112] CMS collaboration, “Performance of CMS muon reconstruction in pp collision
 3414 events at $\sqrt{s} = 7 \text{ TeV}$ ”, JINST 7 P10002 2012, [arXiv:1206.4071].
- 3415 [113] Coco, Victor and Delsart, Pierre-Antoine and Rojo-Chacon, Juan and Soyez,
 3416 Gregory and Sander, Christian, “Jets and jet algorithms”, Proceedings,
 3417 HERA and the LHC Workshop Series on the implications of HERA for LHC
 3418 physics: 2006-2008, pag. 182-204. <http://inspirehep.net/record/866539/files/access.pdf>, (2009), doi:10.3204/DESY-PROC-2009-02/54

- 3420 [114] M. Cacciari, G. P. Salam, and G. Soyez, “The anti- k_t jet clustering algorithm,”
 3421 Journal of High Energy Physics, vol. 04, p. 063, (2008).
- 3422 [115] S. Catani, Y. L. Dokshitzer, M. H. Seymour, and B. R. Webber, “Longitudi-
 3423 nally invariant K_t clustering algorithms for hadron hadron collisions”, Nuclear
 3424 Physics B, vol. 406, pp. 187–224, (1993).
- 3425 [116] Y.L. Dokshitzer, G.D. Leder, S.Moretti, and B.R. Webber, “Better jet clustering
 3426 algorithms,” Journal of High Energy Physics, vol. 08, p. 001, (1997).
- 3427 [117] B. Dorney. “Anatomy of a Jet in CMS”. Quantum Diaries. June
 3428 1st, 2011. Retrieved from [https://www.quantumdiaries.org/2011/06/01/
 3429 anatomy-of-a-jet-in-cms/](https://www.quantumdiaries.org/2011/06/01/anatomy-of-a-jet-in-cms/)
- 3430 [118] The CMS Collaboration.“Event Displays from the high-energy collisions at 7
 3431 TeV”, May 2010, CMS-PHO-EVENTS-2010-007, Retrieved from [https://cds.
 3432 cern.ch/record/1429614](https://cds.cern.ch/record/1429614).
- 3433 [119] The CMS collaboration. “Determination of jet energy calibration and transverse
 3434 momentum resolution in CMS”. JINST 6 P11002 (2011). [http://dx.doi.org/
 3435 10.1088/1748-0221/6/11/P11002](http://dx.doi.org/10.1088/1748-0221/6/11/P11002)
- 3436 [120] The CMS Collaboration, “Introduction to Jet Energy Corrections at
 3437 CMS.”. <https://twiki.cern.ch/twiki/bin/view/CMS/IntroToJEC>, last ac-
 3438 cessed 10.02.2018.
- 3439 [121] CMS Collaboration Collaboration. “Identification of b quark jets at the CMS
 3440 Experiment in the LHC Run 2”. Tech. rep. CMS-PAS-BTV-15-001. Geneva:
 3441 CERN, (2016). <https://cds.cern.ch/record/2138504>.

- 3442 [122] CMS Collaboration Collaboration. “Performance of missing energy reconstruc-
3443 tion in 13 TeV pp collision data using the CMS detector”. Tech. rep. CMS-PAS-
3444 JME16-004. Geneva: CERN, 2016. <https://cds.cern.ch/record/2205284>.
- 3445 [123] CMS Collaboration, “New CMS results at Moriond (Electroweak) 2013”,
3446 Retrieved from <http://cms.web.cern.ch/sites/cms.web.cern.ch/files/>
3447 [styles/large/public/field/image/HIG13004_Event01_0.png?itok=L AwZzPHR](#)
- 3449 [124] CMS Collaboration, “New CMS results at Moriond (Electroweak) 2013”,
3450 Retrieved from <http://cms.web.cern.ch/sites/cms.web.cern.ch/>
3451 [files/styles/large/public/field/image/TOP12035_Event01.png?itok=uMdnSqzC](#)
- 3453 [125] K. Skovpen. “Event displays highlighting the main properties of heavy flavour
3454 jets in the CMS Experiment”, Aug 2017, CMS-PHO-EVENTS-2017-006. Re-
3455 trieval from <https://cds.cern.ch/record/2280025>.
- 3456 [126] G. Cowan. “Topics in statistical data analysis for high-energy physics”.
3457 arXiv:1012.3589v1
- 3458 [127] A. Hoecker et al., “TMVA-Toolkit for multivariate data analysis”
3459 arXiv:physics/0703039v5 (2009)
- 3460 [128] L. Lista. “Statistical Methods for Data Analysis in Particle Physics”, 2nd
3461 ed. Springer International Publishing. (2017) <https://dx.doi.org/10.1007/978-3-319-62840-0>

- 3463 [129] I. Antcheva et al., “ROOT-A C++ framework for petabyte data storage, sta-
 3464 tistical analysis and visualization ,” Computer Physics Communications, vol.
 3465 182, no. 6, pp. 1384â€¢1385, (2011).
- 3466 [130] Y. Coadou. “Boosted decision trees”, ESIPAP, Archamps, 9 Febru-
 3467 ary 2016. Lecture. Retrieved from https://indico.cern.ch/event/472305/contributions/1982360/attachments/1224979/1792797/ESIPAP_MVA160208-BDT.pdf
- 3470 [131] J.H. Friedman. “Greedy function approximation: A gradient boosting ma-
 3471 chine”. Ann. Statist. Volume 29, Number 5 (2001), 1189-1232. https://projecteuclid.org/download/pdf_1/euclid-aos/1013203451.
- 3473 [132] W. Verkerke and D. Kirkby, “The RooFit toolkit for data modeling,” arXiv
 3474 preprint physics, (2003).
- 3475 [133] CMS Collaboration, “Documentation of the RooStats-based statistics
 3476 tools for Higgs PAG”. <https://twiki.cern.ch/twiki/bin/view/CMS/SWGuideHiggsAnalysisCombinedLimit>, last accessed on 08.04.2018.
- 3478 [134] F. James, M. Roos, “MINUIT: Function minimization and error analysis”. Cern
 3479 Computer Centre Program Library, Geneve Long Write-up No. D506, 1989
- 3480 [135] J. Neyman and E. S. Pearson, “On the problem of the most efficient tests of
 3481 statistical hypotheses”. Springer-Verlag, (1992).
- 3482 [136] A.L. Read. “Modified frequentist analysis of search results (the CL_s method),”
 3483 (2000). CERN-OPEN-2000-205.
- 3484 [137] C. Palmer. “Searches for a Light Higgs with CMS”, CMS-CR-2012-215. <https://cds.cern.ch/record/1560435>.

- 3486 [138] A. Wald, “Tests of statistical hypotheses concerning several parameters when
 3487 the number of observations is large”, Transactions of the American Mathematical
 3488 society, vol. 54, no. 3, pp. 426–482, (1943).
- 3489 [139] G. Cowan, K. Cranmer, E. Gross, and O. Vitells, “Asymptotic formulae for
 3490 likelihood-based tests of new physics”, European Physical Journal C, vol. 71,
 3491 p. 1554, (2011).
- 3492 [140] S. S. Wilks, “The Large-Sample Distribution of the Likelihood Ratio for Testing
 3493 Composite Hypotheses”, Annals of Mathematical Statistics, vol. 9, pp. 60–62,
 3494 (03, 1938).
- 3495 [141] B. Hespel, F. Maltoni, and E. Vryonidou, “Higgs and Z boson associated pro-
 3496 duction via gluon fusion in the SM and the 2HDM”, JHEP 06 (2015) 065,
 3497 [https://dx.doi.org/10.1007/JHEP06\(2015\)065](https://dx.doi.org/10.1007/JHEP06(2015)065), arXiv:1503.01656.
- 3498 [142] ATLAS Collaboration, “Measurements of Higgs boson pro-
 3499 duction and couplings in diboson final states with the AT-
 3500 LAS detector at the LHC”, Phys. Lett. B726 (2013) 88–119,
 3501 doi:10.1016/j.physletb.2014.05.011, 10.1016/j.physletb.2013.08.010,
 3502 arXiv:1307.1427. [Erratum: Phys. Lett.B734,406(2014)].
- 3503 [143] CMS Collaboration, “Search for the associated production of a Higgs boson
 3504 with a single top quark in proton-proton collisions at $\sqrt{s} = 8$ TeV”, JHEP 06
 3505 (2016) 177, doi:10.1007/JHEP06(2016)177, arXiv:1509.08159.
- 3506 [144] B. Stieger, C. Jorda Lope et al., “Search for Associated Production of a Single
 3507 Top Quark and a Higgs Boson in Leptonic Channels”, CMS Analysis Note CMS
 3508 AN-14-140, 2014.

- 3509 [145] M. Peruzzi, C. Mueller, B. Stieger et al., “Search for ttH in multilepton final
3510 states at $\sqrt{s} = 13$ TeV”, CMS Analysis Note CMS AN-16-211, 2016.
- 3511 [146] CMS Collaboration, “Search for H to bbar in association with a single top quark
3512 as a test of Higgs boson couplings at $\sqrt{s} = 13$ TeV”, CMS Physics Analysis
3513 Summary CMS-PAS-HIG-16-019, 2016.
- 3514 [147] CMS Collaboration, “Search for production of a Higgs boson and a single top
3515 quark in multilepton final states in proton collisions at $\sqrt{s} = 13$ TeV”, CMS
3516 Physics Analysis Summary CMS-PAS-HIG-17-005, 2016.
- 3517 [148] CMS Collaboration, “PdmV2016Analysis,” (2016). <https://twiki.cern.ch/twiki/bin/viewauth/CMS/PdmV2016Analysis#DATA>, last accessed 11.04.2016.
- 3519 [149] M. Peruzzi, F. Romeo, B. Stieger et al., “Search for ttH in multilepton final1
3520 states at $\sqrt{s} = 13$ TeV”, CMS Analysis Note CMS AN-17-029, 2017.
- 3521 [150] B. Maier, “SingleTopHiggProduction13TeV”, February, 2016. <https://twiki.cern.ch/twiki/bin/viewauth/CMS/SingleTopHiggsGeneration13TeV>.
- 3523 [151] B. WG, “BtagRecommendation80XReReco”, February, 2017. <https://twiki.cern.ch/twiki/bin/view/CMS/BtagRecommendation80XReReco>.
- 3525 [152] CMS Collaboration, “Identification of b quark jets at the CMS Experiment
3526 in the LHC Run 2”, CMS Physics Analysis Summary CMS-PAS-BTV-15-001,
3527 2016.
- 3528 [153] CMS Collaboration, “Baseline muon selections for Run-II.” <https://twiki.cern.ch/twiki/bin/view/CMSPublic/SWGuideMuonIdRun2>, last accessed on
3529 24.02.2018.

- 3531 [154] G. Petrucciani and C. Botta, “Two step prompt muon identification”, January,
3532 2015. [https://indico.cern.ch/event/368007/contribution/2/material/
3533 slides/0.pdf](https://indico.cern.ch/event/368007/contribution/2/material/slides/0.pdf).
- 3534 [155] H. Brun and C. Ochando, “Updated Results on MVA eID with 13 TeV samples”,
3535 October, 2014. [https://indico.cern.ch/event/298249/contribution/3/
3536 material/slides/0.pdf](https://indico.cern.ch/event/298249/contribution/3/material/slides/0.pdf).
- 3537 [156] K. Rehermann and B. Tweedie, “Efficient Identification of Boosted Semileptonic
3538 Top Quarks at the LHC”, JHEP 03 (2011) 059, [https://dx.doi:10.1007/
3539 JHEP03\(2011\)059](https://dx.doi.org/10.1007/JHEP03(2011)059), arXiv:1007.2221.
- 3540 [157] CMS Collaboration. “Tag and Probe”, [https://twiki.cern.ch/twiki/bin/
3541 view/CMS/TagAndProbe](https://twiki.cern.ch/twiki/bin/view/CMS/TagAndProbe), last accessed on 02.03.2018.